

# **IMPLEMENTATION AND VALIDATION OF A UNB VIENNA MAPPING FUNCTIONS SERVICE**

**MATTHEW MCADAM**

**May 2013**



**TECHNICAL REPORT  
NO. 284**

**IMPLEMENTATION AND VALIDATION  
OF A UNB VIENNA MAPPING FUNCTIONS  
SERVICE**

Matthew McAdam

Department of Geodesy and Geomatics Engineering  
University of New Brunswick  
P.O. Box 4400  
Fredericton, N.B.  
Canada  
E3B 5A3

May 2013

© Matthew McAdam, 2013



## PREFACE

This technical report is a reproduction of a thesis submitted in partial fulfillment of the requirements for the degree of Master of Science in Engineering in the Department of Geodesy and Geomatics Engineering, May 2013. The research was supervised by Dr. Marcelo Santos, and support was provided by the Natural Sciences and Engineering Research Council of Canada.

As with any copyrighted material, permission to reprint or quote extensively from this report must be received from the author. The citation to this work should appear as follows:

McAdam, Matthew (2013). *Implementation and Validation of a UNB Vienna Mapping Functions Service*. M.Sc.E. thesis, Department of Geodesy and Geomatics Engineering Technical Report No. 284, University of New Brunswick, Fredericton, New Brunswick, Canada, 305 pp.

# Abstract

The mitigation of space borne radio signal perturbations in the neutral atmosphere is necessary for high precision position applications. Over the years there have been many methods for dealing with these perturbations, but the most popular modern method to deal with such effects is to model the signal delay at zenith with a corresponding mapping function that describes the elevation angle dependency of the signal. There have been many formulations and realizations of mapping functions, but the Vienna Mapping Functions (VMF) have proven to be most accurate to date. The Vienna Mapping Functions (VMF) are unique in that they rely solely on information from an external data source, namely a numerical weather prediction model (NWP). The development of the VMF represents a shifting paradigm in which geodetic corrections are moving from simple mathematical closed form type solutions to solutions based on large amounts of external data. However, there have been many differing institutions creating many differing corrections based on many differing underlying models and datasets.

The intent of this work is to investigate the influence of differing external datasets and modelling algorithms with a new realization of the VMF1. This is accomplished with the creation of a UNB Vienna Mapping Functions Service (VMF1) where several VMF1 products have been created with an independent data source (NCEP and CMC) and independent ray-tracing algorithms (UNB Ray tracer). The new service will not only improve the redundancy of currently available corrections, stimulate the use of the VMF1 corrections and add to the creation of a consistent set of corrections based on the same

underlying external datasets, but the new service will help to appreciate the influence of the application of these external datasets.

The resulting UNB-VMF1 service has been validated against the existing service operated at TU Vienna. Three realizations have been created: (a) an NCEP based product, (b) CMC (GDPS) based product, and a (c) forecast products based on 24-42h hour forecast from the CMC. The validation of the NCEP based product has been conducted over an 11-year period and the remaining products have been evaluated over an 8-month period. All products have been evaluated in the gridded domain and the position domain with the comparison of PPP solutions. With respect to the existing VMF1 service, all products are considered equivalent at the  $1\sigma$  level, but the NCEP based product exceeds the accuracy of the VMF1 at the  $3\sigma$  level. In particular, the NCEP based product performs poorly in regions of steep topography due to limitations of the model's integration of the underlying orography.

In addition to the validation of the service, the NCEP and CMC numerical weather prediction models (NWP), and an empirical model known as the GPT, have been assessed against measured in-situ meteorological measurements (pressure, temperature and humidity) and hydrostatic zenith delays computed by in-situ measurements. The NCEP dataset performed the worst out of the selected NWPs and the GPT performed worse in general. The GPT and NCEP exhibited a latitude dependent bias in the RMS of the difference in pressure and hydrostatic zenith delay. The CMC results did not exhibit any noticeable latitude dependency for these parameters. Each dataset exhibited a seasonal trend where the RMS of the difference is larger during the winter months for the pressure parameter. Both the CMC and NCEP models exhibited a trend where the RMS of the difference in humidity correlated with the season and latitude. In regions and times of the year when water vapour content is largest, both NWPs experienced a degradation in their ability to model the humidity parameter.

# Dedication

*for Alison*

# Acknowledgements

I would like to acknowledge the following for the help and support in the preparation of this thesis:

I would like to thank Dr. Marcelo Santos, my supervisor, for affording me the opportunity to study at the University. Dr. Santos' wealth of knowledge, kind nature and confidence in me kept me focused (as long as I was not trying to build electric motors out of paper clips and magnets) and his willingness to always help with any difficulties that arise was indispensable.

I would like to thank Dr. Adam Chrzanowski for convincing me that I could study at the graduate level. This thesis would not have existed without this conversation. I would also like to thank Dr. Chrzanowski for always having interesting work for me, which allowed me gain essential practical experience to go along with the theoretical foundations I have studied. Additionally, I would like to thank Dr. Richard Langley for always being gracious with my physics questions and Dr. James Secord for always being available for any survey related questions.

I would also like to thank ACE-NET for access to their computing resources. Without the super computing resources at ACE-NET the realization of this work would have been exceedingly tedious and enormously time consuming. In particular, I would like to thank the help of Joey Bernard for his continual technical expertise in the technical implementation of the service described herein as well as any computational (or philosophical) quandary I may have found myself in.

I would like to thank the weather services, National Centers for Environmental Prediction (NCEP) for access to the Re-Analysi 1 datasets, and the Canadian Meteorological Centre (CMC) for access to their global (GDPS), regional (RDPS), and high-resolution (HRDPS) datasets. I would also like to extend my thanks to the International GNSS Service (IGS) for access to their GNSS datasets (orbital, clock and observation products).

I would like to thank all the students, both graduate and undergraduate, that have help me along the way. In particular, I would like to thank Felipe Nievinski for his invaluable help in teaching me the details of the UNB ray tracer, as well as showing me why commenting code is completely unnecessary. I would like to thank Landon Urquhart and Alex Garcia for taking time to help me get acquainted with GAPS. I would also like to thanks those who I shared E-19 with, James and Justine.

I would also like to thank the National Science and Research Council for their financial contributions in support of this work. I could not have embarked on these studies without their kind contribution.

Lastly, I would like to offer my deepest gratitude to my wife Alison. Her support, patience and unyielding confidence in me was invaluable, and this thesis could not have been realized without her. I look forward to teaching our soon to be little minion how to cut the lawn together!

# Table of Contents

<b>Abstract</b>	<b>ii</b>
<b>Dedication</b>	<b>iv</b>
<b>Acknowledgments</b>	<b>v</b>
<b>Table of Contents</b>	<b>vii</b>
<b>List of Tables</b>	<b>xi</b>
<b>List of Figures</b>	<b>xiii</b>
<b>Abbreviations</b>	<b>xx</b>
<b>1 Introduction</b>	<b>1</b>
1.1 Motivation . . . . .	5
1.2 Contribution . . . . .	9
1.3 Outline . . . . .	10
1.3.1 Additional Notes on Notation . . . . .	10
<b>2 Background: Modelling GNSS Signals in the Neutral Atmosphere</b>	<b>11</b>
2.1 The Neutral Atmosphere . . . . .	11
2.2 Delay in the Neutral Atmosphere . . . . .	13
2.2.1 Index of Refraction . . . . .	14
2.2.2 Refractivity . . . . .	17
2.2.3 Signal Delay in the Neutral Atmosphere . . . . .	21
2.3 Modelling in the Neutral Atmosphere Revisited . . . . .	22
2.3.1 Ray Tracing . . . . .	24
2.3.2 Zenith Delays . . . . .	25
2.3.3 Mapping Functions . . . . .	26
2.4 Numerical Weather Prediction Models . . . . .	28
2.4.1 Model Dynamics . . . . .	29
2.4.2 Model Types . . . . .	30
2.4.3 Parameterization . . . . .	32
2.4.4 Assimilation . . . . .	32
<b>3 Assessment of Numerical Weather Prediction Models</b>	<b>36</b>

3.1	Numerical Weather Prediction Models . . . . .	37
3.2	Previous Work . . . . .	45
3.3	Assessment of NWP's . . . . .	48
3.3.1	Description of Experiment . . . . .	48
3.3.2	Discussion and Results . . . . .	52
3.3.2.1	Pressure . . . . .	55
3.3.2.2	Temperature . . . . .	61
3.3.2.3	Specific Humidity . . . . .	66
3.3.2.4	Hydrostatic Zenith Delay . . . . .	69
3.4	Effect of Numerical Weather Model Grid Resolution . . . . .	72
3.4.1	Description of Experiment . . . . .	74
3.4.2	Discussion and Results . . . . .	76
3.5	Summary . . . . .	85
<b>4</b>	<b>The UNB Vienna Mapping Function Service</b>	<b>88</b>
4.1	Existing VMF1 Service . . . . .	90
4.2	The UNB Vienna Mapping Function Service . . . . .	92
4.2.1	Mission Description . . . . .	92
4.2.2	Description of Fundamental Models . . . . .	92
4.2.2.1	Mapping Function Model . . . . .	92
4.2.2.2	Ray Tracing Algorithm . . . . .	96
4.2.2.3	Numerical Weather Prediction Models . . . . .	98
4.2.2.4	Orography . . . . .	99
4.2.3	System Integration . . . . .	102
4.2.3.1	UNB-VMF1 System Architecture . . . . .	105
4.2.4	Product Description . . . . .	108
4.2.4.1	Grid Definition . . . . .	109
4.2.4.2	unbvmfG . . . . .	109
4.2.4.3	unbvmfGcmc . . . . .	112
4.2.4.4	unbvmfP . . . . .	114
4.2.4.5	File Naming Conventions . . . . .	116
4.2.5	End-User Interface . . . . .	116
4.3	Summary . . . . .	117
<b>5</b>	<b>Validation of the UNB Vienna Mapping Function Service</b>	<b>122</b>
5.1	Comparison of VMF1 Gridded Products . . . . .	123
5.1.1	Previous Work . . . . .	123
5.1.2	Description of Experiment . . . . .	124
5.1.3	Comparison of UNB-VMF1 Products . . . . .	127
5.1.3.1	UNB-VMF1(NCEP) vs VMF1(ECMWF) . . . . .	127
5.1.3.1.1	Hydrostatic Zenith Delays . . . . .	128
5.1.3.1.2	Non-Hydrostatic Zenith Delays . . . . .	131
5.1.3.1.3	Hydrostatic Equivalent Height Error . . . . .	138
5.1.3.1.4	Non-Hydrostatic Equivalent Height Error . . . . .	154
5.1.3.2	UNB-VMF1(CMC) vs VMF1(ECMWF) . . . . .	158



5.1.3.2.1	Hydrostatic Equivalent Height Error . . . . .	160
5.1.3.2.2	Non-Hydrostatic Equivalent Height Error . . . . .	162
5.1.3.3	Forecast UNB-VMF1(CMC) vs UNB-VMF1 (CMC) . . . . .	164
5.1.3.3.1	Hydrostatic Equivalent Height Error . . . . .	164
5.1.3.3.2	Non-Hydrostatic Equivalent Height Error . . . . .	166
5.1.3.4	Forecast UNB-VMF1(CMC) vs Forecast VMF1(ECMWF) . . . . .	168
5.1.3.4.1	Hydrostatic Equivalent Height Error . . . . .	168
5.1.3.4.2	Non-Hydrostatic Equivalent Height Error . . . . .	170
5.1.4	Summary and Recommendations . . . . .	172
5.2	Comparison of VMF1 Gridded Products in the Position Domain . . . . .	177
5.2.1	Description of Experiment . . . . .	177
5.2.2	Precise Point Positioning . . . . .	180
5.2.3	Results and Discussion . . . . .	184
5.2.3.1	UNB-VMF1 (NCEP) vs VMF1 (ECMWF) . . . . .	186
5.2.3.2	UNB-VMF1 vs VMF1 (All Products) . . . . .	196
5.2.4	Elevation Angle Cut-Off . . . . .	201
5.2.5	Summary and Recommendations . . . . .	204
<b>6</b>	<b>Conclusions and Recommendations</b> . . . . .	<b>207</b>
6.1	Summary . . . . .	207
6.2	Recommendations . . . . .	214
6.3	Future Work . . . . .	216
	<b>References</b> . . . . .	<b>219</b>
<b>A</b>	<b>Meteorological Parameter Comparison Supplemental</b> . . . . .	<b>229</b>
A.1	Meteorological Data Comparison . . . . .	229
A.1.1	Hydrostatic Zenith Delay . . . . .	235
<b>B</b>	<b>UNB-VMF1 Service Supplemental</b> . . . . .	<b>242</b>
B.1	UNB-VMF1 Process . . . . .	242
B.1.1	UNB-VMF1 Output File Format . . . . .	246
B.1.2	Download Process . . . . .	246
B.1.3	Submission Process . . . . .	248
B.1.4	Run Process . . . . .	250
B.1.5	Upload Process . . . . .	251
B.1.6	Miscellaneous Scripts . . . . .	253
<b>C</b>	<b>UNB-VMF1 Grid Comparison Supplemental</b> . . . . .	<b>254</b>
C.1	Additional Grid Comparison Plots . . . . .	254
C.1.1	UNB-VMF1 (NCEP) versus VMF1 (ECMWF) . . . . .	254
C.1.2	UNB-VMF1 (CMC) versus VMF1 (ECMWF) . . . . .	272
C.1.3	Forecast UNB-VMF1 (CMC-P) versus UNB-VMF1 (CMC) . . . . .	274
C.1.4	Forecast UNB-VMF1 (CMC-P) versus Forecast VMF1 (ECMWF) . . . . .	276
<b>D</b>	<b>UNB-VMF1 Position Domain Supplemental</b> . . . . .	<b>278</b>

D.1	Position Domain Comparisons . . . . .	278
D.1.1	UNB-VMF1 (NCEP) versus VMF1 (ECMWF) . . . . .	278
D.1.2	UNB-VMF1 versus VMF1 (ECMWF) - All Products . . . . .	297

**Vita**

# List of Tables

3.1	Summary of global mean, standard deviation, max absolute value of the difference in pressure for all 35 stations. January 1st to December 31st 2010. All measurements in millibars. . . . .	61
3.2	Summary of global mean, standard deviation, max absolute value of the difference in temperature for all 35 stations. January 1st to December 31st 2010. All measurements in Kelvin. . . . .	65
3.3	Summary of global mean, standard deviation, max absolute value of the difference in specific humidity for all 35 stations. January 1st to December 31st 2010. All measurements in kg/kg. . . . .	69
3.4	Summary of global mean, standard deviation, max absolute value of the difference in zenith hydrostatic delay for all 35 stations. January 1st to December 31st 2010. All measurements in mm. . . . .	72
3.5	Station Summary for grid resolution assessment . . . . .	75
3.6	Difference zenith hydrostatic delay for each station separated by epoch (ray-traced minus Saastamoinen). All measurements in mm. . . . .	84
4.1	Values for hydrostatic $c$ coefficient implemented by the UNB-VMF1 service (from Boehm et al., 2006). . . . .	95
4.2	Values for height reduction coefficients used by $f(e, a_{ht}, b_{ht}, c_{ht})$ and implemented by the UNB-VMF1 service (from Niell [1996]). . . . .	96
4.3	Non-hydrostatic coefficients implemented by the UNB-VMF1 service (from Niell [1996] at $\phi = 45^\circ$ ). . . . .	96
4.4	Distinguishing characteristics of NWP's implemented in the UNB-VMF1 service . . . . .	99
4.5	Example of sample data (showing only a portion of full vertical profile) from CMC's GDPS that can result in erroneous extrapolations . . . . .	101
4.6	ACEnet cluster uptime from March 2011 until March 2012 . . . . .	103
4.7	File naming conventions for UNB-VMF1 service . . . . .	116
4.8	Directory Structure for stored final UNB-VMF1 products . . . . .	117
4.9	Summary of UNB-VMF1 products . . . . .	118
4.10	Summary of VMF1 products from the existing VMF1 service . . . . .	119
5.1	Summary of grid comparisons and computed parameters for UNB-VMF1 validation . . . . .	128
5.2	Summary of global combined yearly mean and standard deviation separated by 4 times daily epochs for the difference in hydrostatic zenith delay. unbvmfG (NCEP) minus vmfG (ECMWF). (all values in millimetres). . .	132

5.3	Summary of global combined yearly mean bias and standard deviation separated by each 4 times daily epochs for the difference in non-hydrostatic zenith delay. unbvmfG (NCEP) minus vmfG (ECMWF) (all values in millimetres). . . . .	137
5.4	Summary of global combined yearly mean bias and standard deviation separated by each 4 times daily epochs for the equivalent height error due to the hydrostatic mapping function. unbvmfG (NCEP) minus vmfG (ECMWF) (all values in millimetres). . . . .	142
5.5	Summary of global combined yearly mean and standard deviation separated by each 4 times daily epochs for the equivalent height error due to the non-hydrostatic component. unbvmfG (NCEP) minus vmfG (ECMWF) (all values in millimetres). . . . .	157
5.6	Summary of difference in ray-traced zenith delays for all comparisons at each epoch of the 4× daily products. All values in millimetres. . . . .	174
5.7	Summary of difference in mapping functions expressed as equivalent height error for all comparisons at each epoch of the 4× daily products. All values in millimetres. . . . .	175
5.8	Summary of 3σ global discrepancies. All values in millimetres. . . . .	176
5.9	Summary of comparisons made in the position domain . . . . .	179
5.10	Summary of yearly bias and RMSE for UNB-VMF1 (NCEP) minus VMF1 (ECMWF) for 2001 to 2011. All dimensions in millimetres. . . . .	187
5.11	Summary of difference in the height component for all UNB-VMF1 comparisons for mean bias, RMSE, standard deviation, and maximum absolute difference. All values in millimetres for the year 2012. . . . .	201
5.12	Summary of elevation angle dependance for UNB-VMF1 (NCEP) minus VMF1 (ECMWF). Results for the interval January 1st, 2012 to August 31, 2012 (includes all stations). Dimensions in millimetres. . . . .	204
A.1	Summary of meteorological sensor metadata for each sensor used in the meteorological parameter comparison in Chapter 3. . . . .	230
A.2	Summary of mean difference and standard deviation for the difference in pressure. January 1st to December 31st, 2010 (all values in mbar) . . . . .	232
A.3	Summary of mean difference and standard deviation for the difference in temperature. January 1st to December 31st, 2010 (all values in K) . . . . .	233
A.4	Summary of mean difference and standard deviation for the difference in specific humidity. January 1st to December 31st, 2010 (all values in kg/kg) . . . . .	234
A.5	Summary of statistics for computed hydrostatic zenith delay differences (all values in mm) . . . . .	235
B.1	Summary of download scripts for each cluster on ACE-NET. The date implemented, execution time, and script name are listed for each NWP type.	243
B.2	Summary of computation scripts for each cluster on ACE-NET. Includes both the submit and run scripts. The date implemented, execution time, and script name are listed for each NWP type. . . . .	244

B.3	Summary of maintenance scripts for each cluster on ACE-NET. Includes both the submit and run scripts. The date implemented, execution time, and script name are listed for each NWP type. . . . .	245
B.4	Description of UNB-VMF1 product header . . . . .	247
D.1	Summary of yearly difference in height between PPP solution with UNB-VMF1 (NCEP) and VMF1 (ECMWF) - (NCEP minus ECMWF). All measurements in millimetres. . . . .	279
D.2	Summary of bias, RMSE, standard deviation, and $3\sigma$ range of values for the difference in height by PPP between UNB-VMF1 (NCEP) minus VMF1 (ECMWF). Epoch: 2001 to 2011. . . . .	280
D.3	Summary of the PPP solution for the difference in height for UNB-VMF1 (NCEP and CMC) minus VMF1 (ECMWF). January 1st to August 31st 2012. All dimensions in millimetres . . . . .	298
D.4	Summary of the PPP solution for the difference in height for the forecast product, unbvmfP. UNB-VMF1 (CMC-P) minus VMF1 (ECMWF). The columns listed as CMC-P minus CMC is relative to the unbvmfGcmc product. Match 17th to August 31st 2012. All dimensions in millimetres . . . . .	299

## List of Figures

2.1	Refraction of an electromagnetic wave through glass. The arrows represent the direction of travel and the dashed lines are the wave crests. $\lambda_o$ is the incident wavelength and $\lambda$ is the wavelength after refraction. After Feynmann (1963). . . . .	15
2.2	ECMWF observation coverage for January 15th, 2012 00UTC. (a) Ship and terrestrial stations; (b) Aircraft; (c) GPSRO, and (d) IASI. From ECMWF, (2012b). . . . .	34
2.3	Typical intermittent process flow for a global numerical weather prediction model analysis cycle performed at 00, 06, 12 and 18 UTC. After Kalnay (2003). . . . .	35
3.1	Difference in Non-Hydrostatic refractivity - NCEP minus CMC . . . . .	40
3.2	RMSE for Mean Sea Level Pressure; 24h forecast verified with NWP analysis. From 1996 to present (from ECMWF, 2012) . . . . .	43
3.3	RMSE for Temperature at 850 hPa; 24h forecast verified with observations. From 1996 to present (from ECMWF, 2012). . . . .	44
3.4	Location of IGS Stations . . . . .	50
3.5	Weekly standard deviation of the difference in pressure (a) Northern Hemisphere; and (b) Southern Hemisphere. Note the scale difference for each subplot. . . . .	57

3.6	Mean Sea Level Pressure from CMC (GDPS) (a) February 21, 2012; and (b) August 1, 2012 . . . . .	59
3.7	Mean and standard deviation of the difference in pressure with respect to latitude. January 1st to December 31st, 2010. . . . .	60
3.8	Histogram of difference in pressure for the GPT, NCEP Re-Analysis 1, and CMC (GDPS) . . . . .	62
3.9	Mean and standard deviation of the difference in temperature with respect to latitude. January 1st to December 31st, 2010. . . . .	63
3.10	Weekly mean of the difference in temperature (a) Northern Hemisphere; and (b) Southern Hemisphere (note the scale difference on the y-axis) . . . . .	64
3.11	Histogram of difference in temperature (in Kelvin) for the GPT, NCEP Re-Analysis 1, and CMC (GDPS) . . . . .	65
3.12	Mean and standard deviation of the difference in specific humidity with respect to latitude. January 1st to December 31st, 2010. . . . .	67
3.13	Weekly mean of the difference in specific humidity (a) Northern Hemisphere; and (b) Southern Hemisphere (note the scale difference on the y-axis) . . . . .	68
3.14	Histogram of difference in specific humidity (kg/kg) for the GPT, NCEP Re-Analysis 1, and CMC (GDPS) . . . . .	70
3.15	Mean and standard deviation of the difference in ZHD with respect to latitude. January 1st to December 31st, 2010. . . . .	71
3.16	Histogram of difference in ZHD for the NCEP Re-Analysis 1(blue), and CMC (GDPS)(red) . . . . .	72
3.17	Difference in (a) hydrostatic, and (b) non-hydrostatic slant delays. August 15, 2012. Station: WSLR. . . . .	77
3.18	Difference in mapping function at an elevation angle of 5° expressed as equivalent height error. August 15, 2012. . . . .	78
3.19	Difference in pressure (NWP minus Measured) - HRDPS(blue), GDPS(red), and RDPS(green). All measurements in mbar. April 4th to August 31st 2012 . . . . .	79
3.20	Mean difference in meteorological parameters (NWP minus Measured) - HRDPS(blue), GDPS(red), and RDPS(green). Top: Pressure (mbar); Middle: Temperature (K); Bottom: Specific Humidity (kg/kg). April 4th to August 31st, 2012 . . . . .	81
3.21	Standard deviation difference in meteorological parameters (NWP minus Measured) - HRDPS(blue), GDPS(red), and RDPS(green). Top: Pressure (mbar); Middle: Temperature (K); Bottom: Specific Humidity (kg/kg). April 4th to August 31st, 2012 . . . . .	82
3.22	Mean and standard deviation of the difference in ZHD with respect to ZHD computed by Saastamoinen with measured pressure. April 4th to August 31st 2012 . . . . .	83
4.1	Aspects of building the UNB Vienna Mapping Function Service . . . . .	89
4.2	Typical extrapolation configuration when height of UNB-VMF1 grid point lies outside of NWP as defined by <i>orography.ell</i> . . . . .	100
4.3	Computational efficiency when parallelizing jobs on ACEnet . . . . .	105

4.4	UNB-VMF1 System Architecture . . . . .	106
4.5	UNB-VMF1 grid definition (not to scale) . . . . .	110
4.6	Standard availability of unbvmfG . . . . .	111
4.7	Standard availability of unbvmfGcmc . . . . .	113
4.8	Standard availability of unbvmfP . . . . .	115
5.1	Data model used for grid comparisons . . . . .	125
5.2	Combined difference in hydrostatic zenith delay for the years 2001 to 2011 for unbvmfG (NCEP) minus vmfG (ECMWF). (a) Combined mean bias (b) Combined standard deviation. . . . .	129
5.3	Maximum absolute values of the difference between unbvmfG (NCEP) and vmfG (ECMWF) hydrostatic zenith delays for the years 2001 to 2011. . . . .	131
5.4	Histogram for the difference between unbvmfG (NCEP) and vmfG (ECMWF) hydrostatic zenith delays for the years 2001 to 2011. . . . .	132
5.5	Difference in non-hydrostatic zenith delay for the years 2001 to 2011 for unbvmfG (NCEP) minus vmfG (ECMWF). (a) Combined mean bias (b) Combined standard deviation. . . . .	134
5.6	Maximum absolute values of the difference between unbvmfG (NCEP) and vmfG (ECMWF) non-hydrostatic zenith delays for the years 2001 to 2011. . . . .	135
5.7	Histogram for the difference between unbvmfG (NCEP) and vmfG (ECMWF) non-hydrostatic zenith delays for the years 2001 to 2011. . . . .	136
5.8	Equivalent height error due to the hydrostatic mapping function for the years 2001 to 2011 for unbvmfG (NCEP) minus vmfG (ECMWF). (a) Combined mean bias (b) Combined standard deviation. . . . .	139
5.9	Maximum absolute difference of the equivalent height error due to the hydrostatic mapping function for unbvmfG (NCEP) minus vmfG (ECMWF). (a) 2001 to 2011 (b) 2002 to 2004. . . . .	140
5.10	Histogram for the difference between unbvmfG (NCEP) and vmfG (ECMWF) expressed as an equivalent height error for the years 2001 to 2011. . . . .	141
5.11	Difference in the hydrostatic mapping functions expressed as an equivalent height error for unbvmfG (NCEP) minus unbvmfGcmc (CMC). Epoch: January 1st to August 30th 2012. . . . .	143
5.12	Difference in the hydrostatic mapping functions expressed as an equivalent height error for UNB-VMF1 (NCEP) minus VMF1 (ECMWF) where a constant radius of the Earth has been used for the UNB-VMF1 product. Epoch: August 1st to August 30th 2012. . . . .	144
5.13	Land-sea masks for (b) NCEP Re-Analysis 1 (unbvmfG) (c) ECMWF and (d) CMC GDPS (unbvmfGcmc). Illustrates the strong spatial correlation of the increased standard deviation for the equivalent height error of the hydrostatic component (as shown in (a)) due to the differences in land-sea masks. . . . .	146
5.14	Difference in hydrostatic refractivity profile between NCEP Re-Analysis 1 and CMC (GDPS) - (NCEP minus CMC) - on May 15th, 2012 12UTC for station COPO located at an elevation of 479 m. . . . .	148

5.15	NCEP Re-Analysis 1 orography given by the surface geopotential height.	150
5.16	Cross-section at 30°S from NCEP Re-Analysis 1 and CMC (GDPS) surface geopotential height field . . . . .	151
5.17	Differences of NWP model parameters (a) pressure and (b) temperature between NCEP Re-Analysis 1 and CMC GDPS for April 15 to April 21 2012 . . . . .	153
5.18	Equivalent height error due to the non-hydrostatic mapping function for the years 2001 to 2011 for unbvmfG (NCEP) minus vmfG (ECMWF). (a) Combined mean bias (b) Combined standard deviation. . . . .	155
5.19	Maximum absolute values of the difference between unbvmfG (NCEP) and vmfG (ECMWF) mapping functions expressed as an equivalent height error for the years 2001 to 2011. . . . .	156
5.20	Differences of NWP model parameter specific humidity between NCEP Re-Analysis 1 and CMC GDPS for April 15 to April 21 2012. . . . .	158
5.21	Specific humidity (kg/kg) at the 1000mb pressure level for (a) NCEP Re-Analysis 1 and (b) CMC (GDPS) on April 18th, 2012 at 12UTC. . . . .	159
5.22	Equivalent height error due to the hydrostatic mapping function for the year 2012 for unbvmfGcmc (CMC) minus vmfG (ECMWF). (a) Mmean bias (b) Standard deviation. January 1st to September 30th 2012. . . . .	161
5.23	Equivalent height error due to the non-hydrostatic mapping function for the year 2012 for unbvmfGcmc (CMC) minus vmfG (ECMWF). (a) Mean (b) Standard deviation. January 1st to September 30th 2012. . . . .	163
5.24	Equivalent height error due to the hydrostatic mapping function for the year 2012 for unbvmfP (CMC) minus unbvmfGcmc (CMC). (a) Mean bias (b) Standard deviation. March 17th to September 30th 2012. . . . .	165
5.25	Equivalent height error due to the non-hydrostatic mapping function for the year 2012 for unbvmfP (CMC) minus unbvmfGcmc (CMC). (a) Mean bias (b) Standard deviation. March 17th to September 30th 2012. . . . .	167
5.26	Equivalent height error due to the hydrostatic mapping function for the year 2012 for unbvmfP (CMC) minus vmfG-FC (ECMWF). (a) Mean bias (b) Standard deviation. March 17th to September 30th 2012. . . . .	169
5.27	Equivalent height error due to the non-hydrostatic mapping function for the year 2012 for unbvmfP (CMC) minus Forecast vmfG-FC (ECMWF). (a) Mean bias (b) Standard deviation. March 17th to September 30th 2012. . . . .	171
5.28	Summary of 32 IGS stations used for GNSS positioning analysis. . . . .	178
5.29	Station OHI2 time series of the difference in height for (a) PPP results (red); (b) due to the hydrostatic component (blue); and (c) due to the non-hydrostatic component. . . . .	185
5.30	Yearly bias for UNB-VMF1 (NCEP) minus VMF1 (ECMWF) for all 32 stations and associated error bars. . . . .	188
5.31	Position differences from the PPP solution fro station SCUB. unbvmfG (NCEP) minus vmfG (ECMWF). 2001 to 2011. . . . .	189
5.32	All differences in height for all 32 stations, for all daily solutions from 2001 to 2011. unbvmfG (NCEP) minus vmfG (ECMWF). . . . .	190



5.33	Difference in height from the PPP solution (red) and hydrostatic/non-hydrostatic mapping function separation error (blue). unbvmfG (NCEP) minus vmfG (ECMWF). . . . .	192
5.34	Difference in height from the PPP solution (red) and non-hydrostatic equivalent height error (green), and hydrostatic equivalent height error (blue). unbvmfG (NCEP) minus vmfG (ECMWF). . . . .	193
5.35	Difference in height from the PPP solution (red) and non-hydrostatic equivalent height error (green), and hydrostatic equivalent height error (blue) for stations (a) YELL and (b) THU3. unbvmfG (NCEP) minus vmfG (ECMWF). . . . .	194
5.36	RMSE of the difference in height with respect to latitude for all 32 stations. unbvmfG (NCEP) minus vmfG (ECMWF). 2001 to 2011. . . . .	196
5.37	Mean Bias for the difference in height for all 32 stations. unbvmfG (NCEP) minus vmfG (ECMWF). 2001 to 2011. . . . .	197
5.38	(a) Mean and (b) RMSE of the difference in height between UNB-VMF1 and VMF1 for (i) unbvmfG (NCEP) minus vmfG (ECMWF) shown in green and (b) unbvmfGcmc (CMC) minus vmfG (ECMWF) shown in yellow. January 1st to August 31st, 2012. All values in millimetres. . . . .	198
5.39	Histogram for the difference in height for (a) unbvmfG (NCEP) minus vmfG (ECMWF) shown in blue, (b) unbvmfGcmc (CMC) minus vmfG (ECMWF) shown in red. . . . .	199
5.40	(a) Mean and (b) RMSE difference in height for (i) unbvmfP (CMC) minus unbvmfGcmc (CMC) (ii) unbvmfGcmc (CMC) minus vmfG (ECMWF); and (iii) unbvmfP (CMC) minus vmfG (ECMWF). March 17th to August 31st, 2012. Please note item (ii) extends from January 1st to August 31st, 2012. All dimensions in millimetres. . . . .	200
A.1	Difference in ray-traced zenith hydrostatic delay from zenith hydrostatic delay computed from site pressure. (NWP minus SITE). January 1st to December 31st 2010. . . . .	236
B.1	Sample Output from the UNB-VMF1 service for the unbvmfG product on January 1, 2012 . . . . .	246
B.2	UNB-VMF1 NWP data download for NCEP process flow . . . . .	248
B.3	UNB-VMF1 submission script process flow for unbvmfG. . . . .	249
B.4	UNB-VMF1 run script for unbvmfG. . . . .	252
C.1	Difference in hydrostatic (C.1.1 and C.1.2) and non-hydrostatic (C.1.3 and C.1.4) mapping functions expressed as equivalent height errors for UNB-VMF1 (NCEP) minus VMF1 (ECMWF). EPOCH: 2001. . . . .	255
C.2	Difference in hydrostatic (C.2.1 and C.2.2) and non-hydrostatic (C.2.3 and C.2.4) mapping functions expressed as equivalent height errors for UNB-VMF1 (NCEP) minus VMF1 (ECMWF). EPOCH: 2002. . . . .	256
C.3	Difference in hydrostatic (C.3.1 and C.3.2) and non-hydrostatic (C.3.3 and C.3.4) mapping functions expressed as equivalent height errors for UNB-VMF1 (NCEP) minus VMF1 (ECMWF). EPOCH: 2003. . . . .	257

C.4	Difference in hydrostatic (C.4.1 and C.4.2) and non-hydrostatic (C.4.3 and C.4.4) mapping functions expressed as equivalent height errors for UNB-VMF1 (NCEP) minus VMF1 (ECMWF). EPOCH: 2004. . . . .	258
C.5	Difference in hydrostatic (C.5.1 and C.5.2) and non-hydrostatic (C.5.3 and C.5.4) mapping functions expressed as equivalent height errors for UNB-VMF1 (NCEP) minus VMF1 (ECMWF). EPOCH: 2005. . . . .	259
C.6	Difference in hydrostatic (C.6.1 and C.6.2) and non-hydrostatic (C.6.3 and C.6.4) mapping functions expressed as equivalent height errors for UNB-VMF1 (NCEP) minus VMF1 (ECMWF). EPOCH: 2006. . . . .	260
C.7	Difference in hydrostatic (C.7.1 and C.7.2) and non-hydrostatic (C.7.3 and C.7.4) mapping functions expressed as equivalent height errors for UNB-VMF1 (NCEP) minus VMF1 (ECMWF). EPOCH: 2007. . . . .	261
C.8	Difference in hydrostatic (C.8.1 and C.8.2) and non-hydrostatic (C.8.3 and C.8.4) mapping functions expressed as equivalent height errors for UNB-VMF1 (NCEP) minus VMF1 (ECMWF). EPOCH: 2008. . . . .	262
C.9	Difference in hydrostatic (C.9.1 and C.9.2) and non-hydrostatic (C.9.3 and C.9.4) mapping functions expressed as equivalent height errors for UNB-VMF1 (NCEP) minus VMF1 (ECMWF). EPOCH: 2009. . . . .	263
C.10	Difference in hydrostatic (C.10.1 and C.10.2) and non-hydrostatic (C.10.3 and C.10.4) mapping functions expressed as equivalent height errors for UNB-VMF1 (NCEP) minus VMF1 (ECMWF). EPOCH: 2010. . . . .	264
C.11	Difference in hydrostatic (C.11.1 and C.11.2) and non-hydrostatic (C.11.3 and C.11.4) mapping functions expressed as equivalent height errors for UNB-VMF1 (NCEP) minus VMF1 (ECMWF). EPOCH: 2011. . . . .	265
C.12	Absolute value of the difference in hydrostatic mapping functions expressed as equivalent height errors for UNB-VMF1 (NCEP) minus VMF1 (ECMWF). 2001-2011 . . . . .	266
C.13	Absolute value of the difference in non-hydrostatic mapping functions expressed as equivalent height errors for UNB-VMF1 (NCEP) minus VMF1 (ECMWF). 2001 - 2011 . . . . .	269
C.14	Difference in the hydrostatic zenith delay for the year 2012 for UNB-VMF1 (CMC) minus VMF1 (ECMWF). (a) Mean (b) Standard deviation. January 1st to September 30th 2012. . . . .	272
C.15	Difference in the hydrostatic zenith delay for the year 2012 for UNB-VMF1 (CMC) minus VMF1 (ECMWF). (a) Mean (b) Standard deviation. January 1st to September 30th 2012. . . . .	273
C.16	Difference in the hydrostatic zenith delay for the year 2012 for UNB-VMF1 (CMC-P) minus UNB-VMF1 (CMC). (a) Mean (b) Standard deviation. March 17th to September 30th 2012. . . . .	274
C.17	Difference in the non-hydrostatic zenith delay for the year 2012 for UNB-VMF1 (CMC-P) minus UNB-VMF1 (CMC). (a) Mean (b) Standard deviation. March 17th to September 30th 2012. . . . .	275
C.18	Difference in the hydrostatic zenith delay for the year 2012 for UNB-VMF1 (CMC-P) minus VMF1 (ECMWF). (a) Mean (b) Standard deviation. March 17th to September 30th 2012. . . . .	276

C.19	Difference in the non-hydrostatic zenith delay for the year 2012 for UNB-VMF1 (CMC-P) minus VMF1 (ECMWF). (a) Mean (b) Standard deviation. March 17th to September 30th 2012. . . . .	277
D.1	PPP coordinate time series difference for UNB-VMF1 (NCEP) minus VMF1 (ECMWF) for years 2001 to 2012. Top: Latitude; Middle: Longitude; Bottom: Height. . . . .	281
D.2	PPP coordinate time series difference for unbvmfG (NCEP), unbvmfGcmc (CMC), and unbvmfP (CMC-P) minus VMF1 (ECMWF). For unbvmfG and unbvmfGcmc: January 1st to August 31st. For unbvmfP: March 17th to August 31st 2012. All dimensions in millimetres. . . . .	300

# List of Symbols and Abbreviations

$zwd$	Non-hydrostatic zenith delay	m
$zhd$	Hydrostatic zenith delay	m
$\alpha$	azimuth	rads
$\epsilon$	elevation angle	rads
$\Delta L$	total delay	m
$\Delta L^z$	total zenith delay	m
$LHG$	Linear Horizontal Gradients	
$a_h$	Hydrostatic a-coefficient from hydrostatic mapping function	unitless
$a_w$	Non-hydrostatic a-coefficient from non-hydrostatic mapping function	unitless
$mf_h$	hydrostatic mapping function	unitless
$mh_w$	non-hydrostatic mapping function	unitless
$\tau$	total delay in units of time	s
$c$	vacuum speed of light	m/s
$v$	electromagnetic speed	m/s
$\lambda$	longitude	degrees
$\phi$	latitude	degrees
$h$	geodetic height	m
$H$	orthometric height	m
$q_E$	electric charge	Coloumbs
$\epsilon_o$	permittivity of free space	$m^{-3} kg^{-1} s^4 A^2$

$\omega$	angular frequency of radiation	rad/s
$\omega_o$	resonant frequency of an electron bound to an atom	rad/s
$\gamma$	dissipation constant	unitless
$m$	mass of an electron	kg
$\rho$	total density of air	$kg/m^3$
$k_1$	coefficient of refractivity	$\frac{K}{Pa}$
$k'_1$	coefficient of refractivity	$\frac{K}{Pa}$
$k_2$	coefficient of refractivity	$\frac{K}{Pa}$
$k_3$	coefficient of refractivity	$\frac{K^2}{Pa}$
$n$	index of refraction	unitless
$N_o$	real component of total refractivity	unit less
$N'$	dispersive component of total refractivity	unitless
$N''$	absorption component of total refractivity	unitless
$N$	refractivity	unitless
$N_h$	hydrostatic refractivity	unitless
$N_{nh}$	non-hydrostatic refractivity	unitless
$T$	Temperature	$^{\circ}K$
$RH$	Relative humidity	unitless
$q$	specific humidity	kg/kg
$P_d$	partial pressure of dry air	Pa
$P_w$	partial pressure of water vapour	Pa
$e_s$	saturation vapour pressure	Pa
$R_d$	dry gas constant	$\frac{J}{kg} K$
$R_w$	water vapour gas constant	$\frac{J}{kg} K$
$Z_w^{-1}$	inverse compressibility factor	unitless
$M_d$	molar mass of dry gas	$\frac{kg}{kmol}$
$M_w$	molar mass of water vapour	$\frac{kg}{kmol}$

$\ell$	along path distance	m
$\nabla \mathbf{n}$	gradient of refractivity	1/m
$\mathbf{r}$	position vector	m
NWP	Numerical Weather Prediction Models	
NCEP	National Centers for Environmental Prediction	
CMC	Canadian Meteorological Centre	
ECMWF	European Centre for Medium-Range Weather Forecasts	
IGS	International GNSS Service	
IERS	International Earth Rotation and Reference Systems Service	
GGOS	Global Geodetic Observing System	
NMF	Niell Mapping Function	
IMF	Isobaric Mapping Function	
VMF	Vienna Mapping Functions	
VMF1	Vienna Mapping Functions 1	
GMF	Global Mapping Functions	
GPT	Global Pressure and Temperature	
TRF	Terrestrial Reference Frame	
CRF	Celestial Reference Frame	
§	Section	

# Chapter 1

## Introduction

In the most basic sense, satellite based positioning systems are ranging systems that rely on the precise measurement of the transmission time for the emitted radio signals. Therefore, any perturbation of the transmitted radio signal along its path or any system timing errors will result in range errors that propagate into the positioning results. This work is focused solely on the propagation of the radio signals from satellite to receiver, so any system timing errors are outside of the scope. Moreover, the propagation errors studied are considered to be free of any extraneous effects due to the local receiving site. Therefore, any effects that are a result of multi-path or diffraction are not considered.

In the context of the propagation of radio signals from space-borne satellites, the signal's path is largely determined by two major interfaces: (a) the ionosphere, and the (b) neutral atmosphere. The ionosphere is that part of the atmosphere that extends from approximately 50 km to over a 1000 km overhead, and is electrically charged due to the interaction with the sun causing neutral atoms to be split into negatively charged electrons and positive ions. The ionosphere is a dispersive medium (meaning the index of refraction is frequency dependent) and first order effects can be dealt with effectively with the application of dual frequency receivers on Earth with the ionosphere-free linear combination. The focus of this work deals with the effects within the neutral atmosphere, so the effects

of the ionosphere are outside the scope<sup>1</sup>.

The neutral atmosphere is that electrically neutral part (within a certain frequency band which GNSS signals fall) of the atmosphere extending from the surface of the earth to about 80 km overhead. The neutral atmosphere has a delaying effect on transmitted radio waves, so the travel time of the signal is increased, which results in a positive range error. Traditionally, this effect has been referred to as the just the troposphere delay, and this is entirely valid since 75% of the total signal delay occurs in the troposphere, but not entirely correct [Spilker, 1996]. Since 25% of the signal delay still occurs outside of the troposphere, the more precise term is the neutral atmosphere delay. In any case, the delaying effect that has propagated into the satellite observations must be dealt with appropriately to achieve precise positioning results.

In particular, the effects of the neutral atmosphere propagate mainly into the vertical component of the position solution. Typically, the neutral atmosphere delay is separated into two components: (a) delay due to dry components, (b) delay due to water vapour. These two delays are referred to as the hydrostatic and non-hydrostatic delays respectively (it is recognized that the hydrostatic delay also includes some influence of the water vapour due to the density term - see §2.2.1). The hydrostatic component can be modelled very accurately, but the highly variable water vapour make it difficult to model so the non-hydrostatic component is estimated along with the position (see §2.3 for details). In addition to the effects of the neutral atmosphere, the vertical component will inherently be more variable due to a geometric weakness in the satellite distribution. Due to this geometric weakness, the variability of the vertical solution will typically be approximately 3 times more variable than that of the horizontal solution. If the neutral atmosphere is not properly dealt with, that difference could reach up to 10 times the horizontal position uncertainty (Yunck, 1993). Yunck (1993) illustrated that the neutral atmosphere delay is

---

<sup>1</sup>In spite of the fact that the resulting phenomena due to the interaction of radio waves with plasma was the inspiration that eventually led to understanding of how the W and Z bosons acquire mass, which ultimately led to the quest for the Higgs boson [Close, 2011])



highly correlated with the vertical solution, and this correlation is reduced as the elevation angle of the satellite is reduced. This means that it will be difficult to separate the neutral atmosphere delay from the vertical solution during the estimation process unless lower elevation angle satellites are available. Since the non-hydrostatic delay must be estimated, the addition of lower elevation angles are necessary to improve the vertical solution, but the addition of the lower elevation satellites requires a more accurate knowledge of the neutral atmosphere.

The representation of the atmosphere in GNSS positioning has traditionally been embodied in the modelled hydrostatic zenith delay and an associated mapping function that maps the zenith delay to the elevation angle of the observed satellite (see §2.3 for details). Research in this area has typically been focused in several areas, most notably: (a) the functional formulation of the mapping function, (b) the realization of the mapping function, (c) computation of the delay itself for use in the positioning. Concerning item (a), work by Mendes (1999), Ghouddousi-Fard (2009), and more recently Urquhart (2011a) provide an excellent review of the various mapping function formulations and their relative accuracy. Item (c) refers to the use of ray-tracing methods to compute the total delay (hydrostatic + non-hydrostatic) explicitly at the specified elevation angle of the satellite, which is then subsequently applied in the positioning analysis. Work in this area has centred on the use of numerical weather prediction models to define the atmosphere. Hobiger et al. (2008), and more recently Urquhart et al. (2011a), have explored the use of ray-traced total delays explicitly in GNSS positioning by PPP (precise point positioning), and have concluded that the numerical weather models are still insufficient in describing the water vapour content of the atmosphere. The positioning results from Hobiger et al., (2008) and Urquhart et al. (2011a) demonstrated that the height component exhibited cm-level repeatability versus mm-level for the results that estimated the non-hydrostatic delay.

The last item to be discussed is (b), the realization of the mapping function, which is

the focus of this work. The realization of the mapping function is to fit the functional form to a definition of the atmosphere. The various mapping functions have not only separated themselves by the functional form, but also by the definition of the atmosphere. Many mapping functions have shared the same functional form (i.e., Niell, IMF, and VMF), but their definition of the atmosphere has differed. For example, mapping functions have been fitted to standard atmospheres (Chao, 1974), radiosonde data (Niell, 1996), and now numerical weather prediction models as shown by Niell (2001) and Boehm et al. (2006). The application of numerical weather prediction models to the realization of the mapping function is a relatively new concept that has flourished in the last decade. Rocken et al. (2001) compared ray-traced slant delays through a numerical weather prediction model and compared those delays to slant delays mapped by the Niell mapping function. Rocken et al. (2001) concluded that the application of the ray-traced delays significantly reduced the seasonal and latitudinal bias exhibited by the Niell mapping function. Boehm et al. (2003) presented the Vienna Mapping Functions, which were updated with Boehm et al. (2006). The Vienna Mapping Functions are entirely realized with a numerical weather prediction model, which demonstrated an overall improvement over the Niell mapping functions especially in regions where the climatology used to realize the Niell mapping functions do not fit well to the region. The potential gains with the application of these numerical weather prediction models can be huge. With regard to geodetic correction products, numerical weather prediction models not only have been applied to the neutral atmosphere, they have been applied to the computation of atmospheric angular momentum and length of day (Schindelegger et al., 2011; AERS, 2012), atmospheric gravity field coefficients (GGOS, 2011), and atmospheric pressure loading (Petrov and Boy, 2004; GGOS, 2011; GGFC, 2010). As the horizontal/vertical/temporal resolution and the physical representation of the atmosphere within the model improves, the corresponding realization of the mapping function and all other geodetic corrections will improve in tandem.

## 1.1 Motivation

The Vienna Mapping Functions (VMF) are unique in that they rely solely on information from an external data source, namely, a numerical weather prediction model (NWP) (it is recognized that the VMF is not the first, since the isobaric mapping functions from Niell (2000) applied a NWP, but only at the 200 hPa pressure level). The development of the VMF represents a shifting paradigm in which geodetic corrections are moving from simple mathematical closed form type solutions to solutions based on large amounts of external data (Boehm and Van Dam, 2009). However, there have been many differing institutions creating many differing corrections based on many differing underlying models and datasets. For example, we have atmospheric pressure loading corrections offered by the University of Luxembourg and by the Goddard Geodetic VLBI group. Both correction services utilize external datasets from the National Centers for Environmental Prediction (NCEP), but their underlying models are different (van Dam and Wahr, 1987; Petrov and Boy, 2004 respectively). Recently, there have been efforts put forward by the geodetic community to try and understand the impacts of these new external dataset based corrections with the Global Geodetic Observing System (GGOS) Unified Analysis Workshops beginning in 2007. The community has recognized that there are still systematic deficiencies and inconsistencies, and beginning with the Second GGOS Unified Analysis Workshop in 2009 the group has included a session dedicated to modelling deficiencies and modelling based on external data (Session 2 of aforementioned 2009 workshop). The basic motivation of the UNB-VMF1 service is borne out of this effort to understand and standardize this paradigm shift. The UNB-VMF1 intends to make a contribution to this effort with the addition of an atmospheric delay based product aimed at improving our appreciation of these external datasets, as well as promoting the use of the most accurate corrections available. This contribution is achieved through the production of the most accurate mapping functions to date, the Vienna Mapping Functions (actually, the VMF1), with the service aiming at improving the consistency of existing products (when used to-

gether with other data based corrections), the availability, as well as stimulating research into future corrections.

The demands of the geodetic community are continually evolving and the desire for more accurate results are eternal. The Vienna Mapping Functions have demonstrated to be the most accurate mapping functions to date. Several studies into the benefits of the application of the VMF1 have been completed by Boehm et al. (2003), Boehm et al. (2006), Tesmer et al. (2007), Kouba (2009), and Fund et al. (2010). Boehm et al. (2003), which was the first publications of the Vienna Mapping Functions, demonstrated in a VLBI analysis a 10.7% improvement in baseline repeatability with respect to baselines utilizing the Niell mapping functions (NMF). Boehm et al. (2006) presented improvements to the original formulation of the VMF (referred to as VMF1), and demonstrated in a VLBI baseline length repeatability analysis that out of 40 baselines, 33 showed an improvement over the original VMF. Tesmer et al. (2007) evaluated the effect of different mapping functions on the TRF, CRF and VLBI time series, and demonstrated that the best precision in terms of stations height was obtained when the VMF1 mapping function was used (a 5 to 7 % improvement was made over the GMF, IMF and NMF). Kouba (2009) compared the use of GPT zenith delays with GMF mapping functions to that of ECMWF zenith delays an VMF1 mapping functions. Kouba (2009) found that the use of GPT/GMF inadequate for IGS type global processing since the combination introduced pressure correlated height biases up to 10 mm (larger for elevation angles less than 10°). Fund et al. (2010) demonstrated using the EUREF network with a-priori zenith hydrostatic delays derived from numerical weather models and the VMF1 mapping functions that the repeatability of northern european stations heights can be improved by 3-4 mm.

With the knowledge regarding the capabilities of the VMF1, it makes sense to make an effort to continue the promulgation of these type of atmospheric delay corrections. In this context, the UNB-VMF1 addresses the issue of redundancy and precision. Currently, atmospheric delay corrections based on VMF are singularly offered by the Global

Geodetic Observing System - Atmosphere (GGOS-A). This poses a risk to availability if any service outages were to occur. The addition of the UNB-VMF1 service creates redundancy in availability so as to mitigate the risk of service outages. This redundancy improves the reliability of the corrections, which will assist in the stimulation of a more widespread implementation while making the VMF based corrections widely available for a wide array of applications ranging from traditional high precision post-processed to real-time solutions.

With respect to precision, the UNB-VMF1 service will offer VMF1 corrections based on independent state-of-the-art datasets (from NWP's generated by NCEP and the CMC – Canadian Meteorological Centre) and independent state-of-the-art ray-tracing algorithms (developed at UNB). This fact will help with IGS/IERS combinations solutions, since in reality many of the analysis centre solutions are correlated due to the fact that many analysis centres implement similar correction models, and in some cases the same software. The addition of a UNB based VMF1 corrections will alleviate some of these correlations in the combination solutions, since the correction models can be readily made more independent.

Additionally, the validation of the service at UNB will help to further the understanding of the influence the NWP has on geodetic applications. It is not the intention (or necessary) of a geodesist to become a climate scientist and produce their own weather prediction models, but the geodesist must be aware of the strengths and weaknesses of these datasets and how they influence the quantities of interest. Therefore, through the course of validating the new service, the NWP's will be indirectly assessed with respect to each other, thereby providing a valuable source in understanding these datasets in the geodesist's context. Further, the service will allow the addition of products based on new models much simpler.

There is also a belief in the geodetic community that the benefits of these new data based corrections cannot be fully realized unless a consistent set of corrections determined

from the same underlying external datasets are used together in positional computations. The GGOS-A service by the Vienna University of Technology has endeavoured to create a consistent set of corrections based on a common data source with the same underlying meteorological parameters (GGOS, 2011). The GGOS-A has created a service that provides the international scientific/geodetic community access to atmospheric pressure loading, angular momentum, delay, and gravity field coefficients for the atmosphere based on high resolution datasets from the ECMWF. Here lies the root of the motivation of the creation of the UNB-VMF1 service, as the UNB-VMF1 service aims at moving towards data source consistency with the addition of atmospheric delay corrections based on data from NCEP. The addition of atmospheric delay products from NCEP would provide an expanded set of corrections based on a consistent source of underlying meteorological parameters and models (i.e., pressure, temperature, wind speed, etc). Therefore, with the inclusion of the UNB-VMF1 service, the following consistent set of corrections can be obtained based on NCEP's Re-Analysis 1 dataset (all url's are valid as of the date of this publication):

1. Angular momentum [[http://ftp.aer.com/pub/anon\\_collaborations/sba/](http://ftp.aer.com/pub/anon_collaborations/sba/)];
2. Atmospheric pressure loading [[http://geophy.uni.lu/ggfc\\_atmosphere/NCEP-loading.html](http://geophy.uni.lu/ggfc_atmosphere/NCEP-loading.html) and <http://gemini.gsfc.nasa.gov/aplo/>];
3. Atmospheric Delay [<http://unb-vmf1.gge.unb.ca/>]

Finally, it is the hope that with the addition of the UNB-VMF1 service, it will serve as a means to stimulate future research in atmospheric delay modelling. The creation of the UNB-VMF1 will serve as the foundation where improvements to atmospheric delay modelling can continue to be made. The tools implemented along with the service (ray-tracing, NWP knowledge) will provide the means to expand the scope of the current suite of atmospheric corrections. In particular, the service will allow the continual research into improved ray-tracing methodologies along with the understanding of how the underlying

NWP models help describe atmospheric phenomena. Research in this area can extend to the development of linear horizontal atmospheric gradient models and ray-tracing at the observation level, which would help to explain some of the systematic deficiencies still remaining in geodesy.

## 1.2 Contribution

The main contributions from this work can be summarized as follows:

- Development and implementation of an on-line atmospheric corrections service producing mapping function coefficients and ray-traced zenith delays based on the Vienna Mapping Functions (variant of VMF produced: VMF1) in a global domain, which serves the international geodetic/scientific community.
- Development of three realizations of the VMF1, independent of the existing realization, based on two independent numerical weather prediction models and ray-tracing methods;
- Global validation of all realizations of the VMF1 produced by the service over an 11 year and 1 year time period across 32 stations in the position domain (and gridded domain);
- Assessment of numerical weather prediction model parameters most influential to geodetic analysis (pressure, temperature, specific humidity), as well derived quantities from those parameters (hydrostatic zenith delay) over a one-year time period;
- Assessment of the influence of numerical weather prediction model horizontal grid resolution with respect to meteorological parameters (pressure, temperature and specific humidity) and geodetic analysis (hydrostatic zenith delay) over a 5 month period.

## 1.3 Outline

This following describes the outline of the this thesis beyond this introductory chapter. Chapter 2 provides some background documentation relating to the propagation of GNSS signals in the troposphere. This will provide the necessary background understanding and formulae for the chapters that follow. Chapter 3 discusses numerical weather prediction models and their impact on ray traced delays. This chapter characterizes different numerical weather prediction models through the comparison of model parameters to real measured values and through investigating the impact of differing grid resolutions. Chapter 4 discusses the outline and implementation of the UNB-VMF1 service. This chapter provides describes the function, integration, and interface of the newly implemented UNB-VMF1 service. Chapter 5 describes the validation of the UNB-VMF1. A summary of the testing that has been completed to evaluate the quality of the products being produced can be found in this chapter. The products have been evaluated against the existing VMF1 service in both the delay domain and the position domain over an eleven year period. Finally, chapter 6 provides a summary of conclusions and recommendations based on the experimental results observed throughout this thesis.

### 1.3.1 Additional Notes on Notation

When referencing the Vienna Mapping Service created and administered by Johannes Boehm at the Vienna University of Technology in the Department of Geodesy and Geoinformation, the term: *existing VMF1 service* will be used.



# Chapter 2

## Background: Modelling GNSS Signals in the Neutral Atmosphere

It is the intention of this chapter to provide the general framework typically employed for modelling GNSS signals in the neutral atmosphere. The chapter will define the neutral atmosphere and some of its properties followed by a discussion regarding the modern methods of modelling its effects in GNSS applications. Additionally, since modern techniques of modelling the neutral atmosphere delay has now encompassed the application of numerical weather prediction models (NWP), some basics to understanding the makeup of those products are discussed.

### 2.1 The Neutral Atmosphere

As previously mentioned the neutral atmosphere is that part of the atmosphere that extends from the surface to approximately 80 km overhead. As a result, the neutral atmosphere is composed of not only the troposphere (0 to ~12 km), but the stratosphere (from ~12 km to ~50 km), and mesosphere (from ~50 km to ~80 km) (Langley, 1996). The neutral atmosphere's vertical structure is characterized by a decreasing pressure (and density) with respect to height. The temperature characteristics are a little more complex. In the

troposphere, the temperature will also decrease with respect to height, but at the interface with the stratosphere the temperature will remain constant (the tropopause), and then continue to increase due to the concentration of ozone in this region (Lutgens and Tarbuck, 2010). At the interface with the mesosphere, known as the stratopause, the temperature continues to decrease with respect to height. The important aspect of this characterization, is the decrease of density with respect to height. The delay in the neutral atmosphere is dependent on the atomic density of the medium (as shown in §2.2.1), so as the density decreases so will the overall delay, which explains why the majority of the delay occurs in the troposphere. To put this into perspective, at sea level, the number of atoms and molecules per  $cm^3$  of air is approximately  $2 \times 10^{19}$ , but only  $2 \times 10^7$  at a height of 600 km (Lutgens and Tarbuck, 2010). This would mean that at a height of 600 km, the atom or molecule will collide once per minute versus  $7 \times 10^9$  per second at sea level (Lutgens and Tarbuck, 2010).

The neutral atmosphere is made-up of two main constituents, namely the dry components and the water vapour. The interaction of the electromagnetic radio waves with these components are the source of the signal delay. The effect of the dry constituents (i.e.,  $N_2$ ,  $O_2$ ) makeup approximately 90% of the total delay with the remaining delay effectively attributed to the water vapour. The term *effectively* is applied here since Solheim et al. (1999) studied the effects on GNSS signal delay due other particulates (sand, dust, aerosols and volcanic ashe) and hydrometeors, and concluded that the effects of hydrometeors and other particulates are less than 3% of the total delay and difficult to model as range errors.

Additionally, the total neutral atmosphere delay has a seasonal and latitude component. The seasonal effect can be attributed to the fact that the water vapour content varies seasonally across much of the globe (excluding equatorial areas) (Gaffen et al., 1993), and that the overall global pressure increases during the winter months with a maximum in the northern hemisphere winter (Trenberth, 1981). The latitude dependency is also a

combination of the water vapour content<sup>1</sup> and due the fact that the troposphere is thinner at the poles versus the equator (Lutgens and Tarbuck, 2010).

## 2.2 Delay in the Neutral Atmosphere

The delay in the neutral atmosphere is effectively due to refraction<sup>2</sup>. Refraction can be defined as the change of direction of a electromagnetic wave as a consequence of a speed change in a medium (phase or group). Therefore, as a consequence of refraction two effects occur: (a) change in direction - the bending, and (b) speed change - the delay. The electromagnetic signal from the satellite will be refracted due to the fact that the neutral atmosphere exists (not a vacuum), and the total delay in terms of time can be expressed as the difference between the travel time between the satellite and receiver in the neutral atmosphere and the travel time between the satellite and receiver as if they were in a vacuum (if no atmosphere existed):

$$\tau = \int_S \frac{1}{v} dS - \int_{S'} \frac{1}{c} dS' \quad (2.1)$$

where,  $v$  is the phase or group velocity,  $c$  is the speed of light in a vacuum,  $S$  is the electrical path in the neutral atmosphere, and  $S'$  is the path length *in-vacuo*. The neutral atmosphere delay is typically expressed in units of length, so equation 2.1 can be scaled by the speed of light,  $c$ , to obtain:

$$\Delta L = \int_S n(S) dS - \int_{S'} dS' \quad (2.2)$$

where,  $\Delta L$  is the delay in linear units, and  $n(S)$  is the index of refraction as a function of the path (group or phase).

---

<sup>1</sup>Water vapour content expressed as precipitable water can vary from 0.01 to 7.5 g at the polar region to the equatorial (Spilker, 1996).

<sup>2</sup>The total effect includes dispersion and absorption, but these effects are small at GNSS signal frequencies and discussed further in §2.2.2

### 2.2.1 Index of Refraction

The total delay in the neutral atmosphere is a consequence of the index of refraction along the path travelled by the electromagnetic signal. Since the index of refraction play such a primary role in the total delay, it is important to understand what the index of refraction means in greater detail. The index of refraction is defined by the following:

$$n = \frac{c}{v} \quad (2.3)$$

where,  $c$  is the vacuum speed of light, and  $v$  is the phase speed in a medium. Equation 2.3 clearly emphasizes the phase speed of an electromagnetic wave will propagate slower in any medium relative to *in-vacuo*. However, the electromagnetic signal may be modulated so there would be an additional index of refraction known as the group refractive index. The group refractive index can be related to the phase by (Langley, 1996):

$$n_g = n - f \frac{dn}{df} \quad (2.4)$$

where,  $n$  is the phase index of refraction, and  $f$  is frequency. Equation 2.4 is frequency dependent, meaning that the signal modulation will propagate at a different speed than that of the phase in dispersive mediums. However, the neutral atmosphere is effectively non-dispersive, (see §2.2.2) so the group and phase indexes of refraction are the same, which results in the carrier phase and modulation of a GNSS signal propagating at the same speed.

Now that the index of refraction in the neutral atmosphere has been defined, it is worth discussing what this means physically, in other words why the wave is slowed and bent while travelling through the medium. Qualitatively, if we consider an electromagnetic field interacting with any non-dense medium (index of refraction close to 1 - i.e., air), the electrons within the medium are forced into oscillating dipole moments by the incoming wave (Feynmann, 1964). These oscillating electrons result in the production of their own

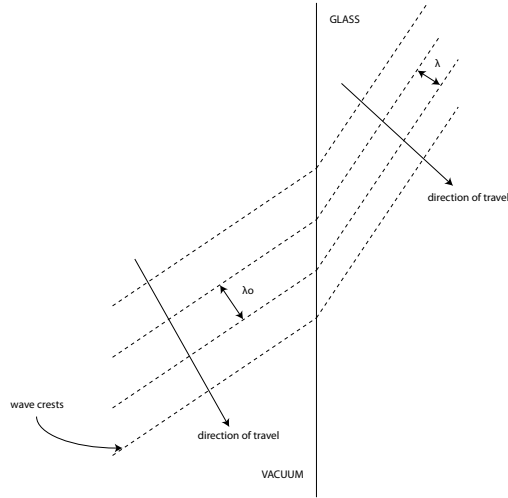


Figure 2.1: Refraction of an electromagnetic wave through glass. The arrows represent the direction of travel and the dashed lines are the wave crests.  $\lambda_o$  is the incident wavelength and  $\lambda$  is the wavelength after refraction. After Feynmann (1963).

electromagnetic field that interacts with the incoming field. The net effect is the vector sum of all the forced electromagnetic fields with the original incoming field results in an effective phase speed and direction change of the incoming field (Feynmann, 1963).

The bending aspect of refraction is due to the fact the speed of the wave is slowed within the medium. As the wave passes through the medium, the phase speed is slowed, but the frequency must remain the same. In order for the frequency of the wave to be maintained, the wavelength must become smaller. Figure 2.1 illustrates an example of a refracted electromagnetic wave. The incoming wave interacts with the glass and is refracted, since the wavelength is reduced to match the reduced phase velocity, the wave must deflect so that the refracted wave fits the incoming wave's frequency at the boundary.

Lastly, the index of refraction can be expressed as a function of several basic atomic quantities. Feynman (1963) presents a excellent derivation of the concept, but the final results are only presented here. So, the index of refraction can be computed by:

$$n = 1 + \frac{q_E^2}{2\epsilon_0 m} \frac{N}{\omega_0^2 - \omega^2 + i\gamma\omega} \quad (2.5)$$

where,  $q_E$  is the electrical charge in coulombs;  $N$  is the atomic density of the medium;  $m$  is the electron mass;  $\epsilon_0$  is the permittivity of free space;  $\omega_0$  is the resonance frequency of the medium;  $\gamma$  is the dissipation constant, and  $\omega$  is the frequency of the incident electromagnetic field.

There three things to consider with equation 2.5. First is the quantity,  $N$ , in which the index of refraction,  $n$ , is directly proportional with.  $N$  is the number atoms per unit volume, which is directly proportional to the medium's density.<sup>3</sup> Therefore, this relationship indicates that as the density of the medium is increased so will the index of refraction. This agrees with the previous assertion that the majority of the delay occurs in the troposphere since this is the layer of the neutral atmosphere that is most dense (highest pressure).

Second, equation 2.5 is frequency dependent. The frequency dependency of equation 2.5 is due to the dispersion of the incoming electromagnetic field. The denominator term  $\omega_0^2 - \omega^2$  is the relevant term for this discussion. Typically, the resonant frequency (or natural frequency) of the electron oscillators are unknown, but for air it is usually at the ultraviolet level (Feynman, 1963). This means that the relative magnitude of the resonant frequency of the electron oscillator to the incident frequency is large, and the index of refraction will remain constant. However, as the frequency of the incident electromagnetic field becomes close to the resonant frequency, the index of refraction will become very large. These results shows that as long as the incoming electromagnetic field is well below the resonant frequency, the dispersion can be safely ignored. This is the reason why dispersion for GNSS signals can be effectively ignored since the frequency of the signals are well below the resonant frequency of the neutral atmosphere (see §2.2.2).

Third, equation 2.5 is actually a complex number with the addition of the  $i\gamma\omega$  term in the denominator. The complex term relates to the absorption in the medium. Typically, the

---

<sup>3</sup>The number of atoms per unit volume,  $N$ , can be related to the mass density by the following:

$$N = \frac{N_A}{M} \rho$$

where,  $N_A$  is Avogadro's Number;  $M$  is the molar mass of the substance, and  $\rho$  is the mass density.

absorption term is quite small relative to the dispersion term  $(\omega_0^2 - \omega^2)$ , but if the frequency of the incoming electromagnetic field is large enough, the dispersion term becomes quite small relative to the complex absorption term. When this occurs, the index of refraction will be dominated by the absorption. As with the dispersion term, at frequencies used by GNSS systems (see §2.2.2), the absorption can be effectively ignored. The complete index of refraction can be expressed as a real and a complex term:

$$n = n' + i \kappa \quad (2.6)$$

where,  $n'$  is due to the refraction and dispersion, and the complex term,  $i \kappa$  is due to the absorption.

## 2.2.2 Refractivity

The previous section illustrated that the index of refraction for air is close to one, that dispersion and absorption can be safely ignored when the relative magnitude of  $(\omega_0^2 - \omega^2)$  is large, and that its magnitude is directly proportional to the density of the medium. Since the index of refraction is so close to one for gases, the refractivity is used in its place and is defined as:

$$N = 10^6 (n - 1) \quad (2.7)$$

The refractivity will follow that of the index of refraction, where the total refractivity will be sum of the non-dispersive effects, dispersion and absorption. This can be expressed by they following:

$$N = N_o + N' + i N'' \quad (2.8)$$

where,  $N_o$  is the non-dispersive effects (refraction);  $N'$  is the dispersive effects, and  $i N''$  is the complex component due to the absorption. Davis (1986) examined the dispersive effects based on the methods by Liebe (1985). Davis (1986) shows that a refractivity that

includes dispersive terms below 30 GHz is due to the water vapour resonance (as well as the tail of the 60 GHz  $O_2$  resonance) and is 0.4% of the non-dispersive refractive index. Hartmann (1993) tabulated the strongest frequencies of lines of  $O_2$  and water vapour for frequencies above 1 GHz. For water vapour, the lowest value is  $\sim 22$  GHz and for  $O_2$  the lowest value is  $\sim 53$  GHz. The signals for GNSS applications, at 1-2 GHz, are well below these values. Further, Liebe (1985) computes the difference in zenith delay for several frequencies, and demonstrates that the additional delay at 40 GHz due to dispersion is only 2.64 ps ( $\sim 0.7$  mm). Since the nearest resonance to GNSS signal frequencies is at 22 GHz, the effects of dispersion can be safely ignored. Lastly, Boehm (2004) computed the absorption,  $\kappa$ , in equation 2.6 using the results from Liebe (1985) for a frequency of 22 GHz with a precipitable water content of  $7.65 \text{ g/m}^3$ . The resulting value was  $3.8 \times 10^{-8}$ , which can effectively be ignored. Therefore, for GNSS signals in the neutral atmosphere, the refractivity (and refractive index) is effectively due to the non-dispersive effects,  $N_o$ . For the remainder of this document,  $N_o$  will now be referred to as  $N$  for convenience.

The refractivity depends on the density of the medium, and can be expressed as a function of temperature and density by Debye (1929):

$$N = \left( A + \frac{B}{T} \right) \rho \quad (2.9)$$

The terms  $A$  and  $B$  must be determined experimentally and vary from molecular species;  $T$  is the absolute temperature, and  $\rho$  is the density of the medium. The first term,  $A$ , in equation 2.9 relates to the induced dipole (polarization) of the molecule, and the second term refers to the orientation effect of the applied electric field on the permanent dipole of the molecules (Davis, 1986). For a mixture, equation 2.9 can be extended to the following relationship:

$$N = \sum_{i=1}^q \left( A_i + \frac{B_i}{T} \right) \rho_i \quad (2.10)$$



This formulation makes it possible to split up the constituents of the neutral atmosphere into the appropriate components. The possibility of splitting the neutral atmosphere into a bulk dry and water vapour components is feasible due to the homogeneity of the dry constituents. The major constituents of the dry component of the neutral atmosphere are nitrogen, oxygen, argon, and carbon dioxide. Davis (1986) illustrates that the fractional volumes of the dry constituents are constant, which allows the treatment of these components as a bulk dry air mass, where the total bulk dry air mass is described by a weighted sum (weighted by their fractional volume) of the individual constituent molar mass.

Now that the neutral atmosphere can be separated into a dry and water vapour component, the total refractivity can be written as presented by Davis et al. (1986):

$$N = k_1 R_d \rho_d + k_2 R_v \rho_v + k_3 R_v \frac{\rho_v}{T} \quad (2.11)$$

where, the subscript  $d$  denotes the dry components and  $v$  denotes the water vapour component;  $R$  refers to the specific gas constant and  $\rho$  is the density. The first term in equation 2.11 is due to the dry constituents, and since there is not a permeant dipole component related to the dry component, the second term in equation 2.9 is zero. The last two terms in equation 2.11 is due to the water vapour and includes both the  $A$  and  $B$  coefficient terms due to the permanent dipole of the water molecule. The coefficients  $k_1$  through  $k_3$  requires determination by experiment.

Davis et al. (1985) also presents a formulation based on Thayer (1974), where the first term has been replaced by a term based on the total density. Davis et al. (1985) presents the refractivity as follows:

$$N = k_1 R_d \rho + k_2' \frac{p_w}{T} Z_w^{-1} + k_3 \frac{p_w}{T^2} Z_w^{-1} \quad (2.12)$$

where,  $\rho$  is the total density;  $k_2' = \left(k_2 - k_1 \frac{M_w}{M_d}\right)$ ;  $p_w$  is the particle pressure of water vapour;  $Z_w^{-1}$  is the compressibility factor for the water vapour,  $R_d$  is the specific gas

constant for the dry component. Thayer's presentation of the total refractivity included the inverse compressibility factors, which are included to deal with the non-ideal behaviour of the atmosphere. However, Mendes (1999) illustrated that these factors only amount to a sub-mm impact at zenith and are only associated with the water vapour, so these values have been set to unity for this work. Lastly, Mendes (1999) termed the phrase *hydrostatic* for the first term and *non-hydrostatic* for the last two terms. This work follows equation 2.12 for the definition of refractivity and follows the notation from Mendes (1999).

The final component to be discussed is the definition of the coefficients of refractivity ( $k_1$ ,  $k_2$ , and  $k_3$ ). There has been several publications that have addressed the definition of these coefficients, where some of the more recent publications include Thayer (1974), Hill et al. (1982), Bevis et al. (1994) and Ruegger (2002). Several publications present a review of the many different values for these coefficients and these include Davis et al. (1985), Hartmann (1993), Thessin (2005) and Ruegger (2002). For this work, the *best averages* from Ruegger have been used.

Recently, there has been some work associated with the definition of total refractivity in the GPS radio occultation (GPSRO) discipline. GPSRO measurements are assimilated into numerical weather prediction models, and recently work by Healy (2011) and Cucurull (2010) have illustrated that the definition of the refractivity coefficients (in particular the  $k_1$  coefficient) and the associated uncertainty with them are non-negligible for numerical weather prediction model purposes. This led to Aparicio and Laroche (2011) re-evaluating the formulation of refractivity and developing a new relationship for frequencies below 10 GHz. Aparicio and Laroche (2011) compare their formulation to five other formulations, namely Smith and Weitraub (1953), Thayer (1974), Bevis et al. (1994), Foelsche (1999) and Ruegger (2002), which only show small differences for dry and moist air. However, these small differences may be significant for numerical weather prediction model assimilation of GPSRO data, but this formulation has yet to be evaluated in a traditional GNSS context.

### 2.2.3 Signal Delay in the Neutral Atmosphere

Now that the definition of refractivity has been established, the definition of the neutral atmosphere delay can be further refined from equation 2.2. The total delay in equation 2.2 can be decomposed as:

$$\Delta L = \int_S [n(S) - 1] dS + \left[ \int_S dS - \int_{S'} dS' \right] \quad (2.13)$$

The first term in equation 2.13 is due to the refractivity in the neutral atmosphere slowing the signal along the electrical path travelled ( $S$  is the electrical path). The second term is due to the bending effect, which is the difference in path length between the bent and the straight line path, which is known as the geometric delay ( $S'$  is the straight line path).

Further, the first term in equation 2.13 can be decomposed further with the knowledge of the two components of the neutral atmosphere, namely the hydrostatic and non-hydrostatic components. The term  $(n(S) - 1)$  is the refractivity, and is defined by equation 2.12. The hydrostatic refractivity,  $N_h$ , is the first term of equation 2.12:

$$N_h = k_1 R_d \rho, \quad (2.14)$$

and the non-hydrostatic refractivity is composed of the final two terms from equation 2.12:

$$N_{nh} = k_2 \frac{p_w}{T} Z_w^{-1} + k_3 \frac{p_w}{T^2} \quad (2.15)$$

Therefore, the first term in equation 2.13 becomes the sum of the hydrostatic and non-hydrostatic components for the along path delays and the second terms remains the same.

The total delay can now be expressed as:

$$\Delta L = 10^6 \int_S N_h dS + 10^6 \int_S N_{nh} dS + \left[ \int_S dS - \int_{S'} dS' \right] \quad (2.16)$$

## 2.3 Modelling in the Neutral Atmosphere Revisited

Since the effects of the neutral atmosphere in a standard GNSS processing scheme cannot be eliminated through observation, they must be modelled mathematically. The general framework for the model has been defined by equation 2.16, which is a deterministic model of the delay where the independent input variables are the meteorological parameters (which are a function of the signal's position in space –  $\phi, \lambda, h$ ) used to compute the state of the atmosphere – the refractivity as defined by equations 2.14 and 2.15. It is necessary to parametrize the model further since the delay will also be dependent on time ( $t$ ), azimuth ( $\alpha$ ) and elevation angle ( $\epsilon$ ) of the satellite. Therefore, the model for the delay is a function of the following:

$$\Delta L = f(\phi, \lambda, h, t, \alpha, \epsilon, N_h, N_{nh}) \quad (2.17)$$

This model can effectively be considered the complete model of delay, but for practical implementations this model will require some further simplifications. Therefore to facilitate these simplifications, the model can be decomposed into a delay in the zenith direction that is scaled by a quantity that describes the elevation angle dependency of the delay – the mapping function. Additionally, since the delay in equation 2.17 has been separated into a hydrostatic and non-hydrostatic component, the same separation can be applied here as follows:

$$\Delta L = \Delta L_h^z m f_h(e) + \Delta L_{nh}^z m f_{nh}(e) \quad (2.18)$$

where,  $\Delta L_h^z$  is the zenith hydrostatic delay;  $\Delta L_{nh}^z$  is the zenith non-hydrostatic delay;  $m f_h(e)$  is the hydrostatic mapping function, and  $m f_{nh}(e)$  is the non-hydrostatic mapping function. The separation into the respective hydrostatic/non-hydrostatic components allows for more flexibility in determining the overall delay. Since the water vapour content in the neutral atmosphere varies considerably in both space (km) and time (minutes), it

is difficult to determine the non-hydrostatic refractivity because the precise measurement (or prediction) of the humidity along the path of the signal is so variable. In contrast, the hydrostatic component is highly dependent on the total pressure in the atmosphere, which is known to be very stable over a large spatial extent (hundreds of km) and over a long period of time (several hours). Therefore, the decomposition of equation 2.18 allows for the prediction of the hydrostatic component and the estimation of the non-hydrostatic component, which is the standard method used in all high precision GNSS positioning methods. Additionally, the parametrized form of equation 2.18 allows for a computationally efficient process. Since the non-hydrostatic delay is estimated, the remaining parameters can be evaluated by simple analytical expressions (equation 2.16 will have to be solved numerically). A brief discussion on the numerical solution to equation 2.16 is given in §2.3.1, and the computation of the zenith delay is discussed in §2.3.2 and the mapping function is discussed in §2.3.3.

Lastly, equation 2.18 addresses the elevation angle dependency of the delay, but not the azimuth dependency of the delay since the mapping functions in 2.18 are symmetric. To address the azimuth dependency of the delay, the following decomposition is added to equation 2.18 (from Petit and Luzum, 2010):

$$LHG = mf_g(e) [G_N \cos(\alpha) + G_E \sin(\alpha)] \quad (2.19)$$

where,  $mf_g(e)$  is the gradient mapping function;  $G_N$  and  $G_E$  are the horizontal gradients in the north-south and east-west direction respectively, and  $\alpha$  is the azimuth. Due to the difficulty in separating the hydrostatic and non-hydrostatic components of the horizontal gradients only the total gradients are applied. Typically, the horizontal gradients are not known *a-priori* and are estimated along with the non-hydrostatic zenith delay from equation 2.18. For this work, the horizontal gradients are ignored as the focus will be only on the realizations of the symmetric mapping functions in equation 2.18. A comprehensive review of the available parametrizations can be found in Ghoddousi-Fard (2009) and

Urquhart (2011).

### 2.3.1 Ray Tracing

The total delay of an electromagnetic signal propagating in the neutral atmosphere presented by equation 2.16 is an exact solution. Realistically, the computation of equation 2.16 must be made numerically with the application of ray-tracing methodologies under the assumptions of geometric optics. The fundamental assumption of geometric optics is that an electromagnetic wave is approximated by a narrow beam called a ray that travels through space in a straight line, as long as the medium is considered homogeneous. This assumption holds as long as the wavelength of the electromagnetic wave is much smaller than the scale of observations. For a GPS signal, the wavelength of the L1 carrier is 19.05 cm, but the observations are observed over scales of kilometres, so the assumption of geometric optics hold and the signal can be described as a single ray travelling through the neutral atmosphere.

Equation 2.16 clearly defines the delay in terms of the refractivity, but the evolution of the signal through the neutral atmosphere is not clear – the path  $S$ . Using the principles of geometric optics, the path of the signal can be defined three-dimensionally by the application of the Eikonal equation (from Born and Wolf, 1999):

$$\frac{d}{d\ell} \left( n \frac{d\mathbf{r}}{d\ell} \right) = \nabla \mathbf{n} \quad (2.20)$$

where,  $n$  is the index of refraction;  $\mathbf{r}$  is the position vector along the path of the signal;  $d\ell$  is the incremental path length, and  $\nabla \mathbf{n}$  is the gradient of the index of refraction. For this work, the solution to the partial differential equation follows Nievinski (2009), where the path is solved iteratively by the perturbation of a straight line path. Once the path has been defined, the delay by equation 2.16 can then be solved by the appropriate refractivity, which has been computed by the meteorological parameters located along the newly

defined path.

It must be noted that the presented three-dimensional ray evolution is the most rigorous. The ray path can also be approximated in a two-dimensional model or a straight line. For elevation angles between zenith and  $30^\circ$ , a straight line model is more than sufficient [Hopfield, 1969]. In fact, Nievinski (2009) showed that the difference between ray-traced delays for the rigorous three-dimensional model and the two-dimensional model are negligible (in the context of a 15 km resolution numerical weather prediction model). Overall, there are many different assumptions that can be made for the tracing of an electromagnetic ray through the neutral atmosphere. Nafisi et al. (2012) presents a benchmarking campaign for several ray-tracing packages (including Nievinski, 2009) in use for geodetic applications and concludes that differences between ray-tracing packages require further research to assess the source of the discrepancies.

### **2.3.2 Zenith Delays**

The zenith delay is defined the propagation delay of the electromagnetic signal at an elevation angle of  $90^\circ$ . In the context of raytracing, the ray path model reduces to a straight line model, which greatly simplifies the computations. However, within the context of equation 2.18, the application of ray-tracing to the zenith delays is unnecessary. The hydrostatic zenith delay can be computed with sufficient accuracy with the application of on-site measured pressure. Saastamoinen (1972), which was subsequently updated by Davis et al. (1985) outlined a simple method for computing the hydrostatic zenith delay (under the assumption that the atmosphere is in hydrostatic equilibrium) with an accuracy at the sub-mm level (evaluated by Mendes, 1999). Since then, Bosser et al. (2007) proposed a new gravity model to be used with the Saastamoinen hydrostatic delay model. Bosser et al. (2007) showed that the error due to the gravity model can be reduced from 0.3 mm to 0.1 mm with the updated formulation. However, if the observations were collected during times where the hydrostatic equilibrium does not hold, additional error may

be present (Davis et al., 1985). Also, if any of the meteorological sensors experience any malfunction or calibration error, additional error can be realized.

The non-hydrostatic zenith delay is estimated in standard GNSS processing schemes due to the difficulty in modelling the water vapour content. Mendes (1999) summarizes several *a-priori* models that attempt to compute the non-hydrostatic zenith delay, and concludes that the best performing models are accurate at the 10 mm level. Although not strictly in the zenith direction, Urquhart et al. (2011a) showed that the application of ray-tracing schemes exclusively (instead of estimating the zenith non-hydrostatic delay with the appropriate mapping function) through numerical weather prediction models are still insufficient for a mm-level height solution. Chapter 5 presents a global comparison of ray-traced zenith non-hydrostatic delays between three numerical weather prediction models.

### 2.3.3 Mapping Functions

A mapping function ( $m_{f_h}(e)$  and  $m_{f_{nh}}(e)$  in equation 2.18) describes the elevation angle dependency of the neutral atmosphere delay. The mapping function is a function of the position, time, elevation angle (azimuth is not included since symmetric mapping functions are only considered), and atmospheric conditions (implicitly). In its most basic form, it is just a scale factor that is the ratio of the slant delay to the zenith delay. The intention of the mapping function is a simple one, map the zenith delay to the appropriate elevation angle of the observed satellite in the most efficient possible manner. Although the mapping function is just a ratio of two delays (slant/zenith) that can be determined by ray-tracing methods, in an operational setting the computational load of ray-tracing would not allow an efficient means of processing the thousands of observations in a typical GNSS observation session. Therefore, the application of a simple analytical equation that maps the zenith delay is attractive. The difficulty, however, is in describing the elevation angle relationship (functional form) and fitting the functional form to an appropriate atmosphere.



The most prevalent functional form in use today is based on the Marini (1972) continued fraction of the term  $1/\sin(\epsilon)$ . The immediate disadvantage of Marini's continued fraction was the fact that it did not yield unity at zenith. Herring (1992) normalized Marini's continued fraction to yield unity at zenith and truncated it at three coefficients. Herring's form is as follows:

$$mf(e) = \frac{1 + \frac{a}{1 + \frac{b}{1+c}}}{\sin(e) + \frac{a}{\sin(e) + \frac{b}{\sin(e)+c}}} \quad (2.21)$$

The continued fractional form is a favourable form since it can be used over a wide range of elevation angles, and Herring's (1992) form has been evaluated to yield RMS values less than 0.2 mm for elevation angles between zenith and  $3^\circ$ . Recently, Urquhart (2011a) evaluated various mapping function functional forms, and verified that the Marini expression can map zenith delays to elevations angles of  $3^\circ$  at sub-mm accuracies. Other forms, such as Saastamoinen (1972), based on a Taylor series expansion cannot offer the same range of elevation angle applicability that the continued fractional form offers. The range correction developed by Saastamoinen (1972) is only applicable to elevation angles above  $20^\circ$ .

It is important to understand that the coefficients in equation 2.23 represent the state of the atmosphere. Equation 2.23 represents the definition of the mapping function, and the determination of the coefficients represent the realization of the mapping function. Modern mapping functions (i.e., Niell, VMF1) have implemented equation 2.23 as the functional form, but have differentiated themselves from each other through the definition of the atmosphere. The typical method for realizing the mapping function is to ray trace at several elevation angles through an atmospheric definition, and then fit the coefficients to the resulting ray traces in a least squares process. The most popular mapping function have been the Niell mapping functions (Niell, 1996), which were fitted to ray traces through temperature and humidity profiles at specific pressure levels given by the US Standard Atmosphere for the northern hemisphere (no southern hemisphere data was used). The

resulting fitted coefficients were then described temporally by a sinusoid, where the only requirements for the computation of the mapping function was latitude, day of year and elevation angle. In contrast, the latest mapping functions – the Vienna Mapping Functions – ray trace through a complete numerical weather prediction model (all pressure levels). Instead of a simple analytical function describing the temporal dependency of the coefficients, the Vienna Mapping Functions (VMF1), provide the  $a$  coefficients for equation 2.21 every 6 hours on a global grid (the  $b$  and  $c$  coefficients have been previously determined – see Chapter 4 for details). The application of the numerical weather model allows for a better representation of the atmosphere, which results in more accurate coefficients defining the atmospheric conditions. In particular, the Niell temporal representation only describes the seasonal fluctuations whereas the VMF1 can represent the daily and sub-daily fluctuations. Comparisons between the two by Niell (2006) have demonstrated that the largest deviations between the two occur at high latitudes where the weather is known to be variable over several days.

## 2.4 Numerical Weather Prediction Models

Improvements to the modelling of the neutral atmosphere can come in the form of: (a) optimized ray-tracing methodologies, (b) new functional forms of the mapping function, or (c) improved modelling of the atmospheric parameters necessary for the computation of refractivity. Inroads have been made in improvements of neutral atmosphere modelling through item (c) with the application of numerical weather prediction models. Numerical weather prediction models can provide a global (or regional/local) representation of the atmospheric conditions at a specific epoch. Therefore, it makes sense to review some of the basic concepts and definitions that makeup these datasets.

A numerical weather prediction model can be defined as a three dimensional numerical representation of the current weather conditions which are then used to drive the pre-

diction of future weather conditions through the application of mathematical models to the physical atmospheric processes. Therefore, the primary purpose of the numerical weather prediction model is to predict the atmospheric state at a future date, where the system is an initial-value problem (although it is a boundary value problem too since the extents of the atmosphere must be defined), initialized by the current state of the atmosphere. The current state of the weather is used to drive the atmospheric models for the determination a future state, so it is very important that the initial state of the atmosphere be as accurate as possible. From a geodesists perspective, the current state of the atmosphere is a valuable tool in describing atmospheric based corrections necessary for high precision positioning. The subject of numerical weather prediction model is dense, so this section will provide some key basic concepts describing numerical weather prediction model characteristics, but an in depth review and mathematical treatment of the subject can be found in Kalnay (2003), Stensrud (2007), and Coiffier (2011).

### **2.4.1 Model Dynamics**

The model dynamics represent the overall underlying physical representation that governs atmospheric flow. The model dynamics are represented by a complete set of equations that describe (Kalnay, 2003):

- Newton's second law of conservation of momentum;
- the continuity equation or conservation of mass;
- the equation of state for ideal gases;
- first law of thermodynamics or conservation of energy;
- conservation equation for water mass.

These equations are second order partial differential equations that are solved as an initial value problem by either finite differences or spectral methods at a specified time step

(see Kalnay (2003) or Coiffier (2011) for a general overview of solution methods). The equations representing the fundamental physical dynamics of the atmosphere are referred to as the primitive equations. Out of the set of primitive equations, the equations that include time derivatives are referred to as prognosis equations and those equations that do not include the time derivative are referred to as diagnosis equations.

## 2.4.2 Model Types

The definition of model type refers to the scale of model or whether the model is grid-point based or spectral based. First, the scale of the model refers to the scale of the atmospheric phenomena, which can range from the synoptic scale (200 - 1000 km) to meso-scale (2 km to 200 km) to small scale (less than 2 km). Therefore, to address specific atmospheric phenomena the appropriate horizontal and vertical resolution must be applied, however, it must be kept in mind that the model cannot resolve grid scale features and the minimum resolvable feature is approximately four to five times the grid resolution (Doyle, 2008). However, increasing the resolution of the model has computational implications where doubling the resolution in three space dimensions requires reducing the time step by half, which results in a computation cost of  $2^4$  (Kalnay, 2003).

Since producing a model at a high resolution on a global domain is computational prohibitive, organizations producing these models will typically provide products with varying resolutions matching their spatial domains. Coarse gridded models are typically for the global domain, and as the resolution is decreased so is the extents of the model domain. For example, the Canadian Meteorological Centre's (CMC) global model (GDPS) is available with a horizontal resolution of 33 and 60 km, but its regional model is available at 10 and 15 km and the high resolution model (HRDPS), which is localized to three separate domains within the regional domain<sup>4</sup>, is 2.5 km. In addition to the restriction in the spatial extent of the model, the forecast time is also reduced. For example, CMC's global

---

<sup>4</sup>CMC's HRDPS is available in three discrete domains, namely East, West and Maritimes

GDPS provides forecasts out to 144 hours from the model's initialization, but the regional model (RDPS) only provides 48 hour forecasts and the high resolution model (HRDPS) provides only 24 hour forecasts. This is the case because many of these higher resolution models are nested within the larger domain model whose forecast provides the boundary conditions, and the initial conditions of the higher resolution model tend to be over powered by the coarser resolution model's boundary conditions (Kalnay, 2003). The result is that the higher resolution model will magnify the conditions of the coarser resolution model (Kalnay, 2003).

Second, the terms grid-point and spectral refer to the methods used to solve the partial differential equations from §2.4.1, which cannot be solved analytically, so they must be solved numerically. The process of solving the equations numerically requires the discretization of the model domain where the model variables are assigned grid points and the solution to the differential equations are obtained by finite-difference methods. In contrast, spectral based models represent the spatial variations of the model variables as a finite series of waves (orthogonal basis functions such as the Fourier series) of differing wavelengths (COMET/UCAR, 2009a). Spectral based model resolutions are typically specified by a  $T$  number that represents the number of waves used to represent the model fields. There is no precise way to express the spectral model's resolution in a grid point manner, but it can be approximated by  $360^\circ/3N$  (COMET/UCAR, 2009b). Additionally, there is the finite-element methods that can be used to represent the model fields where a sum of localized non-orthogonal basis functions are used to represent the model fields (CMC GDPS uses the finite element method – Cote et al., 1998). The most popular models are finite-difference for mesoscale models and spectral for large scale models (synoptic) (Doyle, 2008).

### **2.4.3 Parameterization**

The underlying model dynamics briefly introduced in §2.4.1 describe the atmospheric process at a scale largely defined by the resolution of the model. However, there are an enormity of atmospheric processes that occur at sub-grid scales which cannot be accounted for the general model dynamic equations. For example, processes such as radiation absorbed, scattered or emitted and interactions with the surface play an important role in the atmospheric state, but the scale at which these occur cannot be resolved at the general grid resolution. The process of expressing the sub-grid process in the numerical weather prediction model is called parameterization, and is typically referred to as the model physics. The subject of parameterization has an enormous impact on the forecasts and becomes even more influential as the forecast time increases (Kalnay, 2003). In addition to the numerical schemes introduced in §.2.4.3, the different numerical weather prediction models can use different forms of parameterizations to model the same sub-grid atmospheric process, which will affect the prediction of winds, temperature/humidity at the 2 m level, and precipitation/fog. Parameterization is an enormous subject and a detailed review of the subject can be found in Stensrud (2007).

### **2.4.4 Assimilation**

The assimilation component of the NWP has been defined succinctly by Talagrand (1997) as the process where all available information is used in order to estimate as accurately as possible the state of the atmospheric and oceanic flow. This is the process of data ingestion and initializing the model for the process of stepping the model in time. Observations can come from number of terrestrial in-situ locations such as surface weather stations, ocean buoy, ships at sea and upper air station soundings. In addition to terrestrial measurements, geo-stationary meteorological satellites, polar orbiting satellites, and now GPSRO products from GPS satellites are used as data sources. Although there is an enormous wealth of data, the location of the data is non-uniform. Figure 2.2 present a sample of data coverage

plots from the ECMWF for January 15th 2012 00UTC, and it is evident that regions in North America and Europe/Asia are more densely covered than other regions such as the polar regions and Africa<sup>5</sup>. Figure 2.2 plots the surface and ship stations, aircraft observations, GPSRO observations, and observations from a meteorological satellite IASI<sup>6</sup>.

There are two basic assimilation scheme: (a) sequential, and (b) non-sequential (or retroactive). The sequential scheme only considers observations made in the past up until the assimilation (real-time), and the non-sequential considers observations made in the past and future (such as an re-analysis) (Bouttier and Courtier, 1999). In addition to these terms, there are also intermittent and continuous assimilation. Intermittent assimilation refers to the retrieval of observations at specific intervals, where continuous assimilation refers to the applications of the observations at at each time integration step (Coiffier, 2011). Typically there is a first guess at the state of the atmosphere, which is referred to as the background field. In the past, the background field would be interpolated to the location of the observation where a correction could be computed, which is then interpolated back to the grid point (Talagrand, 1997). These methods were known as optimal interpolation. Since then, variational methods have been developed, namely 3D-var and 4D-var. The variational methods define a cost function that is proportional to the square of the distances between both the analysis and the background and the observations (Kalnay, 2003). The 3D-var approach performs the minimization at a specific epoch whereas the 4D-var system the minimization is performed in time (Coiffier, 2011). Typically an observation window of  $\pm 3$  hours centred on a reference time is used.

Figure 2.3 summarizes the basic process flow of a global model for an intermittent assimilation process. The observations are selected within a specific time window and along with the background field, the model is assimilated and initialized. A feedback loop

---

<sup>5</sup>a complete set of plots can be found at <http://www.ecmwf.int/products/forecasts/d/charts/monitoring/coverage/dcover>. URL current as the date of this publication

<sup>6</sup>IASI is the Infrared Atmospheric Sounding Interferometer from EUMESTAT (European Organisation for the Exploitation of Meteorological Satellites). The IASI provides atmospheric emission spectra to derive temperature and humidity profiles (EUMESTAT, 2013).]

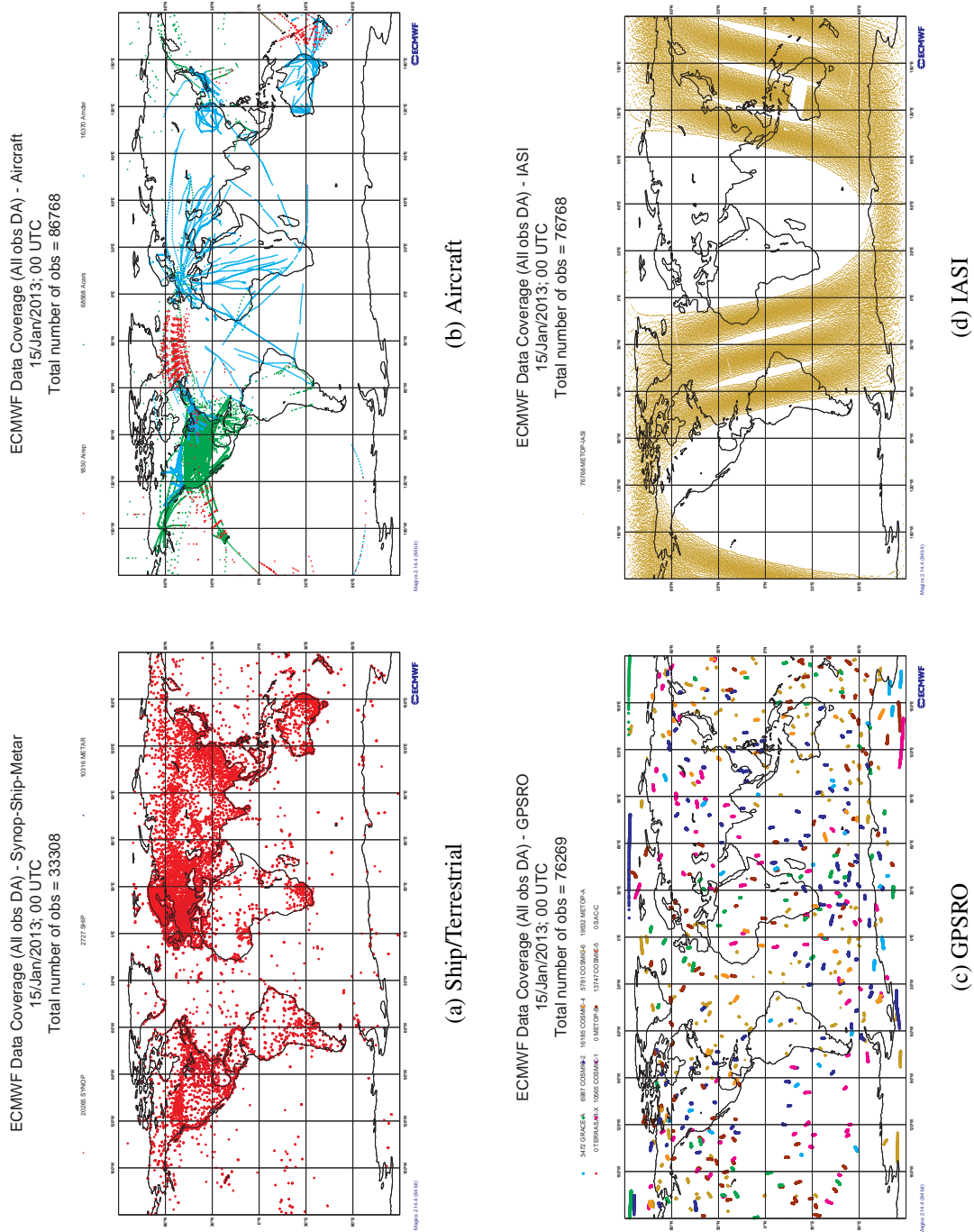


Figure 2.2: ECMWF observation coverage for January 15th, 2012 00UTC. (a) Ship and terrestrial stations; (b) Aircraft; (c) GPSRO, and (d) IASI. From ECMWF, (2012b).



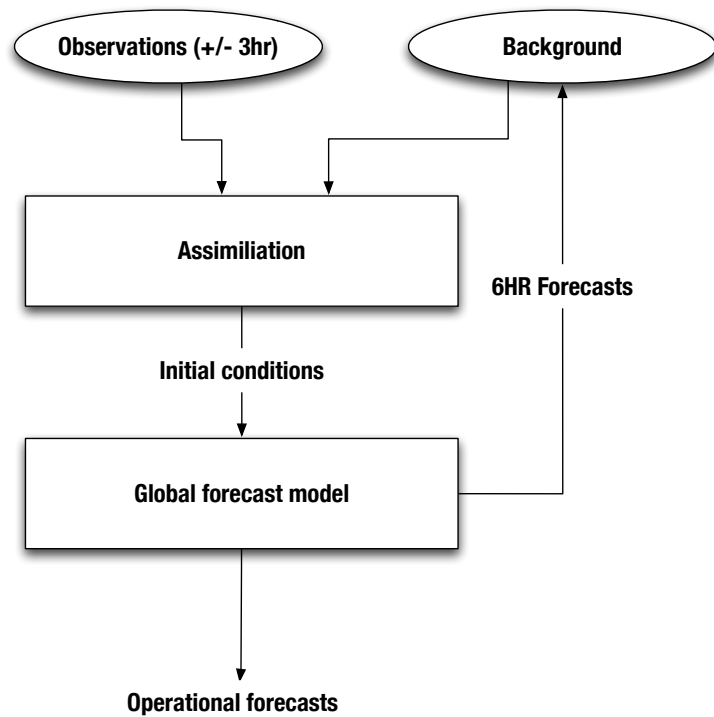


Figure 2.3: Typical intermittent process flow for a global numerical weather prediction model analysis cycle performed at 00, 06, 12 and 18 UTC. After Kalnay (2003).

in the system is created where the forecast is used to generate the background field at the next assimilation. Initially, climatologies have been used to produce the background field, but as forecast have improved they have been applied to the generation of these background field (Kalnay, 2003). In contrast, a regional model would use a smaller time window ( $\pm 30$  min) and the forecast that is used at the background would be a 1 hour forecast instead of a 6 hour forecast (Kalnay, 2003).

# Chapter 3

## Assessment of Numerical Weather

### Prediction Models

The UNB Vienna Mapping Function service will be dependent on the datasets provided from various numerical weather prediction models (NWP's) (a detailed description of the UNB-VMF1 can be found in Chapter 4). It is the intent of this chapter to try to characterize the NWP's performance relative to each other with respect to parameters considered important to geodetic analysis. A greater appreciation of the source dataset capabilities will allow for opportunities to highlight the dataset's strengths and weaknesses such that the end user can use products derived from such datasets more intelligently and with greater efficiency. Further, this knowledge will be applied in selecting source datasets for the UNB-VMF1 service.

This chapter is composed of three sections. The first section, §3.1 will provide some description regarding the NWP's selected for the analysis. §3.2 Previous Work, outlines some of the past efforts and/or typical means to assess and NWP's quality. §3.3 outlines a comparison of the extracted pressure, temperature, and specific humidity from the NWP to that of actual meteorological measurements made on site. This comparison is extended to the the hydrostatic zenith delay since pressure is the dominant quantity effecting that

estimation. The next section §3.4 makes an attempt to compare impact of grid resolution on ray-traced zenith delays. The Canadian Meteorological Centre now offers three NWP's with varying grid resolutions. This comparison will attempt to provide some insight to the need of a fine meshed NWP in geodetic analysis. The final section §3.5 summarizes and concludes results for the chapter.

### **3.1 Numerical Weather Prediction Models**

There are a number of NWP's available for public use that are produced by many differing global agencies. In North America, The Canadian Meteorological Centre (CMC) and the National Centers for Environmental Prediction (NCEP) - which is a component of NOAA in the United States - form two major organizations responsible for the operation and research of NWP's. UCAR (2011) has compiled a matrix of operational NWP's from these North American organizations (also includes ECMWF) that summarizes each of their distinguishing features. The NWP datasets selected for the UNB-VMF1 will be sourced from these organizations.

There are several aspects of numerical weather prediction models that need to be considered when selecting the dataset in geodetic applications. These include data accessibility, coverage (including spatial resolution - horizontal and vertical), currency, ease of integration into existing software packages, and quality. Accessibility speaks to the ability of obtaining these datasets in a robust and consistent manner. In particular, the mode of access is important (e.g., FTP, HTTP, etc) as well as the temporal window of opportunity. Not all products are available indefinitely, and this would command an additional stress on any service based on those products since any connection loss could potentially create gaps in the correction datasets. Both NCEP's GFS/NAM<sup>1</sup> and CMC's products are only available for a 24 hour window. In contrast, NCEP's Re-Analysis 1 product is available

---

<sup>1</sup>GFS is the Global Forecast System and is NCEP's main global operational system. NAM is the North American Mesoscale Model and this is NCEP's operational regional model

all the way back to 1948 in a persistent manner. Although the resolution of NCEP's Re-Analysis 1 product is much coarser than the other products, it does provide a global dataset with an approximate 3-day delay that is much more forgiving in operational circumstances due to the persistent nature of the availability.

The spatial resolution of the NWP will directly impact the ability to model atmospheric conditions effectively. Larger resolution will not be able to detect small local effects, where a NWP will require at least five grid points to define a feature (COMET/UCAR, 2009c). When the NWP is evaluated within the construct of geodetic corrections, the coarse grid resolutions may not be too much of a concern (although this idea is tested in §3.4). The data provided from the NWP is used to define the refractivity along the GNSS signal path, which is then used to compute a hydrostatic and non-hydrostatic delay. For example, the hydrostatic delay varies slowly in time and space on the order of 100 to 1000 km spatially and 3 to 30 hr temporally (Bosser et al., 2007). Even though NCEP's Re-Analysis 1 dataset has a horizontal resolution of  $2.5^\circ \times 2.5^\circ$  (approximately 230 km, where the minimum size of resolvable feature would be  $\sim 1100$  km), although not ideal, it should still be sufficient for estimating the hydrostatic zenith delay (this is evaluated in §3.3 and Chapter 5). However, the non-hydrostatic zenith delay exhibits large variations in both the spatial and temporal domains. One can expect the scale of the variation to be approximately 1 to 100 km spatially, and 1 to 100 min temporally (Bosser et al., 2007). Even the high resolution models (i.e. CMC's GDPS) will have some difficulty dealing with this level of variability (especially temporally). Fortunately, in standard GNSS analysis the non-hydrostatic component is estimated and the hydrostatic component is used *a-priori*.

Thirdly, the ease of integration of the dataset into analysis software must be considered. The UNB ray tracer has been designed to accept datasets describing temperature, geopotential height, and specific humidity defined on isobaric pressure levels. All the global datasets (GFS, Re-Analysis 1, GDPS) listed in Table 3.1 provide the necessary parameters

on isobaric pressure levels compatible with the UNB ray tracer, so this factor can be met by all, and no one model is favoured over the other.

Taking all aspects into consideration, NCEP's Re-Analysis 1 dataset is the appropriate choice for the UNB-VMF1 service. The robustness of data availability is vital to the effective operation of an international scientific geodetic corrections service, and since there are several other geodetic correction products based on it (see Chapter 1) the use of the dataset will help create the consistency in the corrections applied to GNSS computations (which is major component of the motivation for this work). Further, a reanalysis dataset has the added benefit of being isolated from changes to the data assimilation system. The resulting differences will be real or due to changes in the observational network (Bromwich et al., 2005).

Even though NCEP's Re-Analysis 1 will compose the main operational product of the service, it cannot provide predicted (forecast products) and a backup product should be produced in the event of any data interruption. The CMC's GDPS and NCEP's GFS are the natural choice for these products. CMC's GDPS product description is quite similar to that of NCEP's GFS. The availability, coverage, and currency are equivalent. The GFS offers specific humidity on 37 pressure levels (1000 mbar to 100mbar) and 26 levels for temperature and geopotential height (1000 mbar to 10 mbar). In contrast, the CMC offers all parameters at 28 pressure levels (1015 mbar to 50 mbar). Even though the GFS provides specific humidity on 37 levels, CMC's GDPS provides greater vertical resolution closer to the surface. Along with the addition of the 1015 mbar pressure level, CMC provides seven levels between the lowest (1015) and the 900 mbar level, whereas the GFS only provides five. Further, the addition of the lower pressure level will help to reduce the extrapolation that can occur if the target point's height is below the lowest pressure level. Much of the additional pressure levels are located at higher elevations, where the humidity is quite low. The refractivity is largest close to the surface, so it is important to define it as best as possible at these locations. In fact, NCEP's Re-Analysis 1 product only defines

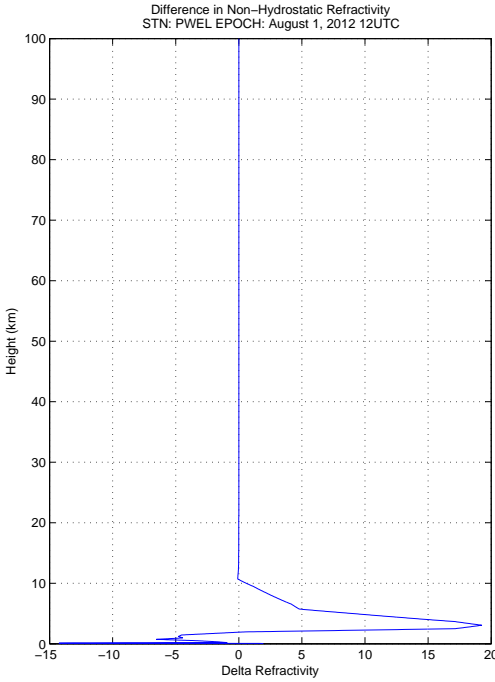


Figure 3.1: Difference in Non-Hydrostatic refractivity - NCEP minus CMC

the specific humidity to the 300 mbar level. Ghoddousi-Fard (2009) showed that the non-hydrostatic refractivity is negligible above altitudes of 10-15km, which is well below the contribution of the atmosphere to the hydrostatic refractivity (~30km). Figure 3.1 illustrates the difference of refractivity between CMC's GDPS and NCEP's Re-Analysis 1 for the August 15, 2012 at 12UTC for station PWEL at an elevation angle of 90°. The non-hydrostatic refractivity from NCEP's Re-Analysis 1 goes to zero at a height of ~10.7km and CMC's GDPS goes to zero at a height of ~19km, but the largest differences are seen at heights below 10km. The differences in the non-hydrostatic refractivity are less than 1 for heights greater than 9.9km, so the fact that there pressure levels are truncated at 300 mbars is negligible and additional vertical resolution in this region would be unnecessary for this application. For these reasons the CMC's GDPS has been selected as a backup product, as well as to provide predicted (forecast) product.

Lastly, the evaluation of the quality of the NWP must be taken into consideration.

This is a function of many differing principles such as the underlying model physics and parameterizations, spatial resolution, and methods employed for model assimilation and initialization to name but a few. The World Meteorological Organization (WMO) defines standards of scores against radiosonde observations and model analysis, which are used to verify NWP products and are defined in the WMO Manual on GDPFS Vol.1 (no.485) Attachment II-7. This attachment describes standards for verification of deterministic NWP products that includes definitions for how the verification is to be computed and the intended scope. Two verifications must be completed, that is verification against the analysis centres (i.e CMC, NCEP, ECMWF, etc) own analysis product, and verification against a set observations from radiosondes. This verification is achieved by the computation of a set of scores that include the following: mean error, root mean square error, correlation coefficient between forecast and analysis, rms vector wind error, mean absolute error, rms anomaly, standard deviation of field, and S1 score (WMO, 2010).

The 16<sup>th</sup> Congress of the WMO in 2011 approved the establishment of the lead centre for deterministic NWP verification (designated to the ECMWF), which has the role of facilitating the standardization of the verification and to ensure that the verification results are shared between analysis centres (ECMWF, 2012). The lead centre provides time series plots of the verification scores defined by the WMO GDFS Manual (attachment II-7) to the public (<http://apps.ecmwf.int/wmolcdnv/>). These time series plot allow for an efficient broad means to assess the current status of NWP quality. The following figures, Figures 3.2 and 3.3, are a time series of the root mean square error for mean sea level pressure and temperature at 850 hPa respectively. The root mean square error is defined by WMO (2010) as:

$$rms = \sqrt{\sum_{i=1}^n w_i (x_f - x_i)_i^2} \quad (3.1)$$

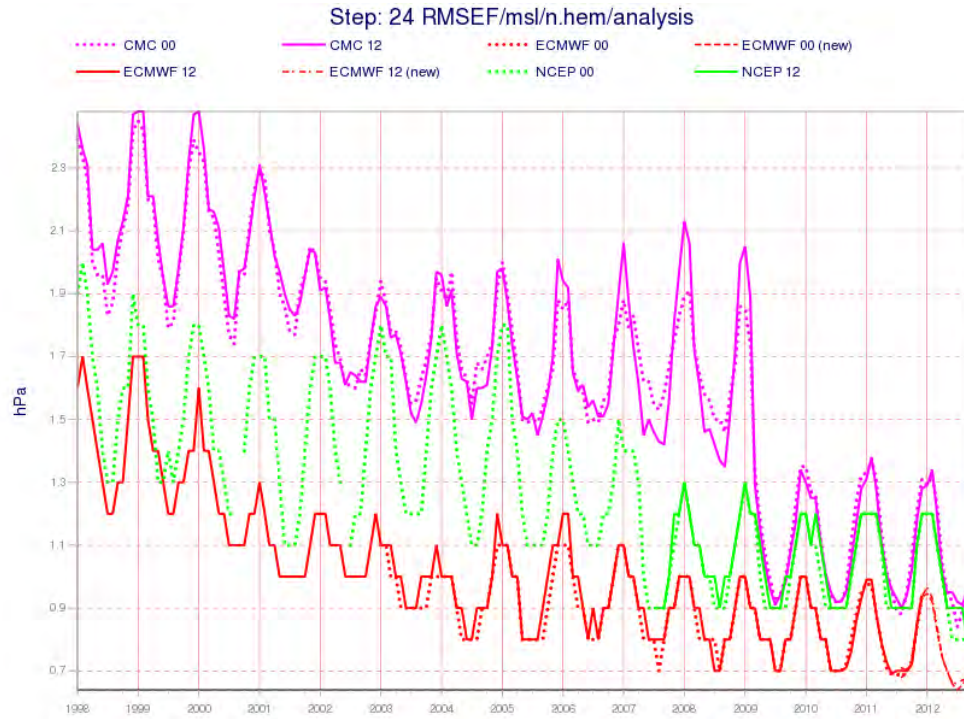
where,

$x_f$  is the forecast value,  $x_v$  is the verification value,  $n$  is the number of grid points or observations in the verification area, and  $w_i$  can be defined by  $\cos\phi_i$  for verification with analysis or  $\frac{1}{n}$  for verification with observations.  $\phi_i$  is the cosine of latitude at the  $i^{th}$  grid point.

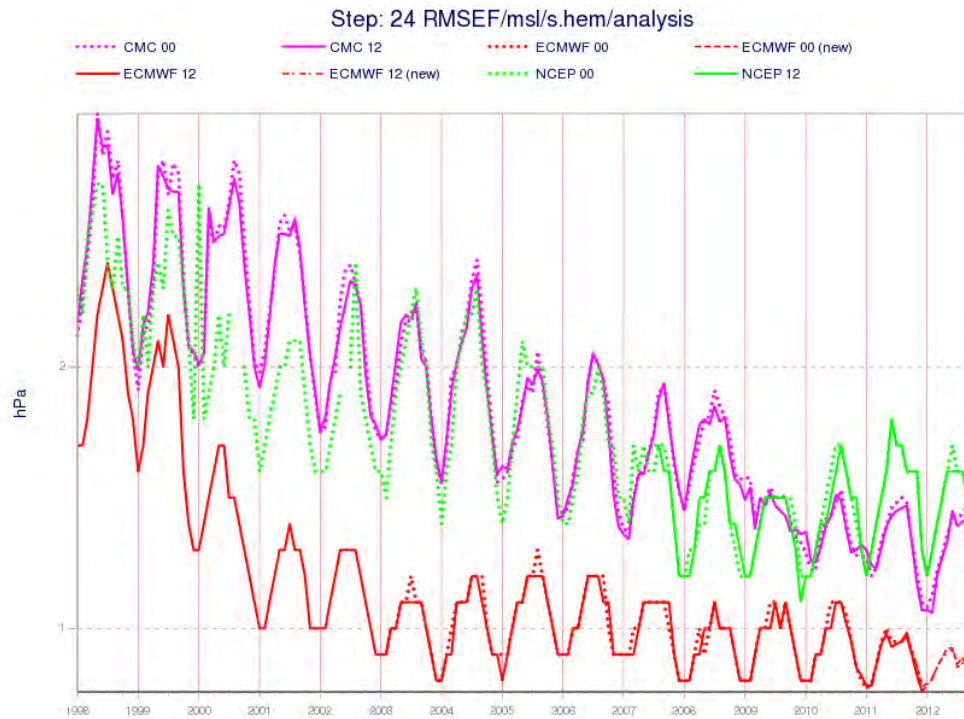
Figure 3.2 illustrates the time series from 1996 until the present of the RMSE error of a 24hr forecast for the mean sea level pressure as compared to the NWP's analysis for ECMWF, CMC (GDPS), and NCEP. Please note that NCEP in this figure is not the Re-Analysis 1 dataset, but the GFS. Since this a verification with the NWP's analysis, the plot represents more of an internal consistency with itself than with ground truths. It is evident that there is a convergence in both the northern and southern hemispheres (which can also be seen in figure 3.3) that demonstrates a continual improvement over the last decade. Most striking is the large drop in RMSE from the CMC's GDPS in the middle of 2009. This drop correlates with the introduction of a new assimilation system in May 2009 and the introduction of higher level atmospheric data ([http://collaboration.cmc.ec.gc.ca/cmc/cmoe/product\\_guide/docs/changes\\_e.html](http://collaboration.cmc.ec.gc.ca/cmc/cmoe/product_guide/docs/changes_e.html)). Secondly, a seasonal oscillation can be clearly seen in both hemispheres with both indicating an increase error in the winter months. Interestingly, the CMC has just updated its regional NWP (RDPS) to version 3.0, which will significantly improve the winter forecasts (CMC, 2012a).

Figure 3.3 illustrates the verification of temperature at the 850 hPa pressure level with respect to radiosonde observations. Again, the time series illustrates the convergence over the past decade, but the differences between each model is small, especially for the southern hemisphere. For temperature, the periodic nature seems to be confined to the northern hemisphere and exhibits an increased RMSE for the winter months. However, in the southern hemisphere there does not appear to be a strong periodic signature in the time series. Overall, it appears that all NWP's perform quite similarly in the recent years, with NCEP performing worst in the winter months of the northern hemisphere.



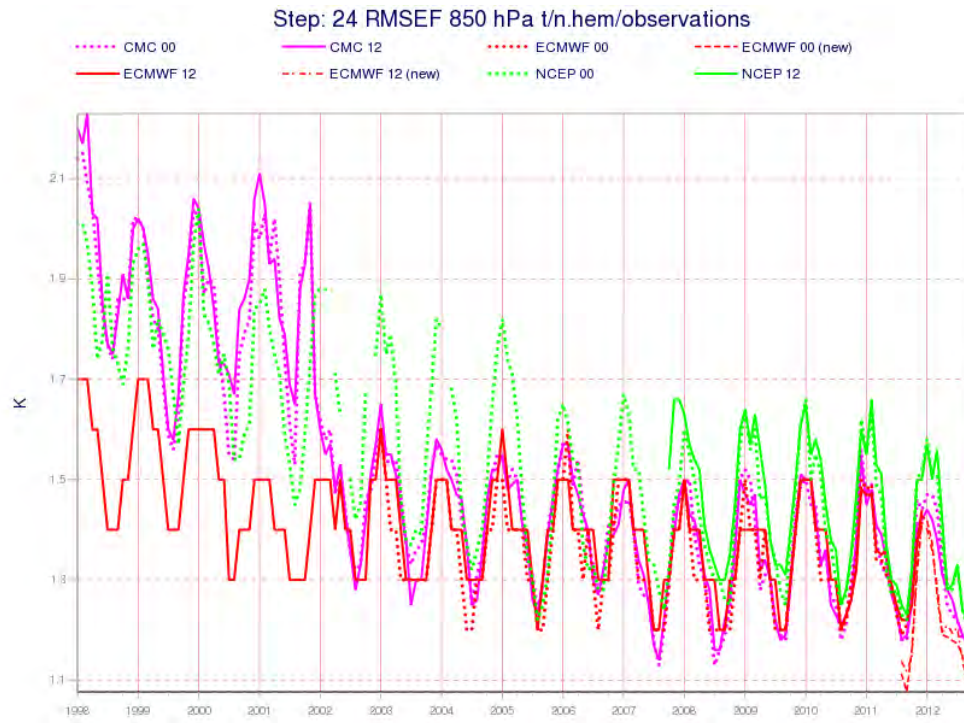


(a) Northern Hemisphere

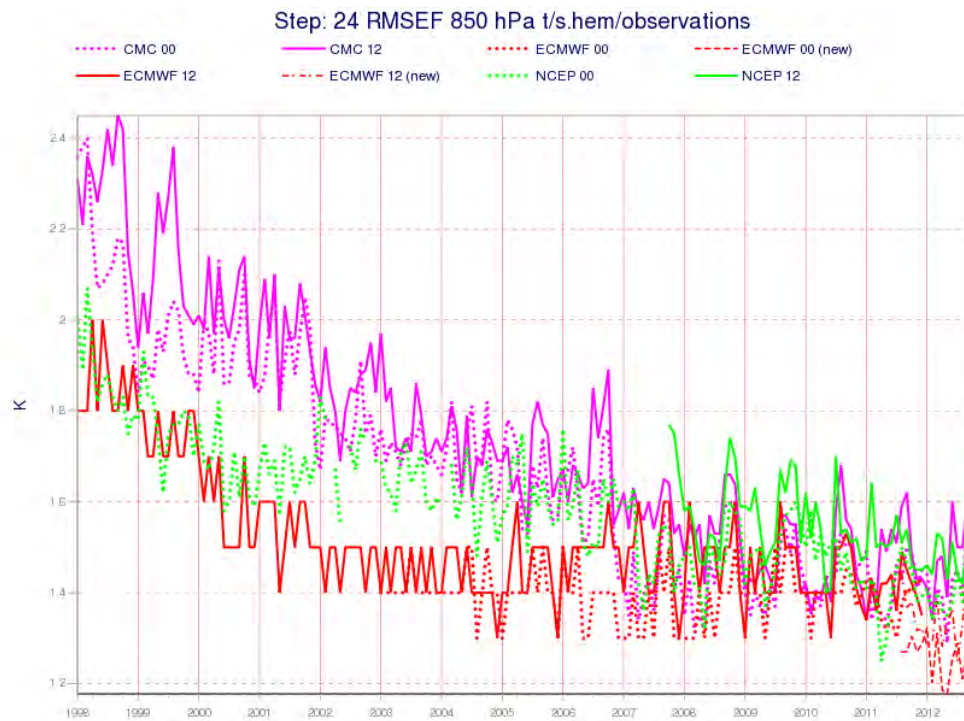


(b) Southern Hemisphere

Figure 3.2: RMSE for Mean Sea Level Pressure; 24h forecast verified with NWP analysis. From 1996 to present (from ECMWF, 2012)



(a) Northern Hemisphere



(b) Southern Hemisphere

Figure 3.3: RMSE for Temperature at 850 hPa; 24h forecast verified with observations. From 1996 to present (from ECMWF, 2012).

In the context of using these datasets for the computation of geodetic corrections, these plots do not tell the whole story. Since the plots are computed for an overall value for a given monthly average, it is unclear how the NWP performs spatially and close to the surface, which can make it difficult to ascertain any topographic effects on the NWP quality. In geodetic applications, the hydrostatic zenith delay is computed *a-priori*, where the non-hydrostatic zenith delay is estimated. The computation of the hydrostatic zenith delay must be as accurate as possible, since errors in the hydrostatic zenith delay cannot be fully absorbed by the estimation of the non-hydrostatic zenith delay, which manifest themselves in station height errors (Kouba, 2008). In the case of the UNB-VMF1 (see Ch.4), the *a-priori* zenith delays are computed by ray tracing through a NWP (integrating the refractivity). The computation of refractivity is a function of pressure, temperature and humidity, so errors in these parameters will propagate into the height estimation. The following sections make an attempt to characterize the NWP by the comparison of these parameters to actual measured values at a subset of IGS station locations.

## 3.2 Previous Work

The assessment of the selected NWP's (i.e NCEP Re-Analysis and CMC's products) is based on the comparison of NWP parameters with actual site observations. This investigation builds on earlier work by Urquhart et al. (2011), which examined the quality of NWP datasets and found that ray-traced hydrostatic zenith delays from NCEP's Re-Analysis 1 dataset exhibit higher variability when compared to those from the CMC's GDPS and ECMWF. Other studies examining the quality of NWP datasets, namely NCEP's Re-Analysis 1, were done by Wahr et al. (1998); Velicogna et al. (2001); Petrov and Boy (2004), which examined the expected accuracy of NCEP's pressure fields. Wahr et al. (1998) differenced monthly averaged pressure fields from the ECMWF to those from NCEP. Wahr et al. (1998) found that there was a significant bias in the Antarctic region

between the two pressure fields where the ECMWF annual varying pressure field had an amplitude of -2 to -3 mbar's and NCEP had an amplitude of -15 to 20 mbar. For all other continental regions, the differences were small. Velicogna et al. (2001) recognizes that the errors estimated in Wahr et al. (1998) underestimate the actual pressure field error since the two datasets are very much correlated. Velicogna et al. (2001) compared observed pressure values to those from NCEP's Re-Analysis 1 datasets for two regions, the United States and the North African/Arabian Peninsula. The map averaged 30-day RMS for the North American region was 0.34 mbar and 1.14 mbar for the 6-hourly difference, and in the Arabian region, these values are 0.34 mbar and 1.34 mbar respectively. Velicogna et al. (2001) also notes that the RMS values are larger in mountainous regions when compared to regions of flatter terrain, which is most likely attributed to the NWP's inability to model smaller wavelength features that typically occur in mountainous regions. Petrov and Boy (2004) evaluated the impact of atmospheric pressure loading where a source of error within their computations lies with the source of the atmospheric pressure fields. Petrov and Boy (2004) compared results computed from NCEP's Re-Analysis 1 and NCEP's Operational Final Analysis (noting that these models are not completely independent). Results showed that stations enclosed by mountains showed larger rms errors, which has been attributed to the difference in spatial resolution of the models (1 degree versus 2.5 degrees). Petrov and Boy's 2004 results follow that of Velicogna et al. (2001).

There have also been a number of studies that have compared the perceptible water content, relative humidity and temperature. Bromwich et al. (2005) compared rawinsonde data to NCEP's Re-Analysis 1 and ERA-15/40 year reanalysis in the region of the arctic. Bromwich et al. (2005) noted that NCEP's Re-Analysis 1 performed worst as compared to the ERA products. However, both products performed well when compared to monthly averages, but when compared to 12-hourly observations the agreement drops significantly. Bromwich et al. (2005) also noted that results were better during the warmer months versus the cooler months. Bock et al. (2009) compared 2-m relative humidity and temper-

ature, and surface pressure to observations at 8 GPS sites in West Africa for three NWP's, namely ECMWF, NCEP Re-Analysis 1, and NCEP Re-Analysis 2 (difference in pressure only reported for the ECMWF). Results from the ECMWF showed the best correlation to measured meteorological parameters at the station sites. Also noted was that there was a latitude dependency of the standard deviation of the differences. As one moves from the south to the north, the standard deviation would increase. The results from the pressure differences were only reported for the ECMWF comparison and exhibited discrepancies up to 2.5 hPa and a standard deviation of 0.7 hPa. The larger differences for the NCEP models were attributed to the coarser horizontal resolution (ECMWF was  $\sim 0.25^\circ$  and NCEP was  $2.5^\circ$ ), differences in model physics and assimilation systems. Jakobson et al., (2012) compared various reanalysis projects (European ERA-Interim, the Japanese JCDAS, and the U.S. NCEP-CFSR, NCEP-DOE, and NASA-MERRA) in the region of the arctic by making comparisons of temperature, humidity and wind speeds to tethersonde sounding data. Jakobson et al., (2012) found that all reanalysis datasets exhibited significant errors in the vertical profiles for temperature and humidity for the region, and these errors tended to be larger than climatological trends. Although, NCEP's Re-Analysis 1 was not included in the study (the dataset implemented for this work), NCEP's Re-Analysis 2 was included, which is an updated version of the Re-Analysis 1<sup>1</sup>. The expectation is that the Re-Analysis 1 dataset will perform similarly or worse. NCEP/DOE was ranked second best out of all reanalysis datasets and outperformed the newest reanalysis from NCEP (NCEP/CFSR) in wind speed and air temperature.

Overall these results identify the following common characteristics:

- Finer resolutions are important for regions of topographic variation;
- NWP's do not perform equally at all locations on the globe (esp. polar regions -

---

<sup>1</sup>NCEP/DOE Re-Analysis 2 (Kanamitsu et al., 2002) is an improved version of NCEP Re-Analysis 1 that fixed errors and improved parameterizations of physical processes. It has not been implemented for this research since it is only available from 1979 to the previous year. Further, it does not offer specific humidity as an output parameter, which would require the use of relative humidity and would add a conversion process to the ray tracing schemes

possibly due to data availability);

- Seasonal trends exist - results were better in warmer months than colder;
- Re-Analysis datasets perform better over long-term time periods than shorter;
- Evidence of increased variability that is correlated with latitude.

### **3.3 Assessment of NWP's**

This section attempts to assess the quality of NWP's in a similar fashion to the previous work. However, much of the previous work has been completed in arctic regions, regions with few observations or generally on a small scale (with the exception of Petrov and Boy, 2004). This section will present a small global assessment of the NWP's intended to be implemented into the UNB-VMF1 service. This process will allow for the greater appreciation of differences in source datasets and their implications of their use in geodetic analysis.

#### **3.3.1 Description of Experiment**

The following summarizes the comparison of ray-traced zenith delays and extracted meteorological parameters (at selected station heights) from two numerical weather prediction models (NWP's). An earlier investigation by Urquhart et al. (2011b) demonstrated that ray traced hydrostatic zenith delays from NCEP's Re-Analysis I (NCEP) dataset proved to exhibit higher variability when compared to those from the Canadian Meteorological Centre's (CMC) Global Deterministic Prediction System (GDPS) and the European Centre for Medium Range Weather Forecasting (ECMWF). This investigation expands on the original by analyzing the variation of the zenith hydrostatic delay (as ray traced through the NWP) and the extracted meteorological parameters at the surface for 35 IGS reference stations for the entire year of 2010.

Two NWP's were selected, NCEP's Re-Analysis I and CMC's GDPS, which were selected since both form the basis for the UNB-VMF1 service. Both models have global coverage, but NCEP's grid resolution is  $2.5 \times 2.5$  degrees as compared to CMC's (GDPS)  $0.6 \times 0.6$  degrees (see table 3.1). Also included in the meteorological parameter comparison is the Global Pressure and Temperature model (GPT). The GPT is a global empirical model of pressure and temperature based on spherical harmonics up to degree and order nine (Boehm et al., 2007). The GPT is based on a NWP, namely three years of the ECMWF (Sept.99 - Aug.02) monthly mean temperature and pressure 40-year re-analysis on a 15 degree grid. The GPT has been included in the comparison because it serves as a backup to VMF1 zenith delays<sup>2</sup> and is used in UNB's GAPS PPP software when reducing VMF1 gridded values to the station height.

The position within the NWP is defined by the position of the IGS reference stations. IGS reference stations are ideal for this analysis since they provide an independent source of meteorological data that has not been assimilated into the NWP (this has been verified by the CMC from personal communication Tremblay, 2012). The position of the reference stations are defined by the IGS weekly solutions with week 52 coordinate values for the year 2010. The weekly solution height was subsequently adjusted by the defined meteorological sensor offset (added or subtracted) as defined by the IGS stations's respective log (Section 8 - Meteorological Instrumentation in IGS log file).

The station selection process was based on an attempt to provide an even distribution across the globe. However, station selection was restricted to the availability of meteorological data (which were selected from a pool of data available on the CDDIS server). Taking into consideration the availability of meteorological data, stations that were at high, mid, and close to equatorial latitudes were selected as well as stations that were close to sea level and located at high elevations. Figure 1, illustrates the location and name of stations selected for this analysis. Gaps in northern South America and north-west Africa

---

<sup>2</sup>See Chapter 4 for full description of UNB-VMF1. The UNB-VMF1 service provides ray-traced zenith delays as well as mapping function parameters



are noted, but meteorological data for stations in these regions were unavailable.

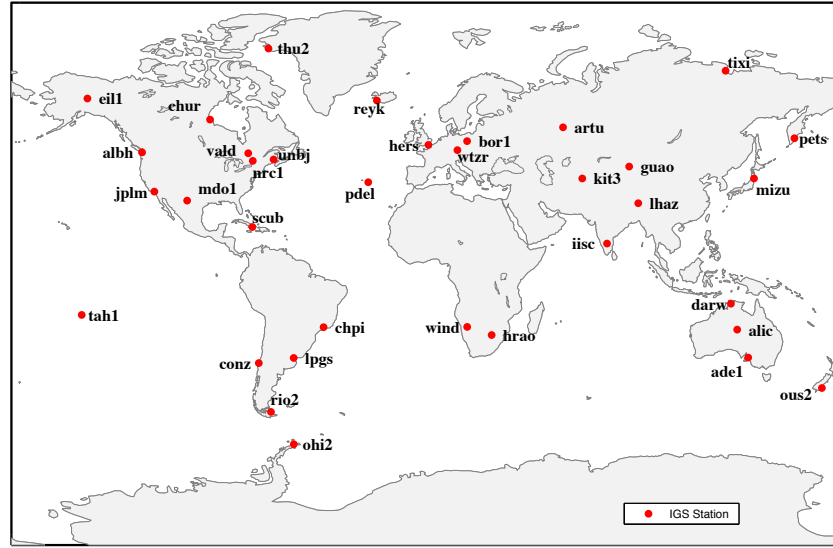


Figure 3.4: Location of IGS Stations

The investigation is based on the following two comparisons:

1. *Extracted meteorological parameters (pressure, temperature and specific humidity) from the NWP (NCEP and CMC (GDPS)) and Global Temperature and Pressure Model (GPT) compared to measured parameters from the site.* Here the parameter is extracted from the NWP 4 times daily at epochs 00h, 06h, 12h and 18h. This is accomplished by linearly interpolating vertically (for pressure, the logarithm of the pressure) at each of the grid nodes surrounding the point of interest to obtain the value at the station's indicated height. To obtain the final parameter value at the station height, the value at each of the grid nodes surrounding the point of interest is linearly interpolated two-dimensionally. The parameters from the IGS meteorological RINEX file was then subtracted from the resulting extracted NWP parameter values (as well as the computed GPT pressure and temperature). For the comparison of specific humidity, the humidity values from the RINEX meteorological files required the conversion to specific humidity from relative humidity. This conversion



was performed by the following:

$$q = \frac{e \frac{M_{wet}}{M_{dry}}}{e \frac{M_{wet}}{M_{dry}} + P_d} \quad (3.2)$$

where,  $q$  is the specific humidity,  $e$  is the partial pressure of water vapour,  $M_{dry}$  and  $M_{wet}$  are the molar masses of dry and wet air respectively, and  $P_d$  is the partial pressure of dry gases. The partial pressure of water vapour can be computed by the following:

$$e = \frac{RH}{100} * e_s \quad (3.3)$$

where,  $RH$  is the relative humidity, and  $e_s$  is the saturation vapour pressure that can be computed by the following from Murphy and Koop (2005):

$$\begin{aligned} \ln(e_s) = & 54.842763 - 6763.22./T - 4.210 * \log(T) + 0.000367 * T \\ & + \tanh(0.0415 * (T - 218.8)) * (53.878 - 1331.22./T \\ & - 9.44523 * \log(T) + 0.014025 * T) \end{aligned} \quad (3.4)$$

2. *Raytraced hydrostatic zenith delay compared to the Saastamoinen hydrostatic zenith computed from the measured site pressure.* In this case, the hydrostatic zenith delay is ray-traced through the NWP using the algorithms developed by Nievinski (2009). There have been no assumptions regarding the atmosphere and the ray-path model, so a full three-dimensional atmosphere and ray-path has been used for these comparisons. The Saastamoinen hydrostatic delay computed with the measured surface pressure from the IGS meteorological RINEX file was then subtracted from the ray-traced hydrostatic zenith delay. The Saastamoinen hydrostatic delay was computed by the following formulation as presented in the IERS Conventions (2010), in which

the formula was given by Saastamoinen (1972) and modified by Davis et al. (1985):

$$D_{hz} = \frac{[0.002278 \pm 0.0000005]P_o}{f_s(\phi, H)} \quad (3.5)$$

$$f_s(\phi, H) = 1 - 0.00266\cos(2\phi) - 0.00000028H \quad (3.6)$$

where,  $D_{zh}$  is the hydrostatic zenith delay,  $P_o$  is the total atmospheric pressure that the antenna reference point in hPa,  $\phi$  is the geodetic latitude and  $H$  is the height above the geoid. For the analysis, the geodetic height was used instead since the equation is quite insensitive to this parameter (Petit and Luzum, 2010).

### 3.3.2 Discussion and Results

The analysis begins with the comparison of extracted pressure values followed then by a comparison of temperature and humidity. The final comparison is that of the hydrostatic zenith delay. In particular, the comparisons are reliant on the RINEX-MET file time tags, so any incorrect time tags in the RINEX-MET files will cause an error in the comparison and contaminate the results. It is difficult to detect a time tag error in the RINEX-MET file, so it is recognized that the following results presented here may contain time tag errors. In addition to this possibility, not all time tags in the RINEX-MET files are listed as an exact match to the NWP time tag. Each parameter has been extracted exactly at 00h, 06h, 12h and 18h UTC from the NWP, but the time tag in the RINEX-MET file may not intersect with these times exactly. Therefore, if the RINEX-MET file's time tag is within fifteen minutes of the NWP's extracted time the measurement from the RINEX-MET file has been included in the comparison. The selection of fifteen minutes has been selected since it is the largest sampling rate of the IGS met stations (the sampling rate of the IGS meteorological stations can range from 60 sec to 300 sec). It is recognized that this decision may impact the extraction of the specific humidity parameter since it varies

strongly in space and time. However, the NWP's temporal resolution is only 6 hours (3 hrs for the CMC's GDPS), so any interpolation in time (which would have been a linear interpolation) on the order of fifteen minutes will be small in relation to size of the overall interval, and the linear assumption may not be valid.

Another source of error that could contaminate the results is the horizontal location of the meteorological sensors in relation to the antenna. It has been assumed that the meteorological sensors are located sufficiently close to the antenna so that any horizontal offset will have an insignificant effect on the extracted parameters. However, this assumption may not be valid at all locations selected. The atmospheric pressure loading service at <http://gemini.gsfc.nasa.gov/aplo/> has tabulated the horizontal offset of the pressure sensor to the IGS stations (no indication as to the direction of the offset is given). An examination of these offsets in relation to the stations selected has revealed a maximum offset of 880 m at station PDEL (not all stations in this analysis are listed and all other stations listed are within 200m of the antenna with the majority of the stations under 100m). The horizontal resolution of NCEP's Re-Analysis is ~233 km, which would make 880m ~0.3% of the grid size, and for CMC's GDPS, this makes the 880m offset ~2.5% of the grid size. Therefore, this is not expected to cause a significant impact in the final extracted meteorological parameters at these horizontal resolutions.

The results from the IGS RINEX-MET files are taken as the reference values, but as already noted errors can exist at these stations. To deal with the possibility of time tag error or erroneous measurements at the station, each of the resulting time series has been inspected manually and any gross outliers have been removed (this may not catch all time tag errors if the difference is not grossly different from the general trend of the time series). Further details of the outlier removal can be found in the following sections describing the results for each parameter comparison.

For each comparison, a time series has been constructed where the mean and standard deviation has been computed to characterize the difference. To deal with the potential of

any bias contaminating the computation of the standard deviation, the following functional form has been fitted to the difference time series:

$$f(t) = a_o + a_1t + a_2t^2 + \sum_{n=1}^{nh} c_n[\sin(2\pi t + \phi_n)] \quad (3.7)$$

where,  $a_o$ ,  $a_1$ , and  $a_2$  are the coefficient of the second order polynomial,  $nh$  is the number of harmonics (4 were used in this case),  $\phi_n$  is the phase of the harmonic, and  $c_n$  is the coefficient of the amplitude.

The results of the fit were then subtracted from the time series to remove any bias that may be contaminating the results. Therefore, the computation of the standard deviation was made by the following relationship:

$$\sigma = \left[ \frac{1}{n-2} \sum_{i=1}^n (\Delta p_{nwp} - \Delta p_{fit})^2 \right]^{\frac{1}{2}} \quad (3.8)$$

where,  $\Delta p_{nwp}$  is the difference between the extracted pressure and measured site pressure,  $\Delta p_{fit}$  is the fitted difference in pressure, and  $n$  is the number of epochs. Two degrees of freedom are lost due to the fitting process. Equation (3.7) holds true for the difference in temperature, specific humidity, and zenith hydrostatic delay, but the difference in temperature, specific humidity, and zenith hydrostatic delay is substituted for  $\Delta p_{nwp}$ , and the fitted difference in zenith hydrostatic delay, temperature, and specific humidity replaces  $\Delta p_{fit}$ .

In all cases (pressure, temperature and humidity), the measurements at the meteorological sensor have been considered the truth and errorless. However, there is no guarantee that all of the meteorological sensors are in peak operational form. Issues of calibration will most likely manifest itself in the computation of bias, and spurious data spikes will impact the computation of the overall standard deviation (this will have an effect on the bias as well). Table A.1 in Appendix A summarizes all of the sensors used in this study

and their associated metadata. What is most striking is the lack of any information regarding when the station was last calibrated. Out of the 35 stations, only 10 report a sensor calibration date. Further, out of the 10 stations, only 5 have been calibrated with the last three years. The IGS Troposphere Working Group outlines in their guidelines for submitting meteorological data that all sensors must be calibrated within the manufactures recommendations (IGS Troposphere WG,2012). Typically, meteorological sensor packages are certified to remain calibrated for a duration of three years, and if left uncalibrated for longer periods, the meteorological sensor package will become less useful (Bar-Sever, 2004). In fact, results from Le Bail et al., (2012) demonstrated that many of the meteorological sensors used by the GSFC for VLBI analysis exhibited large biases, spurious spikes, and periods of missing data. Le Bail et al., (2012), went on to demonstrate that the use a consistent set of meteorological data from the ECMWF showed improvements to the overall results.

Lastly, spurious spikes have been removed from the meteorological sensor time series manually. These values have presented themselves in the time series either as a zero value or an excessive departure from the previous epoch. Stations OHI2, SCUB and MDO1 are examples of stations experiencing erroneous values. In particular, station OHI2 would see spikes on the order of 40 mbar's in the measured pressure time series and up to 60°C in the temperature time series. The spikes in the pressure time series were easy to identify and separate, but for the temperature the time series becomes extremely unstable a quarter of the way through the year. For this reason, OHI2 has been excluded from the temperature and specific humidity comparison.

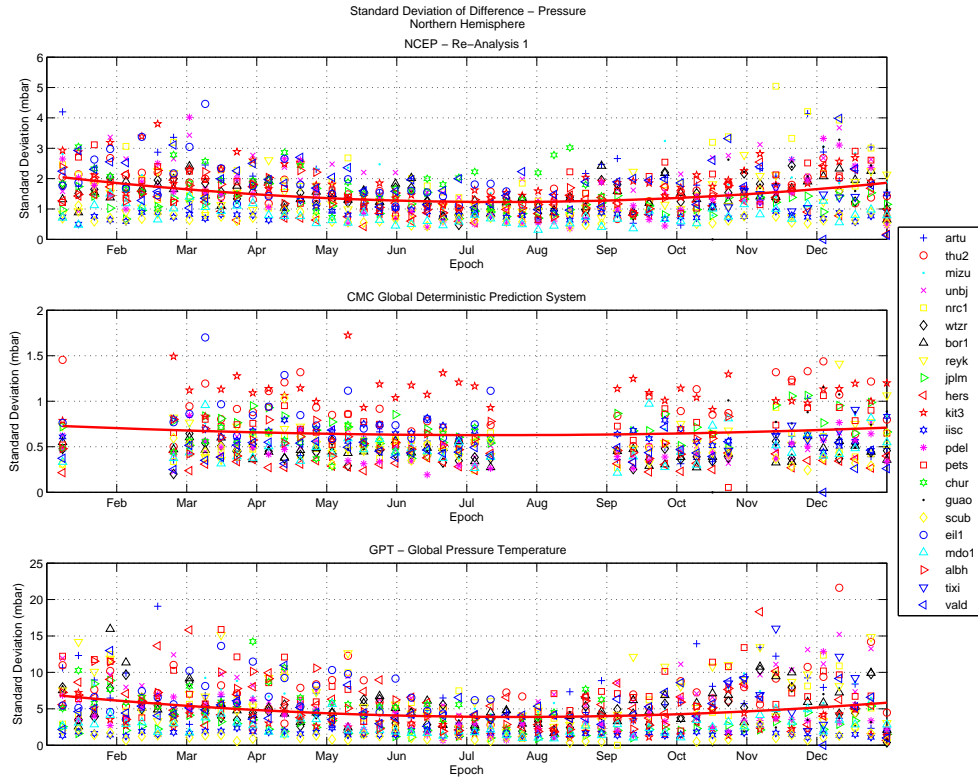
### **3.3.2.1 Pressure**

As noted in section 3.3.1, the pressure has been made in comparison to that of measured pressure at the IGS station. Table A.2 (Appendix A) summarizes the resulting mean difference in pressure and the standard deviation of that difference at each of the 35 IGS

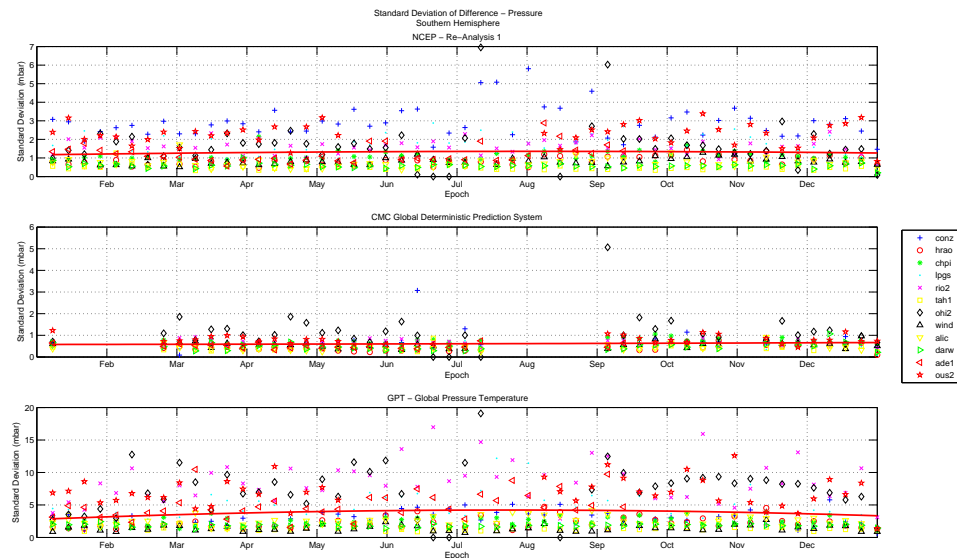
stations for each of the data sources (NCEP, CMC and GPT). Station LHAZ exhibits the largest bias at a magnitude that ranges from 11 to 15 mbar. The source of this bias is most likely due to a calibration issue at the site or possibly an incorrect sensor height reported in the station log file. For this reason, station LHAZ has not been included in the global computation of mean and standard deviation.

In general, the results from the GPT performed the worst followed by NCEP, and the results from the CMC performed best. Overall, the results from the CMC exhibited the smallest biases and standard deviations over the studied interval. The results were then grouped into weekly means and weekly standard deviations. Figure 3.5 plots the weekly standard deviations for the stations located in the northern hemisphere and southern hemispheres with a corresponding second order polynomial describing the overall trend. For both 3.5(a) and (b), the top plot is NCEP, the middle is CMC and the bottom is the GPT (note the scale difference for each subplot). In both cases there is an increased standard deviation during the winter months. This seasonal trend is strongest in the northern hemisphere with the GPT (38% increase) and the dataset from NCEP (30% increase). The trend does exist in the southern hemisphere, but with a much smaller amplitude that is strongest with the GPT dataset. The dataset from the CMC exhibits a more uniform variation across globe as well as the smallest seasonal amplitude (in both hemispheres). The GPT demonstrated the strongest annual variability followed by the dataset from NCEP.

The seasonal dependence of the NWP's were illustrated in Figures 3.2 and 3.3, so Figure 3.5 is a confirmation. A possible source of the increased standard deviation during the winter months could be attributed to fact that the atmosphere during the winter months is more volatile as compared to that in the summer months. Figure 3.6 plots the mean sea-level pressure contours for February 21, 2012 and August 1st, 2012 as predicted by the CMC (GDPS). What is most evident is the fact that the global mean sea level pressure is stable during the summer months in the northern hemisphere as evidenced by the broad contours. However, during the winter months the spatial variability of the pressure



(a) Northern Hemisphere



(b) Southern Hemisphere

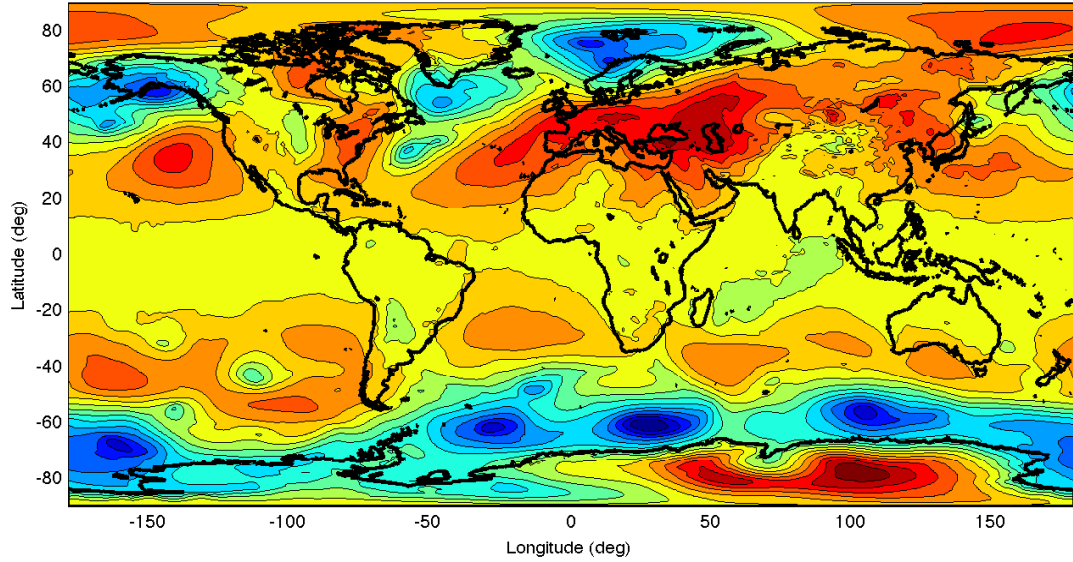
Figure 3.5: Weekly standard deviation of the difference in pressure (a) Northern Hemisphere; and (b) Southern Hemisphere. Note the scale difference for each subplot.

becomes much more unstable. Figure 3.6 also demonstrates that there is also a latitude dependency of the mean sea level pressure. For both seasons the equatorial region is quite stable, but as the latitude become higher (towards the polar region), the pressure is much more variable. The CMC (GDPS) has a horizontal resolution that is approximately  $4\times$  finer than that of NCEP. The finer horizontal resolution can help better define the highly variable winter season, which can explain why the CMC product performed best. GPT is based on monthly means over three years with a 15 degree horizontal resolution (as well as it an expansion of spherical harmonics to degree and order 9) , so it makes sense this empirical model performs worst, since it cannot deal with the high frequency temporal variability of the local pressure.

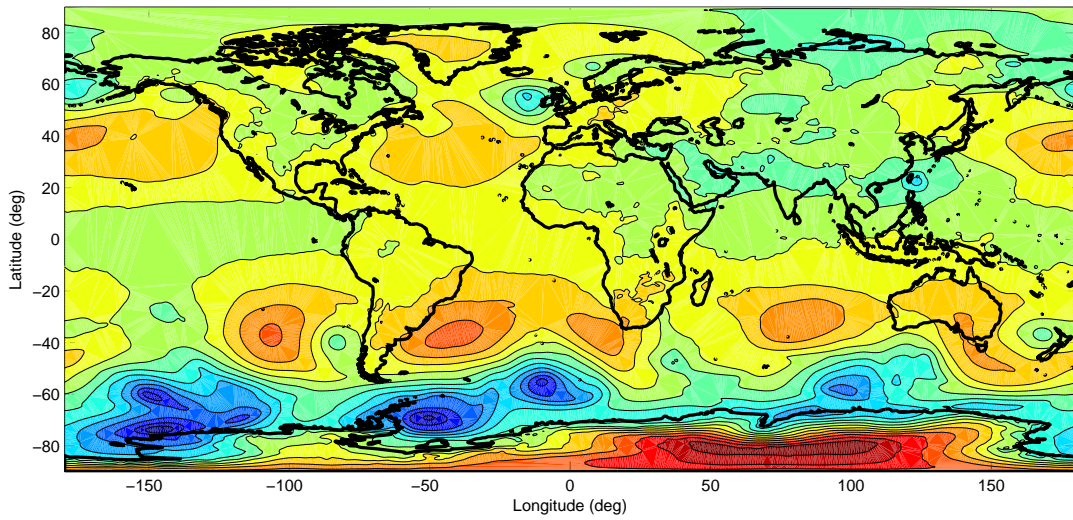
Figures 3.7(a) and 3.7(b) plot the mean and the standard deviation of the difference in pressure respectively. Figure 3.7(a) shows that there is no relationship between the mean difference in latitude, but Figure 3.8 shows a strong relationship between the standard deviation and latitude for the GPT and to a lesser extent the NCEP product. The CMC product does not exhibit any strong relationships to latitude. For NCEP and the GPT, as the station is closer to the equator the performance of the NWP will more closely resemble that of the measured pressure signal. As was shown in Figure 3.6, the pressure is very stable at equatorial latitudes and progressively becomes more variable with increasing latitude. Figure 3.7(b) follows this trend for the NCEP and GPT indicating that these products cannot describe the spatial variability of the pressure as well as the CMC, which is most likely due to the horizontal resolution.

Table 3.1 summarizes the global mean difference and standard deviations for all 35 stations (as well as the maximum absolute differences). Globally, the GPT demonstrates the largest variation followed by NCEP and then the CMC. For the NWP products, NCEP proved to demonstrate 44% higher variability and a 66% reduction in the bias. These results can be used to estimate the impact on height estimates in standard GNSS position computations. Tregoning and Herring (2006) estimated that errors in surface pressure



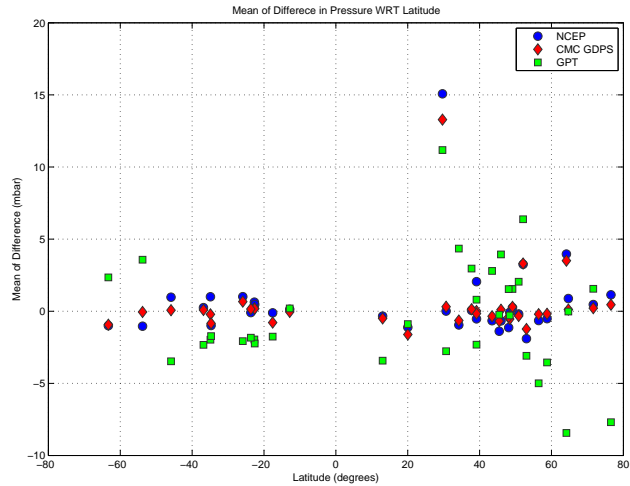


(a) February 21, 2012

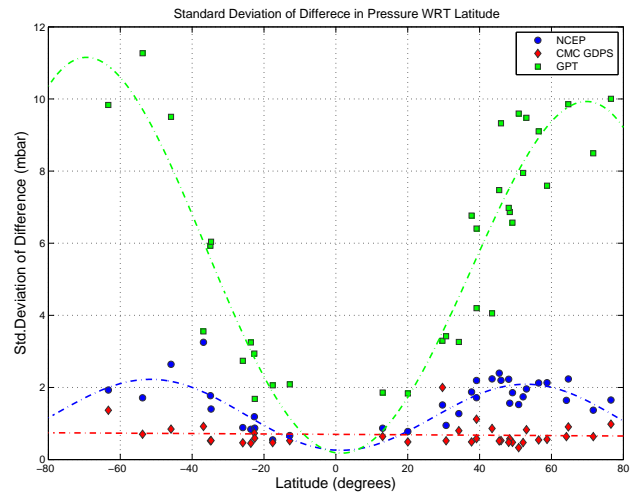


(b) August 1, 2012

Figure 3.6: Mean Sea Level Pressure from CMC (GDPS) (a) February 21, 2012; and (b) August 1, 2012



(a) Mean



(b) Standard Deviation

Figure 3.7: Mean and standard deviation of the difference in pressure with respect to latitude. January 1st to December 31st, 2010.

used to compute *a-priori* zenith hydrostatic delays can propagate into the height solution at a rate of  $-0.2\text{mm/mbar}$ . Assuming the only error in a ray-traced hydrostatic zenith delay is due to pressure only, then the expected error in height can reach almost 5mm at for the GPT, 1.3mm for NCEP and 0.7mm for the CMC at  $3\sigma$ . The maximum absolute differences indicates that differences can reach 50.361 mbars for the GPT. However, this value occurs at station THU2, which is located in the high latitudes ( $76.54^\circ$ ) and the GPT

Table 3.1: Summary of global mean, standard deviation, max absolute value of the difference in pressure for all 35 stations. January 1st to December 31st 2010. All measurements in millibars.

Product	Mean	Std	Max Abs
CMC (GDPS)	0.051	1.251	11.915
NCEP Re-Analysis 1	0.150	2.240	16.987
GPT	-0.781	8.432	50.361

has demonstrated to be insufficient in these areas. Kouba (2009) demonstrated that the GPT can cause pressure correlated height errors up to 10mm in the high latitudes, which matches that maximum absolute value of the difference of 50.361 mbars ( $0.2\text{mm} \times 50.361 = 10.07\text{mm}$ ).

The computation of the global mean and standard deviations do not provide the whole story, so Figure 3.8 plots the histogram of all differences for all 35 stations. The red histogram are the GPT differences, the blue histogram are the NCEP differences and the green histogram are the CMC differences. The histogram for the CMC differences exhibits two peaks, which would indicate two separate means. These are not seen in the GPT or the NCEP histograms due to the fact that it is hidden within the noise. The second peak in the CMC histogram is due to stations BOR1 and REYK, but it is difficult to determine if this second peak is due to the NWP or due to the meteorological sensor. Both sensors do not have any information regarding their calibration (Table A.1), so it is possible that the sensors may not have been calibrated properly.

### 3.3.2.2 Temperature

This section provides a summary of the overall global evaluation for the differences in temperature. Table A.3 in Appendix A summarizes the mean and standard deviation of the difference in temperature for each of the 35 stations studied. Overall, the results from the CMC demonstrated the best agreement with the measured temperature, followed by

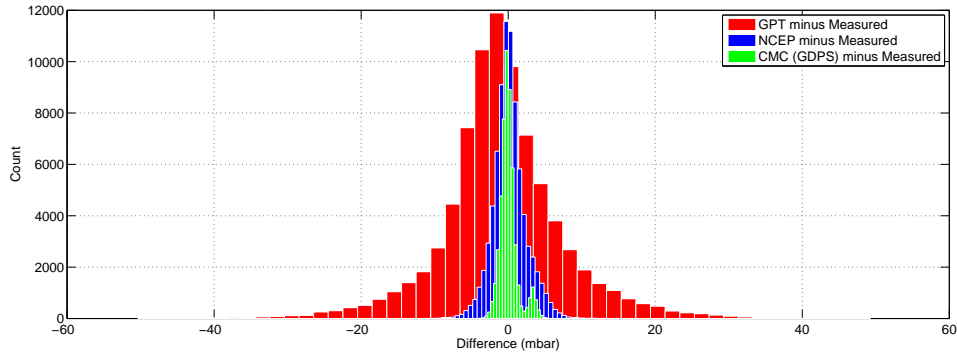
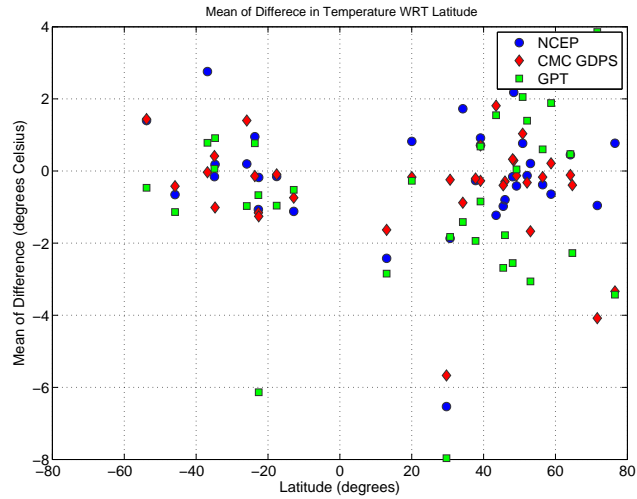
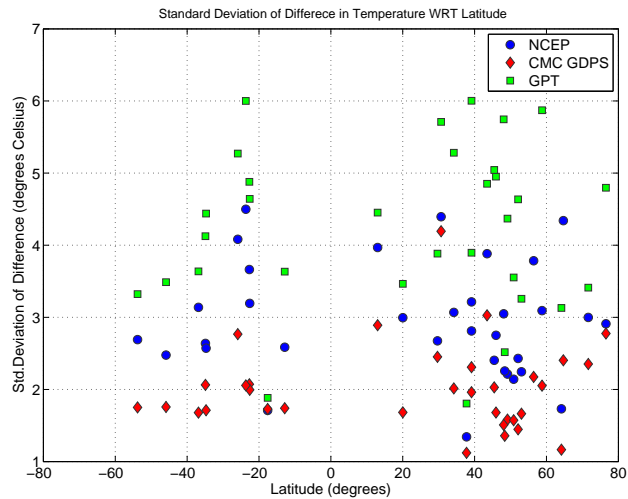


Figure 3.8: Histogram of difference in pressure for the GPT, NCEP Re-Analysis 1, and CMC (GDPS)

NCEP and then the GPT. Figures 3.8(a) and 3.8(b) illustrate the mean and standard deviation of the difference in temperature for all stations (excluding OHI2). Both figures exhibit that a distinct trend with respect to latitude does not exist. The weekly mean and standard deviations were computed in the same fashion as the difference in pressure. Figure 3.9 plots the weekly mean difference for stations located in the northern hemisphere, Figure 3.9(a), and stations located in the southern hemisphere, Figure 3.9(b). The trend (red line) in Figure 3.9 has been shown using a second order polynomial fit. For each subfigure in Figure 3.9, the top figure is NCEP, the middle is the CMC, and the bottom is the GPT (please note the scale difference on the y-axis). The difference in temperature does not show a strong seasonal trend in the standard deviation of the difference (not shown). However, the mean difference in temperature does show a seasonal trend for the GPT, where the mean difference is largest in the winter months. The GPT is an empirical model that has been based on monthly mean temperatures extending from 1999 to 2002 from the ECMWF as opposed to the NCEP/CMC, which are based on the assimilation of the most recent observations. The winter climate conditions during the years 1999-2002 may not be representative of conditions in 2010, which may explain the source of the increased mean difference during those months. Table 3.2 summarizes the overall global mean and standard deviation for each of the products tested. Overall, NCEP demonstrated



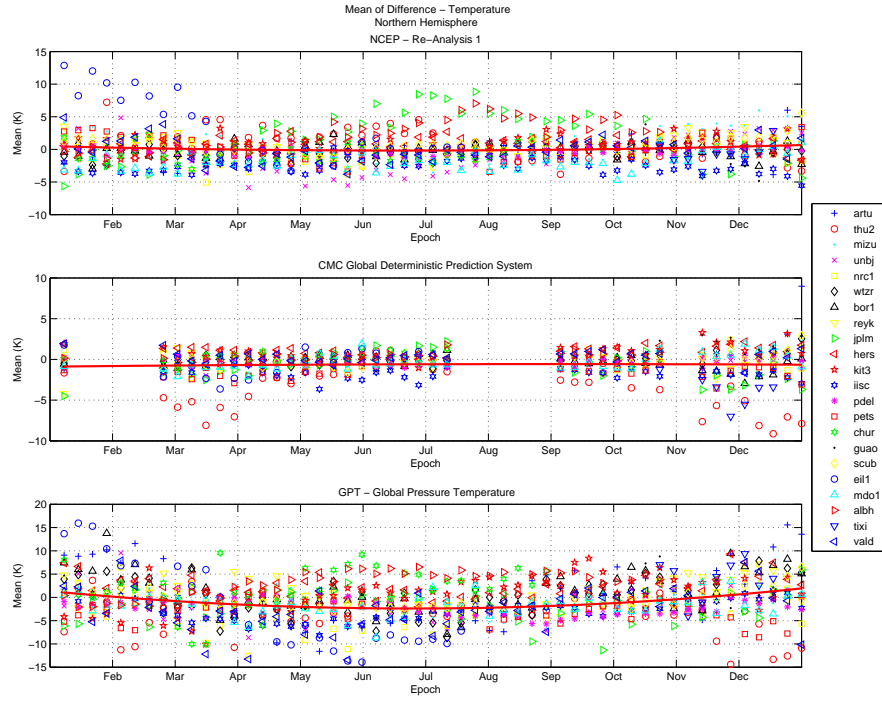
(a) Mean



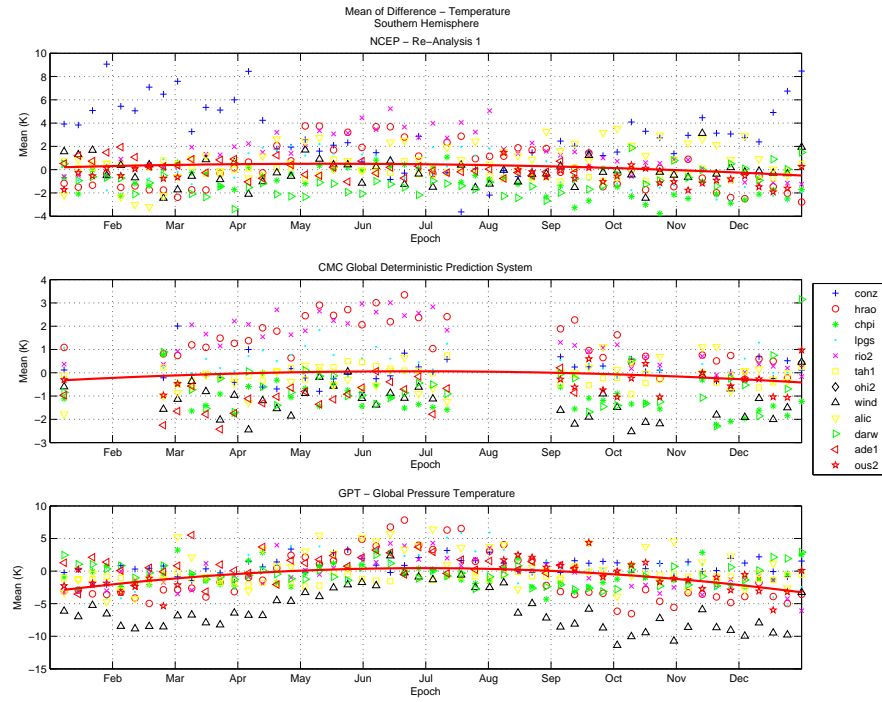
(b) Standard Deviation

Figure 3.9: Mean and standard deviation of the difference in temperature with respect to latitude. January 1st to December 31st, 2010.

the smallest mean difference followed by the CMC then the GPT. The NCEP product exhibits a positive mean difference as opposed to that of the CMC and GPT, which exhibits a negative mean difference. The positive mean difference indicates that the NCEP model overestimates the temperature resulting in a prediction that is on average warmer, and the CMC and GPT are underestimating the temperature resulting in a prediction that is on average cooler.



(a) Northern Hemisphere



(b) Southern Hemisphere

Figure 3.10: Weekly mean of the difference in temperature (a) Northern Hemisphere; and (b) Southern Hemisphere (note the scale difference on the y-axis)

Table 3.2: Summary of global mean, standard deviation, max absolute value of the difference in temperature for all 35 stations. January 1st to December 31st 2010. All measurements in Kelvin.

Product	Mean	Std	Max Abs
CMC (GDPS)	-0.302	2.432	16.362
NCEP Re-Analysis 1	0.158	3.582	36.397
GPT	-0.724	5.595	40.469

Figure 3.11 plots the histogram of all differences in temperature for the GPT (in green), NCEP Re-Analysis 1 (in blue) and the CMC GDPS (in red). Not only does the GPT display the largest standard deviation, it also exhibits the largest maximum absolute value (see Table 3.2). For the GPT and the CMC the largest maximum absolute value occurs at station THU2 and at BOR1 for NCEP. Station THU2 is located at high latitudes, which is known to perform poorly for the GPT. However, the mean difference at station THU2 is approximately  $3.3^{\circ}\text{K}$  for the CMC and GPT, but only  $0.771^{\circ}\text{K}$  for NCEP. Although, the calibration of the sensors at these locations cannot be verified (Table A.1) and the height difference from the sensor to the GPS antenna is not listed; these results would indicate differences in the NWP are the possible cause.

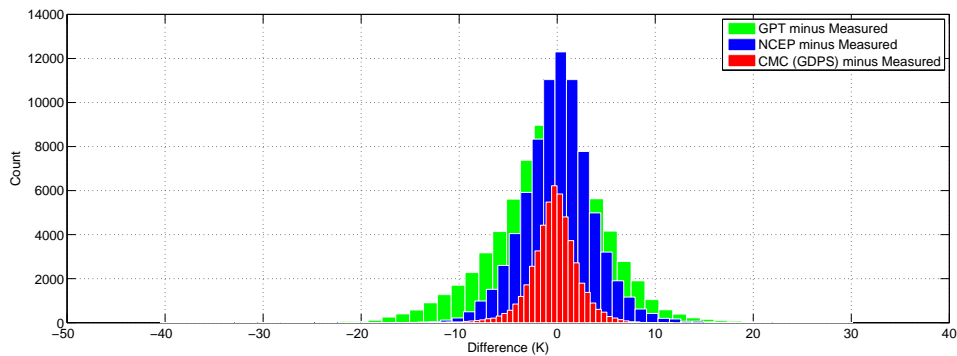


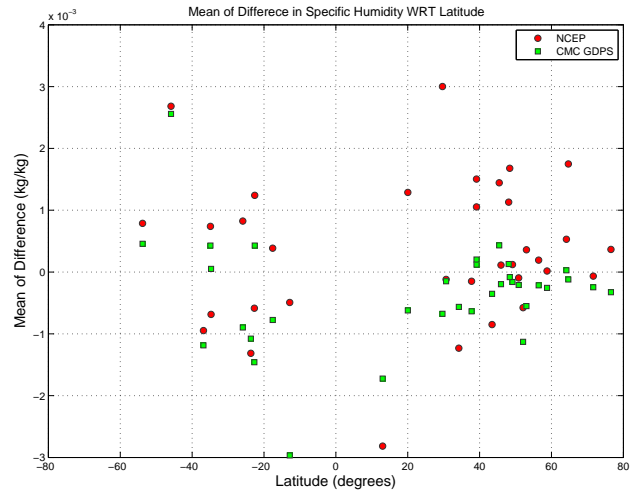
Figure 3.11: Histogram of difference in temperature (in Kelvin) for the GPT, NCEP Re-Analysis 1, and CMC (GDPS)

### 3.3.2.3 Specific Humidity

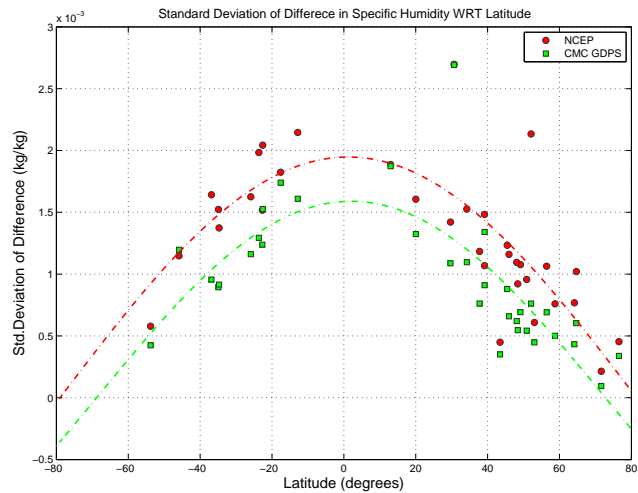
The comparison of specific humidity only includes NCEP's Re-Analysis 1 and CMC (GDPS) since the GPT is only a pressure and temperature empirical model. Table A.4 in Appendix A summarizes the yearly mean and standard deviation of the difference for the specific humidity for each of the 35 stations. The specific humidity, which is measure of the ratio of the water vapour to dry air, has the greatest impact on the computation of the non-hydrostatic delay. Since the water vapour is highly variable in both space and time, this assessment will indirectly help to evaluate the NWP's ability to predict non-hydrostatic delays. Figure 3.10 plots the yearly mean (Figure 3.12(a)) and standard deviations of the difference (Figure 3.12(b)) in specific humidity with respect to latitude. A relationship between the mean difference and the latitude does not exist, but there is a trend with respect to the standard deviation of the difference. Stations that are located closer to the equator experience larger standard deviations. This correlates with the global water vapour distribution, which indicates that both NCEP and CMC experience difficulties with the prediction of water vapour content. Further, it has also been established by Yang et al. (1999) through the comparison of GPS derived precipitable water estimates to those from an NWP, that the RMS differences increase when the precipitable water is growing, so these results follow. Overall, the CMC generally exhibits smaller standard deviations to those of NCEP.

The weekly mean difference and standard deviation has been computed in the same fashion as the pressure and temperature. The mean difference does not exhibit any seasonal trend, but the standard deviation of the difference exhibits exhibits a seasonal trend where the standard deviation worsens during the summer months. Figure 3.13 plots the weekly standard deviation for the difference in specific humidity for stations located in the northern hemisphere and stations located in southern hemisphere (Figure 3.13(a) and 3.13(b) respectively). As with the pressure and temperature, the trend (red line) in Figure 3.13 has been produced using a second order polynomial fit. In each plot, the top subplot





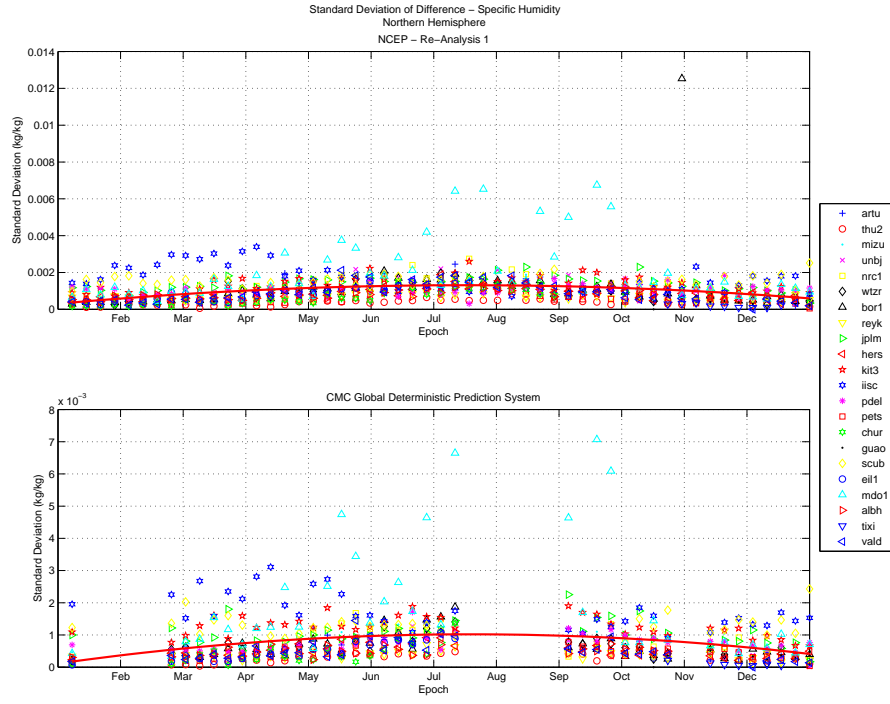
(a) Mean



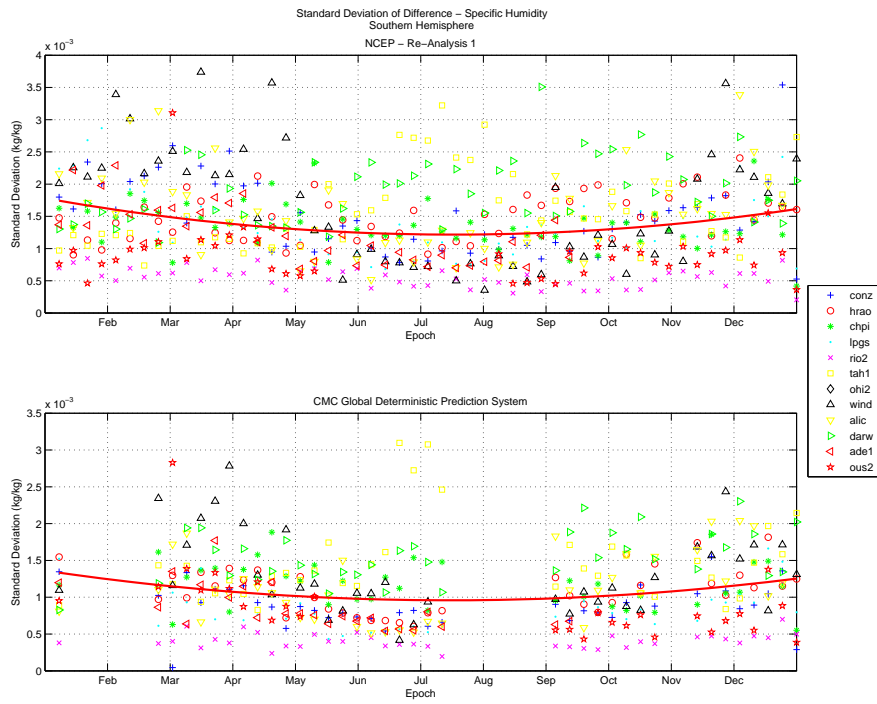
(b) Standard Deviation

Figure 3.12: Mean and standard deviation of the difference in specific humidity with respect to latitude. January 1st to December 31st, 2010.

is NCEP and the bottom is the CMC. The pattern exhibited by each of the NWP's follows the phase of the precipitable water described by Gaffen et al. (1992). Gaffen et al. (1992) demonstrated that the precipitable water during the summer months in the northern hemisphere peaks in August and January/December in the southern hemisphere. Both the CMC and NCEP demonstrate difficulty in describing the water vapour content during these peak periods for all stations.



(a) Northern Hemisphere



(b) Southern Hemisphere

Figure 3.13: Weekly mean of the difference in specific humidity (a) Northern Hemisphere; and (b) Southern Hemisphere (note the scale difference on the y-axis)

Table 3.3 summarizes the overall global mean, standard deviation and the maximum absolute difference for all 35 stations. Although both NWP's exhibit difficulty in describing the humidity of the atmosphere during peak periods of precipitable water, the CMC still demonstrates a smaller overall standard deviation of the difference. The overall mean differences are similar, but NCEP predicts on average a moister climate, and the CMC predicts on average a dryer climate. Taking the difference of the mean and standard deviation between NCEP and the CMC, NCEP would exhibit a 0.0009 kg/kg larger difference at  $1\sigma$ . This would equate to a difference of 6.6 in the non-hydrostatic refractivity. Assuming atmospheric conditions were 1015mb, 15°C, and a relative humidity of 30%, this difference would equate to 28% of the total non-hydrostatic refractivity.

Table 3.3: Summary of global mean, standard deviation, max absolute value of the difference in specific humidity for all 35 stations. January 1st to December 31st 2010. All measurements in kg/kg.

Product	Mean	Std	Max Abs
CMC (GDPS)	-0.0003	0.0016	0.0140
NCEP Re-Analysis 1	0.0002	0.0019	0.0141
GPT	N/A	N/A	N/A

Lastly, Figure 3.14 plots the histogram of all the differences for all 35 stations for both the CMC (red) and NCEP (blue). The maximum absolute value of the differences (Table 3.14) agree well between the two NWP's, which indicates that large spikes can occur in both datasets where no one dataset offers any advantages in this regard.

### 3.3.2.4 Hydrostatic Zenith Delay

The differences in the ray-traced hydrostatic zenith delays will depend mainly on each of the NWP's ability to predict the pressure and temperature at the station. The mean and standard deviations of the differences in the hydrostatic zenith delay for all 35 stations can be found in Table A.5 in Appendix A. This section presents the overall global means and

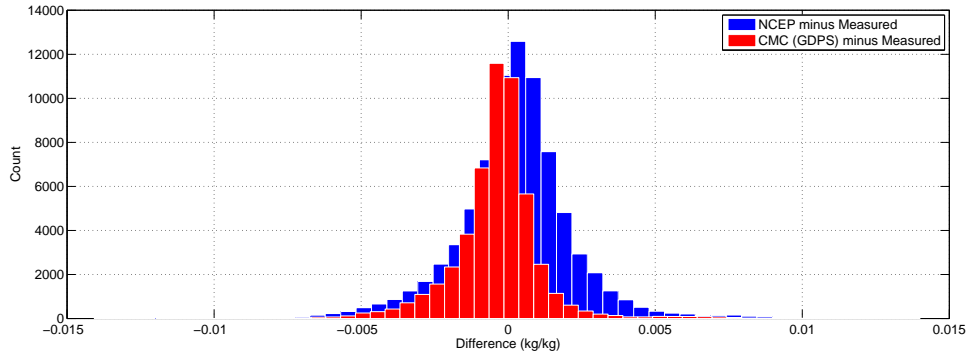
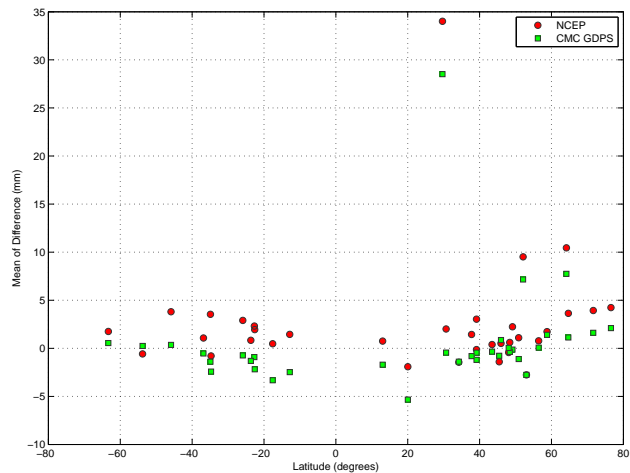


Figure 3.14: Histogram of difference in specific humidity (kg/kg) for the GPT, NCEP Re-Analysis 1, and CMC (GDPS)

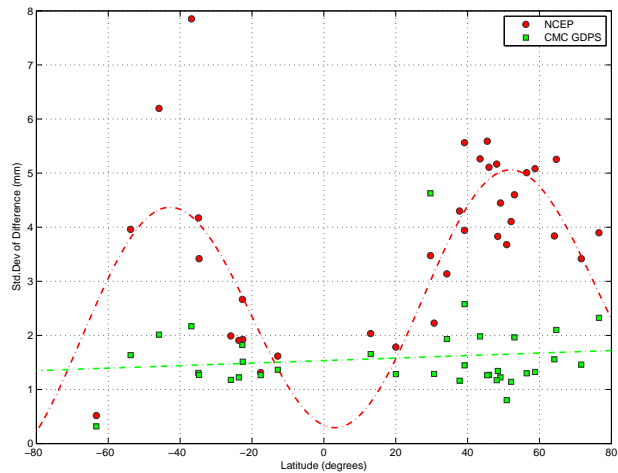
standard deviations of the difference. Firstly, Figure 3.15(a) plots the mean difference with respect to latitude and Figure 3.15(b) plots the standard deviation of the difference with respect to latitude. The mean difference does not show a trend, but the standard deviation of the difference for NCEP exhibits a latitude dependency where the standard deviation increases with latitude. This trend follows that of the difference in pressure.

Examining the weekly means and standard deviations of the differences reveals a similar trend in the winter months for the standard deviations for NCEP. During the winter months, there is an increased standard deviation for both the NCEP Re-Analysis 1 and the CMC (GDPS). The NCEP based product exhibits a larger increase over the winter months. NCEP experiences an increase of approximately 30% whereas CMC only experiences an increase of approximately 11%. Since the pattern matches that of the difference in pressure, the cause is most likely for the same reasons discussed in §3.3.2.1.

Table 3.4 summarizes the overall global mean, standard deviation, and absolute value of the difference in hydrostatic zenith delay. The results from the CMC exhibit a 44% reduction in the standard deviation and a 30% reduction in the overall mean difference with respect to the NCEP results. Figure 3.16 illustrates the histogram for all possible differences at all 35 stations. NCEP is shown in blue and CMC is shown in red. The results from the CMC exhibit the same double peak as the difference in pressure histogram



(a) Mean



(b) Standard Deviation

Figure 3.15: Mean and standard deviation of the difference in ZHD with respect to latitude. January 1st to December 31st, 2010.

(Figure 3.8). The second peak is due to the same two stations REYK and BOR1, so the same conclusions can be drawn here as was done with the difference in pressure. To put these results into terms familiar to geodesists, the differences in the hydrostatic zenith delays can be used to estimate of the impact on the height component for a positioning solution (Boehm et al., 2006 - see Chapter 5 for details). Assuming a cutoff elevation angle of  $5^\circ$ , and taking the global error in the hydrostatic zenith delay to be 2.810 mm

(CMC) and 5.095 mm (NCEP) the impact on the height component will be at the sub-mm level, 0.281 mm and 0.607 mm respectively. However, evaluating the worst performing station (see table A.5 in Appendix A) REYK, the zenith hydrostatic delay differences (bias +  $1\sigma$  standard deviation) of 14 mm (NCEP) and 9.3 mm (CMC) would result in an error in the height component of 1.7 mm for NCEP and 1.1 mm for CMC.

Table 3.4: Summary of global mean, standard deviation, max absolute value of the difference in zenith hydrostatic delay for all 35 stations. January 1st to December 31st 2010. All measurements in mm.

Product	Mean	Std	Max Abs
CMC (GDPS)	0.281	2.810	27.159
NCEP Re-Analysis 1	0.406	5.096	38.697
GPT	N/A	N/A	N/A

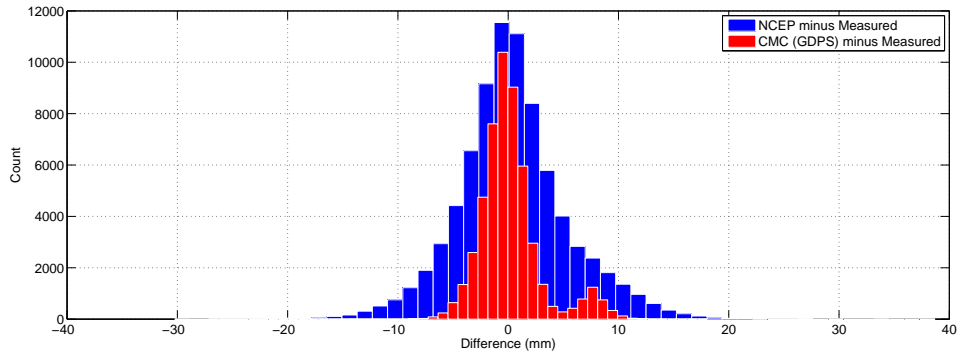


Figure 3.16: Histogram of difference in ZHD for the NCEP Re-Analysis 1(blue), and CMC (GDPS)(red)

### 3.4 Effect of Numerical Weather Model Grid Resolution

The previous section, §3.3, assessed the ability for two NWP’s to predict meteorological parameters used in the computation in signal delays. The results from the NCEP products consistently experienced larger standard deviations and mean differences for all of

the meteorological parameters. The horizontal grid resolution of the NCEP product is approximately 4 times as coarse than the CMC based product. Typically, as the horizontal resolution is reduced smaller scale weather patterns can be described, the weather patterns can be more precisely shaped (Erfani et al., 2005), and the topography within the model can be better represented, which will help to better describe atmospheric flows in more complex terrain (Salvador, et al., 1999). The subject of horizontal resolution has been investigated intensively and a good summary up to 2002 can be found in Mass et al., (2002). Mass et al.(2002) summarizes that in general many studies have subjectively concluded that increasing the horizontal resolution results in more realistic and better defined weather patterns. However, Mass et al., (2002) states that few studies have demonstrated that forecast accuracy has been improved at resolutions below 10-15 km. More recently, high resolution models have been developed in conjunction with various Olympic games (Satuffer et al., 2007; Mailhot et al., 2012). Results from these studies indicate that the high resolution systems do indeed perform better in regions of complex terrain. In contrast to these results, Hobiger et al. (2010) presented the use of a high resolution NWP in a geodetic context, which showed mixed results depending on the weather conditions. The high-resolution model used in this study was a storm simulator, so during the times of storm passage the high-resolution model performed better. However, outside of these extreme events the high-resolution model performed marginally better and sometimes worse. The Hobiger et al. (2010) study did show an overall general improvement for stations located in complex terrain, but there were still several stations located in complex terrain that showed a degradation in the zenith total delays when compared to GPS results.

The results from §3.3 are based on global NWPs, but the CMC now offers three distinct deterministic prediction models at different horizontal resolutions. This provides an opportunity to assess the impact of finer horizontally gridded models in the context of producing geodetic correction for GNSS atmospheric signal delays. This section provides a summary of a small assessment of the impact of NWP horizontal grid resolution on

GNSS signal delays in the neutral atmosphere.

### 3.4.1 Description of Experiment

To evaluate the effect of the grid resolution the use of three NWP's from the CMC have been used, namely the GDPS (Global Deterministic Prediction System; Cote et al., 1998), RDPS (Regional Prediction System; Mailhot et al. 2006) and the HRDPS (High Resolution Deterministic Prediction System<sup>2</sup>). The GDPS and RDPS provides data on a 33 km and 15 km grid respectively, and the HRDPS is provided on a 2.5 km grid. The HRDPS provides data for discrete domains nested within the RDPS, namely the West, East, Maritimes, Arctic and Lancaster where all but the West are still considered experimental (CMC, 2012b). For this work four stations in NRCAN's permanent active control network have been selected (plus 1 station in the IGS tracking network - UNBJ) in three domains: West, East and the Maritimes.

In light of the previous work with high resolution models, it is necessary to select stations that represent regions that will show an improvement. Therefore, stations have been selected in regions of complex terrain, such as WSLR (Whistler, BC), PWEL, HLFX, and SC04. WSLR is located in a mountainous region, and PWEL/HLFX/SC04 are located along coastlines. UNBJ was added as an example of uncomplicated terrain. Table 3.5 summarizes the stations selected, their positions, and the HRDPS domain they reside in. The second consideration is the location relative to the bounds of the HRDPS domain. The tests performed require the determination of ray-traced GNSS signal delays, so it is necessary for the ray to remain within the model until the ray pierce through the top of the NWP. Since the domains are small relative to the GDPS and RDPS there is a risk that the ray can pierce through the side of the NWP instead of the top. The selected stations have also been selected under this consideration.

---

<sup>2</sup>There has not been a direct paper for the HRDPS, but Erfani et al., (2005) discusses the implementation of a high resolution model at the CMC. Since then several papers describing the high-resolution system at the 2010 Vancouver Olympics by Mailhot et al., (2010) and Mailhot et al., (2012) have described changes to the system in Erfani et al., (2005), which have made their way into CMC's 2.5 km model.



Table 3.5: Station Summary for grid resolution assessment

Station	Latitude (deg)	Longitude (deg)	Height (m)	Domain
PWEL	43° 14' 12.239"	-079° 13' 10.801"	43.855	East
SC04	48° 55' 23.386"	-123° 42' 14.872"	14.930	West
WSLR	50° 07' 35.541"	-122° 55' 16.283"	909.295	West
UNBJ	45° 57' 00.753"	-066° 38' 30.137"	22.761	Maritimes
HLFX	44° 41' 00.778"	-063° 36' 40.606"	152.828	Maritimes

The evaluation has included two tests. The first test is a simple proof of concept. For each of the five selected stations, the hydrostatic and non-hydrostatic slant delays have been computed for each of the NWP (GDPS, RDPS and HRDPS) at the following elevation angles: 90, 70, 50, 30, 20, 15, 10, 5, and 3 degrees, and at an azimuth of 30 degrees. An azimuth of 30 degrees has been selected to ensure that the ray pierces the top of the NWP, not the side. For the ray-tracing, no assumptions have been made regarding the structure of the atmosphere or the ray-path. Therefore, the atmospheric structure and ray-path have been considered in full three-dimensions. The epoch of the ray-trace is August 15th, 2012, but the time of the day varies from 06UTC for the maritime domain to 12UTC for the eastern and western domains. The reason for this is that each of the domains have a single model initialization time, which may be different from domain to domain and the intention is to ray-trace at the model initialization time. For the comparison, the ray-traced slant delays are then differenced with respect to the HRDPS and the corresponding equivalent height error for each station computed. The equivalent height error has been computed as one-fifth the mapping function error at an elevation angle of 5°. The hydrostatic and non-hydrostatic mapping function has been computed by equations 4.5 and 4.6. For the computation of equivalent height error, a value of 2300 mm and 230 mm has been used for the hydrostatic and non-hydrostatic zenith delay respectively to express the mapping function differences in linear units.

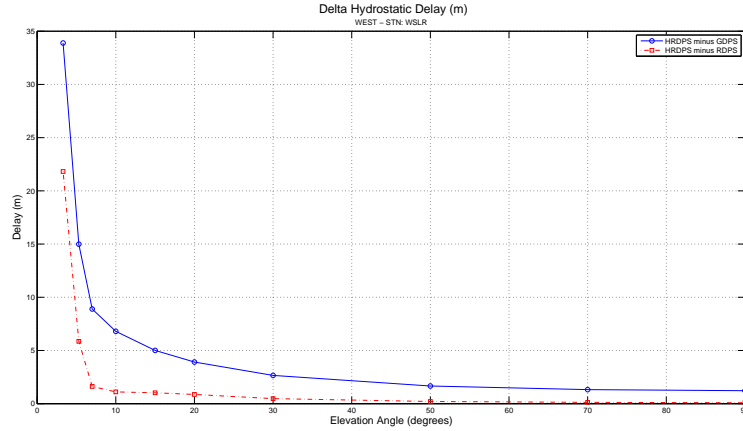
The second test includes a comparison of the meteorological parameters as was com-

pleted in §3.3. The difference in pressure, temperature, specific humidity, and hydrostatic zenith delay has been computed for only three of the five stations, namely PWEL, SC04 and UNBJ. The reason for this is due to meteorological data availability from NRCAN. It is recognized that not all stations are located in very complex (or rugged) terrain, but SC04 and PWEL are located along a coastline. Each of the meteorological parameters and the ray-traced ZHD has been extracted from the respective NWP 4 times daily at 0,6,12 and 18H UTC. The time period extends from April 4th, 2012 to August 31, 2012.

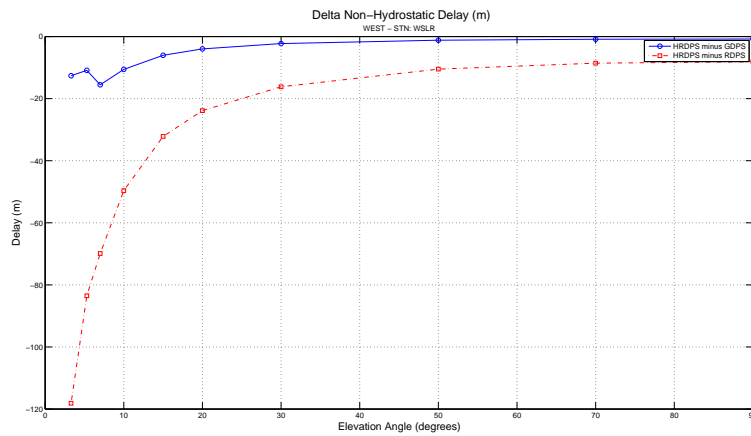
### **3.4.2 Discussion and Results**

Figure 3.17 plots the difference in slant delay for station WSLR, where Figure 3.17(a) is the hydrostatic delay and Figure 3.17(b) is the non-hydrostatic delay. Station WSLR has been shown since it is located in the most topographically varied terrain, and the differences are largest for the hydrostatic component. For the hydrostatic slant delay, the differences start to become large below an elevation angle of  $10^\circ$  for the RDPS and  $20^\circ$  for the GDPS. The differences below these elevation angles reach values above 5 mm. For the non-hydrostatic differences, the differences are much larger than those of the hydrostatic component, and the differences start to diverge at higher satellite elevation angles. The non-hydrostatic component begins to diverge significantly at elevations below  $30^\circ$  for the RDPS and  $20^\circ$  for the GDPS. The variability is still large between NWPs for the prediction of the non-hydrostatic component, which is indicative of the difficulty in modelling the water vapour content in the atmosphere. Overall, difference between models at the zenith direction are at the sub-mm level for the hydrostatic delay, except for station WSLR where the difference is 1.1 mm. The non-hydrostatic component exhibits much more variability where differences at zenith range from mm-level to cm-level for both the RDPS and the GDPS.

The results for all five stations indicate that the agreement between the GDPS and RDPS with the HRDPS are entirely random. For example, the differences with the RDPS



(a) Hydrostatic



(b) Non-Hydrostatic

Figure 3.17: Difference in (a) hydrostatic, and (b) non-hydrostatic slant delays. August 15, 2012. Station: WSLR.

may be smaller for the hydrostatic delay at one station, but at another the GDPS is in better agreement (the same is true for the non-hydrostatic). Since the differences are made with respect to the HRDPS, these results reflect the variability of the HRDPS and illustrates that there is no clear trend with respect to the horizontal resolution. The expectation would be that the difference between models should become smaller as the resolution is increased.

Figure 3.18 plots the mapping function differences expressed as equivalent height errors for all five stations. For the hydrostatic component, all the mapping function differences are at the sub-mm level, with station WSLR exhibiting the largest differences. At an

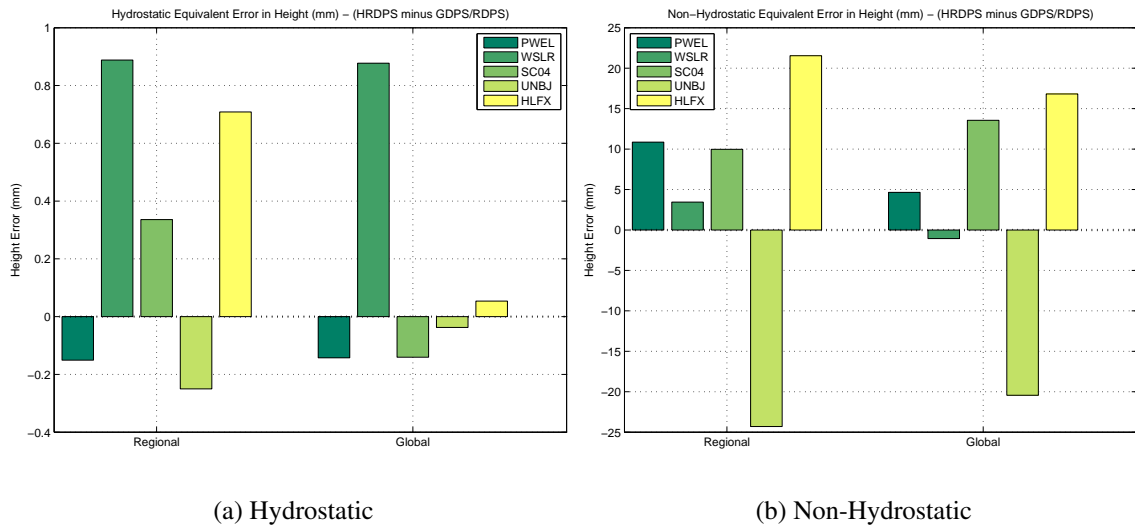


Figure 3.18: Difference in mapping function at an elevation angle of 5° expressed as equivalent height error. August 15, 2012.

initial glance this may seem to be expected since WSLR is located in a mountainous region, but the difference between the GDPS (at 33 km) and the RDPS (at 15 km) for station WSLR is negligible, indicating that there is no appreciable improvement when reducing the horizontal resolution at this station (this is based on the assumption that the HRDPS is the best solution). Further supporting this claim is the fact that station HLFX's results from the GDPS agree much better with the HRDPS than the regional model. This same trend follows with the non-hydrostatic equivalent height error, where four of the five stations from the global model better agree with the HRDPS versus the regional model. The main difference from the hydrostatic component is that the non-hydrostatic differences are at the millimetre and centimetre level for both the global and regional model further supporting the conclusion that the NWP's still have difficulty with the prediction of the water vapour in the atmosphere.

The results of this initial test are limited since they refer only a single day and epoch. The intent of the following test is to produce a sufficiently long time series of the meteorological parameters and hydrostatic zenith delay from each model and compare those to

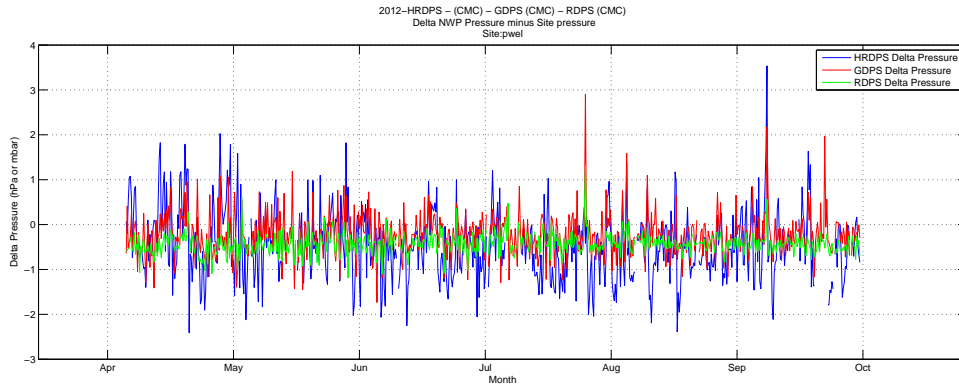


Figure 3.19: Difference in pressure (NWP minus Measured) - HRDPS(blue), GDPS(red), and RDPS(green). All measurements in mbar. April 4th to August 31st 2012

the measured values, which are considered to be truth. These results will be compared to an independent dataset so the assessment at each resolution can be considered absolutely. Figure 3.19 plots the difference in pressure for station PWEL. Figure 3.19 is typical for all meteorological parameters where the HRDPS is the noisiest solution with respect to the site pressure, followed then by the GDPS, and the RDPS performs the best. The comparison shown in Figure 3.19 is not a fair comparison since the HRDPS is only initialized once per day (6H for maritimes and 12H for east and west). In comparison, the GDPS is initialized every 12 hours and the RDPS every 6 hours. The result of only initializing once per day is that the data included in the time series for HRDPS actually included forecasts up to 24 hours. Due to the addition of forecast data it makes sense why the HRDPS exhibits the largest variation. Therefore, the differences have been separated into their respective epochs (0,6,12 and 18) and then compared, so only the initialization times are evaluated.

Figures 3.20 and 3.21 plots the difference in pressure, temperature, specific humidity separated into epoch (0,6,12 and 18). Figure 3.20 plots the mean difference and Figure 3.21 plot the standard deviation of the difference. Examining only the initialization periods, which is 6H for UNBJ and 12H for SC04 and PWEL, there is not a clear definitive result indicating that the high resolution model provides better results. The HRDPS extracted pressure for SC04 provides the smallest mean differences at it's initialization times, but

for PWEL and UNBJ the largest mean difference are from the HRDPS model. For temperature, the HRDPS exhibits the smallest mean difference at UNBJ, but the largest at PWEL and SC04. For specific humidity, the HRDPS exhibits the smallest mean difference for stations PWEL and SC04, but exhibits the largest at UNBJ. The results for the specific humidity agree with Yang et al. (1999) where it was determined that the quality of water vapour modelling is independent of horizontal grid resolution. Moreover, in the case where the HRDPS performed best, the differences between the models are small. For example pressure, the HRDPS performed best for station SC04 with a mean difference of 0.038 mbar (at 12H), where the mean difference for the RDPS of 0.268 mbar and 0.220 for the GDPS. This would indicate a reduction of the bias by approximately 0.230 mbar for the station. The application of the rule of thumb by Tregoning and Herring (2006) (see §3.3.2.1) would mean that this error in pressure would only cause an 0.046 mm error in the height solution in a standard GNSS positioning computation.

For the standard deviation of the difference, shown in Figure 3.21, the difference in pressure for the RDPS clearly shows the best results compared to that of the HRDPS and GDPS. The pressure exhibits the greatest sensitivity to the initialization. Since the RDPS is initialize every 6H, the results do not exhibit any real spikes. However for the GDPS, which is initialized at 0H and 12H, there are clear increases in the standard deviation at the 6H forecasts. The same pattern exists for the HRDPS where the dips in the standard deviation occur at the model initialization times. For temperature, the RDPS exhibits the smallest standard deviations, but for the specific humidity no one model clearly performs better than the other.

When evaluating the difference in pressure, the RDPS provides standard deviations on the order of 0.2 mbar as opposed to the HRDPS, which provide standard deviations of the pressure on the order 0.5 mbar. The difference between these two is 0.9 mbar at  $3\sigma$ , which would mean that an error of 0.9 mbar would cause an error in the height solution of approximately 0.18 mm. Again, as with the differences in the mean pressure, the overall

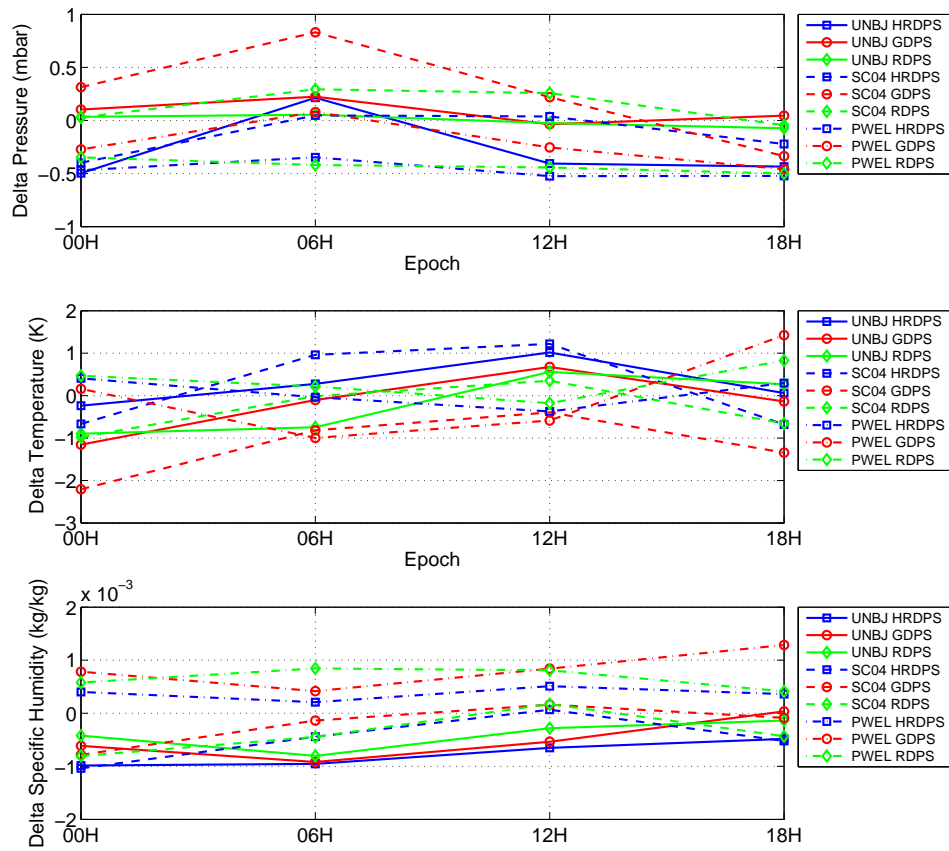


Figure 3.20: Mean difference in meteorological parameters (NWP minus Measured) - HRDPS(blue), GDPS(red), and RDPS(green). Top: Pressure (mbar); Middle: Temperature (K); Bottom: Specific Humidity (kg/kg). April 4th to August 31st, 2012

influence of the NWP differences are at the sub-mm level when applied to standard GNSS positioning.

Lastly, is the difference in hydrostatic zenith delay. Figure 3.22 and Table 3.6 summarizes the differences in ray traced hydrostatic zenith delay versus the hydrostatic zenith delay computed by equations 3.5 and 3.6. Figure 3.22(a) plots the mean differences and 3.22(b) plots the standard deviation of the difference. The difference in zenith hydrostatic delay follow that of the pressure, where the solution from the RDPS performed best, followed by the GDPS, and the HRDPS performed worst. As with the difference in pressure, SC04 was the only station were the HRDPS performed best with regard to the mean

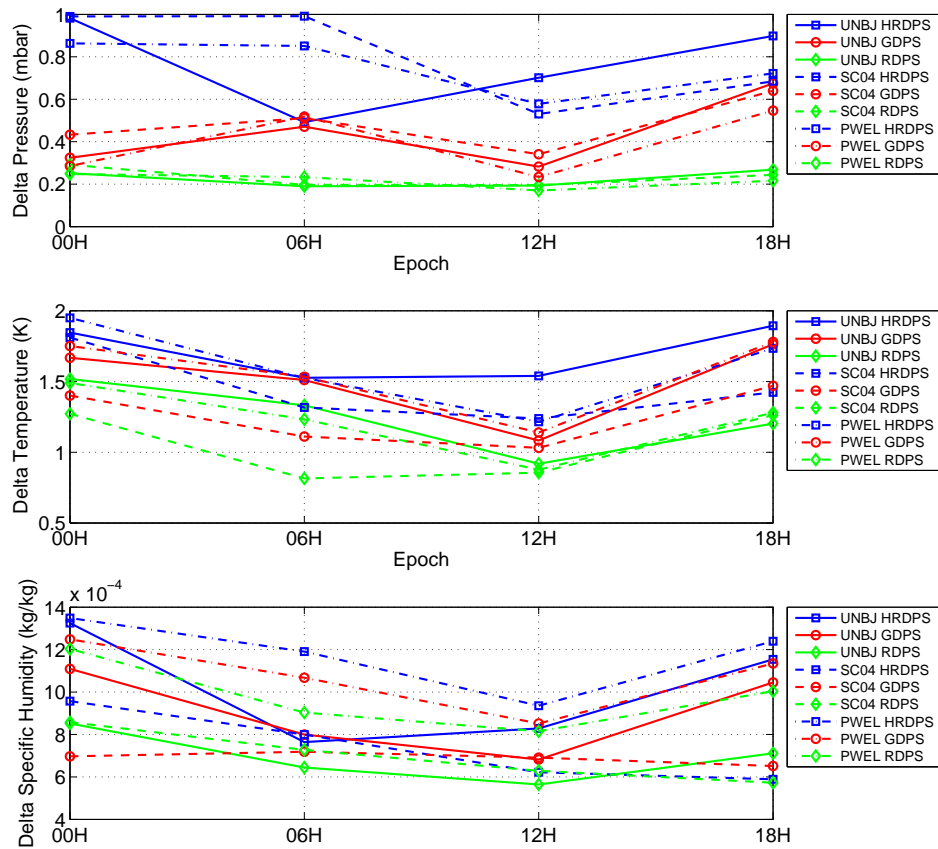
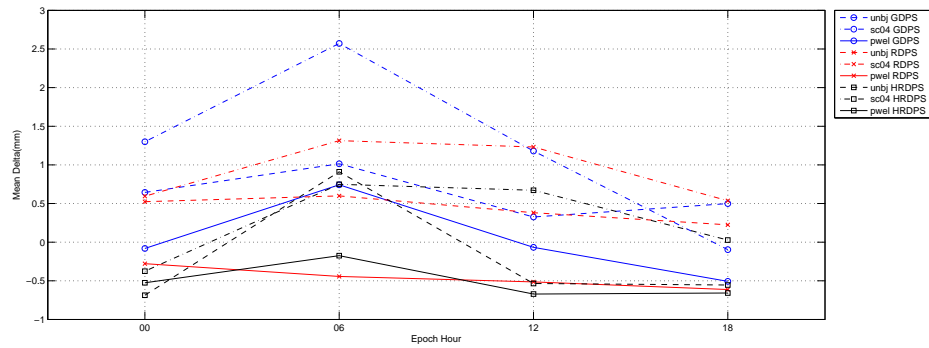


Figure 3.21: Standard deviation difference in meteorological parameters (NWP minus Measured) - HRDPS(blue), GDPS(red), and RDPS(green). Top: Pressure (mbar); Middle: Temperature (K); Bottom: Specific Humidity (kg/kg). April 4th to August 31st, 2012

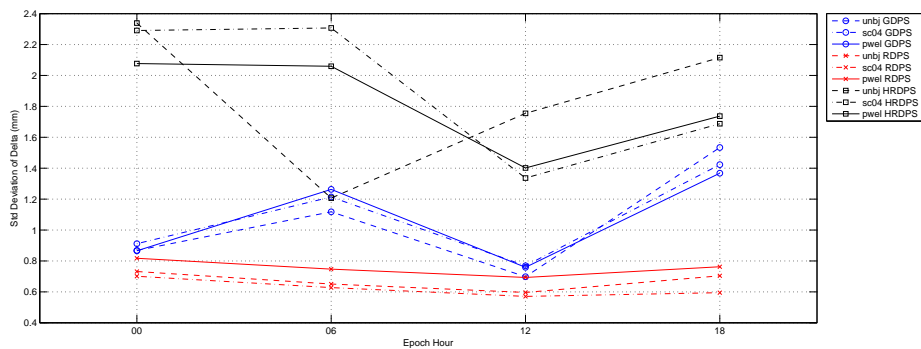
difference. In all other instances the HRDPS performed worst.

The fact that the HRDPS performed worst was unexpected, so it is worth examining why this is the case. Lorenz (1969) studied the predictability of fluid systems and concluded that scales less than 40 km could not be predicted longer than one hour. However, the inclusion of lateral boundary conditions will significantly slow this error growth where Anthes et al. (1985) demonstrated that high resolution models depend critically on accurate lateral boundary conditions. The HRDPS does not have its own assimilation system, and the HRDPS relies on the RDPS to set its initial and boundary conditions (and on the global model system upstream) (CMC, 2012b). So, if there are any issues with the RDPS,





(a) Mean



(b) Standard Deviation

Figure 3.22: Mean and standard deviation of the difference in ZHD with respect to ZHD computed by Saastamoinen with measured pressure. April 4th to August 31st 2012

these tend to be magnified in the HRDPS (CMC, 2012b). Further, the description of the 2.5 km model by Erfani et al. (2005) states that the model domains in the east and west have been initialized by the 15 km RDPS<sup>3</sup> at the 12 hour forecast from the 00 UTC run. If this is still the case, then this can be a clear indication as to why the the HRDPS performed worse. NWP's are extremely sensitive to initial conditions and the 00 hour forecasts (analysis) can be considered the optimum description of the atmosphere, and any step in time from this point will result in some uncertainty. The possibility exists that the HRDPS has been initialized with a less than optimum description of the atmosphere since the 12 hour forecast has been used for initialization instead of a 12 UTC initialization.

Secondly, since the HRDPS does not have its own assimilation system it stands to

<sup>3</sup>in Erfani et al. (2005) the HRDPS and RDPS are referred to as GEM 15 and GEM 2.5 respectively

Table 3.6: Difference zenith hydrostatic delay for each station separated by epoch (ray-traced minus Saastamoinen). All measurements in mm.

NWP	Station	00H		06H		12H		18H	
		Mean	Std	Mean	Std	Mean	Std	Mean	Std
GDPS	unbj	0.644	0.863	1.015	1.126	0.326	0.694	0.499	1.538
RDPS	unbj	0.524	0.726	0.599	0.675	0.381	0.621	0.224	0.719
HRDPS	unbj	-0.687	2.339	0.911	1.206	-0.535	1.772	-0.554	2.126
GDPS	sc04	1.299	0.932	2.571	1.218	1.179	0.750	-0.097	1.477
RDPS	sc04	0.595	0.713	1.314	0.654	1.232	0.602	0.536	0.608
HRDPS	sc04	-0.376	2.379	0.748	2.382	0.672	1.328	0.027	1.683
GDPS	pwel	-0.082	0.874	0.743	1.257	-0.067	0.773	-0.507	1.373
RDPS	pwel	-0.278	0.822	-0.443	0.760	-0.514	0.700	-0.613	0.775
HRDPS	pwel	-0.526	2.119	-0.175	2.067	-0.671	1.414	-0.658	1.806

reason that the overall observational density has not been increased to match the increased resolution. Without the appropriate observational density small scale weather features may be missed or improperly characterized, which will degrade verification scores where the lower resolution models exhibit better scores (Mass et al., 2002). Results at the Torino Olympics by Stauffer et al. (2007) showed improvement over complex terrain, but the specialized high density observation system developed for the games was assimilated into the model, thus the density of the observations correlated well with the resolution of the model.

Additionally, errors with timing and position are amplified as the resolution is increased. Although, the definition of the weather feature is more accurately represented, the timing and position errors will increase with point based verification (Mass et al., 2002). Rife and Davis (2005) summarize several previous studies that indicate that high resolution NWP's have shown little or no improvement over coarser resolution models when using standard point based verification techniques. In general, the coarser resolution models will provide average conditions over a larger area as compared to the high resolution models, which results in better verification scores. The results here are also point based

verifications, and follow those of previous studies in that the HRDPS exhibited little or no improvement over the RDPS and the GDPS. From the geodetic perspective, point based verification is a more valid approach since it very important to define the conditions at a specified point on Earth. A better defined shape of the weather system is not as important as correctly placing that system in time and space.

### **3.5 Summary**

The intention of this chapter was to discuss some of the defining characteristics of the NWP's selected and assess their differences. §3.2 discussed the various NWP models available for selection and reasons for selecting NCEP and the CMC (GDPS). NCEP Re-Analysis 1 has been selected for superior availability, consistent model definition, and for compatibility with other geodetic corrections that have been derived from it. The shortcomings of the model are the coarse horizontal resolution and the fact that the NWP's operational underpinnings that define its physics and parameterizations have been frozen to the system definition in the mid-nineties. To provide a modern option, the CMC has been selected to produce a backup product to the UNB-VMF1. The benefit of the CMC (GDPS) is that it is a modern operational model that contains the latest application of atmospheric physics and parameterizations. The shortcoming of the CMC (GDPS) is the fact that the data is only available for a 24 hour period which makes it less robust for an operational service.

§3.3 performed the assessment of two NWP's, NCEP Re-Analysis 1 and CMC (GDPS), and an empirical model based on a NWP, the GPT. The assessment consisted of the comparison of three meteorological parameters: pressure, temperature and specific humidity, and ray-traced hydrostatic zenith delays. In all cases, the results from the CMC exhibited the smallest mean differences and exhibited the smallest standard deviations of the difference. In all cases the GPT performed worst, but this is not unexpected since the GPT

is a spherical harmonic expansion truncated at degree and order nine, and based on the ECMWF 40-year Re-Analysis for the years 1999 to 2002. The GPT models the seasonal and annual amplitudes of the pressure and temperature, but cannot deal with the daily fluctuations well. Additionally, any conditions that differ largely from the 3-year interval it has been based on will create further uncertainty.

Further, the assessment of the models exhibited seasonal trends where the standard deviations were larger during the winter months for pressure and temperature for all stations located in both the northern and southern hemisphere. The specific humidity experienced larger standard deviations during the summer months, which correlate well with the periods of increased precipitable water. For pressure and temperature, the GPT experienced the largest increase followed by NCEP and then the CMC. For specific humidity, the increase during the summer months is similar where NCEP experienced a 32% increase and the CMC experienced a 34% increase.

The results for the standard deviation of the difference for pressure from NCEP and the GPT exhibited a latitude dependent trend, and the results for specific humidity from NCEP and the CMC also exhibited a latitude dependent trend. Results for the pressure illustrated that stations at higher latitudes experience larger standard deviations, where the GPT exhibited the largest standard deviations. For the specific humidity stations closer to the equator experienced larger standard deviations where the water vapour content is largest.

Lastly, a comparison of three different NWP models from the CMC with differing horizontal resolutions was made. Three models at 33 km (GDPS), 15 km (RDPS) and 2.5 km (HRDPS) were assessed against each other and against an independent dataset. The intention was to assess the value of high resolution NWP models in geodetic applications. The initial assessment compared the three models relative to each other. The HRDPS was used as the reference and the differences were computed for the RDPS and GDPS. These results indicated that there was no appreciable difference in terms of the hydrostatic mapping

function expressed as equivalent height error. However, for the non-hydrostatic case, differences were observed up to the cm-level for the mapping function differences, but the higher resolution regional model performed worse relative to the HRDPS as opposed to the global GDPS, which indicates the current variability between NWP models in predicting the atmospheric water vapour content. The second test, maybe the more definitive one, tested against measured meteorological parameters and hydrostatic zenith delays computed by Saastamoinen at three locations in Canada. Results indicated that there was no appreciable improvement with the use of the high resolution model (HRDPS) and the regional model at 15 km (RDPS) generally performed best among all three models in terms of the standard deviation of the difference. However, it must be noted that due to the availability of meteorological data the stations studied are not located in the most complex terrain available. More stations in steep mountainous regions should be tested for a complete analysis.

# Chapter 4

## The UNB Vienna Mapping Function

### Service

This chapter provides a detailed description of the UNB Vienna Mapping Function Service (UNB-VMF1). The opening section of the chapter, §4.1, looks at the existing services available to the geodetic/scientific community and how the services have been defined, implemented and used by the community. This serves as a basis in which to model the UNB-VMF1, and a starting point for the motivation of the creation of an additional service, which is discussed in §4.1.

The creation of the UNB-VMF1 service requires the definition of the following: (a) mission; (b) models, and the (c) system, which are embodied and verified in the (d) validation. Figure 4.1 provides a quick definition of this structure, where to find each aspect in this chapter, and some key questions that must be addressed in order to create a robust service (which are addressed in the respective sections). Item (d), the validation of the service, will be discussed in detail in Chapter 5.

The definition of UNB-VMF1's mission is critical to the success of the service, as it ensures that the service will be focused and that there will be a clear understanding from its user base as to what the service provides and how it will help them. These aspects of

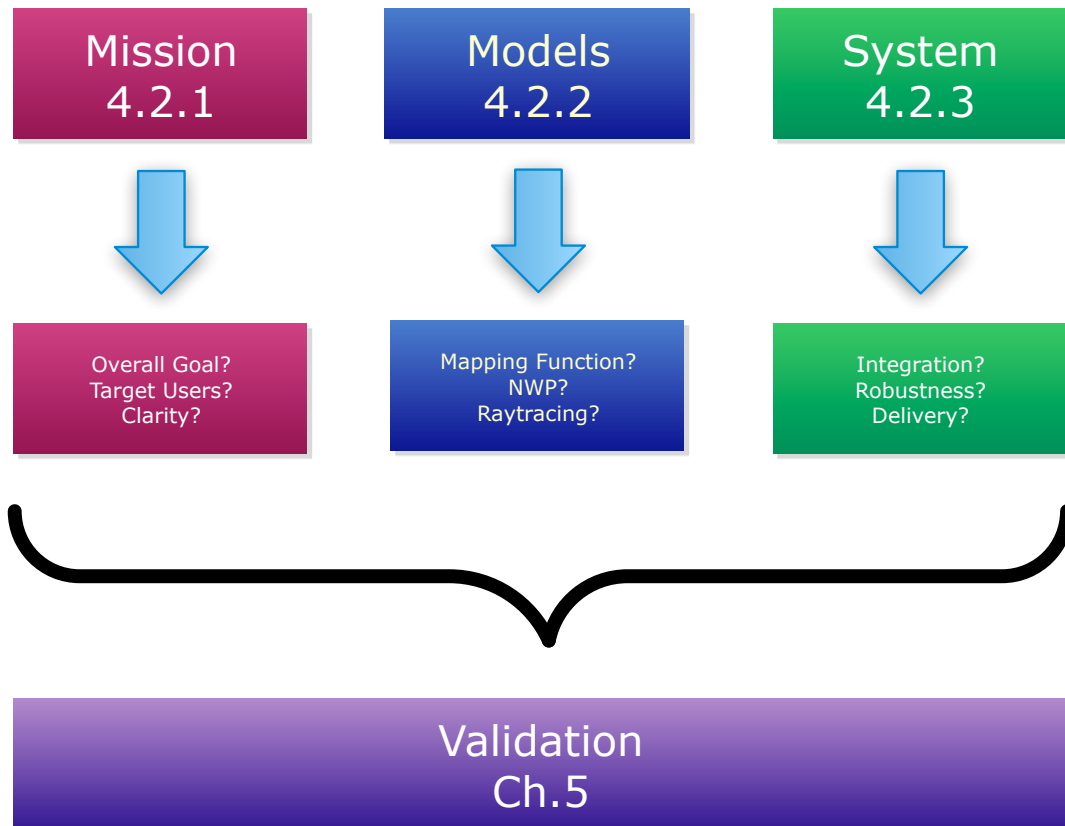


Figure 4.1: Aspects of building the UNB Vienna Mapping Function Service

the service are described in §4.2.1 describes these aspects of the service.

The description of the model and system (items (b) and (c) respectively) can be found in §4.2. In particular, §4.2.2 summarizes the implemented models (i.e mapping functions, numerical weather prediction models), and Section 4.2.3 describes the system integration (i.e. systems and processes required to build a robust computation and delivery system). The final two sections, §4.2.4 and §4.2.5 describe the available products and how the user can interact with the system respectively. Finally, a summary is provided describing the key aspects of the service.

## 4.1 Existing VMF1 Service

A review of the existing VMF1 service will serve as a foundation for the UNB-VMF1 such that it can maintain as much continuity as possible for the user base. The existing VMF1 service interface is a web based HTML interface, currently located at the following url: <http://ggosatm.hg.tuwien.ac.at/DELAY/>, where the user can access the various products offered by the service by HTML (in a standard web browser), or by remote access with programs such as *wget*. This is a no frills interface, as the user is presented with just a directory structure containing the offered products with a readme file describing the contents. However spartan, it serves its purpose well.

The existing VMF1 service offers many differing products, where a summary of the VMF1 based products are presented in Table 4.10. In addition to VMF1 based products, the current service also provides empirical models such as the global mapping functions (GMF) and the global pressure and temperature model (GPT). Further, the service also provides products classified as “other parameter”, where the user can find the following datasets:

- (a) Height of the 200 hPa pressure level: which is an input parameter for the isobaric mapping functions (IMF – Niell, 2001). Can currently be found at <http://ggosatm.hg.tuwien.ac.at/DELAY/ETC/Z200>,
- (b) Mean temperature,  $T_{mean}$ : which can be used to convert the wet zenith delays to precipitable water. Can currently be found at <http://ggosatm.hg.tuwien.ac.at/DELAY/ETC/TMEAN>,
- (c) Linear horizontal gradients: both hydrostatic and wet linear horizontal gradients can be found for the same stations in which the VMF1 site product have been determined (IGS, IVS, and IDS stations<sup>1</sup>). Can currently be found at <http://ggosatm.hg.tuwien.ac.at/DELAY/ETC/LHG>.

---

<sup>1</sup>IGS refers to GPS stations. IVS are the VLBI stations, and IDS are the DORIS stations



These “other parameter” datasets and the empirical models are outside the scope of the UNB-VMF1 service, as the service is currently focused on only producing VMF1 based products.

Of the VMF1 based products (shown in Table 4.10), the gridded products are the focus of the UNB-VMF1 service. The gridded products are produced according to Boehm et al. (2006), in which the UNB-VMF1 service follows (service commonalities and differences are described in detail in §4.3). Boehm et al. (2006) applies the methods described within to site specific VMF1 solutions, but Kouba (2008) has demonstrated that the use of the VMF1 in a globally gridded format is equivalent to that of the site specific solutions. Further, for GNSS and DORIS applications, the VMF1 service recommends the use of gridded products as well (VMF1, 2012a). The gridded format now allows any user to compute VMF1 solutions for any location on the globe by common interpolation methods.

The gridded products (forecast and standard) are available 4 times daily at 6 hour intervals, namely 00h, 06h, 12h, and 18h. The gridded products are produced on a global grid with a resolution of  $2.0^\circ$  in latitude, and  $2.5^\circ$  in longitude, where each grid point an associated hydrostatic and non-hydrostatic  $a$  coefficient (see §4.2.2.1 equation 4.1) and zenith delay is computed. Each grid point is referred to a standard ellipsoidal height that is defined in a file named *orography.ell*, and can currently be found at the following location: <http://ggosatm.hg.tuwien.ac.at/DELAY/GRID/>. However, the hydrostatic  $a$  coefficient is reduced to a 0 height, and all other parameters refer to the height stipulated in *orography.ell*. The final gridded products are presented to the user in two output formats (both ASCII) referred to as: (a) standard, and (b) row-based. The standard format presents to the user separate files for each computed parameter (i.e for hydrostatic  $a$  coefficient), where in contrast the row-based format delivers a single file with all computed parameters listed.

## **4.2 The UNB Vienna Mapping Function Service**

### **4.2.1 Mission Description**

An effective mission statement for the VMF1 service at UNB must address what the service hopes to achieve with consideration for who the target audience is and how the service is expected to be used or may be used in the future in a clear and concise manner. Therefore, in the context of the motivations described in Chapter 1, the mission of the UNB-VMF1 is such that it is designed to:

- Support the geodetic and scientific community through research providing state of the art corrections to the troposphere delay for space geodetic techniques;
- Improve the availability of tropospheric delay products with the addition of an independent source derived from an independent data source and independent ray-tracing algorithms;
- Support the geodetic and scientific community data processing efforts and achieve greater compatibility with other derived corrections, such as atmospheric pressure loading, using the same numerical weather prediction models.

### **4.2.2 Description of Fundamental Models**

#### **4.2.2.1 Mapping Function Model**

The UNB-VMF1 follows the description for the Vienna Mapping Functions (VMF) first published by Boehm et al. (2003), and Boehm et al. (2004), which was subsequently revised by Boehm et al. (2006). The foundation of the mapping function is based on Marini's continued fraction form (Marini, 1972), which has been normalized to produce

unity at zenith by Herring (1992):

$$mf(e) = \frac{1 + \frac{a}{1 + \frac{b}{1+c}}}{\sin(e) + \frac{a}{\sin(e) + \frac{b}{\sin(e)+c}}} \quad (4.1)$$

where,  $a$ ,  $b$ , and  $c$  are the mapping function coefficients to be solved, and  $e$  is the outgoing vacuum elevation angle. The evolution of mapping functions has continued with the VMF in that it applies the use of numerical weather prediction model data when solving for the  $a$ ,  $b$ , and  $c$  coefficients of equation (4.1). In the past, these coefficients have been fitted to standard atmospheres (Chao, 1974), and radiosonde data (Niell, 1996), but recently these coefficients have been fitted to numerical weather prediction model data (Niell, 2000), which was followed by the development of the VMF.

The coefficients can be solved by two methods: (a) rigorous, or (b) fast. The fast method is the method of choice for the UNB-VMF1 service, which is a simplification of the rigorous method. Solving for the coefficients rigorously involves ray tracing through a numerical weather prediction model at several pre-defined elevation angles in which the coefficients of equation (4.1) can then be subsequently estimated in a least-squares approach (Boehm et al., 2006 ray-traces at 10 initial elevation angles). To produce a gridded product by this method would require 10 ray traces, 4 times per day on a global grid. This number of ray-traces has an enormous computational cost, which drove the development of method (b) by Boehm et al. (2003) and Boehm et al. (2006). The fast method utilizes pre-determined values for the  $b$  and  $c$  coefficients, with only one ray-trace at an initial elevation angle of  $3.3^\circ$  followed by the determination of the  $a$  coefficient by inverting equation (4.1). Boehm et al. (2006) evaluated the differences between the fast and rigorous implementations and found that there are no differences at an elevation angle of  $3^\circ$  since the fast version is tuned for this elevation angle. Further, as the elevation angle is increased towards zenith the differences become smaller, where at an elevation angle of  $5^\circ$  differences were always smaller than 8 mm corresponding to an estimated station

height error of 1.6 mm.

Originally, the coefficients for the hydrostatic mapping function,  $mf_h$ , followed that of the hydrostatic component of the isobaric mapping functions (IMF) (Boehm et al. 2003). However, these coefficients were re-evaluated in Boehm et al. (2006), and these re-evaluated coefficients have been implemented in the UNB-VMF1 service, which are referred to as VMF1. The revised hydrostatic  $b$  and  $c$  coefficients,  $b_h$  and  $c_h$ , were realized from a rigorous determination from a global grid of 156 points for 12 months at 4 times daily in which the meteorological parameters were defined by the ERA-40 (ECMWF Re-Analysis 40-years) for the year 2001 (Boehm et al., 2006). The hydrostatic  $b$  coefficient is then determined by taking a mean of all individually rigorously determined  $b_h$  coefficients, which results in a value of 0.0029.

For the hydrostatic  $c$  coefficient,  $c_h$ , the process was repeated with only the  $c_h$  and  $a_h$  coefficients estimated, where  $b_h$  was held fixed to 0.0029. The results for  $c_h$  demonstrated seasonal and a latitude variation, with the addition of an asymmetry about the equator (Boehm et al. 2006). Therefore, the following function is used to model the seasonal, latitude, and equatorial variability for the  $c_h$  coefficient (Boehm et al., 2006):

$$c = c_0 + \left[ \left( \cos \left( \frac{doy - 28}{365} 2\pi + \psi \right) + 1 \right) \frac{c_{11}}{2} + c_{10} \right] (1 - \cos\phi) \quad (4.2)$$

where, the values of  $c_0$ ,  $c_{10}$ , and  $c_{11}$  are found in table 4.XX,  $\phi$  is equal to the geodetic latitude,  $\psi$  is either 0 or  $\pi$  depending on if the location is in the northern or southern hemisphere respectively, and  $doy$  is the day of year.

The solution of the hydrostatic  $a$  coefficient,  $a_h$ , is reduced to a zero height in the final UNB-VMF1 products (following the current VMF1 service). Boehm et al. (2003) recommends that the  $a_h$  coefficient be reduced to a zero height since the spatial interpolation results will be improved. The UNB-VMF1 follows this recommendation and reduces the  $a_h$  coefficient to a zero height by the following relationships as described by Niell

Table 4.1: Values for hydrostatic  $c$  coefficient implemented by the UNB-VMF1 service (from Boehm et al., 2006).

Hemisphere	$c_0$	$c_{10}$	$c_{11}$	$\psi$
northern	0.062	0.001	0.005	0
southern	0.062	0.002	0.007	$\pi$

(1996) (which also follows the existing VMF1 service):

$$\frac{dm_h(e)}{dh} = \frac{1}{\sin(e)} - f(e, a_{ht}, b_{ht}, c_{ht}) \quad (4.3)$$

where,  $\frac{dm_h(e)}{dh}$  is the change in the hydrostatic mapping function with respect to height,  $e$  is the same outgoing elevation angle defined in equation 4.1, and  $f(e, a_{ht}, b_{ht}, c_{ht})$  is equation 4.1 evaluated with the coefficients  $a_{ht}$ ,  $b_{ht}$ , and  $c_{ht}$ . These coefficients are subscripted with  $ht$  to identify these as the height correction coefficients, which are different than the VMF1 coefficients. These coefficients have been determined by Niell (1996) and are summarized in Table 4.2. Once the change in the hydrostatic mapping function with respect to height has been determined ( $\frac{dm_h(e)}{dh}$ ), then it is applied to the mapping function as follows (Niell, 1996):

$$mf_h(e) = mf_h(e) - \Delta m_h(e) \quad (4.4)$$

$$\Delta m(e) = \frac{dm(e)}{dh} H \quad (4.5)$$

where,  $H$  is the height above sea-level, and  $mf_h(e)$  is the hydrostatic mapping function,  $\Delta mf_h(e)$  is the hydrostatic mapping function height correction term. Now that the hydrostatic mapping function has now been reduced to a zero height, it can now be inverted to solve for the  $a_h$  coefficient at the same zero height.

Boehm et al. (2006) expresses that the variation of the coefficients  $b_w$  and  $c_w$  for the non-hydrostatic mapping function is not significant, and since the non-hydrostatic zenith

Table 4.2: Values for height reduction coefficients used by  $f(e, a_{ht}, b_{ht}, c_{ht})$  and implemented by the UNB-VMF1 service (from Niell [1996]).

Coefficient	Value
$a_{ht}$	2.53e-5
$b_{ht}$	5.49e-3
$c_{ht}$	1.14e-3

delays are smaller by a factor of approximately 10, the coefficients need not be updated and remain as those outlined by Niell (1996) at a latitude of  $45^\circ$ . These coefficients can be found in Table 4.3. The resulting non-hydrostatic  $a$  coefficient,  $a_w$ , is not reduced to a zero height, it is referred to the height given in *orography.ell* (see §.4.2.2.4 and 4.2.4.1). Equations (4.3) through (4.5) do not apply to the non-hydrostatic components since the water vapour is not in hydrostatic equilibrium and the height distribution of the water vapour is not expected to be predictable from the station height (Niell, 1996).

Table 4.3: Non-hydrostatic coefficients implemented by the UNB-VMF1 service (from Niell [1996] at  $\phi = 45^\circ$ ).

Coefficient	Value
$b_w$	0.00146
$c_w$	0.04391

#### 4.2.2.2 Ray Tracing Algorithm

The UNB-VMF1 implements the ray-tracing algorithms as described by Nievinski (2009) and Urquhart (2011). Some key aspects of the ray-tracing should be outlined here for greater understanding of how the method is applied to mapping functions, however a detailed description can be found in each of the noted references. In particular, a mapping function can also be determined from the following relationships (modified from Nievin-

ski, 2009):

$$mf_h(e_o) = \frac{d_h(e_o) + d_g(e_o)}{d_h^z} \quad (4.6)$$

$$mf_w(e_o) = \frac{d_w(e_o)}{d_w^z} \quad (4.7)$$

where,  $e_o$  is the elevation angle,  $mf_h(e_o)$  and  $mf_w(e_o)$  are the hydrostatic and non-hydrostatic mapping functions respectively,  $d_h(e_o)$ ,  $d_g(e_o)$ ,  $d_w(e_o)$  are the hydrostatic, geometric, and non-hydrostatic slant delays respectively, and  $d_h^z$ ,  $d_w^z$  are the hydrostatic and non-hydrostatic zenith delays. In the case of the hydrostatic mapping function,  $mf_h(e_o)$ , the geometric slant delay,  $d_g(e_o)$ , is added. The geometric delay is the difference between the geometric bent ray path and the straight line ray path between a receiver and satellite (in a GNSS application), and when decomposing the delay into hydrostatic and non-hydrostatic components (see Chapter 2) the integration still occurs along the same path Nievinski, (2009). Therefore, the geometric delay cannot be separated into a hydrostatic and non-hydrostatic component. The solution of the zenith delay (hydrostatic and non-hydrostatic) can be found by ray-tracing or by applying surface meteorological parameters to the modified Saastamoinen relationship (Davis et al., 1985). The UNB-VMF1 service applies the UNB ray-tracing algorithms in the zenith direction through the specified numerical weather prediction model to solve for the hydrostatic and non-hydrostatic zenith delays.

As noted in §4.2.2.1, the UNB-VMF1 service has implemented the fast method of the VMF1 procedure. Therefore, the elevation angle noted in equations 4.6 and 4.7 is set to  $3.3^\circ$ , and is different from the elevation angle used for equations 4.1, 4.3, 4.4, and 4.5, so it has been noted as  $e_o$  and can be referred to the initial elevation angle. The elevation angle is set to  $3.3^\circ$  due to the bending effect the neutral atmosphere applied to the incoming GNSS radio signal. The bending effect of the neutral atmosphere will slightly increase the elevation angle at the receiver, so the initial ray-traced elevation angle must be increased so as to ensure the outgoing elevation angle is close to  $3^\circ$ , the actual elevation angle of

the satellite. When determining the VMF1 parameters, the elevation angle,  $e$ , in equations 4.1, 4.3, 4.4 and 4.5 is the outgoing elevation angle when the satellite signal exits the neutral atmosphere. The value of  $3^\circ$  is somewhat arbitrary, but it is selected so that satellites at the lowest possible elevation angle can be effectively used in the GNSS solution. Herring (1992) demonstrated that equation (4.1) can be used to represent elevation angle dependence of the neutral atmosphere delay with an RMS  $< 0.2\text{mm}$  for elevation angles between 90 and 3 degrees, giving evidence that  $3^\circ$  is the lower limit of this functional form.

Lastly, the VMF1 is an azimuthally symmetric mapping function, meaning that a delay at an elevation angle of  $10^\circ$  is the same regardless of the azimuth of the signal source. The selection of the atmospheric model in the ray-tracing has this fact in consideration. The UNB-VMF1 utilizes a spherically osculating atmospheric structure with a Gaussian radius of curvature ( $R = \sqrt{MN}$ ). Nievinski (2009) has demonstrated that a spherically osculating atmospheric structure is azimuthally symmetric, and is best suited for GNSS applications since elevation angles are reckoned from the ellipsoidal horizon, which is coincident with the horizon of the spherical osculating atmosphere (as opposed to a spherically concentric). In addition to the compatibility, a spherically osculating atmosphere (which implies a bent 2-D ray path model) is computationally more efficient than a fully 3-D ray-trace (due to the simplification), which allows for an easier and more flexible implementation into operational services. Nievinski (2009) further demonstrated that the application of a bent 2-D ray path model introduced negligible errors as compared to a fully 3-D model in a 15 km resolution numerical weather prediction model.

#### **4.2.2.3 Numerical Weather Prediction Models**

The UNB-VMF1 utilizes two main numerical weather prediction models (NWP's), which is necessary to perform the ray-tracing as described in §4.3.2.2. First is the Re-Analysis 1 dataset provided by the National Centers for Environmental Prediction (NCEP), which is



a part of NCEP’s re-analysis project (Kalnay et al., 1996). Second is the Global Deterministic Prediction System (GDPS) provided by the Canadian Meteorological Centre (CMC) (CMC, 2012c). Table 4.4 summarizes some of the distinguishing features that describe each of the numerical weather prediction models applied in the UNB-VMF1 service in its distributed data form. Most obvious is the stark difference in the horizontal and vertical resolution. CMC’s dataset provides approximately  $4\times$  the horizontal resolution and  $1.5\times$  the vertical resolution, and  $3\times$  the vertical resolution for specific humidity.

Table 4.4: Distinguishing characteristics of NWP’s implemented in the UNB-VMF1 service

Characteristic	NCEP Re-Analysis 1	CMC GDPS
Domain	Global	Global
Grid Resolution	2.5 x 2.5 deg	0.6 x 0.6 deg
Model	Re-Analysis	Forecast
Availability	1948 - present	past 24 hrs
Output	$4\times$ Daily 00h, 06h, 12h and 18h	144h forecasts from 00h and 12h
Pressure Levels	17 (only 9 levels for specific humidity)	28 for all parameters used by UNB-VMF1

#### 4.2.2.4 Orography

The orography gives each of the data points in the UNB-VMF1 grids a specified height, which follows that of the existing VMF1 service. The heights of the grid points are defined in a file named *orography.ell*, which is an ASCII formatted text file describing the ellipsoidal height of each grid point in each of the UNB-VMF1’s final products (see §4.2.4). Again, one of the goals of the UNB-VMF1 service is to maintain as much compatibility with the existing user base as possible, so utilizing the same orography will help in that respect. However, there are some numerical aspects that should be considered.

In particular, the relationship of the orography to the lowest isobaric pressure level in the NWP can create some numerical instability in the right circumstances. If the height of the grid point lies outside of the NWP, then the corresponding meteorological parameters must be extrapolated from the lowest isobaric pressure level of the NWP. The UNB ray tracer extrapolates linearly the specific humidity, temperature, and the log of pressure, which is highly dependent on the rate of change of the meteorological parameter with respect to geo-potential height prior to exiting the NWP. This situation can occur when using a NWP surface layer in conjunction with isobaric pressure level data products.

This is best illustrated with the specific humidity parameter. CMC's GDPS provides the specific humidity at isobaric pressure levels and at the surface in units of  $kgkg^{-1}$ . Figure 4.2 illustrates a typical configuration where an extrapolation is necessary. Points A and B represent grid points within the NWP and point C represent the point of interest, located outside the NWP. The height of points A and B,  $z_A$  and  $z_B$ , are defined by the NWP (as

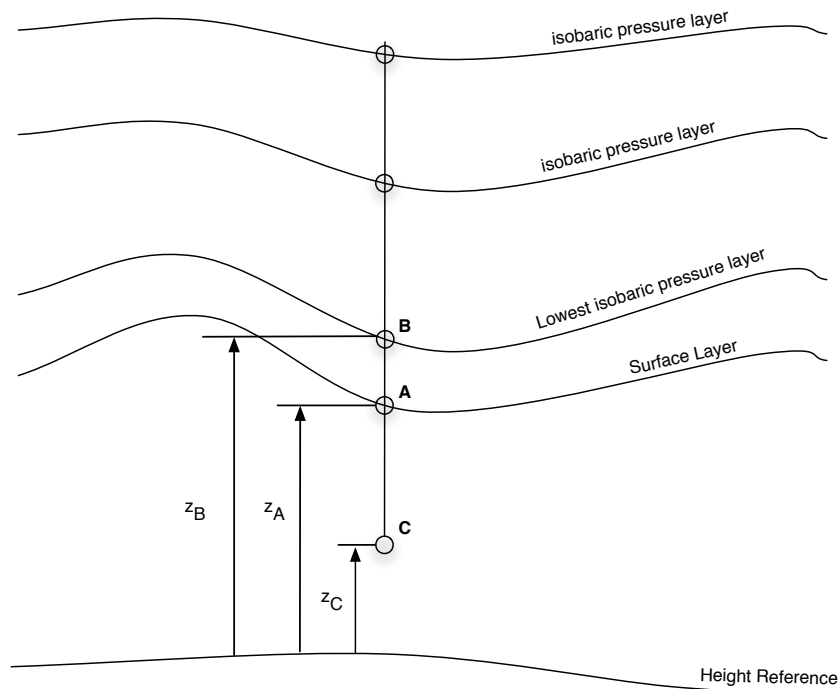


Figure 4.2: Typical extrapolation configuration when height of UNB-VMF1 grid point lies outside of NWP as defined by *orography.ell*

geopotential heights) and the height of point is C,  $z_C$ , is defined by the file *orography.ell* transformed to the NWP height system. Points A and B will have an associated specific humidity and the specific humidity at point C is to be determined. If the height difference between points A and B is small enough and the change in specific humidity is large (between points A and B), then the extrapolated value could become erroneous (sometimes negative) if point C is located far enough outside the NWP. These erroneous meteorological parameter values are manifested as negative  $a_w$  coefficient values, as well as incorrect zenith delays and  $a_h$  coefficients. However, the  $a_w$  coefficients are most readily detectable. The following table, Table 4.5 illustrates an example of a typical extrapolation of specific humidity in this situation (actual values from CMC GDPS).

Table 4.5: Example of sample data (showing only a portion of full vertical profile) from CMC’s GDPS that can result in erroneous extrapolations

Geopotential Height (m)	Specific Humidity ( $kgkg^{-1}$ )
0.1434	0.01799
0.1576	0.01147
128.4700	0.01044
258.5869	0.01039
389.8177	0.01035
Height of pt.C	-4.9442 m
Extrapolated value	2.3586 $kgkg^{-1}$

To deal with this condition, two options are available. Firstly, an orography can be determined such that no extrapolations are necessary, only interpolations, but this would have an impact on the continuity at the end-user. The end-user would have to account for a second orography in their implementations, which would create an opportunity for confusion as to what orography was used when reducing the grid values to the station heights (e.g., *a-priori* zenith hydrostatic delays). Therefore, UNB-VMF1 does not include any surface layers in the ray tracing through the NWP data model, only pressure level layers. This removes the potential for this numerical instability, and maintains continuity

at the end user's implementations.

### **4.2.3 System Integration**

The creation of the system architecture for the UNB-VMF1 service is vital in providing a robust continuously operating computational system that services the international geodetic/scientific community without interruption. To achieve such a goal, the service must consist of several components, namely a robust connection to the source data, computational resources, and a robust mechanism for the delivery to the user base. These components can be realized by leveraging the computing resources provided by the Atlantic Computational Excellence Network (ACEnet). ACEnet is a consortium of Atlantic Canadian universities providing researchers with high performance computing resources, collaboration, visualization tools, training and support (ACEnet, 2012a). ACEnet's resources are accessed through a series of clusters located across Atlantic Canada at several academic institutions, namely (cluster names in parentheses): Memorial University (Placentia), St. Francis Xavier University (Brasdor), St. Mary's University (Mahone), University of New Brunswick (Fundy and Courtenay), and Dalhousie University (Glooscap).

The UNB-VMF1 service has been selected to operate simultaneously on three clusters: Placentia, Mahone, and Fundy. The simultaneous operation attempts to mitigate the risks of network outages and maintenance, as well as any other unplanned events. Table 4.6 summarizes the cluster uptime from March 2011 until March 2012, which illustrates that in general each cluster will experience some downtime, but when several clusters are used simultaneously, as in our implementation, the risk can be effectively mitigated (personal communication, Joey Bernard, 2012). The combination of Fundy, Mahone, and Placentia has seen 100 percent uptime since March 2011, and at no time were all three clusters unavailable. Therefore, the use of a three cluster architecture has created a robust redundant system that can meet the criteria of a continuously operating computational system.

Table 4.6: ACEnet cluster uptime from March 2011 until March 2012

Cluster	Uptime (%)
Brasdor	97.8
Mahone	97.0
Glooscap	92.3
Placentia	98.4
Fundy	99.7
Courtenay	98.9

A second important aspect of integrating a system is ensuring that there is a sufficient amount of computational power. On a standard dual core 2.10 GHz machine with 2.0 GB of RAM the required computational time to produce a single UNB-VMF1 gridded file is approximately 60 minutes (only for one epoch, e.g., 00h or 06h, etc). Therefore, the computation of all four epochs will require approximately 4 hours of system resources. On the surface this would appear to be sufficient, but if there are any technical issues with the production of the gridded files the computational time could be a hinderance in providing the corrections of the community in a timely manner. Further, the computational requirements does not lend itself to the generation of corrections for historical dates. Under these conditions it would require 60 days of computation to produce an entire years worth of corrections, and almost 3 years to produce all products going back to 1994.

ACEnet’s computational environment lends itself to parallel computing (although parallel computing can be implemented on a dual core machine, it is limited to two cores, where on ACEnet the number cores can reach up to 16 on Fundy/Placentia), which grants many benefits to high performance computing, one of which is the reduction of computational time. There are several ways of realizing the benefits of parallel computing, where the following are supported by ACEnet (ACEnet, 2012b):

1. "Embarassingly" or "Perfectly" parallel problems which can be treated as independent serial jobs,

2. Message-passing parallel computing (MPI), and
3. Shared memory parallel computing (OpenMP).

The UNB-VMF1 service takes advantage of item (1), as each gridded epoch (00h, 06h, 12h and 18h) is treated as an independent serial job that is parallelized through job control mechanisms (ACEnet's scheduling system, Grid Engine). Items (2) and (3) would require significant changes to the source code of UNB's ray tracer, and as NWP's are improved, the possibility of parallelizing the ray tracing source code should be further investigated if these algorithms are to be used in a more real-time computational environment.

By method (1), instead of 4 hours to complete a single days worth of product, only 40 to 60 minutes (depending on cluster and priority in the queue) are required. This equates to a 75% increase in computational efficiency for the daily product when using ACEnet's resources. As for the generation of historical products, several years of gridded product can be further parallelized across the three clusters as well as being scheduled in parallel on each cluster. A single year can be computed in 2-3 days (depending on cluster load) and 10 years can be computed in approximately 10 days, which is a far cry from 3 years. Figure 4.3 graphically illustrates the computational time required to produce all four daily grids for the month of December 2011 (for product unbvmfG). The sharp drop in computational time occurs when the computation of the grids were parallelized in the scheduler, and the break in Fundy's time series between December 12th and 14th is due to the fact that the products were not computed on those days. The computation time is fairly consistent on all clusters, but there are instances when computation time could be longer based on cluster load and priority in the queue. For example, in Figure 4.3 Fundy shows a slight increase in between dates December 24th and 26th. These events are normal and are to be expected in normal operational use of ACEnet's computational facilities.

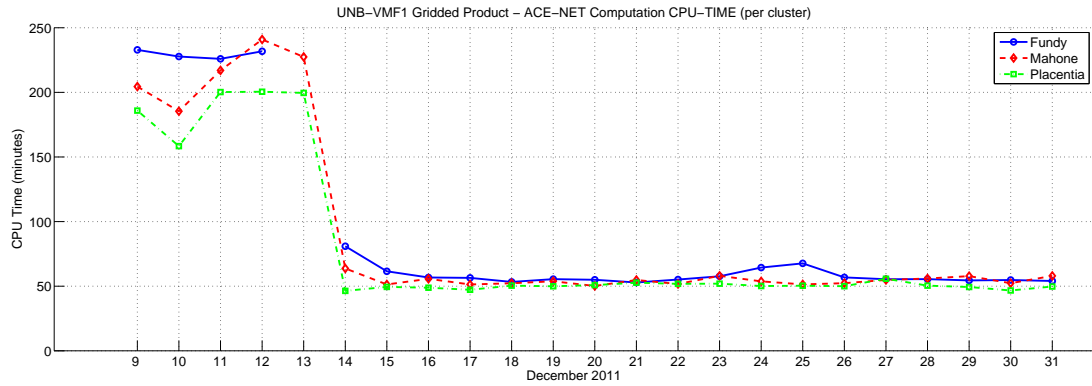


Figure 4.3: Computational efficiency when parallelizing jobs on ACEnet

#### 4.2.3.1 UNB-VMF1 System Architecture

As noted, the UNB-VMF1 service has been constructed to operate simultaneously on three ACEnet clusters. Figure 4.4 illustrates the relationship each cluster has with the overall computational process. The initial step in the computational process is to obtain the NWP data from its respective source (shown on Figure 4.4 by connections A1, A2 and A3). From the figure, it is obvious that this connection in the process flow is the weak link. Although each cluster is connected independently to the data source, if the data source is removed (i.e. due to network outage) then the computations cannot proceed. The impact of this weak link is described in detail in §4.2.4 with respect to the reliability of each product. However, there is the benefit of having multiple connections so that if one download connection is severed two remain ensuring computations continue, thus providing some risk mitigation (full detail of the retrieval scripts can be found in Appendix A). Taking a long term outlook for the service, the assurance of continual data delivery is vital. It would be in the best interest of the service of obtain secure arrangements with the source data providers such that the service’s links to the datasets can be maintained in the event of outages (i.e., CMC’s rolling availability as described in §4.2.4).

The second component is the computational topology. An ACEnet cluster is comprised of a head node and a computational node. The head node holds the computed products, source data, source code, and all shell scripts that operate and manage commu-

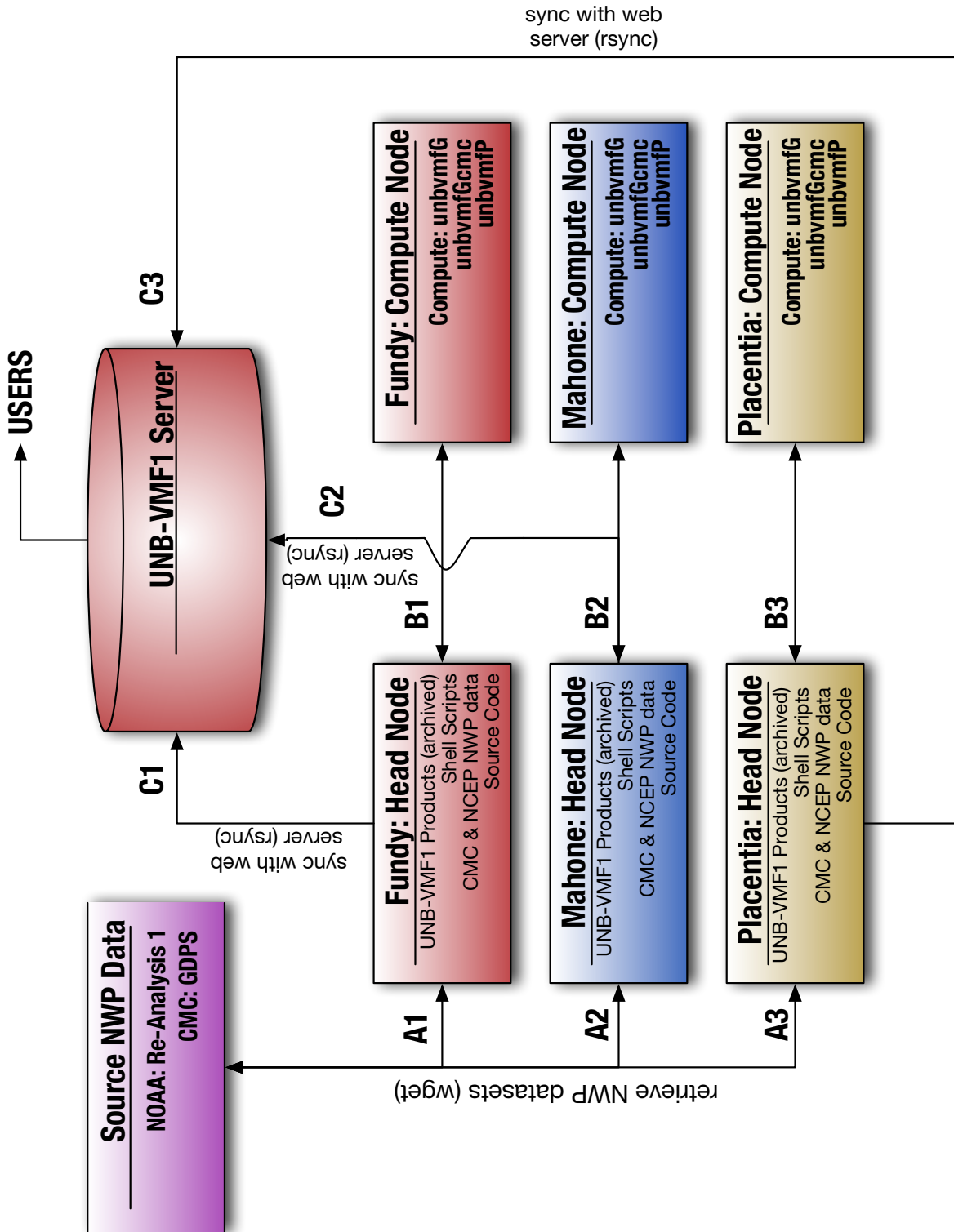


Figure 4.4: UNB-VMF1 System Architecture



nication of the service (all clusters implemented in the UNB-VMF1 service will have identical holdings). Job submission is also controlled on the head node. When a computation is to be computed, a request to submit a job is sent from the head node requesting compute node resources. Here the job is scheduled in the queue, and when compute resources become available the computations are completed, and all output files are transferred to the head node as computations are completed (reason for the double arrow between head and compute nodes in Figure 4.4). As shown in Figure 4.4, each cluster operates in this fashion independently of each other (connections B1, B2 and B3). Originally, a sync between all clusters was planned to ensure that all clusters were up to date, which would deal with an instance of any cluster going offline for any period of time. In practice this is difficult, since sync conflicts cannot be dealt with effectively in a robust automatic manner; a manual inspection must be completed. An example of a sync conflict that could occur involves two computed gridded product files, but each having a different size (indicating a conflict). One file is complete and computed first (indicated by a complete file size); the second product has finished the computations on another cluster, but did not finish successfully (indicated by smaller file size). Which is the correct product to sync, the former or latter? The decision cannot happen without human interaction. Due to this complexity the clusters do not sync with each other, however the operational shell scripts have been designed to automatically detect which files to produce if any files are missing, incomplete or not of standard format, which ensures each cluster is up to date and correct (complete details can be found in Appendix B).

The computational component of the service performs several checks to ensure required data is available prior to computation. This is necessary as it help to prevent the possibility of unwanted partially completed files (although these files will be identified and excluded during the upload sync process). If the NWP data is not available, the computations will not initiate and the system administrator will be notified immediately. Further, if an operation fails (which can happen for unknown sporadic reasons on ACEnet), the

computation script will continue to submit a job until a successful completion of the file is obtained (complete details of the computation scripts can be found in Appendix B).

The final component of the UNB-VMF1 system architecture is the connection (shown by connections C1, C2, and C3 in Figure 4.4) to the user interface (details of the user interface are described in §4.2.5). This link is dependent on the network connection to the UNB-VMF1 web server being operational. Any network outages at UNB will prevent transfer of computed product from ACEnet to the UNB-VMF1 server (as well prevent the product from being available to the community). This link is not as weak as the download link, since a broken link does not prevent the computations from starting. An improvement to the web-server connection would be the creation of a backup server with an automatic failover mechanism. However, for this to be effective, the backup server would have to be located on another network to ensure that it is able to function if UNB's network fails. Ideally, this location would be in another city (other than Fredericton) to ensure that the backup server is completely isolated from the outage. As the service matures and the user base grows, this should be an integral part of the service's long term plan.

The three clusters (Fundy, Placentia and Mahone) sync with the UNB-VMF1 web server independently (each cluster has implemented the program *rsync* to accomplish this task), which provides redundancy if any cluster were to go offline. During upload, each file is checked for completeness (file size) and standard format (file does not contain null characters) prior to syncing. If any anomalies are found within the files, the suspect files are excluded and noted in a daily administrative report for the system administrator (full details of sync scripts can be found in Appendix B).

#### **4.2.4 Product Description**

The UNB-VMF1 offers several product types each with its own distinguishing features. Each of the products are a globally gridded product following the work of Kouba (2009), which demonstrated that the use of a global grid was effectively equivalent to the use of

a site specific determination. These products include: unbvmfG (§4.2.4.2), unbvmGcmc (§4.2.4.3) and unbvmfP (§4.2.4.4). Each of these products share the same grid (described in §4.2.4.1) and output file format (described in §4.2.5). A summary of the main differentiating features of each product can be found in Table 4.9.

#### **4.2.4.1 Grid Definition**

Common to all products is the grid format, which follows the existing VMF1 service for continuity. All products provided by the UNB-VMF1 service are produced on a  $2.0^\circ$  (latitude - j axis) x  $2.5^\circ$  (longitude - i axis) global grid. Figure 4.5 illustrates the distinguishing characteristics of the final product grid definition. The global grid extends from  $90^\circ\text{N}$  to  $90^\circ\text{S}$  and from  $0^\circ\text{E}$  to  $357.5^\circ\text{E}$  defining the North/South and East/West limits. Every (i,j) point defined within these limits has an associated hydrostatic zenith delay ( $zhd$ ) and a-coefficient ( $a_h$ ) as well as a non-hydrostatic zenith delay ( $zwd$ ) and a-coefficient ( $a_w$ ). Finally, every (i,j) point has an associated ellipsoidal height which is defined in a file named *orography.ell*. This is the same orography definition file used by the existing VMF1 service. As noted in §4.3.2, only the hydrostatic a-coefficient ( $a_h$ ) is reduced to a zero height. The remaining parameters,  $zhd$ ,  $zwd$ , and  $a_w$  refer to the ellipsoidal height defined in *orography.ell*.

#### **4.2.4.2 unbvmfG**

The unbvmfG is the main operational product of the UNB-VMF1 service. This product is considered to be the main operational product due to the stability of NWP data availability. The unbvmfG product is produced using NCEP's Re-Analysis 1 dataset, which is available from 1948 until the present date. As shown in §4.3.3, a weak link persists between the source data and the computational system, which makes the service susceptible to data source server outages or network connection issues at the UNB-VMF1 service. Fortunately, NCEP's Re-Analysis 1 dataset availability is persistent. For example, if a

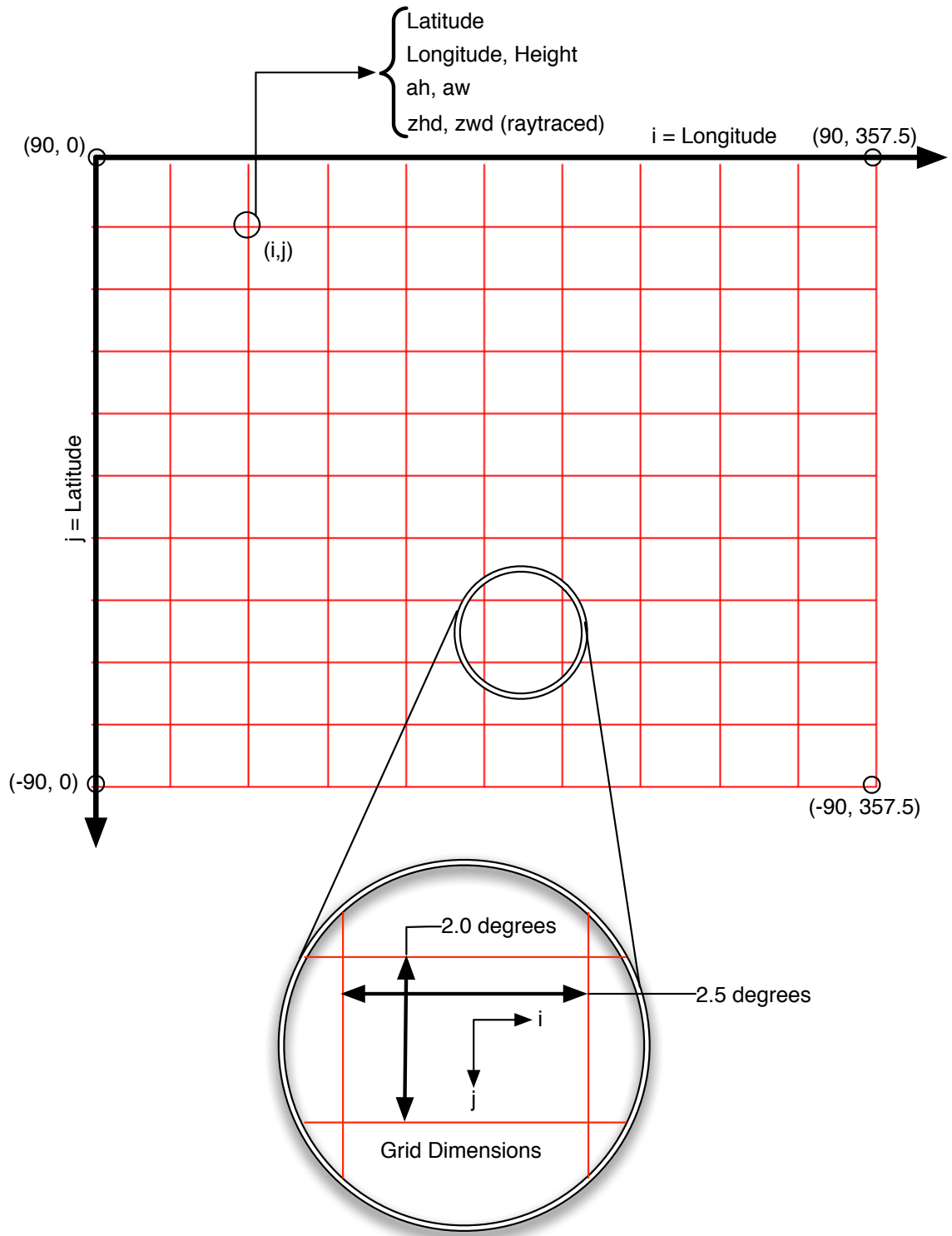


Figure 4.5: UNB-VMF1 grid definition (not to scale)

connection issue were to occur at the UNB-VMF1 service, data will still be available on NCEP's servers, and once the connection has been restored the UNB-VMF1 service would recompute all missing dates. In short, all datasets from 1948-present are continually available and continuously updated (as 2012) on NCEP's servers, which make it highly attractive for a continuously operating service.

NCEP's Re-Analysis 1 dataset has an approximate 3 day availability latency, which limits the minimum latency that the product can be produced with. Figure 4.6 summarizes the availability for the unbvmfG product. The unbvmfG is produced four times daily for epochs 00h, 06h, 12h and 18h (these are actually produced simultaneously as described in §4.2.3), where an individual file is produced for each epoch (00h, 06, 12h, and 18h), and is subsequently uploaded to the web server at 00h AST. To ensure that the UNB-VMF1 computational algorithms continue to operate with minimal interruption the latency for this product has been selected as 7 days. In combination with the knowledge that the IGS final orbit and clock products are available with a 12-18 days latency (IGS, 2012), the unbvmfG will be able to be used effectively with standard network analysis that rely on final IGS products. To summarize the products availability described in Figure 4.6, an example is presented. If today is September 11, 2012 then at 00h AST of said date, all product files (00H,06H,12H and 18H) are made available for September 4th, 2012.

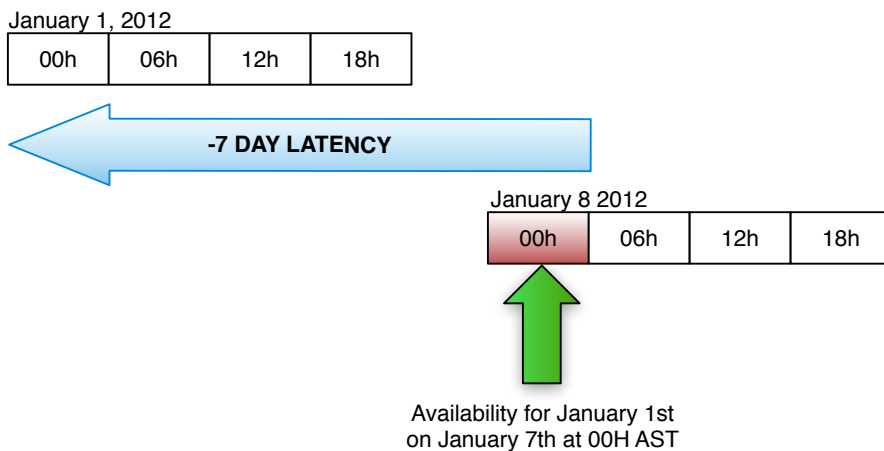


Figure 4.6: Standard availability of unbvmfG

Of course, if the user community desires to have the latency reduced for this product the UNB-VMF1 service can accommodate those needs, but could only realistically reduce that latency to within 24hrs of when the data becomes available. The atmospheric pressure loading service, currently found at <http://gemini.gsfc.nasa.gov/aplo/> (as of June 2012), also utilizes the same NWP dataset from NCEP. The service also tracks the latency of their product since the goal of the service is to provide products within 24 hours of NWP availability. However, only 90 percent of the atmospheric pressure loading time series achieves a latency of 2.6 days. The remaining 10 percent achieve a latency between 4-15 days (Petrov, 2012). This is an important fact to consider, as the unbvmfG product could see latencies up to 15 days. The cause of these increased latencies is most likely related to NCEP data availability. The 7 day delay built into the unbvmfG product means that there is approximately a four day buffer built into the computations, and if any service delays extend beyond four days from NCEP, it will mean there will be delays in making the product available to the community. The UNB-VMF1 service has experienced two occasions since the start of 2012 (during the early internal pre-evaluation phase) where the 7 day latency could not be met due to data delivery issues at NCEP.

Lastly, This product is currently available beginning in 2001 up and to including 7 days prior to the current date. However, additional dates will be added to the service starting for the year 1994 so that a complete set of product covering the interval 1994 to present will be made available to the scientific community. File naming conventions are summarized in Table 4.7 in §4.2.4.5.

#### **4.2.4.3 unbvmfGcmc**

The unbvmfGcmc is a similar product to that of unbvmfG, but it is produced using CMC's GDPS as the source NWP. At the present time, the unbvmfGcmc product is considered experimental due to the nature of the data availability from CMC. Unlike NCEP, CMC's data offerings are not persistent. The CMC offers data for the GDPS on a rolling basis

for a time period of 24 hours. This creates a significant risk for the service if any network disruptions occur at CMC or the UNB-VMF1 service (risks for network outages at the UNB-VMF1 has been effectively mitigated by the redundant architecture as described in §4.3.3, but edge cases cannot be ruled out). These situations are not unheard of at the CMC, as in November of 2011 the CMC suspended dissemination of the regional and global (GDPS) products on the polar stereographic grid from November 21, 2001 until November 23, 2011 due to difficulties in file content [Tremblay, 2011]. Therefore, if any disruptions occur the product will not be produced for that time period and will not be reproduced since the datasets are only available on a rolling basis. This is the reason for experimental status, and this status will remain until more robust arrangements can be made with the CMC.

Figure 4.7 illustrates the availability of unbvfmfGcmc. An advantage of this product over the operational unbvfmfG is the reduction in latency, although the advantage is somewhat tempered by the increased risk of data outages and missing epochs. Figure 4.7

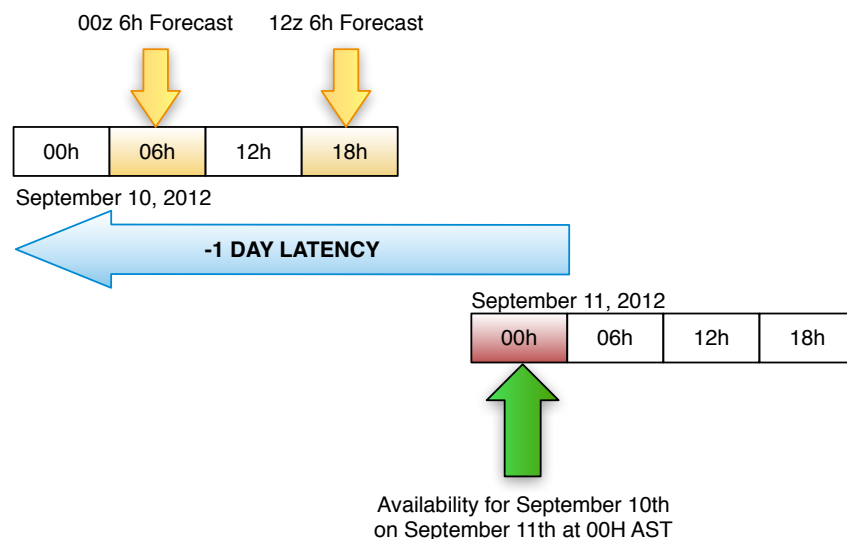


Figure 4.7: Standard availability of unbvfmfGcmc

illustrates that the unbvfmfGcmc is available with a 1 day latency (comparable to the existing VMF1 gridded product) and is placed on the UNB-VMF1 web server at 00h AST.

For example, if the current day is September 11th, 2012 then all of the unbvmfGcmc product files (00H, 06H, 12H and 18H) will be made available to the community for the date September 10th, 2012 on September 11th, 2012 at 00h AST. This latency makes it compatible with IGS final products and rapid products, in which the latter are available with a latency ranging between 17 and 41 hours (in contrast with unbvmfG, which is only compatible with the final IGS products) (IGS, 2012). The unbvmfGcmc is well suited for applications that require the highest consistency and quality (used with IGS final products) as well as for applications that are time dependent (solution required within 24-48hrs) and require high quality results (to be used with IGS rapid products).

The unbvmfGcmc is produced four times daily at epochs 00h, 06h, 12h, and 18h. It should be noted that due to the nature of CMC's GDPS epochs 06h and 18h are produced with forecast data. As noted in §4.3.2.2, the GDPS produces 144 hour forecasts from initialization time of 00h and 12h, which require epochs 06h and 18h to be produced with 6 hour forecasts. The impact of this will be covered in Chapter 5 within the scope of the service's validation. Due to the rolling availability of the CMC's GDPS, unbvmfGcmc is currently only available from January 1st, 2012. Historical computations will not be produced all the way back to 1994 as with the unbvmfG product, but the unbvmfGcmc will be produced starting from June 23, 2009. The reason for this that the CMC does have any humidity parameters archived prior to this date (Tremblay, 2012). File naming conventions can be found in §4.2.4.5 in Table 4.7.

#### **4.2.4.4 unbvmfP**

The unbvmfP is the UNB-VMF1's forecasted product, where the VMF1-FC gridded product of the existing VMF1 service would be its equivalent. The unbvmfP is produced with CMC's GDPS as its source NWP. This product is also considered an experimental product for the same reasons outlined in §4.2.4.3, and will not reproduce any missing epochs for those same reasons.



Figure 4.8 illustrates the availability for unbvmfP, which make it a 0 day latency product. Since the unbvmfG and unbvmGcmc have a 7 day and 1 day latency respectively, they are not suited for real-time or near real-time applications. These near real-time and real-time applications are in the range of applications where the unbvmfP will find its strength in applicability. As shown in Figure 4.8, the unbvmfP is currently made available

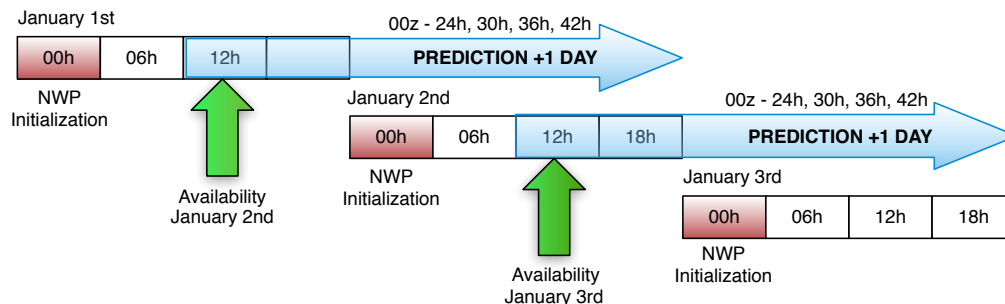


Figure 4.8: Standard availability of unbvmfP

at 12h AST of the current day for the following day. Following the example displayed in Figure 4.8, if today was January 1st, 2012, then at 12h AST all files (00H, 06H, 12H and 18H) for the unbvmfP product becomes available for January 2nd, 2012. So, on January 1st at 12 AST, the user may download the product files for the next day (January 2nd), which allows for a zero latency product ideal for real-time applications. This pattern continues for the entire year, as January 3rd's product files are available on January 2nd at 12h AST, and so on. This means that at the start of each day, corrections based on unbvmfP product files can be applied starting at 00UTC.

The unbvmfP is produced 4 times daily at 00h, 06h, 12h and 18h as with the previous described products. However, unbvmfP is produced from a single reference initialization period - that is 00h. Therefore, epochs 00h, 06h, 12h and 18h are produced with 24h, 30h, 36h and 42h forecasts respectively from 00h, which follows the practice of the existing VMF1 service (Boehm et al., 2009). The basis of selecting these forecast times was explored by Boehm et al. (2007), which illustrated that for the first three to four days the

hydrostatic mapping function error expressed as equivalent height error (see Chapter 5) performed under the established accuracy of the VMF1. Therefore, a 42h forecast will still be within the limits of the VMF1 accuracy. Currently, unbvmfP is only available from March 17, 2012 due to previous download practices employed to save storage space. The implementation of unbvmfP required the acquisition of 24-42h forecasts, where previously only 3-9h forecasts were downloaded since a new initialization would occur every 12 hours. File naming conventions follow those stipulated in Table 4.7 in §4.2.4.5.

#### 4.2.4.5 File Naming Conventions

All products follow a similar naming convention. The difference lies in the base name for each file. The file naming is as follows: **basename.YYYYMMDD.HXX**. The following table, Table 4.7, summarizes the definition of each component of the naming convention.

Table 4.7: File naming conventions for UNB-VMF1 service

Code	Description	Range	Example
basename	UNB-VMF1 product name	unbvmfG, unbvmfGcmc or unbvmfP	unbvmfG
YYYY	four digit year	First Year* - present	2012
MM	two digit month	01-12	07, 11
DD	two digit day	01-31	05, 24
XX	two digit epoch	00h, 06h, 12h and 18h	00, 06

\*First Year varies from product to product. See table 4.9 for details.

#### 4.2.5 End-User Interface

The end user of the UNB-VMF1 service is presented with a standard HTML web interface to interact with that is located at the web address: `unb-vmf1.gge.unb.ca`. The main purpose of the web interface is to provide a portal to access the UNB-VMF1 products, which can be accessed in two ways. The user can download UNB-VMF1 gridded files through direct interaction with the website, or the user can implement automatic down-

load scripts utilizing the program *wget*. The UNB-VMF1 service provides a guide to accessing the gridded products with *wget* located at [http://unb-vmf1.gge.unb.ca/UNBVMF1\\_wget\\_guide.html](http://unb-vmf1.gge.unb.ca/UNBVMF1_wget_guide.html). Table 4.8 summarizes the directory structure created to hold the final gridded products, where the base url is `unb-vmf1.gge.unb.ca/pub/` and is noted in Table 4.8 as *base*.

Table 4.8: Directory Structure for stored final UNB-VMF1 products

Product	Location on Server
unbvmfG	<i>base/unbvmfG/YEAR/filename*</i>
unbvmfGcmc	<i>base/unbvmfGcmc/YEAR/filename*</i>
unbvmfP	<i>base/unbvmfP/YEAR/filename*</i>

\*a description of file naming conventions can be found in §4.2.4.5

The output files produced by the UNB-VMF1 service are a row-based format which follows the existing VMF1 service, and is used by the Bernese software package [VMF1 (2012)]. Each row in the output file consists of the following six elements (in this order), latitude, longitude,  $a_h$ ,  $a_w$ ,  $zhd$ , and  $zwd$ . Column spacing is as follows: 4.1F (latitude), 5.1F (longitude), 1.8F ( $a_h$ ), 1.8F ( $a_w$ ), 4.4F ( $zhd$ ) and 4.4F ( $zwd$ ). A portion of an output file can be found in Appendix B.

### 4.3 Summary

This chapter provided a description for a UNB realization of the Vienna Mapping Functions, where the VMF1 variant has been implemented with an independent ray-tracing system, and an independent numerical weather prediction model from the existing VMF1 service. This new service will provide several benefits to the scientific/geodetic community. Firstly, it will improve the availability of troposphere delay products as this service can act as a backup to the existing one. Any service interruptions that were to occur

Table 4.9: Summary of UNB-VMF1 products

Product	Grid (lat X lon)	NWP Source (Resolution)	Latency	Start Date	Status	Parameters	Notes
unbvmfG	2.0° X 2.5°	NCEP Re-Analysis 1 (2.5° X 2.5°)	7 days	Jan. 1, 2001	Operational	$a_h, a_w,$ $zhd, zwd$	Data to be added going back to 1994.
unbvmfGcmc	2.0° X 2.5°	CMC GDPS (0.6° X 0.6°)	1 day	Jan. 1, 2012	Experimental	$a_h, a_w,$ $zhd, zwd$	Missing epochs will not be replaced.
unbvmfP	2.0° X 2.5°	CMC GDPS (0.6° X 0.6°)	0 day	Mar. 17, 2012	Experimental	$a_h, a_w,$ $zhd, zwd$	Missing epochs will not be replaced.

Table 4.10: Summary of VMF1 products from the existing VMF1 service

Product	Grid (lat X lon)	NWP Source (Resolution)	Latency	Start Date	Status	Parameters	Notes
Gridded VMF1	2.0° X 2.5°	ECMWF (N/A)	< 34hrs	Jan. 1, 1994	Operational	$a_h, a_w,$ $zhd, zwd$	up to 30 June 2009, grid point lat = 30 deg and lon = 87.5 is wrong. Replace with neighbouring grid point.
Forecast (Gridded VMF1)	2.0° X 2.5°	ECMWF (N/A)	0 day	TBD	Operational	$a_h, a_w,$ $zhd, zwd$	Missing epochs will not be replaced.
VMF1 Site <sup>a</sup>	N/A	ECMWF (N/A)	< 34 hrs	Varied <sup>b</sup>	Operational	$a_h, a_w,$ $zhd, zwd$	VMF1 for (IDS), DORIS, IGS (GPS), IVS (VLBI) sites
Forecast VMF1 Site	N/A	ECMWF (N/A)	TBD	TBD	Operational	$a_h, a_w,$ $zhd, zwd$	IVS (VLBI) sites. Missing epochs will not be replaced.

<sup>a</sup>The recommended practice from the VMF1 service is to use the gridded products (i.e., VMF1 gridded)

<sup>b</sup>Early availability is sporadic for all systems except VLBI. The following dates are based on a fully populated year.

GPS: 2005-Jan-01

VLBI: 1979-Jan-01

DORIS: 2005-Jan-01

VLBI-GR: 1992/1993-Jan-01 then from 2009-Jan-01

with the current VMF1 service would result in a delay in the availability of the correction products, which can have an impact on any data processing downstream. The addition of the UNB-VMF1 alleviates this concern since the production of the corrections will now occur in redundant locations. Secondly, the addition of the UNB-VMF1 will help to support data processing efforts by the scientific/geodetic community with the addition of a completely independent source of atmospheric corrections and help to achieve greater compatibility with other corrections derived from the same numerical weather prediction models implemented by this service (e.g. atmospheric pressure loading which uses NCEP Re-Analysis 1). Lastly, the addition of the UNB-VMF1 will help to stimulate research into neutral atmosphere delays and help to understand and characterize the implications of using numerical weather prediction models to compute these corrections.

The UNB-VMF1 offers three products to the community with varying latency and numerical weather prediction model data. First is `unbvmfG`, which is produced with NCEP's Re-Analysis 1 and is available with a 7 day latency. Next is `unbvmfGcmc`, which is produced with CMC's GDPS and is available with a 1 day latency. Lastly, is `unbvmfP`, which is also produced with CMC's GDPS, but applies 24h, 30h, 36h and 42h forecasts in its production. All products are produced 4× daily on a  $2.0^\circ \times 2.5^\circ$  grid at 6H intervals in an ASCII text file format following the existing VMF1 service. All product data files are made available publicly through a web browser interface located at <http://unb-vmf1.gge.unb.ca> or by command line programs such as `wget`.

Important in the development of the UNB-VMF1 is the assurance that the system will operate in a consistent and robust manner. These goals have been met with the implementation of the main computational routines on ACE-NET. The system has been implemented on three nodes across Atlantic Canada (Fundy, Mahone and Placentia) ensuring that all products are produced simultaneously at three separate locations. Not only has the implementation on ACE-NET produced a robust system, it has also greatly reduced computation time with the application of parallel computing. The computation of a single

product has been reduced by 75% with the application of some simple parallel computing principles.

In spite of the efforts to provide a robust system, there are still some weak points in the overall process. Namely, with the computation of the unbvmfGcmc product. The CMC only offers their data on a 24H rolling basis, so if any outage occurs at the UNB-VMF1 service or at the CMC the source data cannot be obtained (without a nominal fee) and the product cannot be reproduced. It is recommended that the CMC should be approached where an agreement can be negotiated so that a secure consistent source of data can be made available to the service. Secondly, the UNB-VMF1 web serve only resides in a single location, which makes it vulnerable to any server or power outages at UNB. It is recommended that a second backup server be implemented off-site that can be switched over automatically if the main server were to go offline. Thirdly, computational time can be further improved with the parallelization of the raytracing code, which is the main bottleneck in the production of all products, and should be investigated for future applications in a more real time setting.

Overall, the UNB-VMF1 service has been operating since January 2012 and was officially launched the following June. The current site averages approximately 250 unique visitors per months with a total of 16, 351 visits. Further, each of the 6-hourly data files have accumulated approximately 5500 hits for the period June to December 2012. In addition, the service has received provisional approval from the GGFC and the IERS Directing Board. All products are part of the GGFC Provisional Products and the service has now embarked on the 2 year evaluation period with the goal of full approval for EGU 2014.

## **Chapter 5**

# **Validation of the UNB Vienna Mapping Function Service**

This chapter provides a summary of the validation activities that have been completed to ensure that the UNB-VMF1 service is operationally capable. The validation efforts in this section are not related to infrastructure testing, but testing of final products to be used in geodetic analysis. Validation of the infrastructure is an ongoing effort and the reader is directed to chapter 4 or Appendix B for details. This chapter describes the validation in the context of geodetic applications. Within this context, the intention of the validation is not to assess the accuracy of the VMF1, but to assess the different realizations of the VMF1. This will be achieved through two comparisons: (a) raw gridded product; and (b) results of a GNSS analysis. Firstly, §5.1 provides the main description and summary of the operational gridded product comparisons with an estimation of the impact in the position domain. Secondly, §5.2 describes the validation of the service in the position domain as the result of computing positions by precise point positioning methods. Lastly, §5.3, summarizes the results and conclusions.



## **5.1 Comparison of VMF1 Gridded Products**

The following section describes the first component of the validation process. Here the raw gridded products are compared to those from existing VMF1 service and to other gridded products from the UNB-VMF1 service. These comparisons will highlight any broad spatially based biases and variations that may be unique to the UNB-VMF1 based products due its ray-tracing algorithms or source datasets (NWP).

### **5.1.1 Previous Work**

This section attempts to summarize previous work that has been completed in the assessment of the VMF1 in the gridded domain, namely the VMF1 realized with the ECMWF. There has been numerous efforts in the assessment of the VMF1 in the position domain through the application of GNSS positioning, but for the assessment of the entire raw grid there have been few examples. The original evaluation of the gridded VMF1 (ECMWF) product was completed by Kouba et al. (2008). Kouba et al. (2008) compared the interpolated gridded VMF1 coefficients (and zenith delays) to that of the site specific VMF1 coefficients. This work was performed on a discrete site by site basis, which makes it difficult to asses any global scale effects due to the different realizations of the VMF1. Boehm et al. (2009) provides an assessment of a version of the VMF1 realized with ECMWF forecast data (the main VMF1 product is produced with ECMWF operational analysis datasets - see Table 4.10) on a global grid where all grid points are evaluated. Boehm et al. (2009) provides a comparison of an estimated impact in the position domain as well as the difference of each of the VMF1 parameters computed for each grid point. Our assessment will follow Boehm et al. (2009) as a basis of the comparisons in the gridded domain.

## 5.1.2 Description of Experiment

This section summarizes the methods and procedures implemented for the evaluation of the UNB-VMF1 products in the gridded domain. The gridded comparisons are based on the globally gridded definition of the UNB-VMF1 service (which is the same as the existing VMF1 service). The UNB-VMF1 produces global grids at a resolution of 2 degrees in latitude and 2.5 degrees in longitude. For each grid point values of the zenith delays and  $a$  coefficients (hydrostatic and non-hydrostatic) are defined, which form the basis of the comparison. The main comparison is with respect to the results from the existing VMF1 (the forecast product, unbvmfP, is compared with both the existing service and with the UNB-VMF1 product, unbvmfGcmc). The main validation will encompass an eleven year period, which will limit the comparison only to the unbvmfG (NCEP) product (see Table 4.9). The time period begins January 1st, 2001 and ends December 31, 2011. However, validation of the UNB-VMF1 service also include provisions for all products produced with data sets from the CMC. Unfortunately, the CMC based products (unbvmfGcmc and unbvmfP) could not be included in the eleven year analysis due to the unavailability of historical datasets from the CMC (see Chapter 4 for a full explanation). For the CMC based products, a comparison is made with the existing VMF1 service, but only for a portion of the year 2012. For the unbvmfGcmc comparison, the time period begins January 1st, 2012 and ends September 30th. For the unbvmfP product comparison, the time period begins March 17th, 2012 and ends September 30th 2012. Table 5.1 summarizes all the comparisons that have been made for all products and the pertinent quantities computed.

For each epoch, the 4 times daily UNB-VMF1 grids (at epochs 00h, 06h, 12h and 18h) are differenced with their corresponding VMF1 grids. The resultant delta VMF1 grids are stacked vertically to create a data cube with the vertical axis representing time. Figure 5.1 presents a visual representation of the data analysis, and table 5.1 summarizes the quantities computed. For the years 2001 thru 30 June 2009, the grid point values from

the existing VMF1 service located at 30° latitude and 87.5° longitude have been replaced with the values from the grid point located directly east (30° latitude and 90° longitude). The gridded values at the original location are incorrect, and the recommended practice is to replace with a neighbouring grid point (VMF1, 2012b). The values of the mapping func-

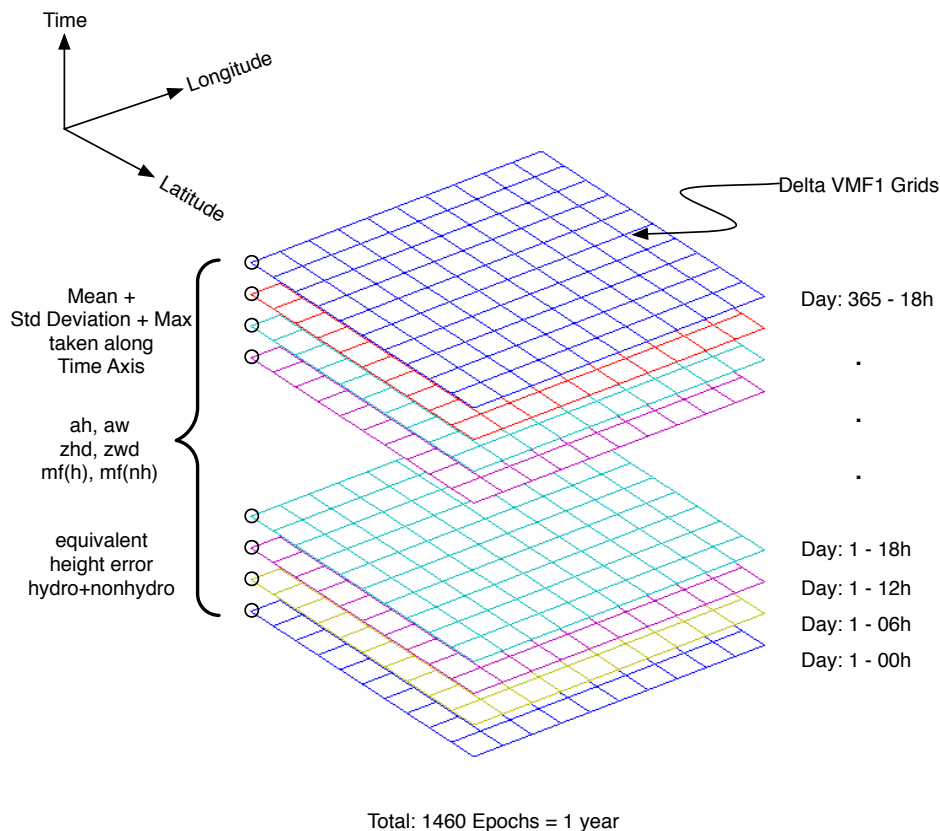


Figure 5.1: Data model used for grid comparisons

tions and the equivalent height error are the computed quantities. The mapping functions are computed as described in Chapter 4 by equations 4.1 and 4.2. For the computation of the hydrostatic mapping functions, the hydrostatic  $a$  coefficients are reduced to the height defined in *orography.ell* as defined by equations 4.3 and 4.4 (since the hydrostatic  $a$  coefficients are reduced to a 0 height in the production of the UNB-VMF1 and VMF1 grids). The mapping function at each grid has been computed with a 5° elevation angle. For the computation of the equivalent height error, the rule of thumb presented by Boehm et al. (2006) has been used. This definition of the equivalent height error states that the error in

height is equivalent to one-fifth the error in the mapping function at a 5° elevation angle. The error in the mapping function is defined as the difference between UNB-VMF1 minus the VMF1 grids, and to put the value into linear units it is scaled by either the hydrostatic or non-hydrostatic zenith delay. Therefore, two values of the equivalent height error are computed: hydrostatic, and non-hydrostatic. The value of the scaling zenith delay is taken as the ray traced zenith delay (from UNB-VMF1) at the grid point in question. This decision was made to provide more realistic estimates of the equivalent height error, since using a constant value may artificially create large discrepancies in regions with smaller zenith delays (i.e. locations of higher elevation). It is recognized that this method may mask some larger mapping function differences.

For each grid point, the yearly mean bias, standard deviation and maximum absolute difference are computed along the time axis at every grid point for each of the specified parameters. The yearly mean bias and standard deviation of each grid point has been computed by the standard *textbook* definition. However, to compute the global mean bias and standard deviation for each year, the combined mean bias and standard deviation has been computed by the following method:

$$\bar{X} = \frac{\sum_{i=1}^{n_g} n_i \bar{x}_i}{\sum_{i=1}^{n_g} n_i} \quad (5.1)$$

$$S_X^2 = \frac{\sum_{i=1}^{n_g} n_i (s_i^2 + (\bar{x}_i - \bar{X})^2)}{\sum_{i=1}^f n_i} \quad (5.2)$$

For equation 5.1,  $\bar{x}_i$  is the yearly mean bias for each grid point,  $n_i$  is the number of samples for each grid point, and  $\bar{X}$  is the combined global mean bias. For equation 5.2,  $s_i$  is the standard deviation of the grid point,  $\bar{x}_i$  is the mean of the grid point,  $n_i$  is the number

samples used to compute the mean of the grid point,  $\bar{X}$  is the combined global mean bias from equation 5.1, and  $S_{\bar{X}}^2$  indicates the combined variance. For both equations  $n_g$  is the total number of grid points for each year, and for this analysis  $n_g$  is 13,104 ( $91 \times 144$ ).

For the computation of the 11-year mean bias and standard deviation, equations 5.1 and 5.2 are also used to combine the yearly results into a combined 11-year global mean bias and standard deviation. For this case,  $\bar{x}_i$  is the yearly global combined mean bias,  $s_i$  is the yearly global combined standard deviation,  $n_g$  will be 11, and  $n_i$  will be 13,104 since the previous yearly global combined mean bias and standard deviations have been derived from this number. In addition to the combined global 11-year mean bias and standard deviation, an 11-year combined mean bias and standard deviation has been computed for each grid point. In this case,  $n_i$  is 1460 (or 1464 in a leap year) since the grids are produced 4 times daily,  $n_g$  is 11,  $x_i$  is the yearly mean bias for the grid point, and  $s_i$  is the yearly standard deviation of the grid point.

Table 5.1 summarizes the comparisons made and the associated parameters computed. In table 5.1, vmfG-FC is the forecast gridded product produced by the existing VMF1 service (see Table 4.10), and  $eqHh$  and  $eqHw$  are the equivalent station height errors. §5.2.2 describes the comparisons with respect to the existing VMF1 service (referred to as vmfG) and §5.2.3 describes the comparisons with respect to other UNB-VMF1 products. Lastly, §5.2.4 will provide a discussion on the results and attempt to explain some of the distinguishing characteristics of the results.

## **5.1.3 Comparison of UNB-VMF1 Products**

### **5.1.3.1 UNB-VMF1(NCEP) vs VMF1(ECMWF)**

The following sections provide comparisons for the hydrostatic (§5.1.3.1.1) and non-hydrostatic zenith delays (§5.1.3.1.2) along with the difference in the mapping functions expressed as equivalent height errors for both the hydrostatic (§5.1.3.1.3) and non-hydrostatic components (§5.1.3.1.4). Overall, all sections within §5.1.3.1 discuss the results for the

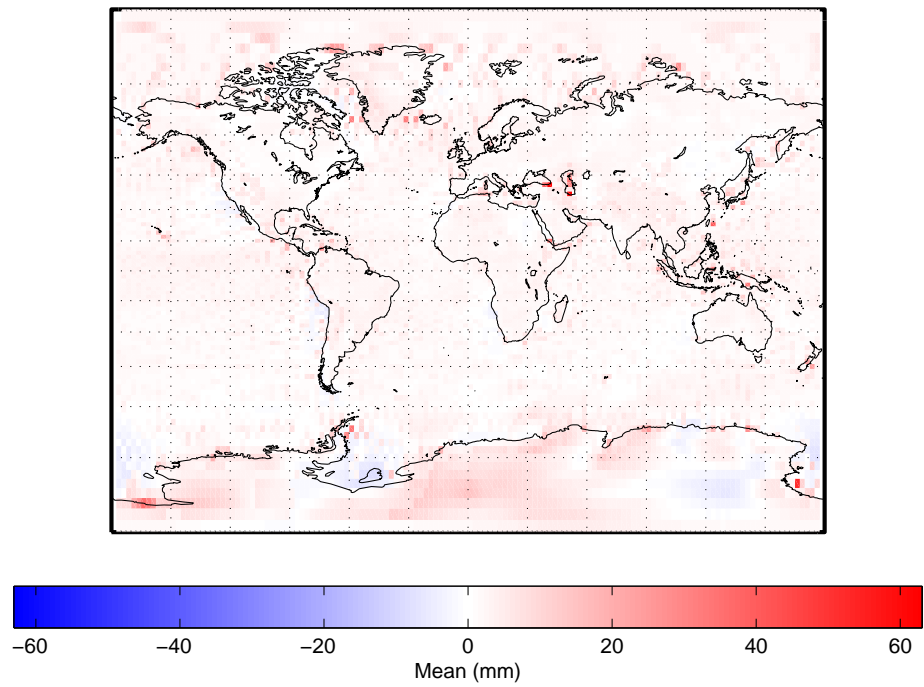
Table 5.1: Summary of grid comparisons and computed parameters for UNB-VMF1 validation

Product	Reference	Parameter	Epochs	Statistic
unbvmfG	vmfG	$zhd, zwd, eqHh, eqHw, ah, aw$	2001 to 2011	mean bias, abs, std
unbvmfG	vmfG	$zhd, zwd, eqHh, eqHw, ah, aw$	2012	mean bias, std, abs
unbvmfGcmc	vmfG	$zhd, zwd, eqHh, eqHw, ah, aw$	2012	mean bias, std, abs
unbvmfP	vmfG-FC	$zhd, zwd, eqHh, eqHw, ah, aw$	2012	mean bias, std, abs
unbvmfP	unbvmfGcmc	$zhd, zwd, eqHh, eqHw, ah, aw$	2012	mean bias, std, abs

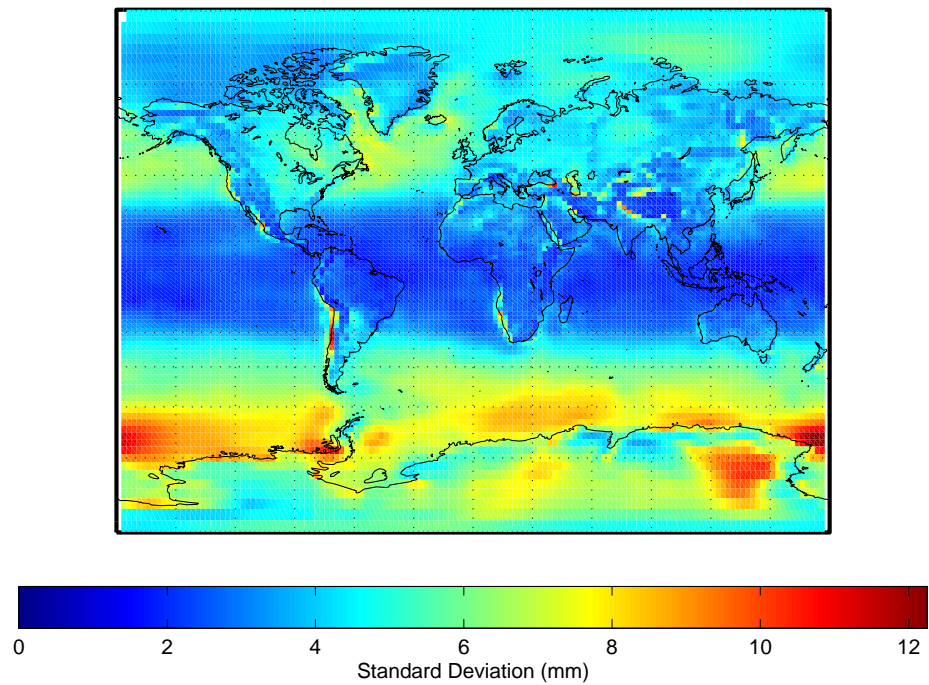
entire 11-year time period, where the yearly results can be found in Appendix C.

**5.1.3.1.1 Hydrostatic Zenith Delays** As noted in the previous section, a total of 11 years of grids for the unbvmfG product have been analyzed with respect to the vmfG product. The following figure, Figure 5.2, illustrates the 11-year combined mean bias and standard deviation of the difference in hydrostatic zenith delay. Figure 5.2(a) illustrates the combined mean bias in the hydrostatic delay, and 5.2(b) illustrates the combined standard deviation of the difference of the hydrostatic delay.

The combined mean bias shown in Figure 5.2(a) is predominantly positive across the globe with respect to hydrostatic zenith delays produced from the ECMWF (meaning NCEP’s hydrostatic delays are consistently larger than those from the ECMWF). The range of values do exceed 60 mm in some locations, but these are confined to regions over the oceans and the mean bias is predominately less than 10mm across the globe. To illustrate this point in greater detail, Figure 5.3 illustrates the spatial relationship of the maximum value of the difference in ray-traced hydrostatic zenith delay over 11-years. Evaluating the maximum absolute value of the difference in the hydrostatic zenith delay



(a) Combined Mean Bias Hydrostatic



(b) Combined Standard Deviation Hydrostatic

Figure 5.2: Combined difference in hydrostatic zenith delay for the years 2001 to 2011 for unbvmfG (NCEP) minus vmfG (ECMWF). (a) Combined mean bias (b) Combined standard deviation.

illustrates that the differences can reach up to 140 mm, but as Figure 5.2 illustrates, all of the large differences are located over the oceans and along the southern shores of the Black and Caspian Seas. Over land, differences can reach 80 mm as shown along the eastern coast of North America. Also evident from figure 5.3 is the fact that the largest absolute differences occur at higher latitudes as opposed to equatorial latitudes. These differences can be attributed due to the differences in the NWP. It was shown in Chapter 3 that the standard deviation of the difference in pressure (NCEP vs Site) was larger at the higher latitudes than equatorial. Since the hydrostatic zenith delay is highly dependent on the pressure, conclusions from the difference in pressure can be applied here. Therefore, the results in Figure 5.3 demonstrates that NCEP's Re-Analysis 1 is less capable in dealing with the increased atmospheric variability at the higher latitudes due its larger horizontal resolution in relation to the ECMWF.

Figure 5.4 is a plot of the histogram for all grid points over the 11-year time span. The histogram provides an efficient means in evaluating the expected difference in the ray-traced hydrostatic zenith delays and the frequency of large discrepancies. Over the course of 11 years the mean bias in hydrostatic zenith delays is on the order of 2.6 mm with a standard deviation of 5.6 mm at standard confidence. Therefore at  $3\sigma$  (at 99% confidence), the expectation is that the hydrostatic zenith delay computed with NCEP's Re-Analysis 1 dataset will be within  $\pm 16.9$  mm of the existing VMF1 service (based on ECMWF). Further, the large decimetre discrepancies illustrated in Figure 5.3 are highly unlikely to occur, with the percentage of discrepancies larger than 60 mm at 0.03% of all discrepancies over the 11 year time period. These results can be expressed as an equivalent height error due to the hydrostatic/non-hydrostatic separation. Taking the mapping function separation to be 0.6, the equivalent height error can then be computed multiplying the difference in zenith delay by 0.6 and then dividing by five (Boehm et al., 2006). Therefore, taking the contribution of both the bias and standard deviation at the  $1\sigma$  level, the overall global difference can reach 8.3 mm. Applying the rule of thumb from Boehm et al. (2006), the



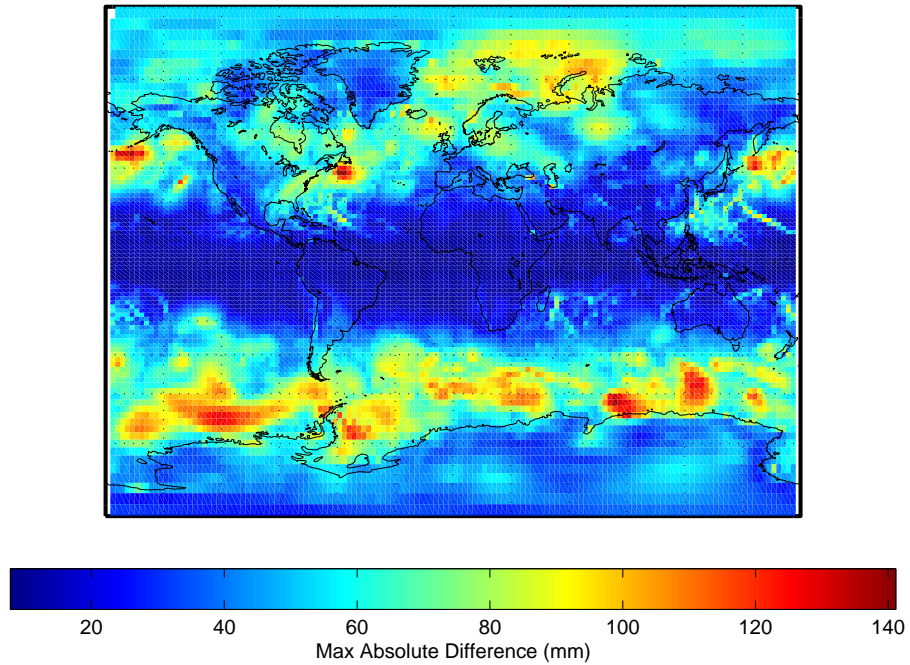


Figure 5.3: Maximum absolute values of the difference between unbvmfG (NCEP) and vmfG (ECMWF) hydrostatic zenith delays for the years 2001 to 2011.

equivalent height error is 1.0 mm.

Table 5.2 summarizes the global combined yearly mean bias and standard deviation as computed by equations 5.1 and 5.2. For table 5.2, the computation of the combined global yearly mean and standard deviation of the difference has been split into the 4 times daily epochs. What is most evident from Table 5.2 is the fact no one epoch outperforms the others as all the differences agree with each other at the sub-mm level.

**5.1.3.1.2 Non-Hydrostatic Zenith Delays** Figure 5.5 illustrates the difference in the non-hydrostatic (ray-traced) zenith delays between unbvmfG (NCEP) and vmfG (ECMWF) products. Figure 5.5(a) illustrates the 11-year combined mean bias and Figure 5.4(b) illustrates the 11-year combined standard deviation of the difference. Figure 5.5(a) illustrates

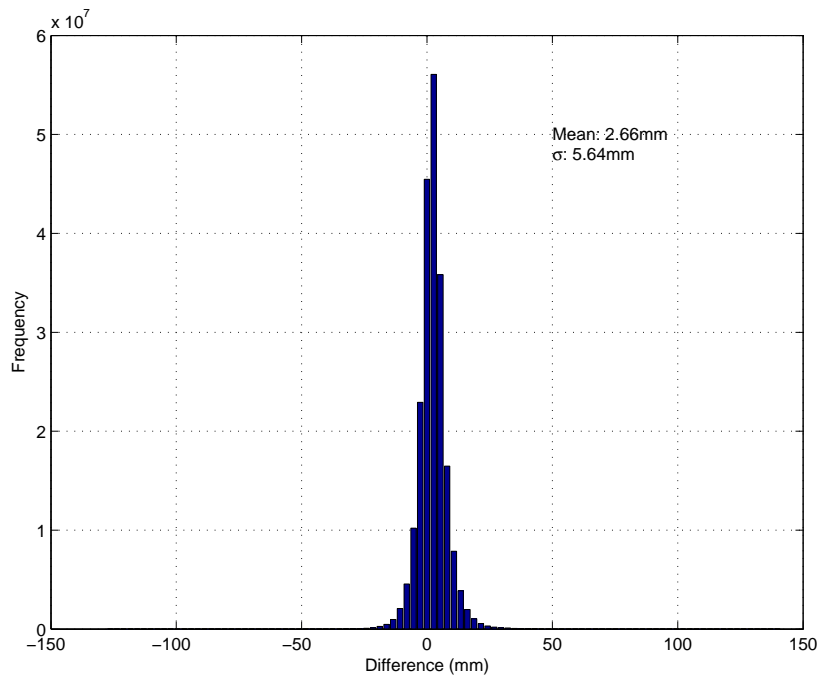


Figure 5.4: Histogram for the difference between unbvfmG (NCEP) and vmfG (ECMWF) hydrostatic zenith delays for the years 2001 to 2011.

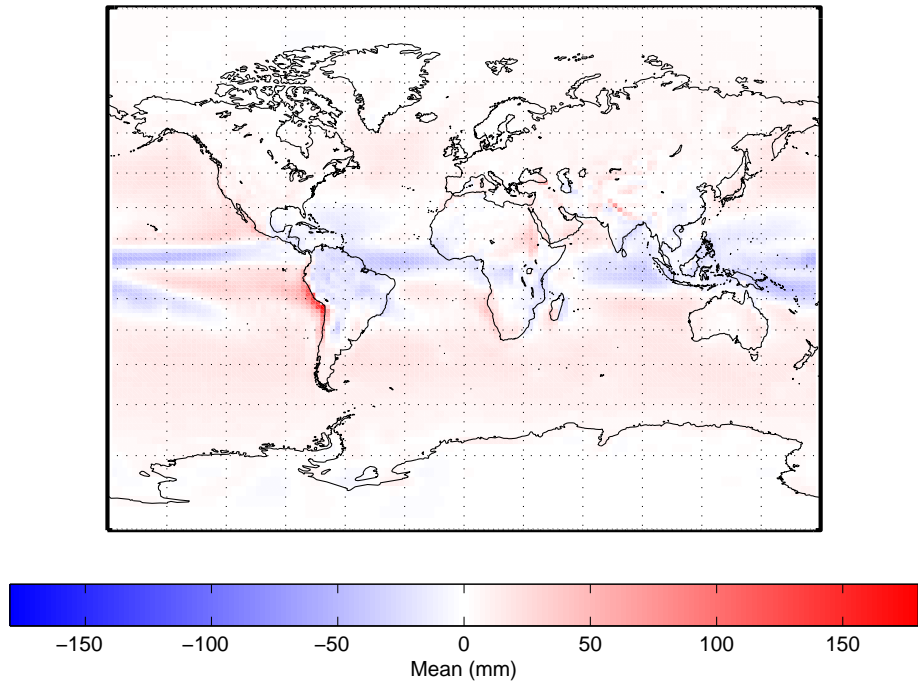
Table 5.2: Summary of global combined yearly mean and standard deviation separated by 4 times daily epochs for the difference in hydrostatic zenith delay. unbvfmG (NCEP) minus vmfG (ECMWF). (all values in millimetres).

	00H		06H		12H		18H	
Year	Mean	Std	Mean	Std	Mean	Std	Mean	Std
2001	2.4	5.6	2.5	5.6	2.3	5.5	2.3	5.6
2002	2.1	5.6	2.2	5.7	2.1	5.5	2.2	5.7
2003	2.5	6.2	2.7	6.2	2.5	6.1	2.6	6.2
2004	2.2	5.9	2.3	5.9	2.2	5.8	2.3	6.0
2005	2.3	5.4	2.3	5.4	2.2	5.3	2.3	5.5
2006	2.2	5.3	2.2	5.4	2.1	5.3	2.1	5.4
2007	2.4	5.4	2.4	5.5	2.3	5.3	2.3	5.4
2008	2.2	5.3	2.2	5.4	2.1	5.2	2.1	5.4
2009	2.3	5.4	2.3	5.5	2.1	5.3	2.2	5.5
2010	2.4	5.6	2.4	5.7	2.3	5.5	2.4	5.7
2011	2.5	5.9	2.5	5.9	2.4	5.8	2.5	5.9
Combined	2.4	5.6	2.4	5.7	2.3	5.6	2.3	5.7

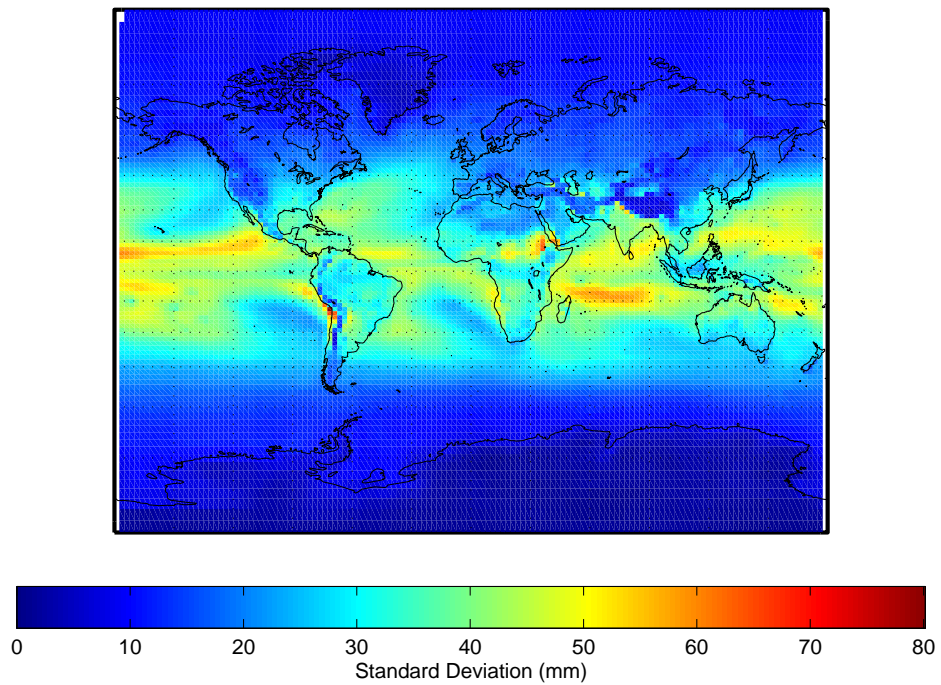
that the majority of the difference occurs in the equatorial region over the oceans. However, a local area exists along the western central coast of South America that exhibits an abnormally large discrepancy on the order of 170 mm. The explanation of this can be found in the discussion of the non-hydrostatic equivalent station height discrepancies (§5.1.3.1.4) as this pattern can be found in those results as well. Unfortunately, the small region around South America is masking the true distribution of non-hydrostatic zenith delays over the continents, but Figure 5.5(a) does indicate that the majority of discrepancies over land are within 30 mm. Lastly, Figure 5.5(b) illustrates that the largest standard deviation of the difference in non-hydrostatic zenith delays mainly occurs in equatorial to low-latitude regions. This is to be expected since the water vapour content of the atmosphere is maximum in equatorial regions (tropics) and decreases towards the polar regions.

Figure 5.6 is the plot of the maximum absolute differences of the non-hydrostatic zenith delay between unbvmfG (NCEP) and vmfG (ECMWF). Although, the overall global mean bias is well below 30 mm (Figure 5.5(a)), the region located around the western coast of South America can see differences up to 400 mm with the majority of continental locations seeing differences up to 200 mm. Figure 5.6 exhibits a similar trend to that of Figure 5.5(b), where the largest absolute differences occur in the equatorial regions to low-latitudes with the polar regions showing the smallest differences. Figure 5.7 plots the histogram of all grid points from the years 2001 to 2011 for the difference in non-hydrostatic zenith delays. From Figure 5.7, the total 11-year combined mean and standard deviation is 4.4 mm and 30.2 mm respectively. Therefore, taking  $3\sigma$  of the combined standard deviation would indicate at 99% confidence that the difference in the non-hydrostatic zenith delays are within  $\pm 90.6$  mm.

In contrast with the hydrostatic zenith delay results, the range of values shown in Figure 5.4(a) for the non-hydrostatic zenith delay differences are more than two times larger than those for the hydrostatic component (shown in Figure 5.2(a)). Further, the



(a) Combined Mean Bias Non-Hydrostatic



(b) Combined Standard Deviation Non-Hydrostatic

Figure 5.5: Difference in non-hydrostatic zenith delay for the years 2001 to 2011 for unbvmfG (NCEP) minus vmfG (ECMWF). (a) Combined mean bias (b) Combined standard deviation.

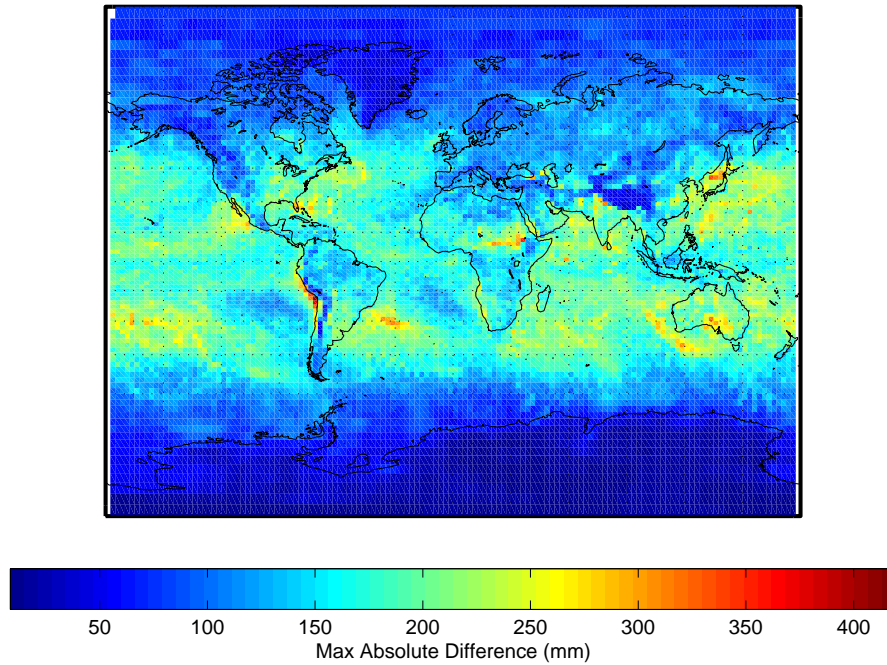


Figure 5.6: Maximum absolute values of the difference between unbvmfG (NCEP) and vmfG (ECMWF) non-hydrostatic zenith delays for the years 2001 to 2011.

range of values of the non-hydrostatic standard deviation is approximately eight times larger than that of the hydrostatic component. This correlates well with the overall 11-year global combined mean bias and standard deviation where the differences in the non-hydrostatic components are two times and six times larger for the mean and standard deviation respectively. The source of these differences can be two possibilities: (a) the ray tracing, or (b) differences in the NWP. A ray-tracing benchmarking campaign by Nafisi et al. (2012) demonstrated the variability due to ray-tracing techniques by the use of differing ray-tracing packages using the same NWP source dataset. Zenith delays were compared at two stations using different ray tracing packages (including UNB's), and the differences were on the order of mm for both the hydrostatic and non-hydrostatic zenith delays. Differences exhibited here are on the order of cm, so the ray-tracing is not the

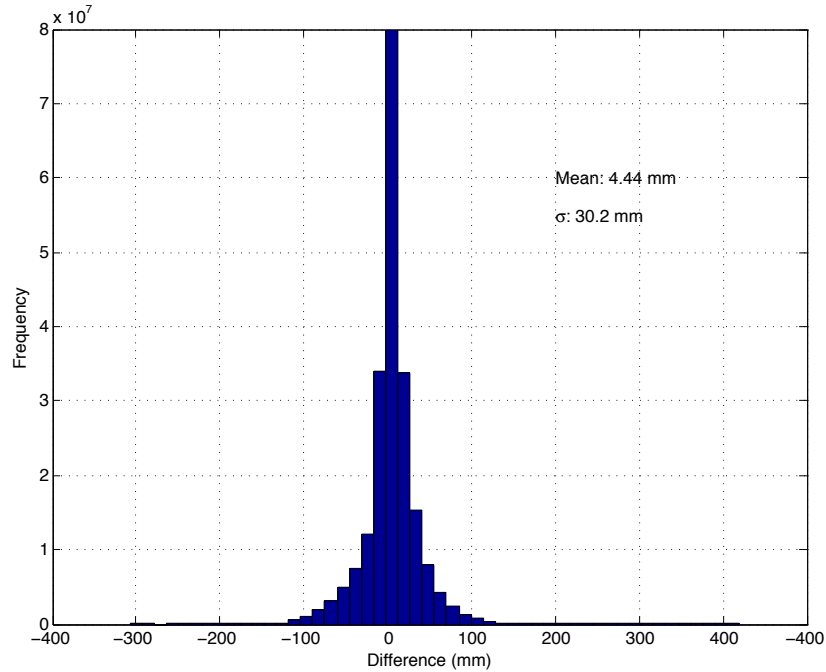


Figure 5.7: Histogram for the difference between unbvmfG (NCEP) and vmfG (ECMWF) non-hydrostatic zenith delays for the years 2001 to 2011.

cause, it is due to the differences in the NWPs.

Although the humidity has some effect on the computation of the hydrostatic refractivity, it is small in comparison with the effect it has on the non-hydrostatic component, which is why there is such a stark difference between the two quantities. It is well known that the water vapour content in the atmosphere is highly variable both in space and time, and these results demonstrate the difficulty in achieving a consistent prediction of humidity between differing NWPs. As was shown in Chapter 3, the differences in extracted specific humidity between NCEP's Re-Analysis 1 product and CMC's GDPS did not differ substantially even though CMC's horizontal resolution is approximately four times finer. The use of ray-traced non-hydrostatic delays at the observation level are not sufficient to be used in achieving mm-level height solutions. Urquhart (2011b) demonstrated this by showing that the use of ray-traced delays instead of estimating the non-hydrostatic component in the computation of positions resulted in a degradation of the height solution from

Table 5.3: Summary of global combined yearly mean bias and standard deviation separated by each 4 times daily epochs for the difference in non-hydrostatic zenith delay. unbvmfG (NCEP) minus vmfG (ECMWF) (all values in millimetres).

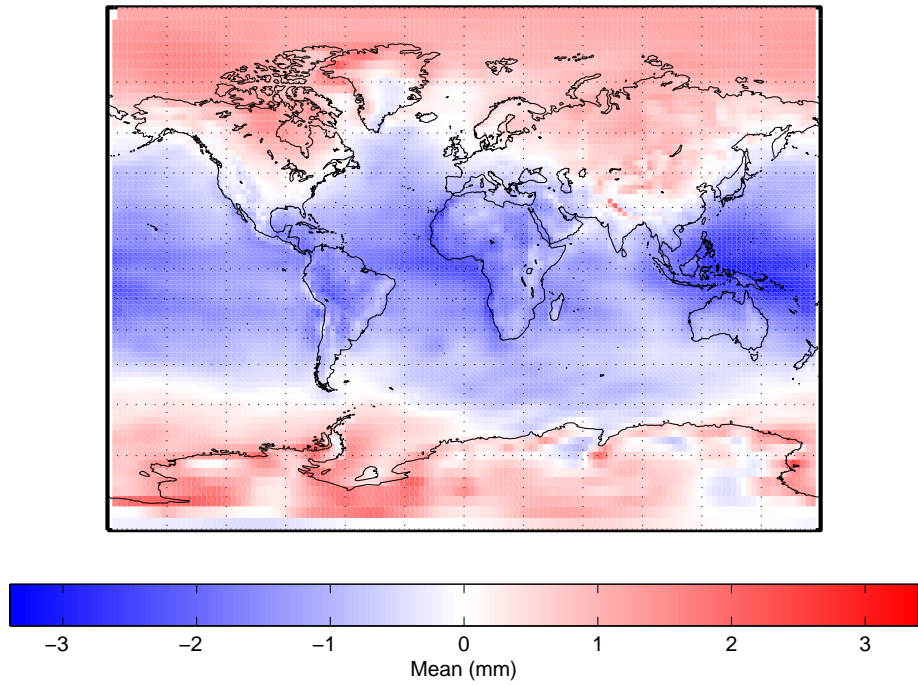
Year	00H		06H		12H		18H	
	Mean	Std	Mean	Std	Mean	Std	Mean	Std
2001	-1.4	30.4	-1.5	30.6	-1.4	30.1	-1.6	30.7
2002	3.3	30.1	3.2	30.4	3.3	29.9	3.1	30.7
2003	4.0	31.2	4.2	31.3	4.0	30.8	4.1	31.6
2004	3.7	30.1	4.0	30.0	3.7	29.8	4.0	30.3
2005	5.0	29.5	5.4	29.4	5.0	29.1	5.4	29.6
2006	4.7	29.2	5.2	29.0	4.7	28.9	5.2	29.3
2007	5.2	29.5	5.8	29.2	5.3	29.1	5.8	29.5
2008	4.5	29.6	4.9	29.5	4.5	29.3	4.9	29.8
2009	5.0	30.6	5.4	30.5	5.0	30.3	5.3	30.8
2010	6.2	31.4	6.5	31.3	6.2	31.0	6.4	31.5
2011	6.3	30.4	6.6	30.2	6.2	30.1	6.5	30.5
Combined	4.7	30.3	4.5	30.3	4.3	29.9	4.5	30.5

mm-level to cm-level.

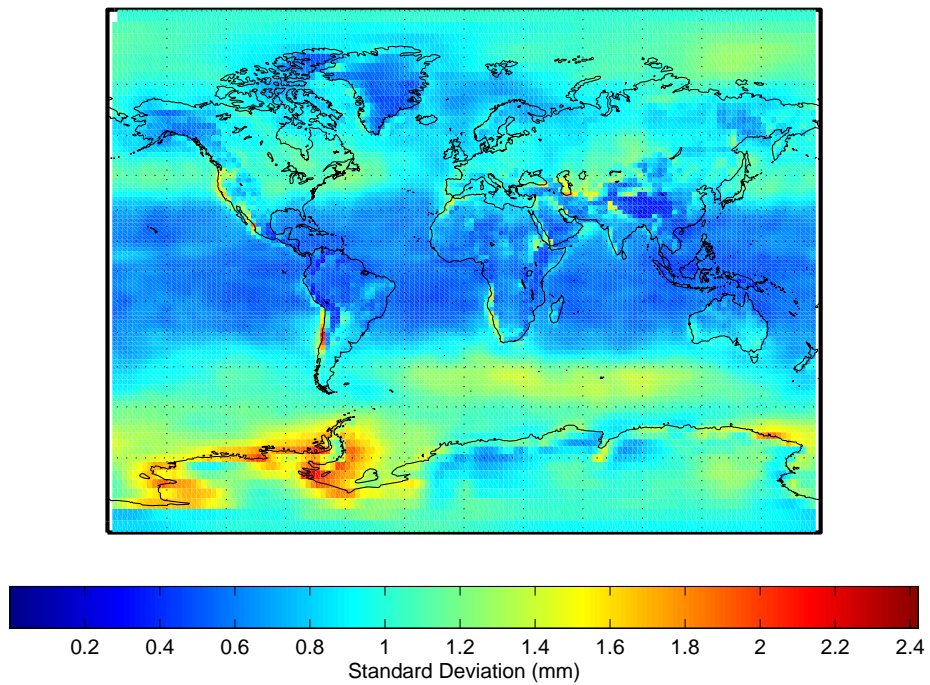
Table 5.3 summarizes the combined global mean bias and standard deviation of the difference in the non-hydrostatic zenith delays. As with the hydrostatic delays, all epochs agree with each other at the sub-mm level in the context of the combined mean standard deviation. However, the combined mean bias for the year 2001 shows a negative bias, which is in contrast with all other years that are positive. The cause of this difference is unknown, but it is speculated to be due to differences in the NWP (NCEP vs ECMWF). Also, the years 2010 and 2011 exhibit an increased mean bias as compared to the other years in the time series. All epochs for the years 2010-2011 (00H-18H) show a mean difference greater than 6 mm as compared to a mean difference of approximately 5 mm or less for all other years. This behaviour is also in contrast with the hydrostatic zenith delay differences which are very consistent across the entire time series (see Table 5.2). Again, the reason for this is most likely due to differences in the NWP.

**5.1.3.1.3 Hydrostatic Equivalent Height Error** The following figures illustrate the difference in mapping functions expressed as an equivalent height error as computed by the description in §5.2.1. Figure 5.8 illustrates the equivalent height error due to the hydrostatic component as computed by equations 5.1 and 5.2. Figure 5.8(a) is the combined 11-year mean bias and Figure 5.8(b) is the combined 11-year standard deviation of the difference. Overall, Figure 5.8(a) indicates that the largest combined mean bias is on the order of -3.3 mm and that it occurs over the Indonesian/Philippines region, however the majority of locations on the globe are within  $\pm 1$  mm. Figure 5.8(b) indicates that the maximum combined standard deviation over the 11-year period is on the order of 2.4 mm, with the majority of locations on the globe less than 1.2 mm. Plotting the maximum absolute value of the equivalent height error, as shown in Figure 5.9, allows for the appreciation of all potential possibilities. Figure 5.9(a) illustrates that although the majority of grid points in Figure 5.8(a) are within  $\pm 1$  mm, differences in the mapping functions can cause equivalent height errors at the cm level. Additionally, Figure 5.9(a) indicates that the equivalent height error can reach up to 18 mm, but these large differences occur only in the years from 2002 to 2004. Figure 5.9(b) illustrates the maximum absolute equivalent height error for the years 2002-2004, and it is evident from this figure that the majority of the differences originate from these epochs as the spatial patterns match very well between 5.9(a) and (b). For all other epochs in the time series (2001, 2005-2011), the maximum absolute equivalent height error is less than 8 mm (all plots for each individual year can be found in Appendix C). Further, a histogram for all equivalent height errors for all grid points for the 11-year time series is plotted in Figure 5.10. The 11-year histogram demonstrates that the frequency of cm-level equivalent height errors occurring are of a very low probability equating to just 0.003% of all grid points over 11 years. The overall combined global mean bias and standard deviation is -0.7 mm and 1.3 mm respectively. Therefore, the expectation is that the global difference in the mapping functions as expressed as an equivalent height error agree to  $\pm 3.9$  mm at the  $3\sigma$  level. Lastly, Table 5.4 summarizes the



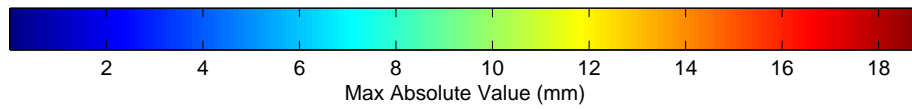
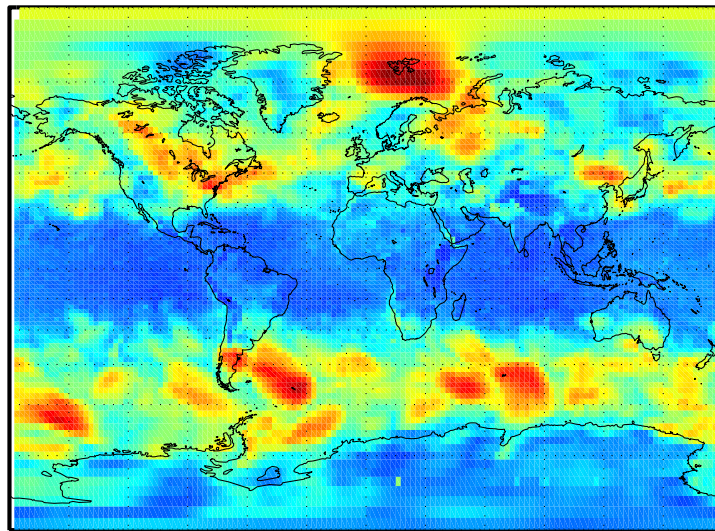


(a) Combined Mean Bias

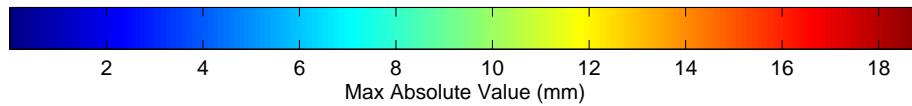
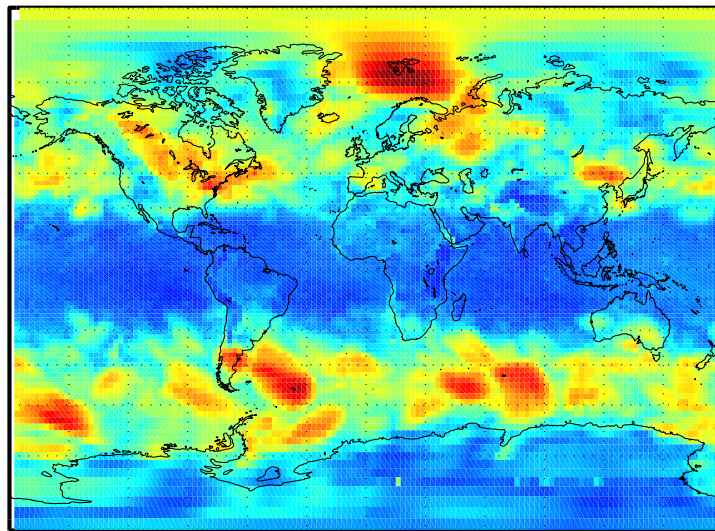


(b) Combined Standard Deviation

Figure 5.8: Equivalent height error due to the hydrostatic mapping function for the years 2001 to 2011 for unbvmfG (NCEP) minus vmfG (ECMWF). (a) Combined mean bias (b) Combined standard deviation.



(a) 2001 to 2011



(b) 2002 to 2004

Figure 5.9: Maximum absolute difference of the equivalent height error due to the hydrostatic mapping function for unbvmfG (NCEP) minus vmfG (ECMWF). (a) 2001 to 2011 (b) 2002 to 2004.

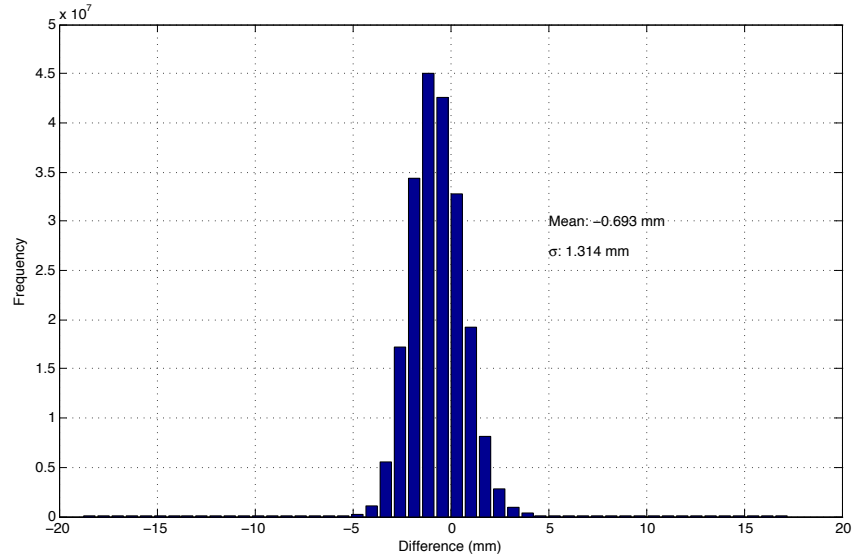


Figure 5.10: Histogram for the difference between unbvmfG (NCEP) and vmfG (ECMWF) expressed as an equivalent height error for the years 2001 to 2011.

yearly combined global mean bias and standard of the difference in the mapping functions as expressed as an equivalent height error. The values have been separated into the 4 times daily epochs, where all combined global values agree across the entire time series at the sub-mm level and at each of the 4 times daily epochs.

Returning to Figure 5.8(a), the dominant characteristic exhibited is the strong latitude dependent bias. This latitude dependent bias begins as a negative bias in the equatorial region, which transitions to a zero bias in the high latitude regions that finally settles on a positive bias in the polar regions of the globe. The magnitude of this bias is approximately on the order of 2 mm. It is hypothesized that the source of this latitude dependent bias can be attributed to differences in the raytracing scheme employed at the existing VMF1 service and at UNB. Urquhart (2011) demonstrated that differences in the definition of the radius of curvature can cause a bias up to 8 mm in height at the equator when comparing site specific VMF1 mapping functions produced with a gaussian mean radius and constant radius to mapping functions defined by 3D ray traces. This has also been confirmed by Nafisi et al. (2012), which illustrated the effect of the radius of curvature the Earth on

Table 5.4: Summary of global combined yearly mean bias and standard deviation separated by each 4 times daily epochs for the equivalent height error due to the hydrostatic mapping function. unbvmfG (NCEP) minus vmfG (ECMWF) (all values in millimetres).

Year	00H		06H		12H		18H	
	Mean	Std	Mean	Std	Mean	Std	Mean	Std
2001	-0.5	1.4	-0.4	1.4	-0.3	1.4	-0.5	1.4
2002	-0.5	1.3	-0.6	1.3	-0.6	1.3	-0.7	1.3
2003	-0.7	1.3	-0.8	1.3	-0.7	1.4	-0.8	1.5
2004	-0.7	1.3	-0.8	1.3	-0.7	1.3	-0.8	1.4
2005	-0.7	1.2	-0.8	1.2	-0.7	1.3	-0.9	1.3
2006	-0.6	1.2	-0.6	1.2	-0.6	1.3	-0.7	1.2
2007	-0.5	1.2	-0.6	1.2	-0.6	1.2	-0.6	1.2
2008	-0.6	1.2	-0.7	1.2	-0.6	1.3	-0.7	1.3
2009	-0.7	1.2	-0.7	1.2	-0.7	1.3	-0.8	1.2
2010	-0.7	1.2	-0.8	1.2	-0.8	1.2	-0.8	1.2
2011	-0.6	1.3	-0.7	1.2	-0.7	1.3	-0.7	1.3
Combined	-0.6	1.3	-0.7	1.3	-0.6	1.3	-0.7	1.3

slant factor differences with respect to Eulers formula. As noted in Chapter 4, the UNB-VMF1 products are produced with a mean gaussian radius of the Earth, and the existing VMF1 service produces products with a constant radius of the Earth (Boehm, 2004). To test this assertion, a comparison was made between two UNB-VMF1 products, namely unbvmfG and unbvmfGcmc. These two products have been produced utilizing the same ray-tracing scheme (spherically osculating with a mean gaussian radius of the Earth), but with different source NWP datasets, so the expected difference between the two products should not exhibit any latitude dependent bias. The differences in these two products have been expressed as an equivalent height error and are plotted in Figure 5.11 for the dates January 1st to August 30th 2012. Figure 5.11 illustrates that the latitude dependent bias does not exist for these products with respect to each other.

As a more definitive test, the UNB-VMF1 product (unbvmfG) has been re-computed using a constant radius in the ray-tracing scheme and compared to the product from the existing VMF1 service. For this test, the UNB ray-tracer employed a spherically oscu-

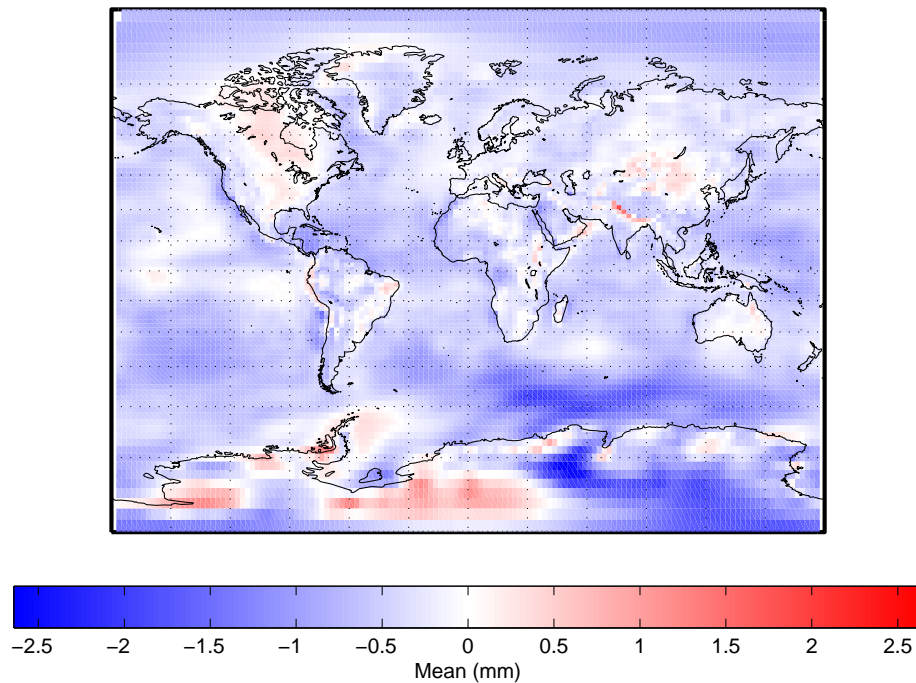


Figure 5.11: Difference in the hydrostatic mapping functions expressed as an equivalent height error for unbvmfG (NCEP) minus unbvmfGcmc (CMC). Epoch: January 1st to August 30th 2012.

lating atmosphere as in the original product, but the radius of the osculating sphere was defined as a constant radius instead of a mean gaussian<sup>1</sup>. The test timeframe encompassed the dates August 1st to August 30th 2012 inclusively. Again, the parameter of comparison is the difference in the mapping functions expressed as an equivalent height error. The results from this test are presented in Figure 5.12, which demonstrates that the latitude dependent bias has been removed. Therefore, based on these two tests it can be concluded confidently that the latitude dependent bias is due to the definition of the radius of Earth in the raytracing schemes employed.

A closer inspection of Figure 5.8(b) reveals that there are several isolated locations on the globe that exhibit an increased standard deviation, namely the Pacific northwest in North America, the western coast of South America, the southwest coast of Africa (also

<sup>1</sup>The UNB-VMF1 product, unbvmfG, has been produced with a radius of 6378.1 km and the existing VMF1 is produced with a radius of 6378 km (Boehm, 2004).

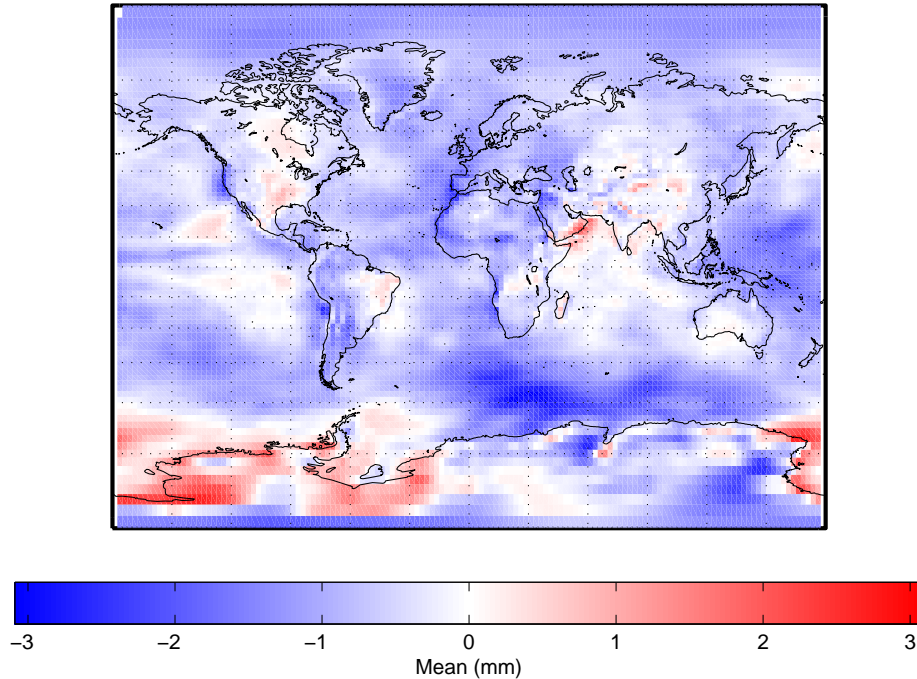


Figure 5.12: Difference in the hydrostatic mapping functions expressed as an equivalent height error for UNB-VMF1 (NCEP) minus VMF1 (ECMWF) where a constant radius of the Earth has been used for the UNB-VMF1 product. Epoch: August 1st to August 30th 2012.

the northwest coast of Morocco), and the southern shores of the Caspian Sea. All of these locations share a common feature in that they are all locations where a coast interacts with land that varies topographically (i.e. mountainous regions). These regions can also occur inland, such as along the front of the Himalayas as this is also an area where the terrain transitions from a flatter topography to a more mountainous one. A potential cause of these regions of increased variability can be related to the differences in the source datasets in which the delays are ray traced through - the NWP. The following paragraphs examine this assertion.

The most obvious difference in the NWP (NCEP and ECMWF) is the difference in the horizontal resolution. From 2003 onwards, the existing VMF1 service has implemented operational ECMWF datasets with a horizontal resolution of approximately 0.3



degrees with a vertical resolution of 21 pressure levels (Boehm et al, 2004). In contrast, NCEP's Re-Analysis 1 dataset is produced with a  $2.5 \times 2.5$  degree horizontal resolution with only 17 pressure levels (only 10 pressure levels for the humidity parameter) (Kalnay, et al., 1996). If the land-sea masks<sup>2</sup> are plotted for each of the respective data sources, the effect of the horizontal grid resolution can be better appreciated. Figure 5.13 plots the land-sea masks for an ECMWF dataset, the CMC (GDPS) and NCEP Re-Analysis 1 for the southwestern coastal region of South America along the Andes. NCEP's Re-Analysis product is shown in Figure 5.13(b), which illustrates the difficulty the NCEP dataset has in defining the coastline with respect to the other datasets that are produced with a finer resolution.

Figure 5.13 illustrates that in some models, a location may be considered to be an sea point and in others it may be classified as a land point. For example, station CONZ is completely located in a region classified as the sea whereas in the CMC and ECMWF NWP's the station is located on land. These differences in the land-sea mask have implications on the sub-grid model parameterizations since the land/atmosphere interface is very different from those of a land/sea interface. The delays caused by the troposphere will be predominantly influenced by the atmospheric conditions close to the surface, so differences in the NWP's prediction in this region of the atmosphere will have the largest impact on the final ray-traced delay. In particular, the separation of solar radiation and long wave radiation (infrared radiation emitted by the atmosphere) into storage and sensible/latent heat fluxes has a direct affect on the meteorological parameters such as humidity and temperature near the surface (Stensrud, 2007). These sensible/latent heat fluxes are highly variable spatially, which are affected by the ground surface conditions such as soil/vegetation type and soil moisture (Stensrud, 2007). Further, these fluxes provide lower-boundary conditions to the boundary-layer parameterization of turbulence<sup>3</sup>, which distributes heat and moisture

---

<sup>2</sup>A land-sea mask is defines the percentage of the grid square that is either land or water (where 1 indicates land and 0 indicates sea). Typically if the grid point is greater than 50% land it is classified as land otherwise it is classified as sea (UK Met Office, 2012)

<sup>3</sup>The boundary layer is that part of the atmosphere that is directly affected by by the Earth's surface. The

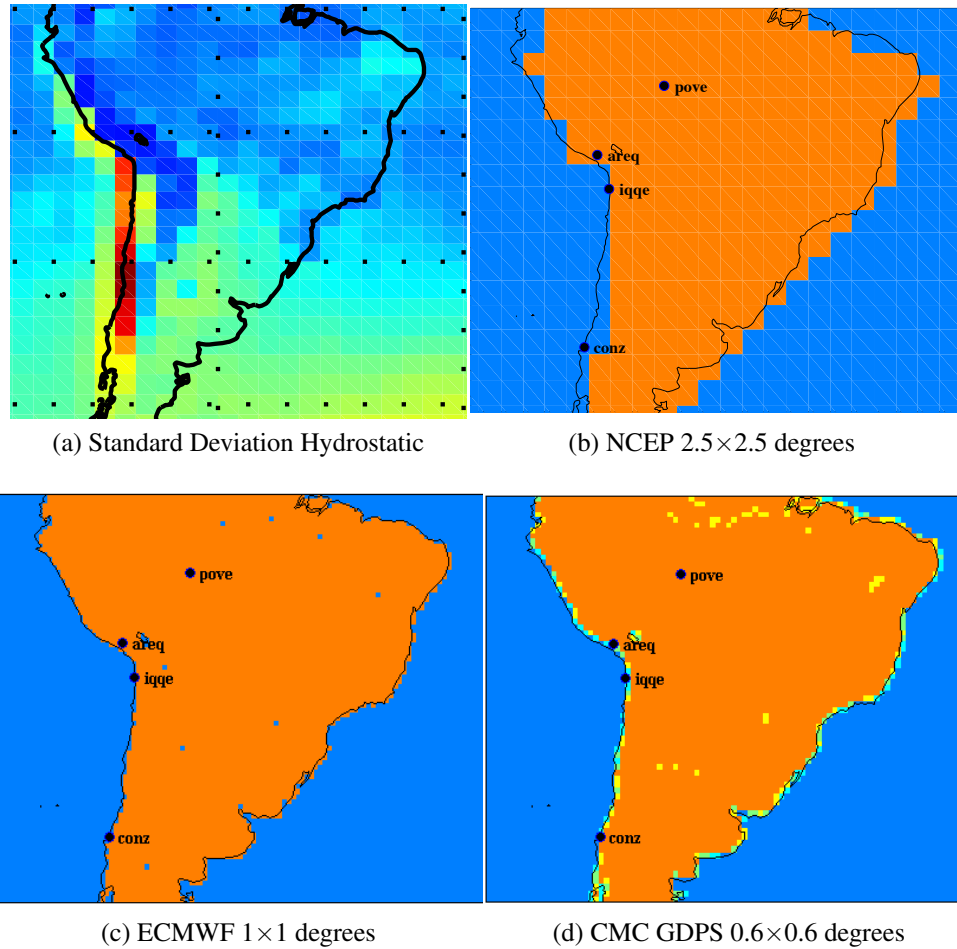


Figure 5.13: Land-sea masks for (b) NCEP Re-Analysis 1 (unbvmfG) (c) ECMWF and (d) CMC GDPS (unbvmfGcmc). Illustrates the strong spatial correlation of the increased standard deviation for the equivalent height error of the hydrostatic component (as shown in (a)) due to the differences in land-sea masks.

through the lower atmosphere (Warner, 2011). Over water, the atmospheric circulation is further complicated since the wind stresses cause currents, waves, and vertical mixing of the water that affects the surface temperature and evaporation (Warner, 2011). Figure 5.14 plots the difference in the hydrostatic refractivity for station COPO which resides in this region of increased variability along the western coast of South America. The refractivity

boundary layer extends from the ground to approximately 1500 m (Coiffier, 2011). The parameterization of turbulence is important for the prediction of temperature, humidity, and wind in the boundary layer (Berg et al. 2005). Truncating a ray-trace for the hydrostatic component of the delay at station PWEL indicates that approximately 15% of the total hydrostatic zenith delay occurs in the first 1500 m of the atmosphere.



profiles were extracted from NCEP's Re-Analysis 1 dataset and CMC's (GDPS) on May 15th, 2012 at 12UTC<sup>4</sup>. Figure 5.14(a) and 5.14(b) illustrates that the selected point is considered land in the CMC model and is considered sea in the NCEP model. The difference in refractivity plotted in Figure 5.14(c) shows that the majority of the difference in the hydrostatic refractivity occurs at heights less than 4 km (predominantly in the boundary layer). So whether the grid point is land or sea can have a significant impact on the meteorological conditions in the region of the atmosphere causing the largest delays. These differences in the land-sea mask do correlate well with the location of the regions of increased standard deviation (Figure 5.13(a) and (b)), but increased standard deviations do not occur at all locations where there are large land sea mask differences (e.g. the southern Mediterranean - not shown). Therefore, an additional effect in these regions could be causing the increased variability.

An examination of the various NWP's model orography (mean topography) can help to provide some further insight into the cause of these regions of increased variability. Figure 5.15 is a plot of the surface orography used by NCEP's Re-Analysis 1 dataset. Two distinguishing features of Figure 5.15 is the orographic noise along the western South American coast and the steep orographic gradients that extend into the oceans from the coastlines. First, the orographic noise along the western coast of South America can also be seen along the Pacific northwest of North America and along the southwest coast of Africa - all locations that exhibit the regions of increased standard deviation. This noise is a consequence of the fact that NCEP's Re-Analysis 1 dataset is a spectral based model (see Chapter 2). The orography is usually supplied to the model as a grid point dataset, so it must be transformed to the spectral domain. Typically the number of spectral coefficients used to represent the model field is fewer than the number of grid points than the supplied orography, which truncates the spectrum of the orography and causes this orographic noise called the Gibbs effect at locations where there is a steep change in the topography (Rutt,

---

<sup>4</sup>CMC was used instead of the ECMWF since data from the ECMWF is unavailable and a similar pattern occurs when comparing NCEP based products to products based on the CMC dataset - see Appendix C.

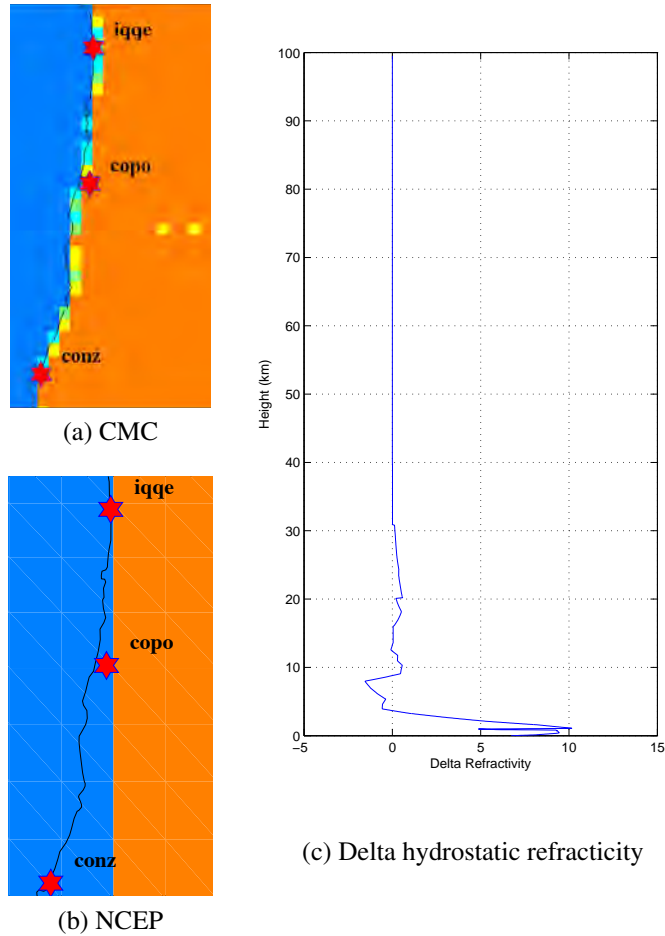


Figure 5.14: Difference in hydrostatic refractivity profile between NCEP Re-Analysis 1 and CMC (GDPS) - (NCEP minus CMC) - on May 15th, 2012 12UTC for station COPO located at an elevation of 479 m.

2003). Each of the locations identified as having an increased standard deviation share the common feature that there is a steep change in topography as the sea interfaces with the coastal mountains. The result of the Gibbs effect is an oscillating orography that is not an accurate representation of the actual topography. In the vicinity of these steep topographical locations, this oscillation is dampened as the distance from the topographic disturbance increases<sup>5</sup>. In coastal areas, elevated ocean grid points act as spurious heat sources (Rutt, 2003), and in general, the Gibbs effect causes problems with precipitation

<sup>5</sup>This Gibbs effect was addressed in NCEP's Re-Analysis 2 dataset to prevent Gibbs-like precipitation and sensible/latent heat fluxes over the oceans near steep topography, which does not exhibit the same phenomena (Kanamitsu et al, 2002)

forecasts, and with the simulation of winds near the surface (Bouteloup, 1995).

Figure 5.16 is a cross-section across Figure 5.15 at a latitude of 30°S, which crosses the regions of increased standard deviation along South America and Africa. From left to right are the continents of South America, Africa and Australia respectively. What is most evident is the obvious oscillation of the orography in the transition from the sea to land in the NCEP dataset (plotted in blue). As a comparison, CMC's GDPS is also plotted (red) and NCEP's Re-Analysis land/sea mask (dashed black). The dataset from CMC illustrates a more accurate representation of the topography since the NCEP dataset exhibits elevated ocean grid points along South America and Africa on the order of 415 m and 355 m above sea level respectively.

The second characteristic identified with regards to Figure 5.15 was the steep orographic gradients that extend into the coastline. The gradients extend into the coastline partly due to the Gibbs effect, but it can also be attributed to the fact that a mean orography is used for NCEP's model (Kanamitsu et al, 1991). Figure 5.15 illustrates this point for the African continent (middle) where there is a steep change in the topography, but no Gibbs effect on the western coast, yet the ocean grid point next to the land grid point is 355 m above sea level. Therefore, taking the mean orography for the grid square will have the consequence of raising the elevation of grid points next to mountain ranges. This effect will be more pronounced with NWP's that have larger horizontal resolutions, since larger areas will be used for the mean orography. A second consequence of taking the mean orography will be the lowering of mountain elevations. Also illustrated by Figure 5.15, is the fact that the mountain peaks along the 30°S parallel are lower than those of the CMC. This is also due to the fact that a mean orography has been implemented for the NCEP dataset.

Bouteloup (1995), Navarra et al. (1994) and Rutt (2003) have pointed out that these orographic issues can cause problems with the simulation of winds near the surface and elevated ocean points can act as spurious heat sources. The expectation would be to see

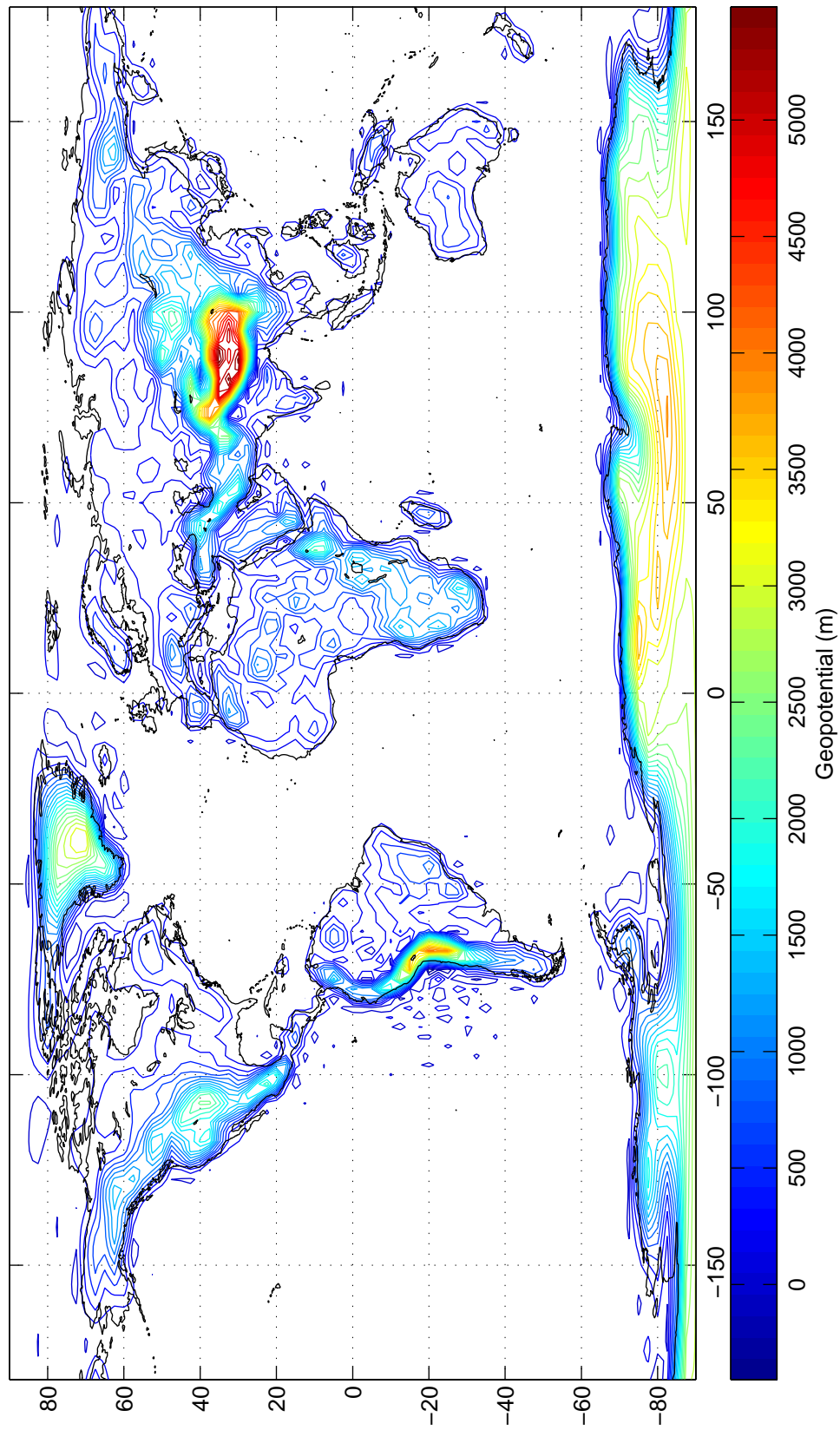


Figure 5.15: NCEP Re-Analysis 1 orography given by the surface geopotential height.

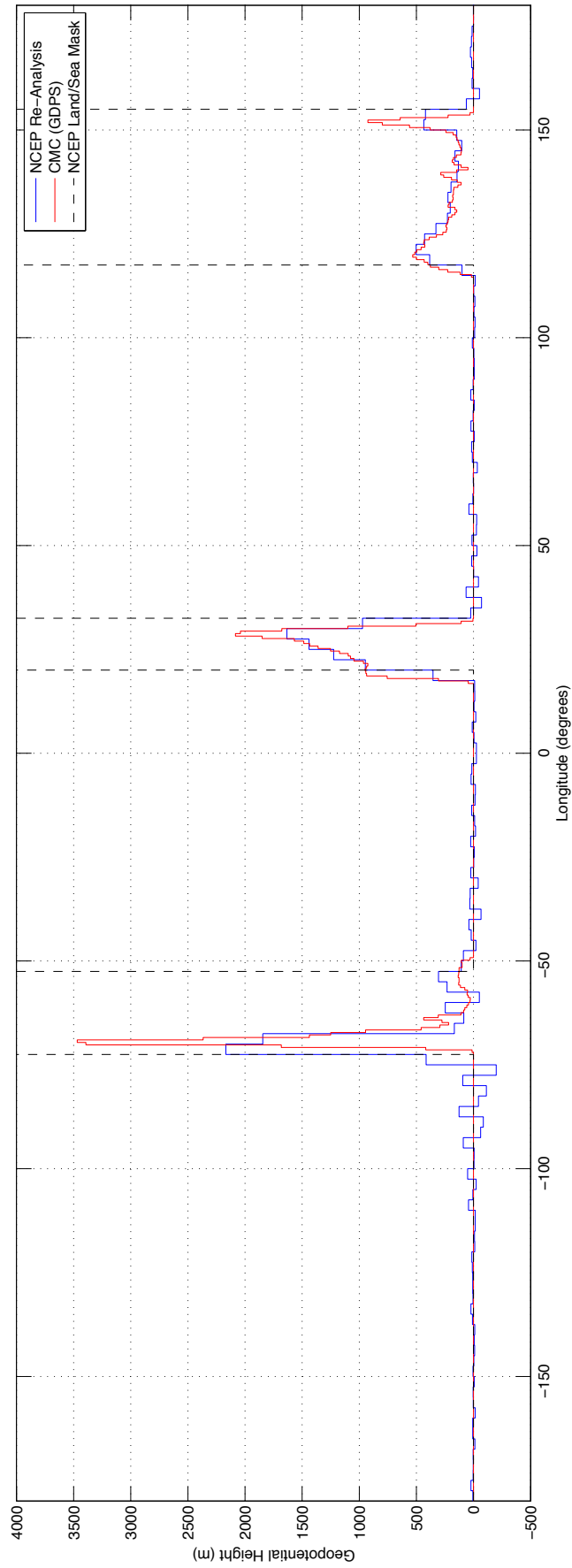


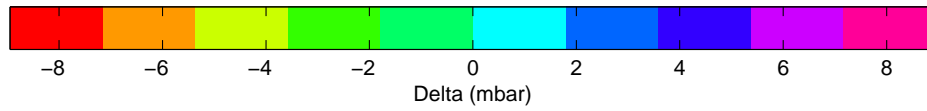
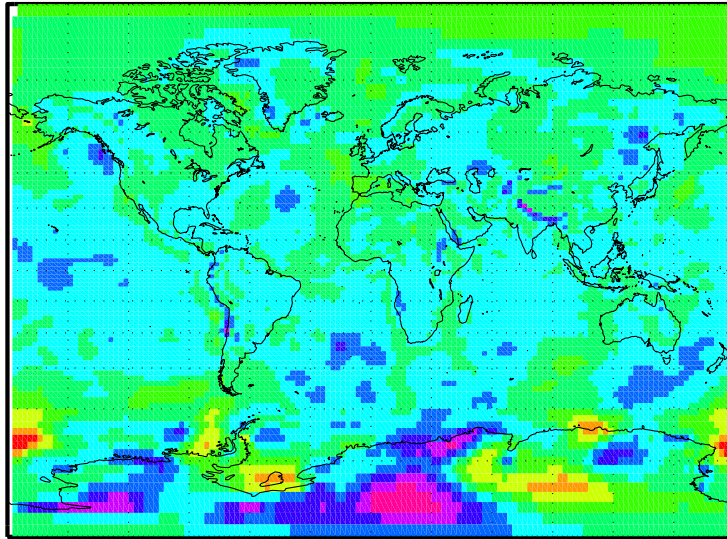
Figure 5.16: Cross-section at 30°S from NCEP Re-Analysis 1 and CMC (GDPS) surface geopotential height field

larger differences in meteorological parameters in the noted regions of increased standard deviation for pressure and temperature<sup>6</sup>. To investigate this further, a comparison has been made between NCEP's Re-Analysis 1 dataset and CMC's GDPS dataset for the three meteorological parameters that make up the computation of refractivity (see Chapter 2). The pressure, temperature and specific humidity have been extracted from each the noted NWP's and differenced for the comparison (NCEP minus CMC). Since the effect of the differences of these parameters will be most significant to the computation of refractivity at topographic elevations it makes sense to evaluate the differences at the specified heights near the surface. Figure 5.17 illustrates the mean differences between pressure and temperature (specific humidity shown in figure 5.20) between NCEP's Re-Analysis 1 and CMC's GDPS for one week starting April 15th and ending April 21st 2012. The pressure, temperature and specific humidity were extracted at the height of the grid point defined by *orography.ell* and are plotted at the UNB-VMF1 grid resolution defined in Chapter 4.

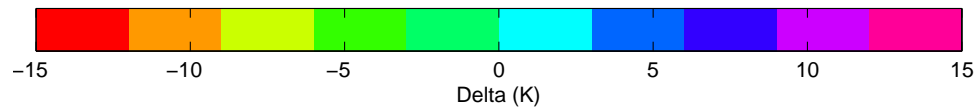
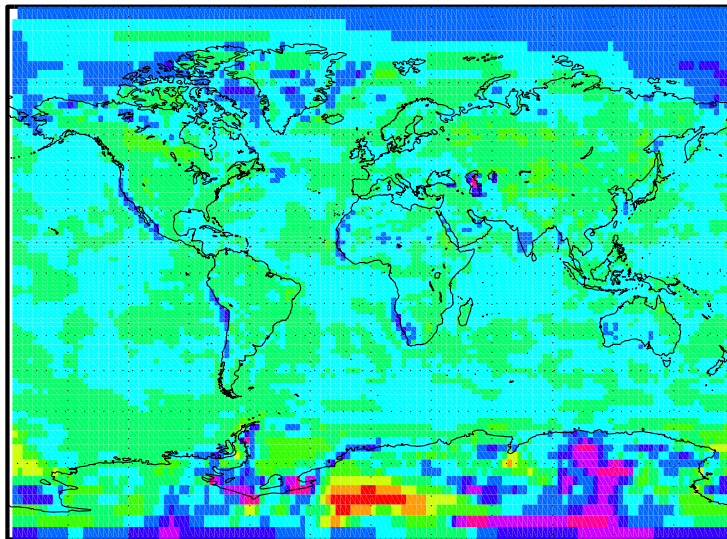
Figure 5.17 reveals that there is a strong correlation to the spatial relationship of the difference in pressure and temperature to that of the regions of increased standard deviation. The patterns associated with the difference in temperature are the most similar in the western coastal regions (pressure is also similarly large along the western coast of South America), and indicate that the temperature from NCEP's Re-Analysis 1 dataset is consistently up to 5°K warmer than the results from the CMC. Since these locations are predominantly ocean grid points and have demonstrated to have non-zero elevations at the grid points next to land (or issues due to the Gibbs effect), it would seem to reinforce the idea of spurious elevated heat sources. Navarre (1994) has pointed that typically in spectral models an adiabatic lapse rate would be used to modify the sea surface temperature to a local terrain height to avoid these issues with elevated heat sources. However, the documentation for NCEP's Re-Analysis project (Kalnay, 1996) does not refer to any corrections for this effect. Locations such as the front along the Himalaya shows that pressure

---

<sup>6</sup>temperature gradients will drive pressure gradients which in turn drive the winds.



(a) Pressure



(b) Temperature

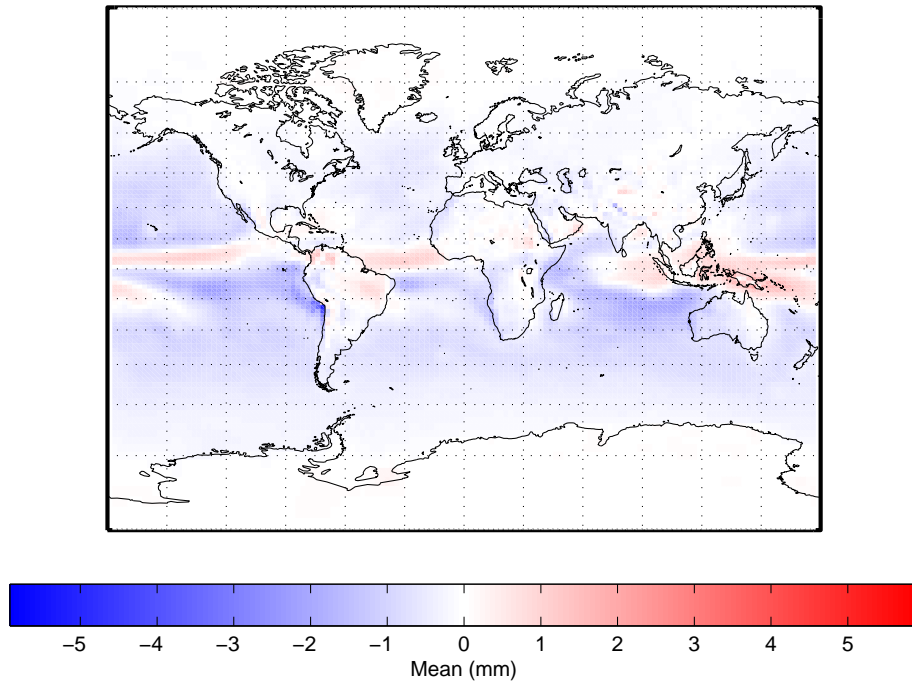
Figure 5.17: Differences of NWP model parameters (a) pressure and (b) temperature between NCEP Re-Analysis 1 and CMC GDPS for April 15 to April 21 2012

is the dominate source contributing to the variability with differences up to 6 mbar (there is also a positive temperature bias on the order of a couple of degrees Kelvin in the same region). Grid points in the vicinity of the Himalayas will also suffer the same orographic effects that have been described for the western coast of South America, which provides a possible explanation for the source of the difference in this region.

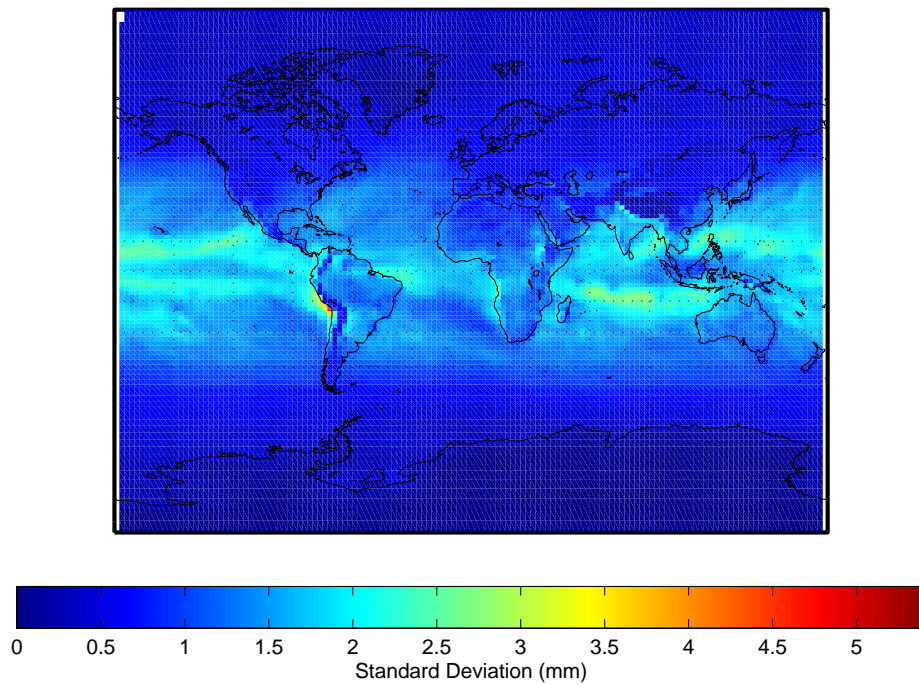
**5.1.3.1.4 Non-Hydrostatic Equivalent Height Error** The difference in mapping function as expressed as an equivalent height error due to the non-hydrostatic component is plotted in Figure 5.18. The overall combined mean bias and combined standard deviations shown in Figure 5.18(a) and (b) illustrates the same pattern as with the non-hydrostatic zenith delays. Again, the effect of the non-hydrostatic component is dominant in the equatorial regions and over the oceans. Overall, a global combined 11-year mean and standard deviation has been computed as -0.4 mm and 1.3 mm respectively. Figure 5.19 plots the maximum absolute value of the difference in equivalent height error, and as with the hydrostatic component differences can reach to values greater than 18 mm. However, the majority of grid points are well below 10 mm with the majority of land based points less than 6 mm. Table 5.5 summarizes the yearly combined global mean bias and standard deviation of the difference for each of the 4 times daily products (the results from the existing VMF1 service are subtracted from the UNB-VMF1 results (NCEP minus ECMWF)). Table 5.5 shows that all epochs agree with each other at the sub-mm level.

The standard deviations are approximately similar to that of the hydrostatic component, but the non-hydrostatic zenith delays are approximately ten times smaller than the hydrostatic. This further reinforces the fact that the NWP still has difficulty in predicting the water vapour content in the atmosphere. The most obvious feature in Figure 5.18(a) and (b) is the large bias and standard deviation that occurs on the western coast of South America (also seen in Figure 5.5). A possible explanation of this condition can also be related to the same difficulties discussed regarding the orography. As noted in §5.2.2.2.1.3, the orography in NCEP's Re-Analysis 1 is a mean orography, which as a consequence can





(a) Combined Bias



(b) Combined Standard Deviation

Figure 5.18: Equivalent height error due to the non-hydrostatic mapping function for the years 2001 to 2011 for unbvmfG (NCEP) minus vmfG (ECMWF). (a) Combined mean bias (b) Combined standard deviation.

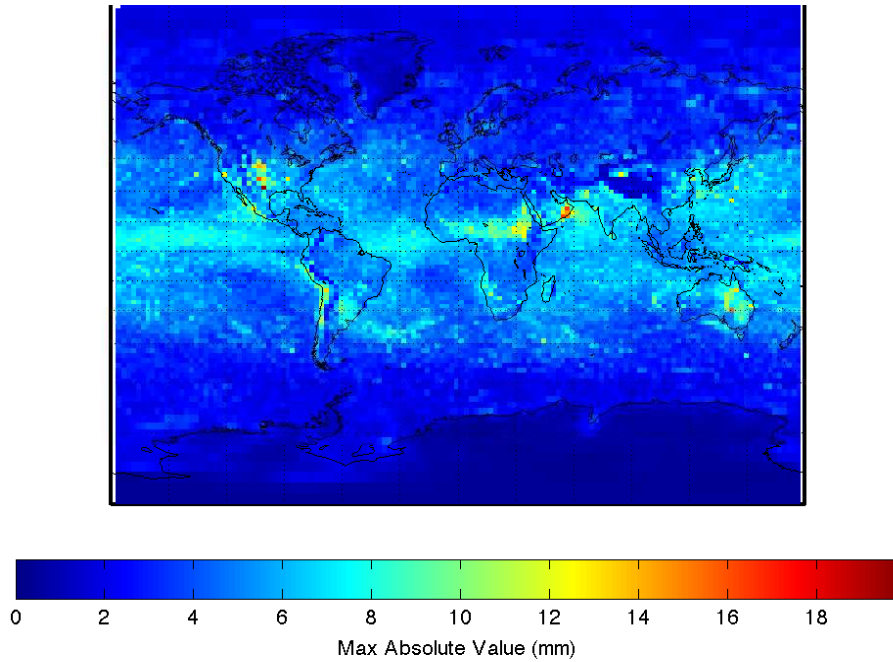


Figure 5.19: Maximum absolute values of the difference between unbvmfG (NCEP) and vmfG (ECMWF) mapping functions expressed as an equivalent height error for the years 2001 to 2011.

cause grid points next to mountains to be raised and mountain peaks to be lowered. In this case, the region is located very close to the Andes. The Andes are a very steep mountain range with two very distinct climates on opposite sides. The Andes block the zonal flow and separate two distinctive climates: a relatively cold and dry climate to the west and a warmer and moister climate to the east (Seluchi et al., 2006). Rutt (2003) suggests that long and high barriers (e.g. Andes) may have the effect diverting flow along the barrier instead of allowing it flow over the barrier. Therefore, the use of a mean orography has the effect of lowering the barrier in this region (Figure 5.16 shows that the Andes are 1500m lower than the CMC's model at a latitude of 30°S), which can have an effect on the atmospheric flow.

Figure 5.20 is a plot of the mean difference in specific humidity between NCEP's Re-Analysis 1 dataset and CMC's GDPS for the time period extending from April 15th to

Table 5.5: Summary of global combined yearly mean and standard deviation separated by each 4 times daily epochs for the equivalent height error due to the non-hydrostatic component. unbvmfG (NCEP) minus vmfG (ECMWF) (all values in millimetres).

Year	00H		06H		12H		18H	
	Mean	Std	Mean	Std	Mean	Std	Mean	Std
2001	-0.3	1.2	-0.3	1.2	-0.3	1.2	-0.3	1.2
2002	-0.4	1.4	-0.4	1.3	-0.4	1.3	-0.4	1.3
2003	-0.4	1.3	-0.4	1.3	-0.4	1.3	-0.4	1.3
2004	-0.4	1.4	-0.4	1.3	-0.4	1.3	-0.4	1.3
2005	-0.4	1.3	-0.5	1.3	-0.4	1.3	-0.4	1.3
2006	-0.4	1.3	-0.4	1.3	-0.4	1.3	-0.4	1.3
2007	-0.4	1.3	-0.4	1.3	-0.4	1.3	-0.4	1.3
2008	-0.3	1.3	-0.4	1.3	-0.4	1.3	-0.4	1.3
2009	-0.4	1.3	-0.4	1.3	-0.4	1.3	-0.4	1.3
2010	-0.4	1.4	-0.4	1.4	-0.4	1.4	-0.4	1.4
2011	-0.4	1.4	-0.4	1.4	-0.4	1.4	-0.4	1.4
Combined	-0.4	1.3	-0.4	1.3	-0.4	1.3	-0.4	1.3

April 21st 2012. The pattern shown in this figure matches the pattern in Figures 5.18 and 5.5, so the difference in specific humidity is source of discrepancy in the non-hydrostatic component (which was to be expected). However, the source of this discrepancy relates to the discussion of the previous paragraph. Figure 5.21 plots the specific humidity at the 1000 mb pressure level for the NCEP Re-Analysis 1 dataset and the CMC GDPS dataset for April 18th, 2012 at 12UTC. The NCEP dataset is shown in Figure 5.21(a) and the CMC in 5.21(b). The dominant difference between the two datasets is the fact that the CMC model does a better job at separating the two climates on opposing sides of the Andes as described by Seluchi et al. (2006). The warmer moist conditions appears to be contained to the eastern side of the Andes, whereas in the NCEP model the warmer moist conditions spill over across the Andes into the adjacent ocean. In this region, the NCEP's height of the Andes differs from the CMC's height from 578 m at  $\sim 17.5^\circ\text{S}$  to 872 m at  $15^\circ\text{S}$  and as much as 1436 m at  $\sim 12.5^\circ\text{S}$ . There also appears to be a moistening of the air across the Andes in the region as well, so the possibility of the differences in atmospheric flow

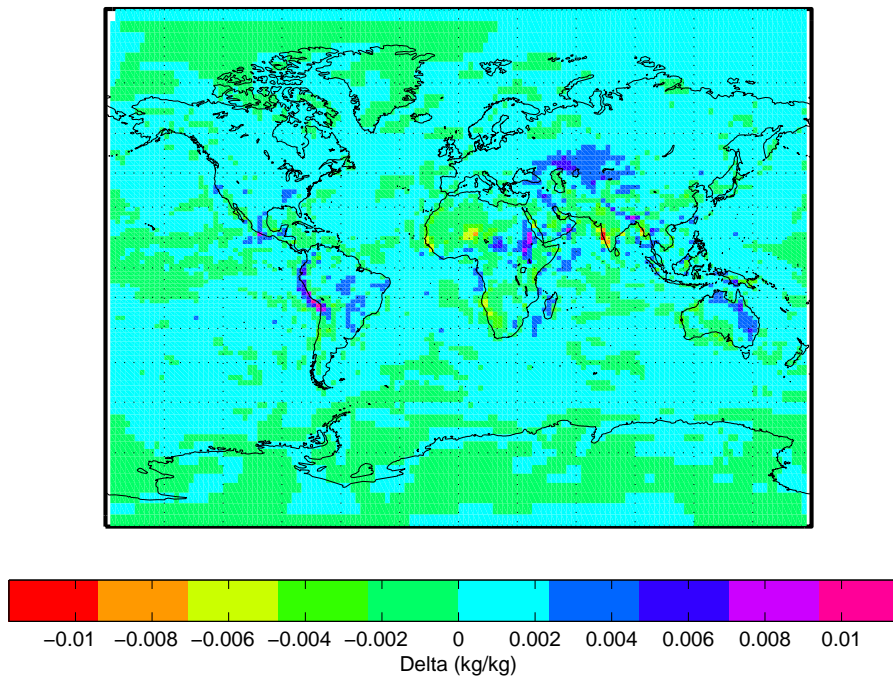
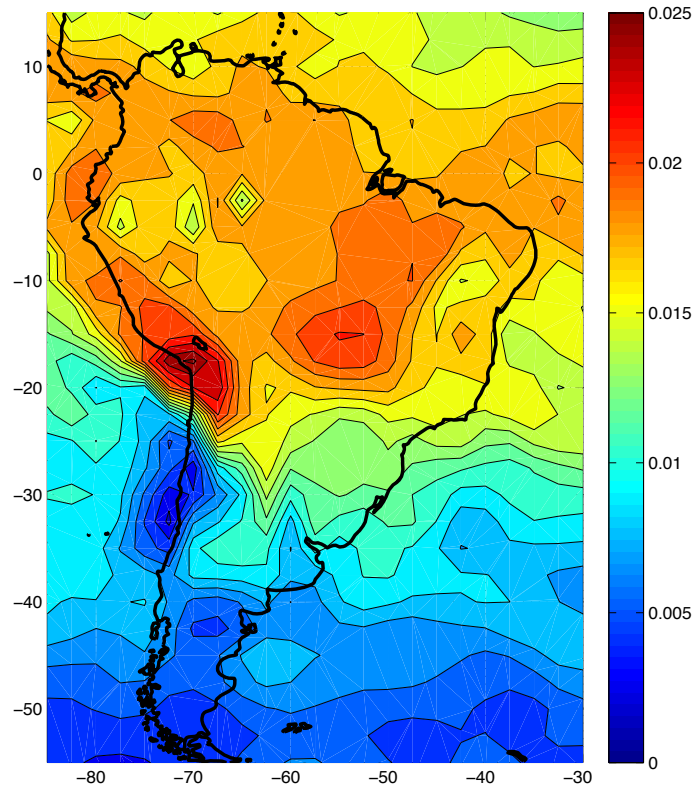


Figure 5.20: Differences of NWP model parameter specific humidity between NCEP Re-Analysis 1 and CMC GDPS for April 15 to April 21 2012.

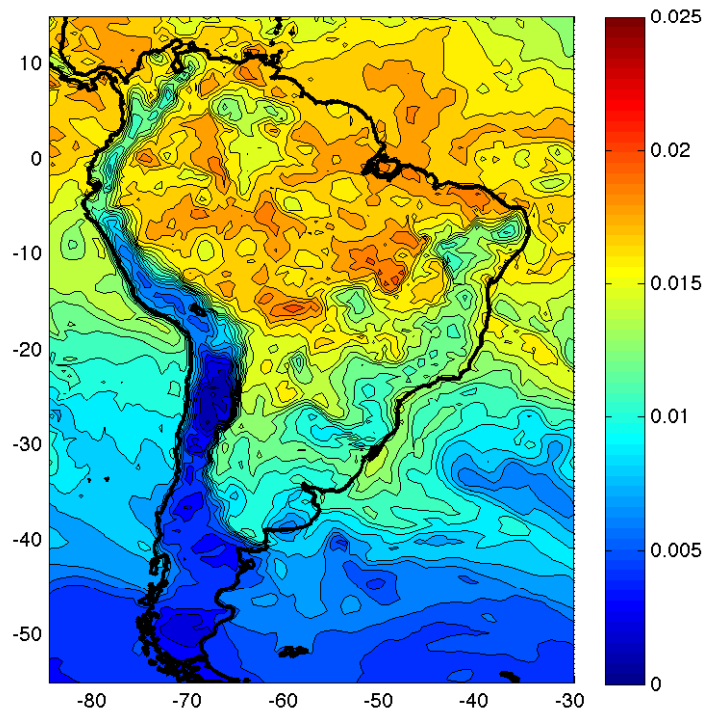
due to the reduced elevations in the NCEP model may only be a component of the whole story explaining NCEP's specific humidity pattern across the Andes. Overall, NCEP's Re-Analysis 1 falls short in accurately describing the atmospheric water vapour content for this region of the globe.

### 5.1.3.2 UNB-VMF1(CMC) vs VMF1(ECMWF)

The following section will focus only on the mapping function differences expressed as equivalent height error. The plots for the zenith delay differences can be found in Appendix C. This section describes the comparison of the UNB-VMF1 product (unbvmfGcmc in Table 4.9) produced with the CMC (GDPS) dataset with respect to the existing VMF1 service (vmfG). The timespan for this comparison extends from January 1st to September 30th, 2012. The reason for this is due to data availability from the CMC and has been explained in detail in Chapter 4 and follows for §5.2.2.3 and §5.2.2.4.



(a) NCEP Re-Analysis 1



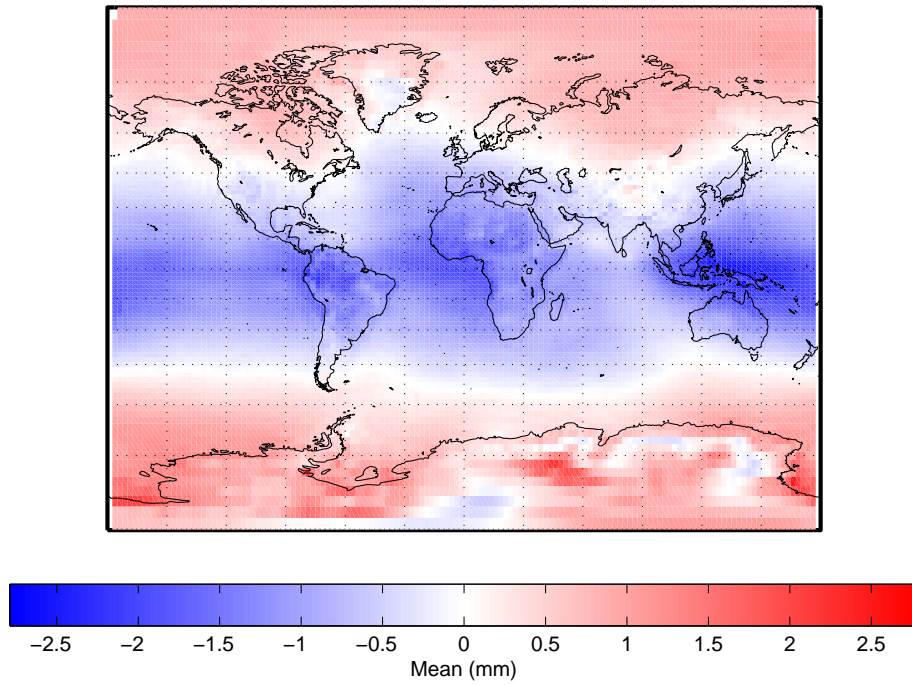
(b) CMC (GDPS)

Figure 5.21: Specific humidity (kg/kg) at the 1000mb pressure level for (a) NCEP Re-Analysis 1 and (b) CMC (GDPS) on April 18th, 2012 at 12UTC.

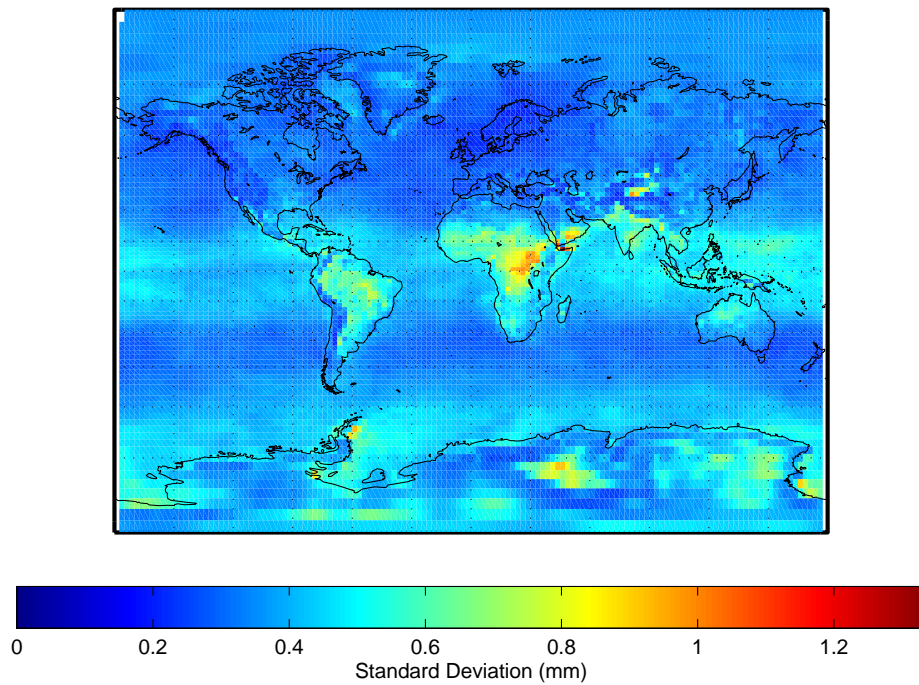
**5.1.3.2.1 Hydrostatic Equivalent Height Error** Figure 5.22 illustrates the difference in mapping functions as expressed as an equivalent height error due to the hydrostatic component. Figure 5.22(a) plots the mean bias for each grid point over the 9 month time span and 5.22 (b) plots the standard deviation of the difference over the same period. For the entire time period, the combined mean bias is -0.2 mm with a combined standard deviation of 1.0 mm. Therefore, at the  $3\sigma$  level the expectation is that the difference in station height will be with  $\pm 3.0$  mm with respect to the existing VMF1 service. For the same time period the products produced with the NCEP Re-Analysis 1 dataset (unbvmfG) show an overall mean of -0.7 mm and a standard deviation of 1.3 mm. At the  $3\sigma$  level the NCEP based product will be within  $\pm 3.9$  mm. The CMC based product shows a 66% reduction in the global mean bias and a 24% reduction in the global standard deviation with respect to the existing VMF1 service over the same time period. Additionally, the CMC based product only exhibits a maximum absolute value of the difference at a magnitude of 6.2 mm as opposed to the NCEP based product which exhibits a maximum absolute value at 10 mm. In both cases, these large absolute values occur over the oceans, but the NCEP based product experiences absolute values over land that can be as much as two times larger than with the CMC based product (4 mm for CMC versus 8 mm for NCEP - see Appendix C for plots).

Figure 5.22(a) exhibits the same latitude dependent bias, which is the result of the raytracing differences (as described in §5.1.3.1). Figure 5.22(b) illustrates that there is an increased standard deviation over the continents in the equatorial region. All grid points outside of equatorial latitudes experience standard deviations at or less than 0.4 mm. Figure 5.22(b) does not exhibit any similar symptoms that the NCEP products experiences with respect to the existing VMF1 service. Figure 5.22(b) show that there is not a strong correlation to topography as is with the NCEP product, however the CMC product appears to experience a marginal increase in standard deviations over land at equatorial latitudes and extending to mid-latitudes in the southern hemisphere ( $\sim 0.4$  mm to 0.5 mm). Also,





(a) Mean Bias



(b) Standard Deviation

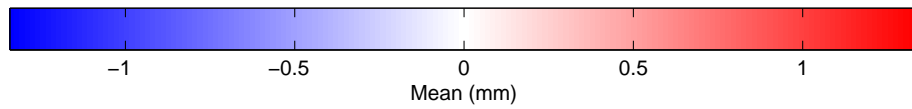
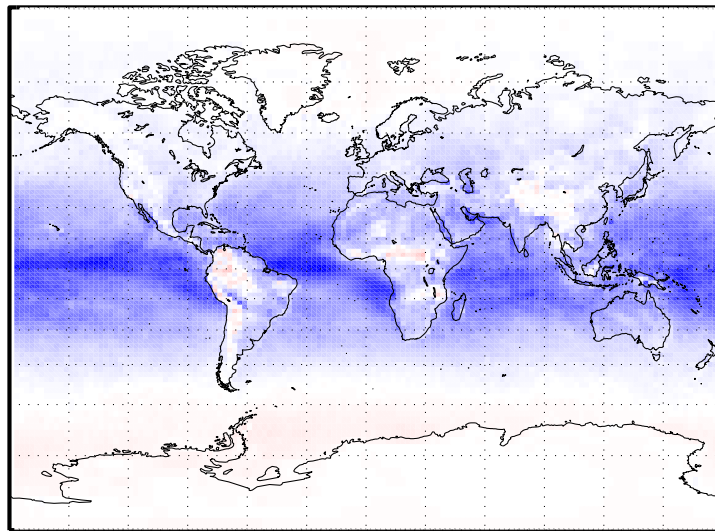
Figure 5.22: Equivalent height error due to the hydrostatic mapping function for the year 2012 for unbvmfGcmc (CMC) minus vmfG (ECMWF). (a) Mmean bias (b) Standard deviation. January 1st to September 30th 2012.

there is a marginal increase in the standard deviation along the Himalayas (approximately from 0.4 mm to 0.8 mm). However, these standard deviations are still sub-mm with a small region in central Africa experiencing standard deviations at the 1 mm level, and a small area along the coast of the Gulf of Aden (Southern coast of Yemen and northern Somalia) that experiences standard deviations in the range of 1.2 to 1.5 mm.

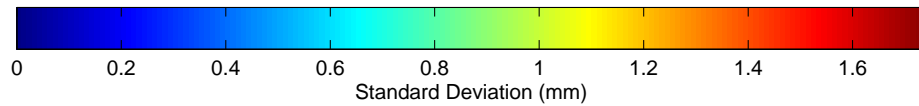
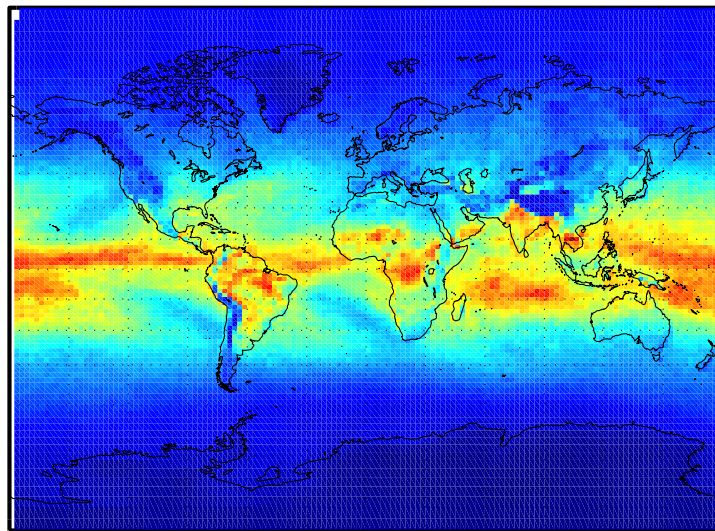
**5.1.3.2.2 Non-Hydrostatic Equivalent Height Error** Figure 5.23 plots the difference in mapping functions expressed as equivalent height error due to the non-hydrostatic component. The plot shows the unbvmfGcmc (CMC) minus the existing service, vmfG (ECMWF) and 5.23(a) is the mean bias and 5.23(b) is the standard deviation over the entire 9 month time period. The global mean bias and standard deviation for the time period is -0.2 mm and 0.7 mm respectively. At the  $3\sigma$  level, the CMC based product can be expected to be within 2.2 mm of the existing VMF1 service product. As a comparison, the mean and standard deviation of the difference between the NCEP based product (unbvmfG) and the existing VMF1 service (ECMWF) was -0.4 mm and 1.4 mm respectively. At the  $3\sigma$  level, the NCEP based product can be expected to be within 4.1 mm of the existing VMF1 service. The CMC based products demonstrates a 40% reduction in the mean difference and a 45% reduction in the standard deviation compared to the NCEP based product with respect to the existing VMF1 service. Further, the maximum absolute value of the difference for the CMC based product is 12.5 mm and 20.5 mm for the NCEP based products.

The mean difference shown in Figure 5.23(a) does not show the large bias along the South American western coast that the NCEP based product experiences. The largest mean biases occur over the oceans in equatorial regions with all land based grid points between  $\pm 0.5$  mm. A similar pattern exists for the 5.23(b) in that the largest standard deviations occur in the equatorial region where the water vapour content is largest. The standard deviations in these regions over land can reach 1.6 mm. Overall, the results are similar with the hydrostatic component in that they agree much better with the existing





(a) Mean



(b) Standard Deviation

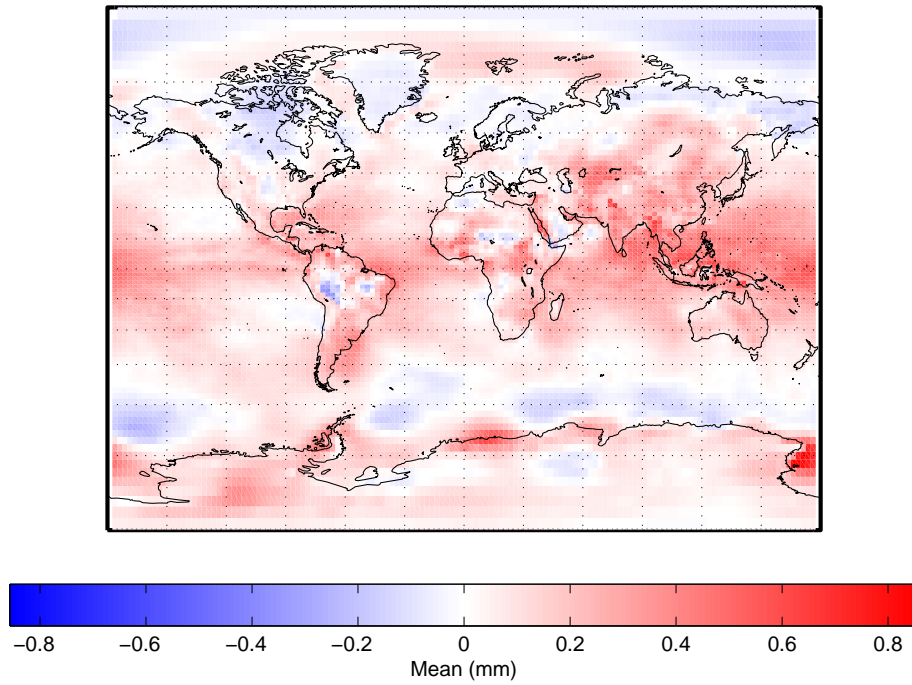
Figure 5.23: Equivalent height error due to the non-hydrostatic mapping function for the year 2012 for unbvmfGcmc (CMC) minus vmfG (ECMWF). (a) Mean (b) Standard deviation. January 1st to September 30th 2012.

VMF1 service than the NCEP based product.

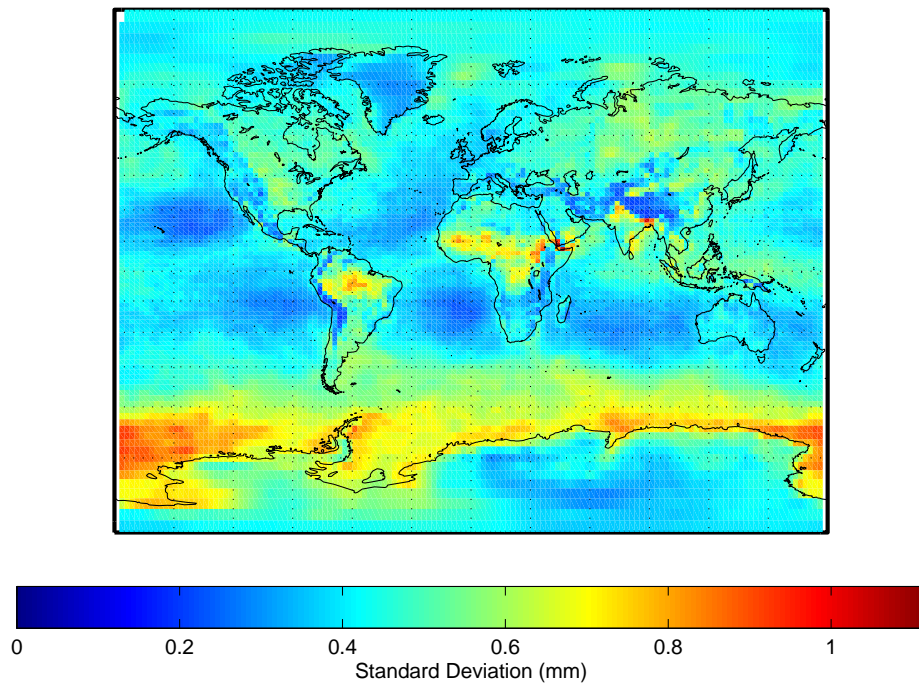
### **5.1.3.3 Forecast UNB-VMF1(CMC) vs UNB-VMF1 (CMC)**

The following section will focus only on the mapping function differences expressed as an equivalent height error. The plots for the zenith delay differences can be found in Appendix C and a summary of the computed results can be found in Table 5.6. This section describes the comparison of the UNB-VMF1 product (unbvmfP in Table 4.9) produced with the CMC (GDPS) dataset with respect to the UNB-VMF1 service's unbvmfGcmc product (see Table 4.9). The original intention was to provide a predicted dataset of similar quality to the original unbvmfGcmc product, but eliminate the latency so that the UNB-VMF1 service could be available to real-time and near real-time applications. Therefore, the scope of this comparison is to evaluate the compatibility of the forecasted product with respect to the standard UNB-VMF1 product based on the CMC (GDPS) dataset. The timespan for this comparison extends from March 17th to September 30th, 2012. Details of the unbvmfP product can be found in §4.3.4.4.

**5.1.3.3.1 Hydrostatic Equivalent Height Error** Figure 5.24 plots the difference in mapping functions due to the hydrostatic component expressed as equivalent height error, where 5.24(a) plots the mean bias and 5.24(b) plots the standard deviation of the difference over the 7 month interval. Figure 5.24(a) does not exhibit the latitude dependent bias as opposed with respect to the existing VMF1 service. This reason for this is due to the ray-tracing scheme (see §5.2.2.1.3 for details). Figure 5.24(a) also illustrates a small positive bias across the globe at the sub-mm level, where the largest differences occur in the equatorial regions and in a small pocket off the coast of the Antarctica. The total range of values in Figure 5.24(a) are sub-mm within  $\pm 0.8$  mm. Figure 5.24(b) illustrates a large band of the increased standard deviation along the shore of the Antarctica, and pockets of increased standard deviation along equatorial Africa and South America. The largest



(a) Mean Bias



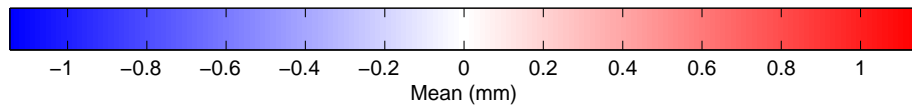
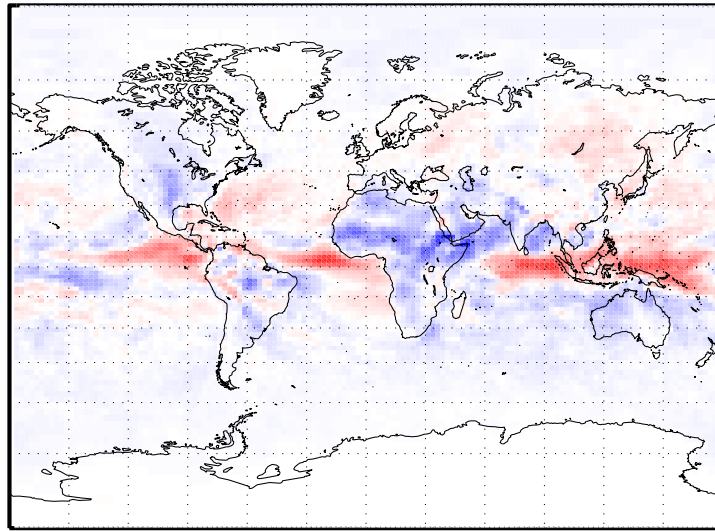
(b) Standard Deviation

Figure 5.24: Equivalent height error due to the hydrostatic mapping function for the year 2012 for unbvmfP (CMC) minus unbvmfGcmc (CMC). (a) Mean bias (b) Standard deviation. March 17th to September 30th 2012.

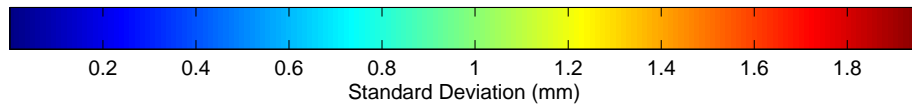
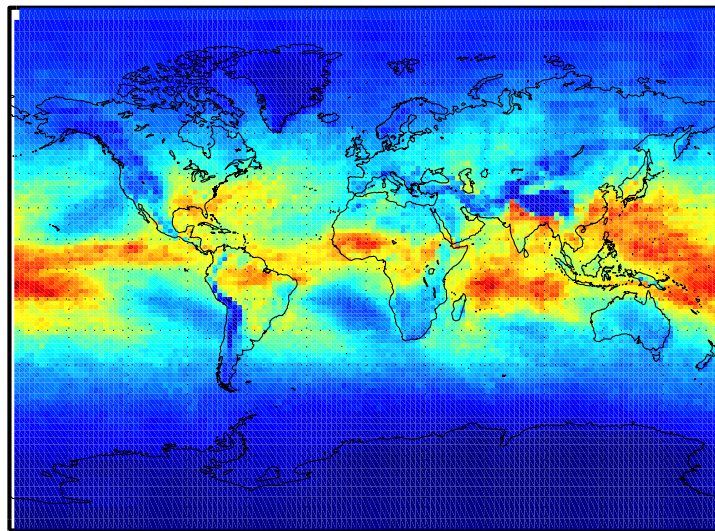
standard deviations are on the order of 1.1 mm that occur in the same location as with the comparison with the existing VMF1 service, that is along the coast of the Bay of Aden. Evaluating the maximum absolute value of the difference, discrepancies on the order of 7.5 mm can occur, but these occur over the oceans. The majority of the maximum absolute values of the differences that occur of land range between 2 and 3 mm (plots can be found in Appendix C). Overall, the global mean bias and standard deviation is 0.1 mm and 0.5 mm respectively, and at the  $3\sigma$  level, the equivalent height error due to the hydrostatic component for the forecast (unbvmfP) product can be expected to be within  $\pm 1.5$  mm of the standard unbvmfGcmc product.

**5.1.3.3.2 Non-Hydrostatic Equivalent Height Error** Figure 5.25 plots the difference in mapping functions due to the non-hydrostatic component expressed as equivalent height error, where 5.25(a) plots the mean bias and 5.25(b) plots the standard deviation of the difference over the 7 month interval. Figure 5.25(a) shows that the largest mean differences occur at equatorial latitudes with the largest mean differences reaching magnitudes of 1 mm. In this case, the majority of differences do occur over land as opposed to occurring predominantly over the oceans as the previous comparisons displayed (Figure 5.18(a) and 5.23(a)). The reason for this could be related to the fact that this comparison is made to a product produced with the same model, so the model dynamics, physics, and orography are the same. With the previous comparisons, differences in the underlying model assumptions (dynamics, physics, and orography) will be a part of the source of differences. In essence, this comparison provides an evaluation of the ability of the CMC's GDPS to forecast over a 42 hour period. Figure 5.25(b) illustrates the fact that locations over the ocean are generally more variable than locations over land. However, this assertion does not hold over equatorial latitudes. In general, locations at equatorial latitudes exhibit larger standard deviations than those locations at mid and high latitudes. This also relates to the fact that the water vapour content is larger and more variable at the equator.

The global mean bias and standard deviation has been computed to be -0.01 mm and



(a) Mean Bias



(b) Standard Deviation

Figure 5.25: Equivalent height error due to the non-hydrostatic mapping function for the year 2012 for unbmvmfP (CMC) minus unbmvfGcmc (CMC). (a) Mean bias (b) Standard deviation. March 17th to September 30th 2012.

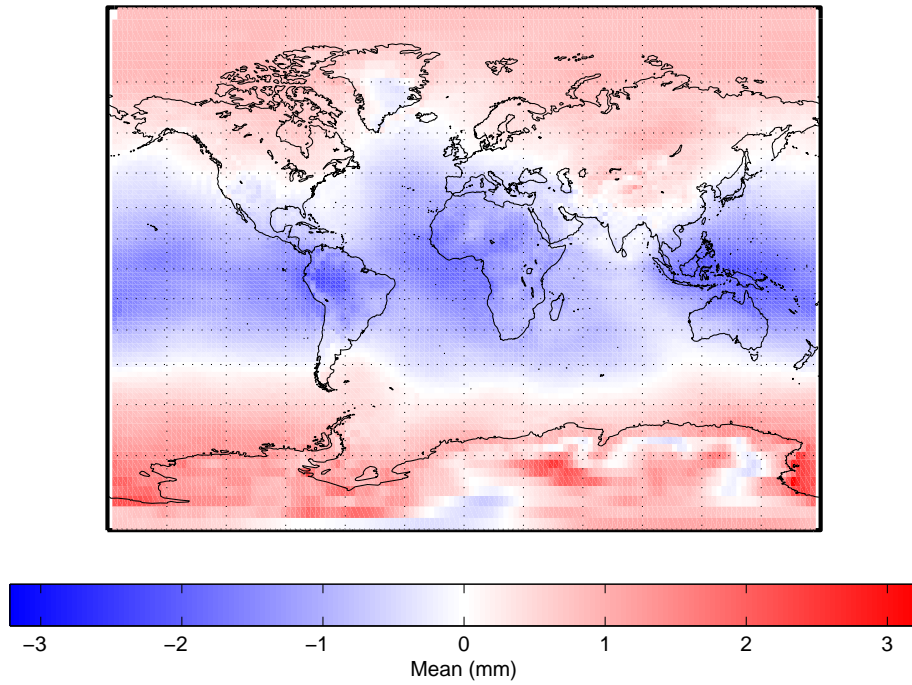
0.8 mm respectively. With respect to the hydrostatic component, the bias is less, but the standard deviation is almost twice as large. This provides an indication that the forecasts of the CMC have more difficulty in predicting the water vapour over time. This is not unexpected and follows the results of Boehm et al. (2007), which illustrated with the ECMWF that differences in equivalent height error for the non-hydrostatic component exceeded the acceptance criteria after the first day of the forecast (24h). In contrast, differences in the equivalent height error due to the hydrostatic component did not see significant deviations until the third day of the forecast. The maximum absolute value of the difference for the entire globe is 17.4 mm, but this occurs over the ocean. However, locations over Japan can reach 15 mm with the majority of land based points falling within the range of 2-8 mm (see Appendix C for plots).

#### **5.1.3.4 Forecast UNB-VMF1(CMC) vs Forecast VMF1(ECMWF)**

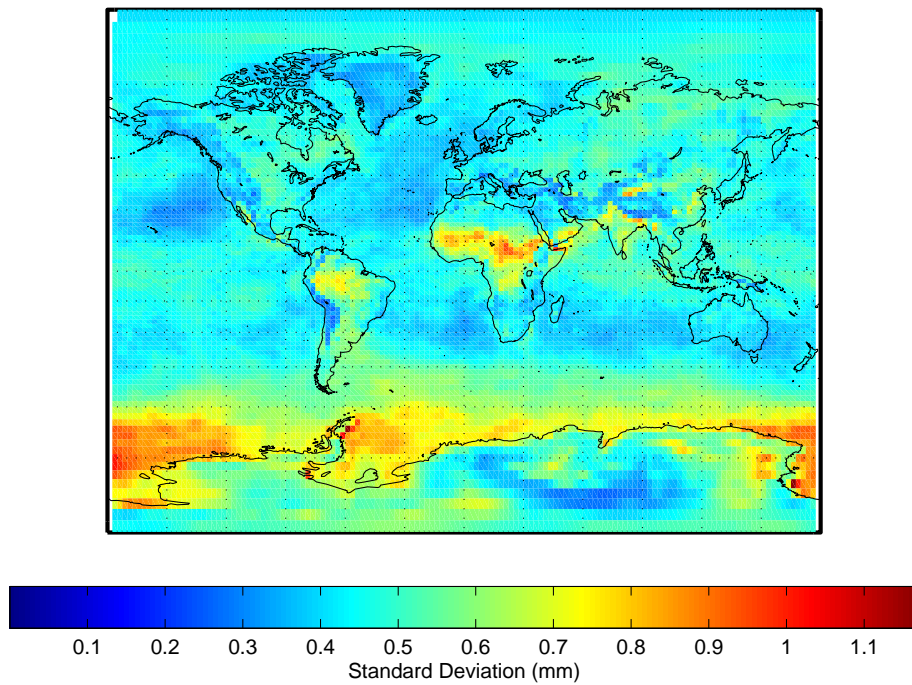
The following section will focus only on the mapping function differences expressed as an equivalent height error. The plots for the zenith delay differences can be found in Appendix C and a summary of the computed results can be found in Table 5.6. This section describes the comparison of the forecast UNB-VMF1 product (unbvmfP in Table 4.9) produced with the CMC (GDPS) dataset with respect to the existing VMF1 service's forecasted product (vmfG-FC). The timespan for this comparison extends from March 17th to September 30th, 2012.

**5.1.3.4.1 Hydrostatic Equivalent Height Error** Figure 5.26 plots the difference in mapping functions expressed as equivalent height error where 5.26(a) plots the mean bias and 5.26(b) plots the standard deviation of the difference over the 7 month time period. Firstly, Figure 5.26(a) exhibits the latitude dependent bias that exists due to the ray-tracing differences (see §5.2.2.1.3 for details). Secondly, The range of values of the mean difference fall within  $\pm 3$  mm with an overall global mean difference of -0.2 mm. The range of





(a) Mean Bias



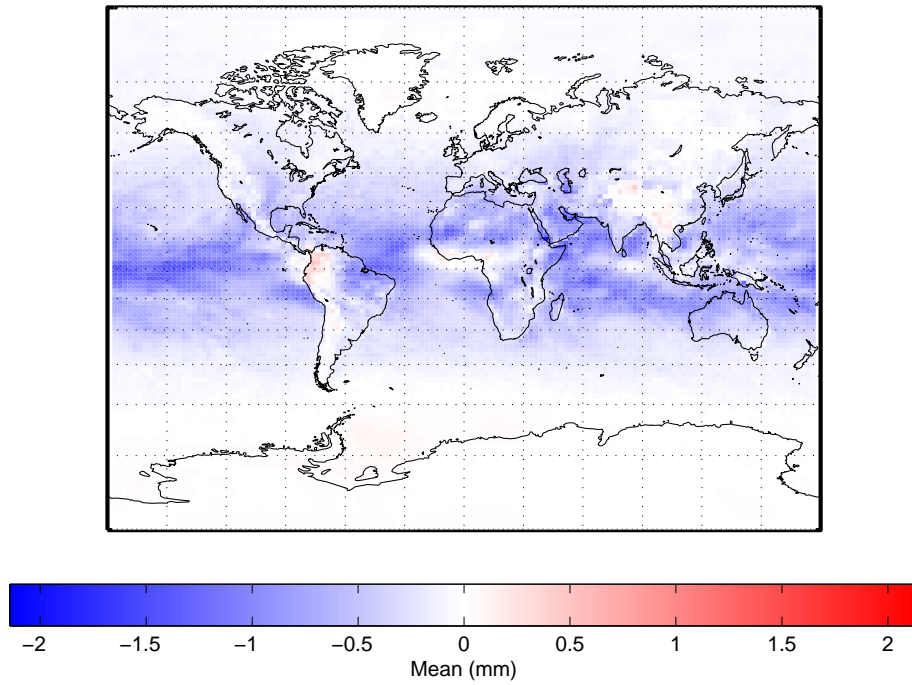
(b) Standard Deviation

Figure 5.26: Equivalent height error due to the hydrostatic mapping function for the year 2012 for unbvmfP (CMC) minus vmfG-FC (ECMWF). (a) Mean bias (b) Standard deviation. March 17th to September 30th 2012.

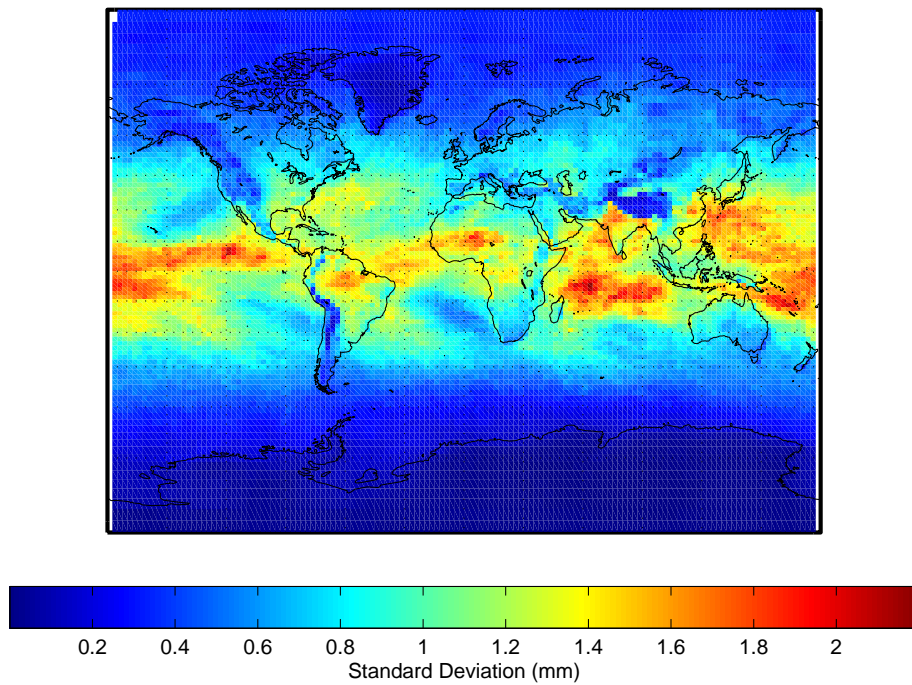
values of the mean difference are similar to that of the comparison with the NCEP based products (see Figure 5.8), but larger than that of the CMC analysis based products (see Figure 5.22). This is to be expected as this comparison deals with forecast based products, which are inherently more variable than an analysis based product (it is recognized that the analysis based product, unbvmfGcmc, consists of two 6H forecasts). The NCEP based product is also an analysis based product, but issues related to the coarse horizontal resolution and orography make it more variable than the finer grid resolution models it is compared with. Figure 5.26(b) illustrates that the range of values of the standard deviation of the difference are less than that of the unbvmfGcmc (Figure 5.22(b)), which is not expected since the unbvmfGcmc comparison is computed for two analysis based products. This is misleading since the larger range of values for the unbvmfGcmc product is due to a small area in the vicinity of the Gulf of Aden. Overall, the majority of grid points are within the range of 0.2 to 0.5 mm for the unbvmfGcmc product, and for this comparison the majority of grid points are within the range of 0.4 to 0.6 mm. The global standard deviation for this comparison has been computed to be 1.0 mm, with the  $3\sigma$  standard deviation computed as  $\pm 3.0$  mm. Lastly, the maximum absolute value of the difference is on the order of 8.8 mm and occurs along the coast of the Antarctica. However, for all of the maximum absolute values that occur over land, the range of values falls within 2-5 mm (plot can be found in Appendix C).

**5.1.3.4.2 Non-Hydrostatic Equivalent Height Error** Figure 5.27 plots the difference in mapping functions as expressed by the equivalent height error, where 5.27(a) plots the mean bias and 5.27(b) plots the standard deviation of the difference for the 7 month time period. Figure 5.27(a) illustrates a predominantly negative bias extending from the equator that transitions to a small negligible bias in the polar regions. The same patterns exist for the standard deviation of the difference in 5.27(b), and this has been the general pattern for all comparisons completed. Overall, the global mean and standard deviation has been computed to be -0.3 mm and 0.9 mm respectively. Similar to the unbvmfGcmc comparison





(a) Mean Bias



(b) Standard Deviation

Figure 5.27: Equivalent height error due to the non-hydrostatic mapping function for the year 2012 for unbvmfP (CMC) minus Forecast vmfG-FC (ECMWF). (a) Mean bias (b) Standard deviation. March 17th to September 30th 2012.

(§5.2.2.2.1), differences can reach 17 mm over Japan, but the majority of grid points over land range from 2-4 mm with small regions that can experience discrepancies on the order of 8-10 mm (all plots in Appendix C).

#### **5.1.4 Summary and Recommendations**

This section provided a description of the validation of the UNB-VMF1 with respect to the existing VMF1 service in Vienna. It was the intention of this section to assess the quality of the gridded products produced by the UNB-VMF1 using the existing service as a benchmark. A common theme throughout the comparisons is the importance in the selection of ray-tracing methods and the selection of the NWP source dataset. All products produced by the UNB-VMF1 service when compared to those of the existing service exhibit a latitude dependent bias, which has been shown to be due to differences in the definition of the radius of the Earth. The UNB-VMF1 products apply a more rigorous definition of the shape of the Earth with the mean gaussian radius as opposed to a constant radius, which has been implemented by the existing VMF1 service. Secondly, differences in the NWP datasets also contribute significantly in the realization of the mapping function. Results from the NCEP comparison (§5.2.2.1) showed that the underlying assumptions regarding the model orography, as well as the horizontal resolution, can create problems with accurately depicting atmospheric phenomena. Specifically, in regions of steep topography and in regions where there is high topographic relief in relation to a body of water the NCEP based mapping function proved to be noisier than those based from the CMC (The CMC's horizontal resolution is approximately four times more fine).

Tables 5.6 and 5.7 summarize the overall global means and standard deviations of the difference between the UNB-VMF1 products to those of the existing VMF1 service. Table 5.6 summarizes the differences in the ray-traced zenith delays for both the hydrostatic (*zhd*) and the non-hydrostatic (*zwd*) components and Table 5.7 summarizes the differences in the mapping functions expressed as equivalent height errors for both hydrostatic

and non-hydrostatic components. Overall, the NCEP based product, unbvmfG, performed the worst with respect to the existing service, and the CMC based product, unbvmfGcmc, performed best.

The unbvmfGcmc product exhibited approximately a 41% reduction in the standard deviation of the ray-traced hydrostatic zenith delay and a reduction of approximately 20% in the mean bias with respect to the unbvmfG. For the non-hydrostatic zenith delay, the unbvmfGcmc product exhibited a reduction of approximately 47% in the standard deviation, however the bias did not change significantly (agree at the sub-mm level). For the equivalent height error, the unbvmfGcmc product exhibited a 66% smaller bias and a 24% reduction in the standard deviation for the hydrostatic component and a 40% and 45% reduction in the mean and standard deviation for the non-hydrostatic component respectively.

The forecast product, unbvmfP, performed well with respect to both the unbvmfGcmc product and the existing service. However, Tables 5.6 and 5.7 illustrate that as the forecast hour increases, so does the standard deviation. This was more evident with the non-hydrostatic component than with the hydrostatic. The hydrostatic standard deviation of the zenith was only raised by 0.8 mm as compared to 2.7 mm for the non-hydrostatic zenith delay. This is a quality that is inherent to the nature of the NWP and unavoidable, since they are highly non-linear and chaotic, which make them very sensitive to small changes at the initial conditions. Lorenz (1963a,b) demonstrated that due to the chaotic nature of the atmosphere, the predictability of the weather (or any dynamic unstable system) has a finite limit, which makes prediction into the distant future impossible. The results of the forecasted products are subject to the chaotic nature of the model, which explains why the standard deviations increase over time, and the results here follow that of Boehm et al. (2007) and Boehm et al. (2008).

Lastly, an acceptance criteria in the evaluation of the results should be decided upon to assist in the forming of meaningful recommendations. Boehm et al. (2007) and Boehm

Table 5.6: Summary of difference in ray-traced zenith delays for all comparisons at each epoch of the 4× daily products. All values in millimetres.

Product	Parameter	NWP	Ref-NWP	Epoch	00H		06H		12H		18H	
					Mean	Std	Mean	Std	Mean	Std	Mean	Std
unbvmfG	zhd	ncep	vmfG	2001-2011	2.3	5.6	2.4	5.7	2.3	5.6	2.3	5.7
unbvmfG	zhd	ncep	vmfG	2012A <sup>a</sup>	2.6	5.8	2.6	5.9	2.5	5.8	2.6	5.9
unbvmfGcmc	zhd	cmc	vmfG	2012A	2.1	3.3	2.1	3.4	2.1	3.3	2.1	3.4
unbvmfFP	zhd	cmcp <sup>b</sup>	unbvmfGcmc	2012B <sup>c</sup>	0.0	2.6	0.0	2.7	0.1	3.4	0.1	3.7
unbvmfFP	zhd	cmcp	vmfG-FC <sup>d</sup>	2012B	2.0	3.6	2.1	3.9	2.0	4.1	2.1	4.4
unbvmfG	zwd	ncep	vmfG	2001-2012	4.7	30.3	4.6	30.3	4.3	29.9	4.5	30.5
unbvmfG	zwd	ncep	vmfG	2012A	5.8	30.8	6.2	30.7	5.7	30.4	6.0	30.9
unbvmfGcmc	zwd	cmc	vmfG	2012A	5.7	15.9	5.6	16.2	5.9	16.0	6.1	16.5
unbvmfFP	zwd	cmcp	unbvmfGcmc	2012B	1.3	16.2	1.6	16.8	1.7	19.1	1.8	19.9
unbvmfFP	zwd	cmcp	vmfG-FC	2012B	7.1	18.5	7.3	19.2	7.7	20.2	7.8	21.2

<sup>a</sup>For all epochs listed as 2012A the period of the comparison extends from January 1st to September 30th 2012

<sup>b</sup>cmcp refers to the CMC(GDPS) but 24h, 30h, 36h and 42h forecasts were used from the 00z initialization to produce the product.

<sup>c</sup>For all epochs listed as 2012B the period of the comparison extends from March 17th to September 30th 2012

<sup>d</sup>ecmwf refers to the ECMWF, but 24h, 30h, 36h, and 42h forecasts have been used to produce the forecast VMF1 product from the existing service.

Table 5.7: Summary of difference in mapping functions expressed as equivalent height error for all comparisons at each epoch of the 4× daily products. All values in millimetres.

Product	Parameter	NWP	Ref-Product	Epoch	00H		06H		12H		18H	
					Mean	Std	Mean	Std	Mean	Std	Mean	Std
unbvmmfG	Hh	ncep	vmfG	2001-2011	-0.6	1.3	-0.7	1.3	-0.6	1.3	-0.7	1.3
unbvmmfG	Hh	ncep	vmfG	2012A <sup>a</sup>	-0.7	1.3	-0.8	1.3	-0.7	1.3	-0.8	1.3
unbvmmfGcmc	Hh	cmc	vmfG	2012A	-0.2	1.0	-0.3	1.0	-0.2	1.0	-0.2	1.0
unbvmmfP	Hh	cmcp <sup>b</sup>	unbvmmfGcmc	2012B <sup>c</sup>	0.1	0.4	0.1	0.4	0.1	0.5	0.1	0.5
unbvmmfP	Hh	cmcp	vmfG-FC <sup>d</sup>	2012B	-0.2	1.0	-0.2	1.0	-0.2	1.0	-0.2	1.0
unbvmmfG	Hw	ncep	vmfG	2001-2011	-0.4	1.3	-0.4	1.3	-0.4	1.3	-0.4	1.3
unbvmmfG	Hw	ncep	vmfG	2012A	-0.4	1.4	-0.4	1.4	-0.4	1.4	-0.4	1.4
unbvmmfGcmc	Hw	cmc	vmfG	2012A	-0.2	0.7	-0.2	0.7	-0.2	0.7	-0.2	0.8
unbvmmfP	Hw	cmcp	unbvmmfGcmc	2012B	-0.0	0.7	-0.0	0.7	-0.0	0.8	-0.0	0.9
unbvmmfP	Hw	cmcp	vmfG-FC	2012B	-0.3	0.9	-0.3	0.9	-0.3	0.9	-0.3	1.0

<sup>a</sup>For all epochs listed as 2012A the period of the comparison extends from January 1st to September 30th 2012

<sup>b</sup>cmcp refers to the CMC(GDPS) but 24h, 30h, 36h and 42h forecasts were used from the 00z initialization to produce the product.

<sup>c</sup>For all epochs listed as 2012B the period of the comparison extends from March 17th to September 30th 2012

<sup>d</sup>vmfG-FC refers to the ECMWF, but 24h, 30h, 36h, and 42h forecasts have been used to produce the forecast VMF1 product from the existing service.

Table 5.8: Summary of  $3\sigma$  global discrepancies. All values in millimetres.

Product	Reference	Parameter	$3\sigma$
unbvmfG	vmfG	Hh	3.9
unbvmfGcmc	vmfG	Hh	2.9
unbvmfP	unbvmfGcmc	Hh	1.5
unbvmfP	vmfG	Hh	3.1
unbvmfG	vmfG	Hw	3.9
unbvmfGcmc	vmfG	Hw	2.2
unbvmfP	unbvmfGcmc	Hw	2.4
unbvmfP	vmfG-FC	Hw	2.8

et al. (2008) used the results from Niell (2006) to form a criteria for evaluating acceptable discrepancies in the VMF1. Niell (2006) demonstrated through the comparison of radiosonde data that the VMF1 is accurate at the 3 mm level (this values refers to height). This work will follow the previous efforts and use this value as a criteria for the determination of significance. The criteria should be thought of in the context of equivalency to the existing VMF1 service and not as an absolute criteria describing the overall accuracy of the product. At the  $1\sigma$  level all differences with respect to the existing VMF1 service and fall below this 3 mm criteria and can be considered equivalent under a global context. Under stricter terms, the results have been expanded to the  $3\sigma$  for this evaluation ( $\sim 99\%$  confidence). Table 5.8 summarizes the  $3\sigma$  standard deviations for each of the comparisons. The results show that the NCEP based product, unbvmfG, exceeds this criteria. However, this is mainly due to the issues NCEP's Re-Analysis product has in coastal locations with steep topography. Therefore, the unbvmfG product can be expected to perform under this criteria outside the identified regions in §5.1.2.1. The CMC based product, unbvmfGcmc, meets this criteria and can be used globally since it does not experience any of those topographic based limitations as does the unbvmfG. The predicted product, unbvmfP can be used interchangeably with the unbvmfGcmc product since their discrepancies are well within the 3 mm criteria. However, the predicted product in re-

lation to the existing forecasted VMF1 service exceeds this criteria, but only by a small amount (sub-mm) and only in the hydrostatic case. Since the intended applications of the predicted product is real-time (or near-real time) applications, this discrepancy is not considered significant.

## **5.2 Comparison of VMF1 Gridded Products in the Position Domain**

This section summarizes the evaluation of the UNB-VMF1 products in the position domain. The previous section, §5.2, estimated the effect in the position domain through the computation of the equivalent height error for different realizations of the VMF1. This section will compute the position of a subset of stations through standard GPS positioning techniques. The GPS positioning technique used for this analysis is precise point positioning (PPP), which provides cm level accuracies to un-differenced carrier-phase observations resulting in absolute positions on Earth (Zumberge et al. (1997); Kouba and Héroux (2001)). The objective of this section is to assess the differences in UNB's realization of the VMF1 to that of the existing VMF1. This chapter will begin with a description of the experiment §5.2.1 followed by a description of the PPP process in §5.2.2. The next section, §5.2.3 will present the results with a discussion, which is then followed by §5.2.4 that describes an experiment illustrating the impact of elevation angle on the previous sections results. The final section, §5.2.5 provides a summary and recommendations.

### **5.2.1 Description of Experiment**

The analysis is based on the computation of positions of a subset of IGS stations through the application of PPP. The essence of the experiment is to compute the positions of 32 IGS stations utilizing the UNB realizations of the VMF1 and compare the resulting positions to those computed using the existing VMF1 service products. The selection of the 32

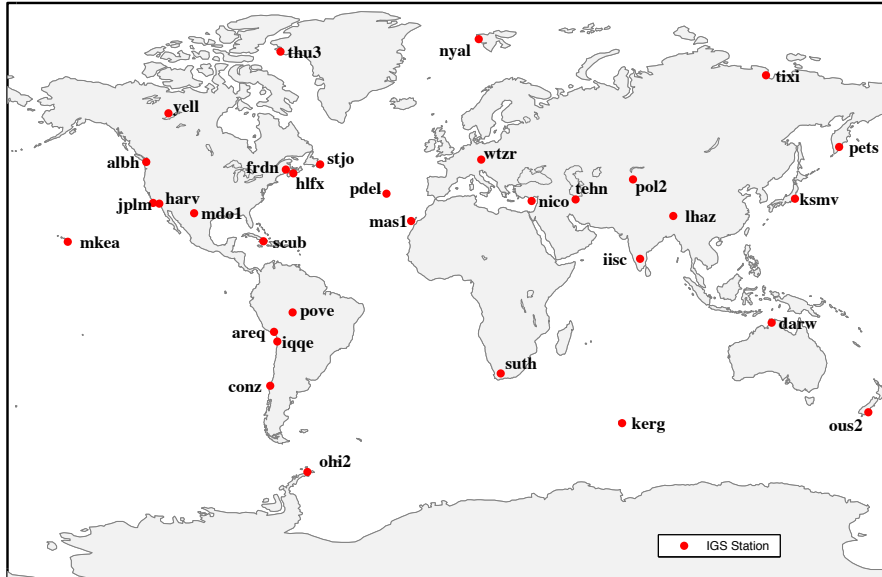


Figure 5.28: Summary of 32 IGS stations used for GNSS positioning analysis.

stations has been made in an attempt to create a uniform distribution of stations around the globe. Stations have also been selected so that they cover regions that have been identified as highly variable for some products, such as the western coast of South America, and regions that show little variations (see §5.1). Figure 5.28 illustrates the locations and names of the IGS stations selected for the analysis.

Station observation data was sourced from the IGS (Dow et al., 2009) where the observations are provided on a daily basis at 30s intervals. Supplied RINEX files from the IGS may include data from multiple constellations, however, this analysis has only used data from the GPS constellation and all observations from the remaining constellations have been discarded (due to software limitations). Standard PPP analysis requires accurate knowledge of the satellite orbits and satellite clock errors. These values have also been provided by the IGS (Dow et al., 2009), where the final orbit and clock products have been used.

Table 5.9 summarizes the comparisons that have been made and the resulting parameters that have been computed. The comparisons made in the position domain follow those



Table 5.9: Summary of comparisons made in the position domain

Product	Reference	Epoch	Parameters
unbvmfG	vmfG	2001-2011	$\Delta\phi, \Delta\lambda, \Delta h$
unbvmfG	vmfG	2012	$\Delta\phi, \Delta\lambda, \Delta h$
unbvmfGcmc	vmfG	2012	$\Delta\phi, \Delta\lambda, \Delta h$
unbvmfP	unbvmfGcmc	2012	$\Delta\phi, \Delta\lambda, \Delta h$
unbvmfP	vmfG	2012	$\Delta\phi, \Delta\lambda, \Delta h$

described in the previous section, §5.1. The main comparison is between the unbvmfG product in relation to the operation gridded product from the existing VMF1 service (first entry in Table 4.10). The interval of the analysis extends from 2001 to 2011. The secondary comparisons involve the CMC based based products, unbvmfGcmc and unbvmfP. The interval for these comparisons extend only from January 1st to August 31, 2012 for the unbvmfGcmc product, and from March 17th to August 31st 2012 for the unbvmfP (the reason for this has been explained in Chapter 4).

Positions have been computed using UNB's GAPS PPP software (Leandro, 2007) modified for the provision of the differing realizations of the VMF1. Once positions have been computed for each of the specified realizations of the VMF1, the coordinate time series is then differenced. The differenced coordinate time series is then used for the analysis, where the mean difference, RMSE, and standard deviation of the difference have been computed for each station. The standard deviation of the coordinate differences have only been computed for the height differences, and have been computed by equation 3.8 (substitute  $\Delta h$  for  $\Delta p$ ), where the fitted differences have been computed by equation 3.7. The standard deviations provide a measure of the overall noise exhibited by each of the VMF1 realizations, since the trend has been removed from its computation.

## 5.2.2 Precise Point Positioning

A detailed discussion regarding the technical implementation of the PPP technique can be found in Zumberge et al. (1997), Kouba and Hèroux (2001) and details for the GAPS process can be found in Leandro (2007). Only the general salient concepts will be presented here. PPP is an autonomous positioning technique that computes absolute positions at the cm-level for a single receiver. The standard approach to positioning with GNSS has been relative techniques which requires the simultaneous collection of data at a second location (two receivers). The PPP technique institutes the typical ionosphere-free linear combination as follows (as does GAPS):

$$P_3 = \rho + c(dT - dt) + T + e_{P_3} \quad (5.3)$$

$$\Phi_3 = \rho + c(dT - dt) + T + N_{if}\lambda_{if} + e_{\Phi_3} \quad (5.4)$$

where,  $\Phi_3$  and  $P_3$  are the carrier-phase and code observation ionosphere-free linear combination;  $\rho$  is the geometrical distance between the satellite and the receiver,  $dT$  and  $dt$  are the satellite and receiver clock errors respectively;  $T$  is the signal delay due to the troposphere;  $N_{if}$  is the ionosphere-free carrier-phase integer ambiguity;  $\lambda_{if}$  is the ionosphere-free effective carrier-phase wavelength;  $e_{P_3}$  and  $e_{\Phi_3}$  are the process noise (and multi path) for the code and carrier-phase measurements respectively; and  $c$  is the vacuum speed of light.

For the PPP analysis,  $dT$  is known from the IGS precise clock products, and the satellite positions within  $\rho$  are known from the precise orbit products from the IGS. Therefore, the unknown parameters are the receiver cartesian coordinates (X,Y,Z), the receiver clock error ( $dt$ ), a residual troposphere parameter (which is actually the non-hydrostatic zenith delay - see Chapter 2 for the decomposition of  $T$ ), and the ionosphere-free integer ambiguity. As opposed to the standard relative positioning techniques (also a limiting factor in PPP), the ionosphere integer ambiguity is actually a floating point value since the hardware

delays and phase biases are absorbed (Leandro, 2007).

Lastly, equations 5.3 and 5.4 are not entirely complete since there are a whole set of errors that need to be applied, such as ocean tide loading, body tide loading, sagnac effect, antenna phase centre offset, etc. These corrections must be applied to achieve the cm-level precisions, and can be thought of adding a correction parameter to equations 5.3 and 5.4. Details of each of the different types of corrections can be found in Kouba and Hèrroux (2001) and Leandro (2007).

For this analysis, all stations have been processed at an elevation angle of  $5^\circ$  for a duration of at least 18 hours in static mode with  $1/\sin\epsilon$  elevation angle dependent weighting. Ocean tidal loading effects have been applied, and a residual troposphere parameter has been estimated for all stations using a random-walk process that is allowed to vary at  $5\text{mm}/\sqrt{\text{hr}}$ . Although the IGS provides observations at 30s intervals, GAPS has processed at 5min intervals matching the IGS precise clock product. The application of atmospheric pressure loading (APL) corrections have not been applied, even though Steigenberger et al. (2009) has recommend the application of this correction when used in conjunction with ray-traced *a-priori* zenith delays. The analysis of this experiment has been made with the differenced coordinate time series, so the APL signal will be constant in each of the discrete coordinate time series (e.g. UNB-VMF1 based and VMF1 based) and thus cancel in the difference.

The *a-priori* hydrostatic zenith delay is defined by the ray-traced values as supplied in the gridded products. The primary recommendation from the IERS Conventions (2010) is the use of on-site measured pressure for the computation of *a-priori* hydrostatic zenith delays with Saastamoinen (equations 3.5 and 3.6). However, not all IGS stations selected for this analysis offer meteorological measurements to the public, and there are issues with the calibration and maintenance of the meteorological sensors on site (see Chapter 3). The lack of availability is recognized by the IERS Conventions (2010) and recommends to use meteorological data from a NWP as a backup. The IERS Conventions (2012) do not

expressly recommend the use of ray-traced zenith delays, but the results from Chapter 3 indicate that the differences between the ray-traced hydrostatic zenith delays and the Saastamoinen hydrostatic zenith delays are at the mm-level. It is recognized that in doing this the application of the different realizations of the VMF1 (e.g. UNB-VMF1 and the existing VMF1) have not been completely isolated, so the addition of the ray-traced zenith delays may introduce additional error into the height solution since a different value of the *a-priori* hydrostatic zenith delay is used for each of the position solutions computed with the differing realizations of the VMF1. However, it is the intention of this experiment to assess the differing VMF1 realizations as a whole package, meaning the application of the coefficients in the computation of the mapping function as well as the application of the corresponding ray-traced *a-priori* zenith delays.

An assumption when performing the GNSS analysis is the the *a-priori* hydrostatic delay is known with sufficient accuracy. Any errors in the *a-priori* hydrostatic zenith delay cannot be fully absorbed by the estimation of the non-hydrostatic zenith delay. This becomes more prevalent as the difference in the mapping functions (hydrostatic and non-hydrostatic) become larger, which typically occurs at lower elevation angles (Boehm et al., 2006; Tregoning and Herring, 2006). The remaining error propagates into the height solution and is referred to as hydrostatic/wet mapping function separation errors (Kouba et al., 2008). Secondly, there is the error in the mapping function itself. In this case, the difference between the mapping functions (UNB-VMF1 and VMF1) can be considered the error. If the *a-priori* hydrostatic zenith delay is considered to be correct, then the error in the mapping function will result in the mapped slant delay being incorrect. Therefore, there are two sources of error that are propagating in to the height and the estimation of the non-hydrostatic zenith delay: (a) due to error in the *a-priori* zenith hydrostatic delay; and (b) error in the mapping function. In a static analysis, the coordinates are constrained quite well, so the expectation is that the estimated zenith delay will absorb the majority of the error.

The UNB-VMF1 gridded product (as well as the existing service product) provide the *a-priori* ray-traced zenith delays at elevations specified in *orography.ell*. Therefore, the hydrostatic zenith delays must be reduced to the station height. The hydrostatic zenith delay reduction implemented for this work follows Steigenberger et al. (2009) where the hydrostatic zenith can be computed by:

$$ZHD(h) = ZHD(h_O) - 2.277 \times 10^{-3} \frac{g}{R} \frac{p(h_O)}{T(h_O)} (h - h_O) \quad (5.5)$$

where,  $ZHD(h)$  is the hydrostatic zenith delay at the station height;  $ZHD(h_O)$  is the hydrostatic zenith delay at grid elevation;  $g$  is gravity;  $R$  is the gas constant; and  $p(h_O)$ ,  $T(h_O)$  are the pressure, temperature at the grid point height. Each of the surrounding grid points are reduced to the station height, then the station hydrostatic *a-priori* zenith delay is interpolated linearly in two-dimensions. For this analysis, the pressure and temperature have been computed using the GPT. Although Chapter 3 concluded the GPT was the worst performing model of the pressure/temperature in relation to site measurements, using the GPT is computational faster (simpler to implement) than extracting information from the NWP. In the context of the size of the dataset, and the fact that any bias introduced by the GPT will be constant across all solutions, thus cancelling when the difference is taken, the use of the GPT is justified. Lastly, since VMF1 products are produced on a 6-hourly basis and GAPS performs a forward sequential least-squares filter at 5 min intervals, a linear interpolation in time must be made at each of the computation intervals.

Steigenberger et al. (2009) recognizes that this formulation is insufficient when the height differences are large between the grid point elevation and the station. Steigenberger et al. (2009) concludes that a large bias at station Mauna Kea is due to the fact that the pressure must be reduced over an elevation of 3km. Fund et al. (2011) investigated different methods in the reduction of the VMF1 gridded hydrostatic zenith delay (including equation 5.3) and concluded that the best results were obtained when the reduction included provisions for both temperature and pressure (e.g. Equation 5.3). Although Fund

et al. (2011) included 363 global IGS stations, there was no mention regarding the height dependency of equation 5.3 as noted by Steigenberger et al (2009).

### 5.2.3 Results and Discussion

The comparison is broken into two main analysis: (a) 11-year time series between unbvmfG and the existing VMF1 service; and (b) 8-month time series between all UNB-VMF1 products and the existing VMF1 service. A typical outlier detection analysis based on the mean and standard deviation has not been completed, since spikes in the time series that represent mapping function differences may be removed. For example, Figure 5.29 plots a time series for the difference in height at station OHI2. Three time series are plotted in figure 5.29, the actual height difference by PPP (red), the equivalent height error due to the hydrostatic component (blue), and the non-hydrostatic component (green). The equivalent height difference has been computed by interpolating at the position of OHI2 and averaging the  $4\times$  daily values in the equivalent height error data cubes (see Figure 5.1). The data spikes shown in the actual time series also exist in the equivalent height error time series. These data spikes may be incorrectly removed with an outlier test based solely on the mean and standard deviation of the difference.

Lastly, for the computation of the standard deviation of the time series, equation 3.7 has been fitted to the resulting coordinate difference time series. The resulting fitted trend has been subtracted from the time series, and the corresponding standard deviation has been computed by equation 3.8.

Therefore, all data points have been considered of equal weight and the removal of any data point in the time series was made if any of the following conditions were experienced:

1. The total number of epochs used to compute the solution was less than 216. Since 5min intervals are used in GAPS, 18 hours equates to a minimum of 216 epochs used to compute the final solution.

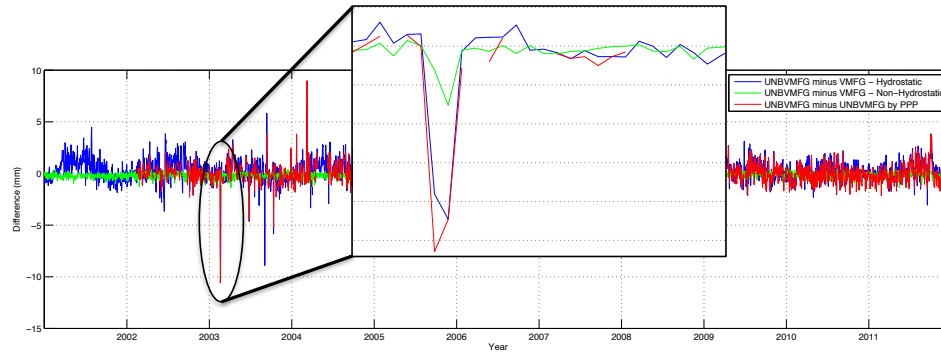


Figure 5.29: Station OHI2 time series of the difference in height for (a) PPP results (red); (b) due to the hydrostatic component (blue); and (c) due to the non-hydrostatic component.

2. The satellites used to compute each solution pair do not match (e.g. unbvfmG and vmfG). In GAPS, the carrier-phase and code measurement residual limits are set to 1 m and 10 m respectively. If the satellite residual exceeds this limit, the satellite is removed from the analysis as an outlier. Occasionally, the substitution of different mapping functions changes the residuals enough that the satellite is rejected from the analysis. Since the satellites used to compute the two solutions are now different, a spike in the time series occurs due to the fact that the geometry of the two solutions has been changed.
3. Excessively large carrier-phase residuals. Occasionally, a solution exhibited excessively large unexplained carrier phase residuals on the order of 0.5-0.8 m.
4. Numerical instability. The initial solution in GAPS can become numerically unstable if the number of satellites is less than the number of parameters. This results in excessively large condition numbers for the matrix of normal equations and manifests itself as enormously large solutions. When this occurs there is not enough time for the solution to converge to an appropriate precision resulting in a spike in the time series.

The application of the above condition has been made for all comparisons. For the 11-year analysis a total of 108,834 solutions have been computed (includes all 32 stations).

The application of the above conditions resulted in the removal of approximately 4% of all solutions across the entire 11-year time span. Gaps in the time series presented in this chapter and Appendix D are the result of the application of the above criteria and data availability at the IGS.

### **5.2.3.1 UNB-VMF1 (NCEP) vs VMF1 (ECMWF)**

The main comparison extends from the year 2001 to 2011 inclusively. Table 5.10 summarizes the overall yearly bias and RMSE for the difference in the latitude and longitude. For the difference in the height component, the mean bias, RMSE, standard deviation and the  $3\sigma$  range has been computed for all 32 stations. The overall effect on the horizontal component is at the sub-mm level and at the mm-level for the height component, so this study will focus on the effect on the height component. Overall, the PPP results for each year agree at the sub-mm level with the predicted equivalent height error estimates (see §5.1). Figure 5.30 plots the yearly bias and their respective RMSE as error bars for the difference in the height component. Figure 5.30 illustrates that the global bias is consistent at the sub-mm level for the entire interval and is consistently negative, meaning that the UNB-VMF1 computed heights are lower than those computed by the existing VMF1 service. The yearly global RMSE is also consistent between all years at the sub-mm level and with respect to the existing service at the mm-level, but a small oscillation is present across the interval. However, the magnitude of this oscillation is at the sub-mm level and it is not considered significant, and is likely related to the fact that some years do not include the same number of stations due to IGS observation file availability. In particular, 2001 only includes 20 stations due to data availability, 28 stations for 2002, 29 stations for 2003, 31 stations from 2004 to 2007 and all 32 stations from 2008 to 2011. Further, station POVE is only included from the years 2008 to 2011, but it exhibits the second largest RMSE errors (See table D-1) for all stations studied, which will result in an increase of the overall yearly RMSE relative to the other years.



Table 5.10: Summary of yearly bias and RMSE for UNB-VMF1 (NCEP) minus VMF1 (ECMWF) for 2001 to 2011. All dimensions in millimetres.

Year	Latitude		Longitude		Height			$3\sigma$ Range	
	Bias	RMSE	Bias	RMSE	Bias	RMSE	$\sigma$	Min	Max
2001	-0.0	0.1	-0.0	0.2	-0.4	1.0	0.8	-2.7	1.9
2002	-0.0	0.1	-0.0	0.1	-0.5	1.2	0.9	-3.3	2.2
2003	-0.0	0.1	-0.0	0.1	-0.6	1.2	0.8	-3.2	2.0
2004	-0.0	0.0	-0.0	0.1	-0.5	1.1	0.8	-3.0	1.8
2005	0.0	0.0	0.0	0.1	-0.6	1.0	0.7	-2.7	1.5
2006	-0.0	0.0	-0.0	0.1	-0.6	1.0	0.7	-2.9	1.7
2007	-0.0	0.0	-0.0	0.1	-0.5	1.0	0.7	-2.7	1.7
2008	0.0	0.0	-0.0	0.1	-0.6	1.2	0.8	-3.1	1.8
2009	-0.0	0.0	0.0	0.1	-0.6	1.2	0.9	-3.2	2.0
2010	-0.0	0.0	-0.0	0.1	-0.7	1.3	0.9	-3.4	2.0
2011	0.0	0.0	-0.0	0.1	-0.7	1.3	0.9	-3.4	2.0
Combined	-0.0	0.0	-0.0	0.1	-0.6	1.2	0.8	-3.2	2.0

Differences can exceed 10 mm with a maximum absolute value of 11.46 mm occurring at station NYAL in the year 2004. The total 11-year bias is -0.6 mm, the total RMSE is 1.2 mm and the overall standard deviation is 0.9 mm. Taking the  $3\sigma$  standard deviation and the overall 11-year bias into account, the overall difference between the UNB-VMF1 (NCEP) and the existing service can be expected to fall within the range of -3.2 mm and 2.0 mm. To assess the significance of these differences a statistical test is typically employed to test if the mean difference is significant at the 95% confidence level. However, the main underlying assumption for many of the statistical tests is that the data sets are independent and normally distributed. Due to the data spikes shifting the distribution from normal, and the fact the two datasets are not independent since they have been produced from the same observations, standard statistical tests of significance cannot be used. Additionally, the size of the dataset increases the power of a standard test on the means to a point where very small differences in the mean will be considered significant. Therefore, the differences will be assessed with respect to the known accuracy of the VMF1 as was done in §5.1. The accuracy of the VMF1 has been determined to be 3 mm by Niell (2006),

so if any results exceed this amount the differences are then considered significant. For the 11-year time series at the  $1\sigma$  level, the differences between the NCEP based UNB-VMF1 (unbvmfG) and the existing service fall well below this criteria, and can be considered equivalent. However, evaluating the  $3\sigma$  values applied to the yearly mean biases, which provides approximately a 99% confidence level, shows that the results can exceed this criteria. The overall global  $3\sigma$  difference in height between the unbvmfG and vmfG solutions exceed this 3 mm criteria for 7 of the 11 years studied, but only at the sub-mm level.

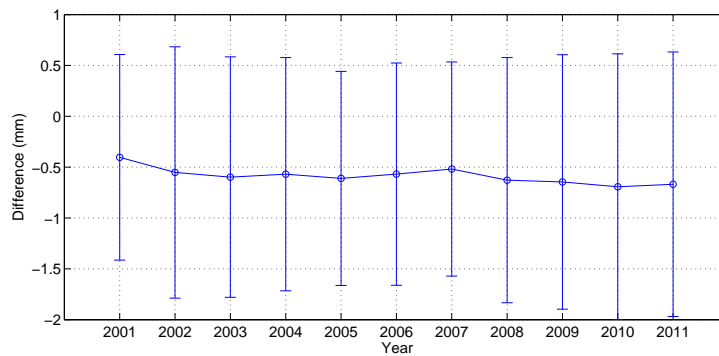


Figure 5.30: Yearly bias for UNB-VMF1 (NCEP) minus VMF1 (ECMWF) for all 32 stations and associated error bars.

Table D.2 in Appendix D tabulates the individual station results for the differences in height between unbvmfG and vmfG covering 2001 to 2011, as well as the overall 11-year result. Taking into consideration the overall 11-year differences in height, out of the 32 stations, only 8 stations exceed the 3 mm limit at the  $3\sigma$  level, namely IQQE, HARV, POVE, PDEL, MAS1, DARW, OUS2, and SCUB. All of these stations are coastal stations, with the exception of POVE, and the previous section (§5.1.3.1.3) has identified that the NCEP Re-Analysis 1 dataset experiences difficulties in coastal locales due to the coarse horizontal resolution and the underlying nature of the model itself (e.g. Gibbs effect and mean orography). Station POVE is located in the Amazon region (close to the equator), so any difficulty the NWP has with predicting the water vapour content will be reflected in these results. Further, these identified stations also exhibit a mean bias larger than 1 mm.

Since the  $3\sigma$  range is centred on the mean bias, any station that experiences a larger bias will be at a greater risk of exceeding the 3 mm criteria. The previous section demonstrated a latitude dependent bias for the difference in the hydrostatic mapping function, so in general, stations closer to the equator will be more prone to exceed the 3 mm criteria even if they have smaller standard deviations. Out of the 8 stations identified, 5 stations are located within  $\pm 20^\circ$  of the equator and 7 stations are location within  $\pm 40^\circ$  of the equator.

Figure 5.31 plots all the height differences for all 32 stations for all daily solutions covering the entire 11-year interval. Although the RMSE is at the mm-level, large cm-level differences can occur. These differences occur between the years 2002 to 2004 (highlighted in yellow). For the remainder of the time series, the maximum differences for all but one station, SCUB, stay below 5 mm. These results correspond with the results of §5.2, where the years 2002-2004 were identified as containing the largest absolute value of the difference in the mapping functions expressed as an equivalent height (see Figure 5.9). Station SCUB identified in Figure 5.31 not only experiences height differences larger than 5 mm, but it also exhibits a strong seasonal oscillation for the studied time period. Out of the 32 stations, 11 stations exhibited a seasonal effect of amplitudes.

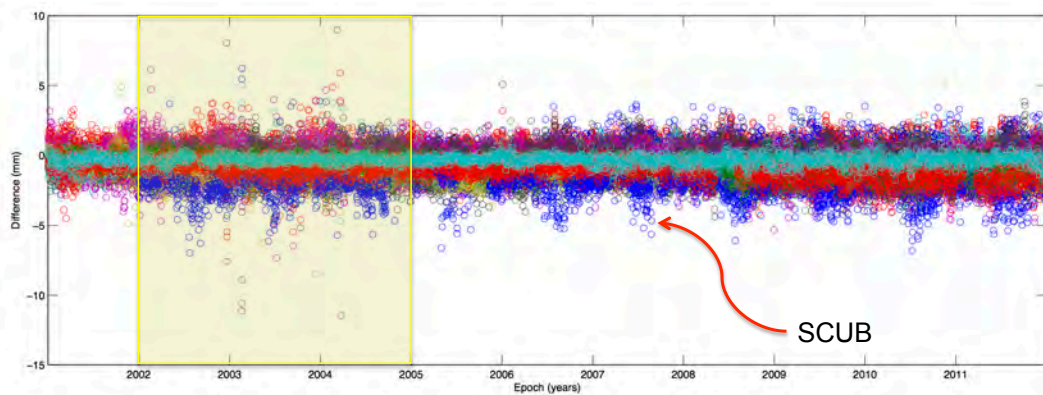


Figure 5.31: Position differences from the PPP solution fro station SCUB. unbvmfG (NCEP) minus vmfG (ECMWF). 2001 to 2011.

Figure 5.32 plots the coordinate differences for station SCUB, which illustrates a typical oscillation in the difference of the height component. The horizontal dashed lines

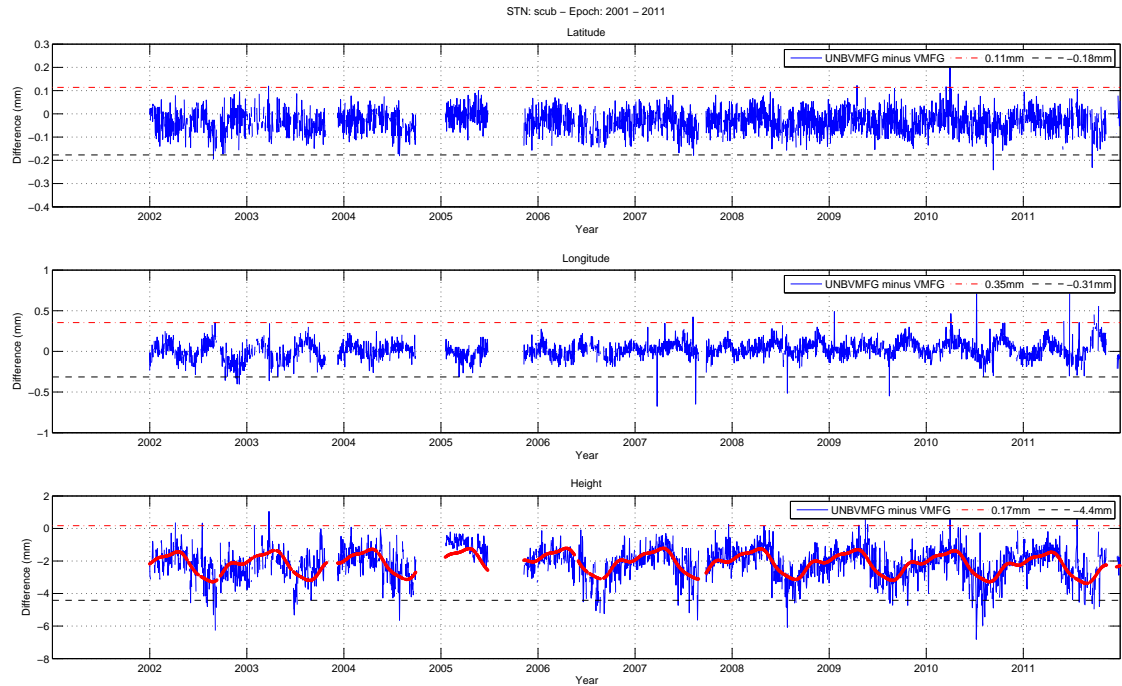


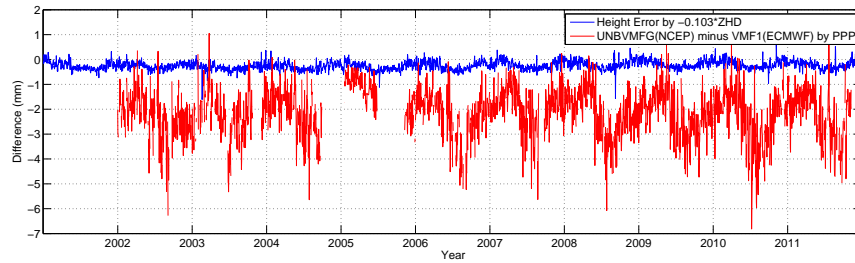
Figure 5.32: All differences in height for all 32 stations, for all daily solutions from 2001 to 2011. unbvmfG (NCEP) minus vmfG (ECMWF).

in the plot represent the  $3\sigma$  differences and the red line in the height time series is the fit by equation 3.7. The fitted trend for station SCUB exhibits a seasonal oscillation on the order of  $\pm 2$  mm, which is the largest for all stations studied. In addition to the seasonal trend in the height component, a similar trend can be found in the difference in longitude component. This seasonal trend found in the longitude difference is present in several of the tested station solutions, but it is at the sub-mm level and is not considered to be significant. All similar plots for all other stations can be found in Appendix D.

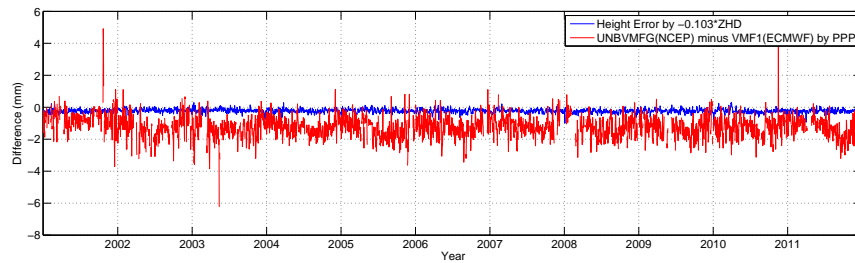
The source of the seasonal trend is ultimately due to differences in the NWP's propagating into the hydrostatic zenith delay and mapping function computations. Chapter 3 illustrated that the NWP's skill is diminished during the winter months (or summer for the specific humidity), where the NWP exhibits a larger RMSE with respect to in-situ measurements. Since each of the NWP's are more variable during these times, it is rea-

sonable to expect the comparison of a height solution computed with different mapping functions and/or hydrostatic zenith delays based on different NWP models will also be more variable. However, it is worthwhile to investigate whether the differences are mainly due to the hydrostatic/non-hydrostatic mapping function separation errors, or due to the differences in the mapping functions. Kouba (2009) evaluated the impact of an error in the *a-priori* hydrostatic delay on the height component in a PPP analysis. Kouba (2009) concluded that, at an elevation angle of  $5^\circ$  with elevation angle dependency weighting ( $1/\sin(\epsilon)$ ) the mean difference in height due to an error of +10 mm in the *a-priori* hydrostatic zenith delay results in a -1.03 mm error in the height component. Therefore, the application of this factor,  $-0.103\Delta zhd$ , to the difference in the hydrostatic zenith delays, and then comparing the results to the actual height difference (by PPP) time series will help to identify if this is the major source of the error. Figure 5.33 plots the actual PPP height error and the corresponding estimated height error due to the hydrostatic/non-hydrostatic mapping function separation for station SCUB and DARW. The hydrostatic zenith delay has been extracted from the gridded products (UNB-VMF1 and VMF1 data cubes - see §5.1.2) by a two-dimensional linear interpolation and then the four 6-hourly values were averaged for an approximate daily value. At SCUB and DARW, the effect of the separation error, as suggested by Kouba (2009), is much too small to be the sole source of the discrepancy, so the differences in the mapping function realizations must be the dominant source of error at these stations. However, other stations exhibited larger influences due to the separation error, such as TEHN and PETS (not shown), but for the majority of stations studied the effect was small in comparison to the effect of the mapping function differences.

Figure 5.34 plots the differences in the hydrostatic (blue) and non-hydrostatic mapping functions (green) expressed as equivalent height error (see §5.1), and the difference in height from the PPP solution (red) for stations SCUB and DARW. As with the hydrostatic/non-hydrostatic separation errors, the hydrostatic/non-hydrostatic mapping function errors have been interpolated two-dimensionally from the gridded product differences



(a) STN: SCUB

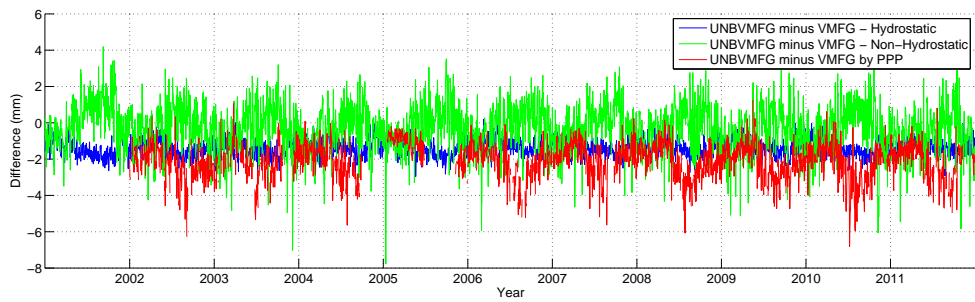


(b) STN: DARW

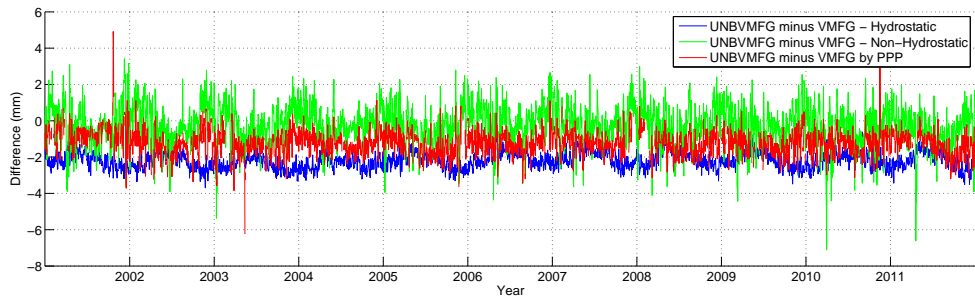
Figure 5.33: Difference in height from the PPP solution (red) and hydrostatic/non-hydrostatic mapping function separation error (blue). unbmvg (NCEP) minus vmfG (ECMWF).

at the specified station coordinates. For station SCUB (5.34(a)), the larger height differences during the summer months are in phase with the non-hydrostatic equivalent height error, but it is opposite in sign. The fact that the results exhibit an opposite sign to the predicted non-hydrostatic equivalent height error is unknown, but the PPP results clearly exhibits an increased RMSE during the summer months following the non-hydrostatic equivalent height error. During the winter months at SCUB, the differences in height from the PPP solution follow the trend of the hydrostatic equivalent height error. For Station DARW (5.34(b)), the differences in the PPP height solution more closely follow the non-hydrostatic equivalent height error in the summer months. The height differences of the PPP solution are pulled away from the hydrostatic equivalent height errors towards the non-hydrostatic errors during the summer months. Moreover, in both cases the non-hydrostatic equivalent height error is much noisier than that of the hydrostatic equivalent height error, which more closely resembles the PPP height solution differences.

Stations SCUB and DARW are stations located close to the equator, and for stations

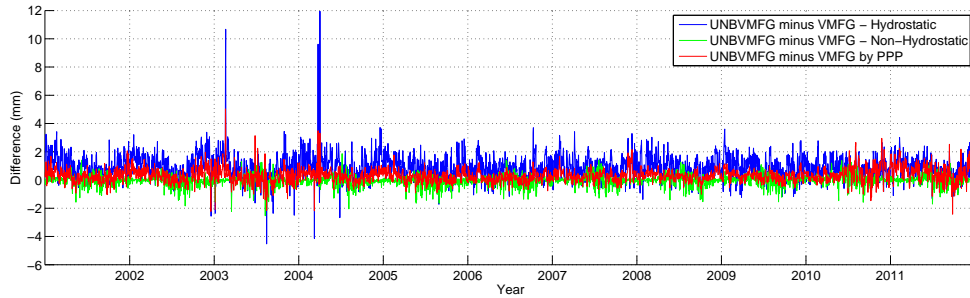


(a) STN: SCUB

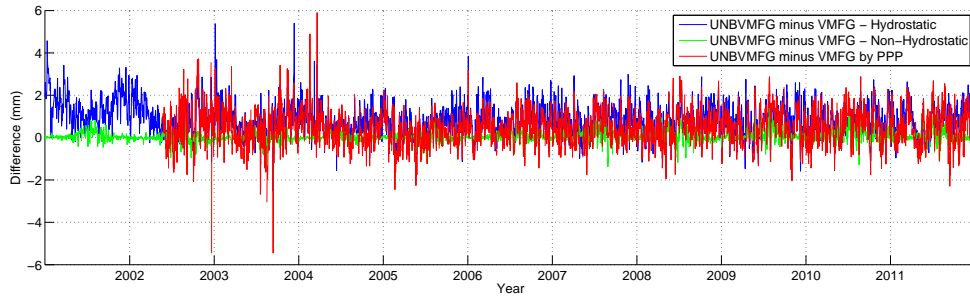


(b) STN: DARW

Figure 5.34: Difference in height from the PPP solution (red) and non-hydrostatic equivalent height error (green), and hydrostatic equivalent height error (blue). unbvmfG (NCEP) minus vmfG (ECMWF).



(a) STN: YELL



(b) STN: THU3

Figure 5.35: Difference in height from the PPP solution (red) and non-hydrostatic equivalent height error (green), and hydrostatic equivalent height error (blue) for stations (a) YELL and (b) THU3. unbvmfG (NCEP) minus vmfG (ECMWF).

located in this region the difference in height from the PPP solution tend to follow the non-hydrostatic mapping function errors. Stations that reside in locations where the water vapour content is much less, the difference in height will tend to follow that of the hydrostatic mapping function error. Figure 5.35 plots the difference in height for stations YELL and THU3, which are located in high latitude regions that exhibit a much smaller water vapour content.

Overall, Figures 5.34 and 5.35 illustrates the general influence of the difference in the NWP's implemented for each product, and illustrates that the largest differences are mainly due to differences in the realization of the mapping functions, not the *a-priori* hydrostatic zenith delays. In geographic locations and seasons where the water vapour content is largest, the NWP has a more difficult time in its prediction (see Chapter 3). This is reflected in the difference in height solution, where stations located in equatorial regions (i.e SCUB/DARW) exhibited trends that followed the differences in the non-hydrostatic



mapping functions more closely. Moreover, Figure 5.36 plots the RMSE for difference in height between unbvmfG (NCEP) and vmfG (ECMWF) at each station with respect to latitude. Also plotted in Figure 5.36 is a line of best fit estimating the overall trend, which is shown with the solid line. The line of best fit has been computed using a summation of sine functions truncated at one coefficient. The following equation describes the fit:

$$y = \sum_n^{i=1} a_1 \sin(b_i x + c_i) \quad (5.6)$$

Figure 5.36 exhibits a small trend where stations located in equatorial regions tend to exhibit a larger RMSE. This makes sense, since the water vapour content in the equatorial region is largest, and previous results have demonstrated that the NWP's experience larger errors when water vapour content is increasing (Yang et al., 1999). Additionally, stations in the southern hemisphere appear to be experiencing a larger RMSE error than stations at equivalent latitudes in the northern hemisphere. This is most likely related to stations selection, in that out of the 9 stations selected in the southern hemisphere, 5 are located in regions identified in §5.1.3 as being marginal due to difference in the NWP (3 along the western coast of South America, 1 along the south western coast of Africa, and 1 in the Antarctica).

Lastly, the results from §5.1 indicated that a latitude dependent bias exists due to the ray-tracing differences between the UNB-VMF1 and the existing VMF1 services. Figure 5.37 plots the mean bias in height between unbvmfG and vmfG from the PPP solutions with respect to latitude. Additionally, a line of best fit has been plotted by equation 5.6 and is shown as a solid line. The magnitude of the bias is on the order of approximately  $\pm 1.5$  mm, which confirms the results from the §5.1.

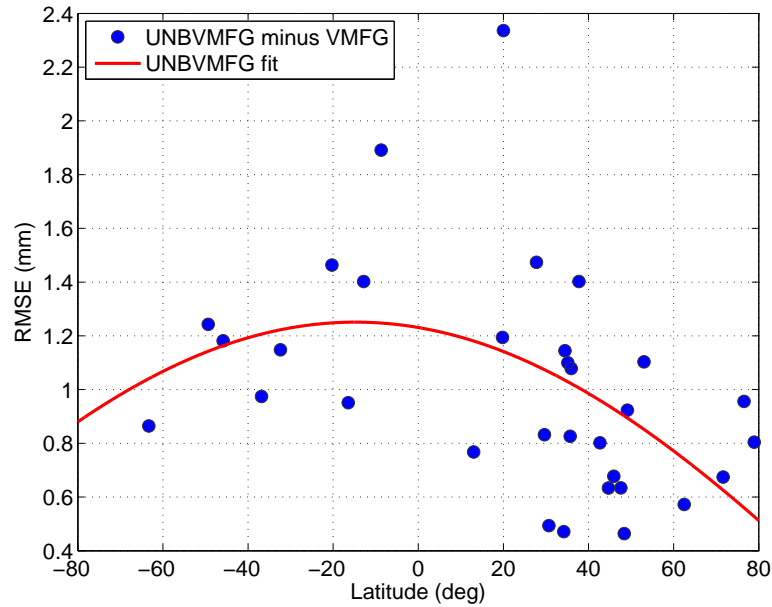


Figure 5.36: RMSE of the difference in height with respect to latitude for all 32 stations. unbvmfG (NCEP) minus vmfG (ECMWF). 2001 to 2011.

### 5.2.3.2 UNB-VMF1 vs VMF1 (All Products)

This section provides a summary of the comparison of PPP results for all of the UNB-VMF1 products, namely: (a) unbvmfG (NCEP); (b) unbvmfGcmc (CMC); (c) unbvmfP (CMC). First, the standard gridded products unbvmfG and unbvmfGcmc with respect to the existing VMF1 service are compared for the year 2012 (January 1st to August 31st). Figure 5.38 plots the difference in height for all 32 stations, where 5.38(a) is the mean bias and 5.38(b) is the RMSE. Overall, the CMC based VMF1, unbvmfGcmc, is a clear improvement with respect to the existing VMF1 service. Out of 32 stations, 25 stations produced with unbvmfGcmc exhibited smaller biases with respect to the existing VMF1 service. Out of the seven stations that exhibited the larger biases from the CMC based product, the majority are located in high latitude regions (4 stations of the identified 7). In general, the polar regions will exhibit larger differences between NWP, since in-situ observations are sparsely available [Asmus et al., 2007]. The NWP is highly dependent on the initial conditions, and as noted by Lorenz (1969), small differences in the initial con-

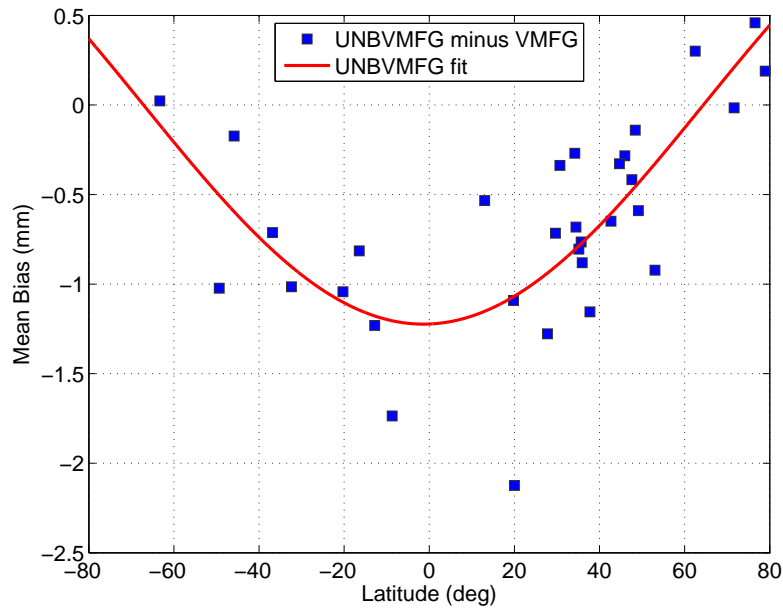
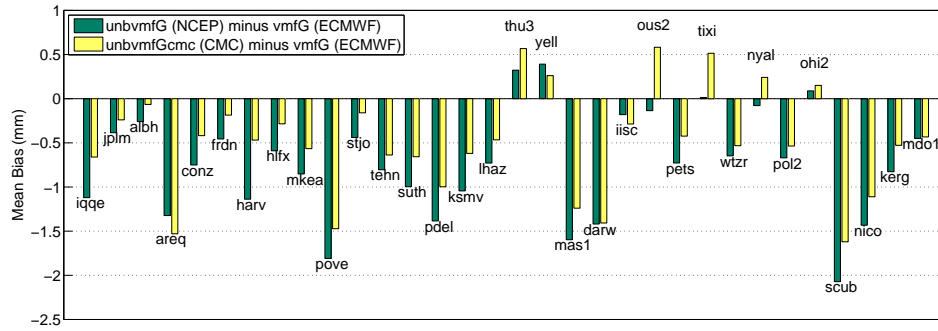


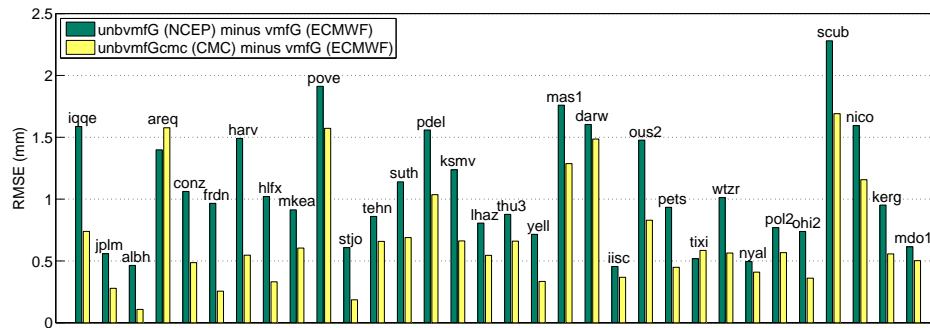
Figure 5.37: Mean Bias for the difference in height for all 32 stations. unbvmfG (NCEP) minus vmfG (ECMWF). 2001 to 2011.

ditions will greatly affect the forecasts, which will be reflected in the VMF1 realizations that will ultimately propagate into the position results. Overall, seven stations produced with unbvmfGcmc exhibited larger biases than unbvmfG (NCEP), and only one station (AREQ) produced with unbvmfGcmc exhibited a larger RMSE value when compared to unbvmfG. As with the 11-year unbvmfG (NCEP) evaluation, unbvmfGcmc exhibits the same latitude dependent bias, and in general, the stations found closer to the equator experience larger RMSE values. For the three stations located along the western coast of South America (AREQ, IQQE and CONZ), unbvmfGcmc exhibited approximately 54% reduction in the RMSE and a 34% reduction in the bias for IQQE and CONZ with respect to unbvmfG. Interestingly, station AREQ experiences an increase in the bias and RMSE, but AREQ is located further north and outside of the identified region of increased variability (see §5.1.3).

Figure 5.39 plots the histogram for all differences at all of the 32 selected stations for unbvmfG and unbvmfGcmc. The NCEP based product, unbvmfG, is shown blue and the



(a) Mean Bias



(b) RMSE

Figure 5.38: (a) Mean and (b) RMSE of the difference in height between UNB-VMF1 and VMF1 for (i) unbvmfG (NCEP) minus vmfG (ECMWF) shown in green and (b) unbvmfGcmc (CMC) minus vmfG (ECMWF) shown in yellow. January 1st to August 31st, 2012. All values in millimetres.

CMC based product is shown in red. The overall mean bias for the unbvmfG is -0.7 mm and -0.5 mm for the unbvmfGcmc. The overall RMSE for unbvmfG is 1.1 mm and 0.8 mm for unbvmfGcmc. Considering all 32 stations, unbvmfGcmc exhibits a 10% smaller bias and a 30% reduction in the RMSE with respect to unbvmfG. Additionally, unbvmfGcmc experiences much smaller data spikes throughout the time series. For example, unbvmfG exhibited spikes as much as 6.4 mm as opposed to 3.5 mm exhibited by unbvmfGcmc. All time series for all stations can be found in Appendix D.

Lastly, is the comparison of the predicted product, unbvmfP. Figure 5.40 summarizes the differences in the height component for the unbvmfP product with respect to

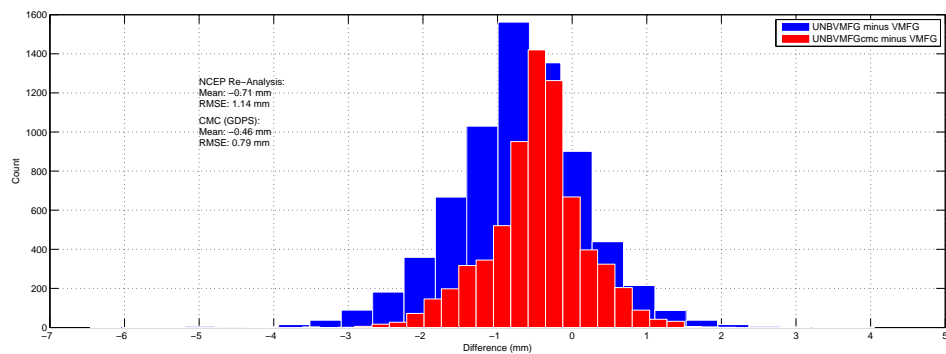
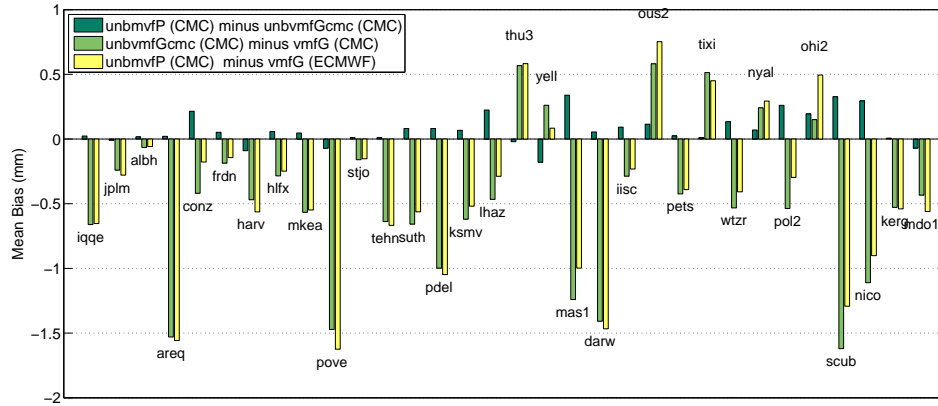
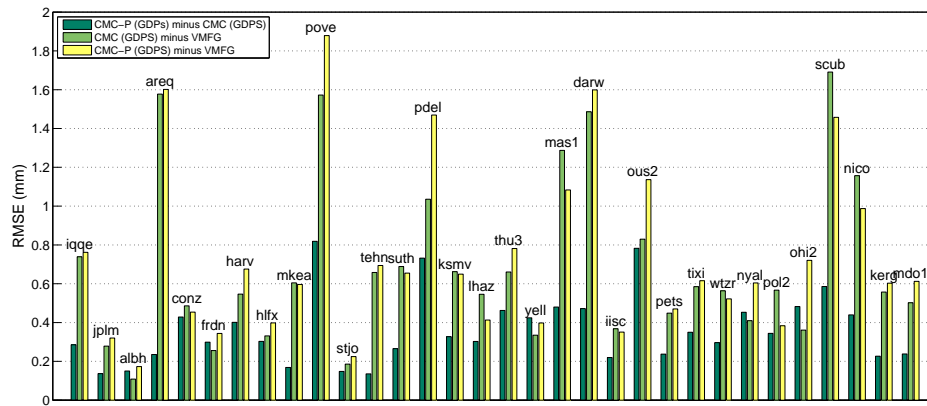


Figure 5.39: Histogram for the difference in height for (a) unbvmfG (NCEP) minus vmfG (ECMWF) shown in blue, (b) unbvmfGcmc (CMC) minus vmfG (ECMWF) shown in red.

the existing VMF1 service and with the unbvmfGcmc. The results of the unbvmfGcmc comparison with respect to the existing VMF1 service is also included in Figure 5.40 as reference. In particular, Figure 5.40 plots the difference of unbvmfP with respect to unbvmfGcmc (dark green), unbvmfGcmc with respect to the existing VMF1 service (light green), and unbvmfP with respect to the existing VMF1 service (yellow). First, the unbvmfP is compared with unbvmfGcmc. Both realizations of the VMF1 agree very well with each other as the results for all stations exhibit a sub-mm mean bias and sub-mm RMSE. When comparing to the existing VMF1 service, the forecast based product, unbvmfP, experiences larger biases and RMSE as compared to unbvmfGcmc. This is to be expected as the NWP skill degrades with time, which is inherent to the NWP. However, there are some stations that actually experience a smaller bias and RMSE. The most likely reason for this is the fact that the comparison of the predicted product begins March 17th as opposed to unbvmfGcmc, which begins January 1st. Chapter 3 established the seasonal trends of the meteorological parameters, where the NWP's exhibited larger variation during the winter months for pressure and summer months for specific humidity. Therefore, the unbvmfP comparison does not include the winter months as does the unbvmfGcmc comparison. In spite of this, the overall mean and RMSE of unbvmfGcmc is still less than unbvmfP.



(a) Mean Bias



(b) RMSE

Figure 5.40: (a) Mean and (b) RMSE difference in height for (i) unbvmfP (CMC) minus unbvmfGcmc (CMC) (ii) unbvmfGcmc (CMC) minus vmfG (ECMWF); and (iii) unbvmfP (CMC) minus vmfG (ECMWF). March 17th to August 31st, 2012. Please note item (ii) extends from January 1st to August 31st, 2012. All dimensions in millimetres.

Table 5.11 summarizes the results for all the comparisons, where the mean bias, RMSE,  $3\sigma$  range, and the maximum absolute value of the differences are summarized. Overall, the standard CMC based product, unbvmfGcmc, performed best. The forecast based product, unbvmfP, performed second best, followed by the NCEP based product, unbvmfG. The overall assessment of these products are made with respect to the 3 mm criteria established by Niell (2006) and implemented in all previous comparisons within

this work. At the  $1\sigma$  level all UNB-VMF1 products can be considered equivalent to the existing VMF1 (as well as the forecast product, unbvmfP, when compared to the standard CMC based product, unbvmfGcmc) as they all fall below this 3 mm criteria. However, evaluating the results at  $3\sigma$ , the unbvmfG (NCEP) product exceeds this criteria, but only at the sub-mm level. These results follow that of the 11-year comparison as well as the global comparison in the gridded domain. Evaluating the individual stations for the NCEP based product, the same eight stations noted in §5.4.2.1 that exceeded the 3 mm criteria also exceed this criteria for the 2012 interval (station NICO also exceeds this amount for the 2012 comparison). In contrast, all of the CMC based products meet this criteria at the  $3\sigma$  level and can be considered equivalent to the product from the existing VMF1 service. For the standard CMC based product (unbvmfGcmc), all stations fall below the 3 mm criteria at the  $3\sigma$  level, and for the forecast based product (unbvmfP) only 2 stations exceeds this amount, but only by a very small amount (station PDEL at -3.1 mm and OUS2 at 3.2 mm). Tables D-2 and D-3 found in Appendix D tabulate all of the individual station results for each of the comparisons listed in Table 5.11.

Table 5.11: Summary of difference in the height component for all UNB-VMF1 comparisons for mean bias, RMSE, standard deviation, and maximum absolute difference. All values in millimetres for the year 2012.

Product	Reference	Epoch	Mean	RMSE	$\sigma$	3 $\sigma$ Range		Max Abs
						Min	Max	
unbvmfG	vmfG	01-01 to 08-31	-0.7	1.1	0.9	-3.4	1.9	6.4
unbvmfGcmc	vmfG	01-01 to 08-31	-0.5	0.8	0.6	-2.4	1.5	3.6
unbvmfP	unbvmfGcmc	03-17 to 08-31	0.1	0.4	0.4	-1.1	1.2	6.6
unbvmfP	vmfG	03-17 to 08-31	-0.4	0.8	0.7	-2.6	1.8	12.8

## 5.2.4 Elevation Angle Cut-Off

In general, the total error in height will be a combination of the geometric effects and the accuracy of the atmospheric model [Niell, 2006]. As the elevation angle is decreased,

differences between atmospheric modelling will become larger and geometric effects will be reduced. In the case of using the Marini continued fractional form for the mapping function, a  $\sin(e)$  term is in the denominator, so as the elevation angle is increased so does the mapping function. Taking the formal error of the Marini continued fraction (equation 4.1) with respect to the  $a$  coefficient only, (this is the only term computed for the VMF1, since the  $b$  and  $c$  coefficient are considered known and errorless) also results in a  $\sin(e)$  term in the denominator of the differential, which is shown in equation 5.7.

$$\sigma_{mf}^2 = \left( \frac{da}{d(mf)} \right)^2 \sigma_a^2 \quad (5.7)$$

$$\frac{da}{d(mf)} = \left( \frac{1}{\left(\frac{b}{c+1}+1\right) \left(\sin(e)+\frac{a}{\sin(e)+\frac{b}{c+\sin(e)}}\right)} - \frac{\frac{\frac{a}{c+1}+1}{\frac{b}{c+1}+1}}{\left(\sin(e)+\frac{a}{\sin(e)+\frac{b}{c+\sin(e)}}\right)^2 \left(\sin(e)+\frac{b}{c+\sin(e)}\right)} \right) \quad (5.8)$$

Therefore, as the elevation angle is increased the value of the differential will also decrease, thus decreasing the formal error of the mapping function, and allowing the form to be less sensitive to errors in the  $a$ -coefficient. For example, assuming that  $\sigma_a$  is  $10^{-5}$ , the day of the year is 196, the latitude is  $46^\circ\text{N}$ ,  $a$  is 0.00126618,  $b$  is 0.0029 and  $c$  is 0.062325457 by equation 4.2, then the value of the differential in equation 5.7 is -159.833 (unitless) at an elevation angle of  $10^\circ$  and -947.921 (unitless) at an elevation angle of  $5^\circ$ . Since  $\sigma_a$  remains the same in both cases (5 and 10 degrees), the formal error is reduced as the elevation angle is increased from 5 to 10 degrees.

When the VMF1 is realized, it is the  $a$  coefficient of the Marini continued fraction that is defined. The definition of the  $a$  coefficient will be dependent on the ray-tracing scheme and the definition of the atmosphere (e.g. a NWP), where differing ray-tracing schemes and NWPs will result in differences in the  $a$  coefficient. For this discussion, the difference in the  $a$  coefficient due to the mapping function realization can be considered to be  $\sigma_a$ . Applying the above results means that as the elevation cutoff angle is increased,



the sensitivity to differences in the  $a$  coefficient is reduced. Therefore, the same formal error can be achieved at higher elevation angles than those at lower elevation angles with a larger  $\sigma_a$ . This also means that at an equivalent  $\sigma_a$ , the differences in mapping function realizations are reduced, resulting in smaller differences in the position components — specifically the height component.

These results are tested through the computation of the coordinates of 32 IGS stations by PPP using three elevation angle cutoff values, namely  $0^\circ$ ,  $5^\circ$ , and  $10^\circ$ . The test was completed only for the NCEP based product, unbvmfG, since it exhibited the largest bias and RMSE in all tests, and it is necessary to establish under which conditions the poorest performing product. The same processing parameters for GAPS that was used for the §5.3.3 and §5.3.4 were also implemented. The only difference being the elevation cutoff angle. The geometric effects will be the same for each of the stations, so the coordinate differences will cancel out this effect and the atmospheric modelling effects should be the major effect remaining. Table 5.12 summarizes the overall mean bias and RMSE for all 32 stations at each of the specified cutoff elevation angles. As expected, the overall mean bias and RMSE has been reduced when the elevation angle is increased. When the cutoff elevation angle is set to  $10^\circ$ , the mean bias and RMSE agrees very well with the standard CMC based product, unbvmfGcmc, at an elevation angle of  $5^\circ$ . Overall, an increase in the elevation angle from  $0^\circ$  to  $5^\circ$  resulted in a 11% reduction in the bias and 26% reduction in the RMSE. The reduction from  $5^\circ$  to  $10^\circ$  resulted in the reduction of the bias by approximately 50% and RMSE by approximately 45%.

Of all stations tested, there were stations that exhibited no real appreciable difference over any elevation angle. Out of the 32 stations tested, 6 stations did not show any appreciable difference, namely IQQE, JPLM, ALBH, STJO, TEHN, and IISC. These results are due to the fact that these stations do not see any satellites below a  $10^\circ$  elevation angle, so the results for each station at  $0^\circ$  and  $5^\circ$  cutoff elevation angles are actually the same as the specified  $10^\circ$  solution. These stations have been excluded from the results presented

Table 5.12: Summary of elevation angle dependance for UNB-VMF1 (NCEP) minus VMF1 (ECMWF). Results for the interval January 1st, 2012 to August 31, 2012 (includes all stations). Dimensions in millimetres.

Elevation Angle (°)	Latitude		Longitude		Height	
	Bias	RMSE	Bias	RMSE	Bias	RMSE
0	0.0	0.0	0.0	0.1	-0.9	1.5
5	0.0	0.0	0.0	0.1	-0.8	1.1
10	0.0	0.0	0.0	0.1	-0.4	0.6

in Table 5.12.

## 5.2.5 Summary and Recommendations

This section provided an assessment of all of the UNB-VMF1 products against the existing VMF1 service’s gridded product in the position domain. UNB’s GAPS PPP software has been implemented for the computation of station positions over three different intervals. First, the NCEP based product, unbvmfG, was compared to the existing service for 11 years starting in January 1st 2001 and ending December 31st 2011. The results of this test illustrated that the overall global bias and RMSE across the 11-years agree well each other at the sub-mm level. The differences in the two realizations of the VMF1 (unbvmfG and vmfG) over the 11-year interval have very little effect on the horizontal component. It was shown that differences in the coordinates were at the sub-mm level for both the bias and RMSE. The greatest effect is on the height component, where the overall 11-year bias and RMSE have been computed to be -0.6 mm and 1.2 mm respectively. The PPP results confirmed the latitude dependent bias and demonstrated a small trend where stations located closer to the equator experienced larger RMSE values. The cause of the latitude dependent bias has been discussed in §5.1, which is due to the simplification of the shape of the Earth by the existing VMF1 service. The reason for the increased RMSE in the equatorial regions has been attributed to the non-hydrostatic mapping function differences

between the two products (unbvmfG and vmfG) as the non-hydrostatic mapping function differences appear to be the dominant source of the difference in these regions. Over the entire 11-year period, unbvmfG can be considered equivalent to the existing VMF1 service (vmfG) at the  $1\sigma$  level, but at the  $3\sigma$  level the overall difference exceeds the 3 mm acceptance criteria at the sub-mm level. Out of the 32 stations studied, only 8 stations exceeded this criteria at the  $3\sigma$  level, where 7 of the 8 stations are located in coastal regions and 1 station is located in the Amazon region (POVE).

A second test was completed that included the comparisons of all products (unbvmfG, unbvmfGcmc and unbvmfP) with respect to the existing VMF1 service covering an 8 and 6 month interval. The comparison of unbvmfG and unbvmfGcmc were completed over 8 months (Jan to Aug 2012) and the forecast base product, unbvmfP, was completed over 6 months (Mar to Aug 2012). In all comparisons, the NCEP based product, unbvmfG, performed worst, and the standard CMC based product, unbvmfGcmc, performed best followed by the forecast based product. The standard CMC based product, unbvmfGcmc, exhibited a 10% smaller bias and a 30% reduction in the RMSE over the standard NCEP product. All stations studied for the standard CMC based product fell below the 3 mm criteria at the  $1\sigma$  and  $3\sigma$  level and can be considered equivalent to the existing VMF1 service at locations. The forecast based product agrees very well with the standard CMC based product and all stations fall well below the 3 mm criteria at the  $3\sigma$  level. When compared to the existing VMF1 service, the forecast based product also falls below the 3 mm acceptance criteria in a global context, but two individual stations exceed this amount at the  $3\sigma$  level (all stations agree at the  $1\sigma$  level).

Lastly, a small examination regarding the effect of the elevation angle on the difference was completed. It was shown that at an elevation angle of  $10^\circ$  the NCEP based product can be considered equivalent to the CMC based product. Further, at a  $10^\circ$  elevation angle the NCEP based product did not exceed the 3 mm criteria at any location at the  $3\sigma$  level and can be considered equivalent to the existing service at all locations on the

globe.

# Chapter 6

## Conclusions and Recommendations

The objective of this research was to create a robust operational mapping function service based on the Vienna Mapping Functions (VMF1) and investigate the implications of the application of different source datasets (NWP) and ray-tracing techniques in the realization of the VMF1.

### 6.1 Summary

A UNB realization of the Vienna Mapping Functions, where the VMF1 variant has been implemented with an independent ray-tracing system, and an independent numerical weather prediction model from the existing VMF1 service has been successfully implemented. This new service will provide several benefits to the scientific/geodetic community. Firstly, it will improve the availability of troposphere delay products as this service can act as a backup to the existing one. Any service interruptions that were to occur with the current VMF1 service would result in a delay in the availability of the correction products, which can have an impact on any data processing downstream. The addition of the UNB-VMF1 alleviates this concern since the production of the corrections will now occur in redundant locations. Secondly, the addition of the UNB-VMF1 will help to support data processing efforts by the scientific/geodetic community with the addition of a completely independent

source of atmospheric corrections and help to achieve greater compatibility with other corrections derived from the same numerical weather prediction models implemented by this service (e.g. atmospheric pressure loading which uses NCEP Re-Analysis 1). Lastly, the addition of the UNB-VMF1 will help to stimulate research into neutral atmosphere delays and help to understand and characterize the implications of using numerical weather prediction models to compute these corrections.

The UNB-VMF1 offers three products to the community with varying latency and numerical weather prediction model data. First is `unbvmfG`, which is produced with NCEP's Re-Analysis 1 and is available with a 7 day latency. Next is `unbvmfGcmc`, which produced with CMC's GDPS and is available with a 1 day latency. Lastly, is `unbvmfP`, which is also produced with CMC's GDPS, but applies 24h,30h,36h and 42h forecasts in its production. All products are produced 4× daily on a  $2.0^{\circ} \times 2.5^{\circ}$  grid at 6H intervals in an ASCII text file format following the existing VMF1 service. All product data files are made available publicly through a web browser interface located at <http://unb-vmf1.gge.unb.ca> or by command line programs such as `wget`.

Important in the development of the UNB-VMF1 is the assurance that the system will operate in a consistent and robust manner. These goals have been met with the implementation of the main computational routines on ACE-NET. The system has been implemented on three nodes across Atlantic Canada (Fundy, Mahone and Placentia) ensuring that all products are produced simultaneously at three separate locations. Not only has the implementation on ACE-NET produced a robust system, it has also greatly reduced computation time with the application of parallel computing. The computation of a single product has been reduced by 75% with the application of some simple parallel computing principles.

Overall, the UNB-VMF1 service has been operating since January 2012 and was officially launched the following June. The current site averages approximately 250 unique visitors per months with a total of 16, 351 visits. Further, each of the 6-hourly data files

have accumulated approximately 5500 hits for the period June to December 2012. In addition, the service has received provisional approval from the GGFC and the IERS Directing Board. All products are part of the GGFC Provisional Products and the service has now embarked on the 2 year evaluation period with the goal of full approval for EGU 2014.

Chapter 3 discussed some of the defining characteristic of the NWP's selected and assessed their differences. §3.2 discussed the various NWP models available for selection and reasons for selecting NCEP and the CMC (GDPS). NCEP Re-Analysis 1 has been selected for superior availability, consistent model definition, and for compatibility with other geodetic corrections that have been derived from it. The shortcomings of the model is the coarse horizontal resolution and the fact that the NWP's operational underpinnings that define its physics and parameterizations have been frozen to the system definition in the mid-nineties. To provide a modern option, the CMC has been selected to produce a backup product to the UNB-VMF1. The benefit of the CMC (GDPS) is that it is modern operational model that contains the latest application of atmospheric physics and parameterizations. The shortcoming of the CMC (GDPS) is the fact that the data is only available for a 24 hour period which makes it less robust for an operational service.

§3.3 performed the assessment of two NWP's, NCEP Re-Analysis 1 and CMC (GDPS), and an empirical model based on a NWP, the GPT. The assessment consisted of the comparison of three meteorological parameters: pressure, temperature and specific humidity, and ray-traced hydrostatic zenith delays. In all cases, the results from the CMC exhibited the smallest mean differences and exhibited the smallest standard deviations of the difference. In all cases the GPT performed worst, but this is not unexpected since the GPT is a spherical harmonic expansion truncated at degree and order nine, and based on the ECMWF 40-year Re-Analysis for the years 1999 to 2002. The GPT models the seasonal and annual amplitudes of the pressure and temperature, but cannot deal with the daily fluctuations well. Additionally, any conditions that differ largely from the 3-year interval it has been based on will create further uncertainty.

Further, the assessment of the models exhibited seasonal trends where the standard deviations were larger during the winter months for pressure and temperature for all stations located in both the northern and southern hemisphere. The specific humidity experienced larger standard deviations during the summer months, which correlate well with the periods of increased precipitable water. For pressure and temperature, the GPT experienced the largest increase followed by NCEP and then the CMC. For specific humidity, the increase during the summer months is similar where NCEP experienced a 32% increase and the CMC experienced a 34% increase.

The results for the standard deviation of the difference for pressure from NCEP and the GPT exhibited a latitude dependent trend, and the results for specific humidity from NCEP and the CMC also exhibited a latitude dependent trend. Results for the pressure illustrated that stations at higher latitudes experience larger standard deviations, where the GPT exhibited the largest standard deviations. For the specific humidity stations closer to the equator experienced larger standard deviations where the water vapour content is largest.

The last experiment completed for Chapter 3 investigated a comparison of three different NWP models from the CMC with differing horizontal resolutions. Three models at 33 km (GDPS), 15 km (RDPS) and 2.5 km (HRDPS) were assessed against each other and against an independent dataset. The intention was to assess the value of high resolution NWP models in geodetic applications. The initial assessment compared the three models relative to each other. The HRDPS was used as the reference and the differences were computed for the RDPS and GDPS. These results indicated that there was no appreciable difference in terms of the hydrostatic mapping function expressed as equivalent height error. However, for the non-hydrostatic case, differences were observed up to the cm-level for the mapping function differences, but the higher resolution regional model performed worse relative to the HRDPS as opposed to the global GDPS, which indicates the current variability between NWP models in predicting the atmospheric water vapour content. The second



test, maybe the more definitive one, tested against measured meteorological parameters and hydrostatic zenith delays computed by Saastamoinen at three locations in Canada. Results indicated that there was no appreciable improvement with the use of the high resolution model (HRDPS) and the regional model at 15 km (RDPS) generally performed best among all three models in terms of the standard deviation of the difference.

Chapter 5 provided the validation of the UNB-VMF1 service against the existing VMF1 service. An assessment of all of the UNB-VMF1 products against the existing VMF1 service's gridded product in the gridded and position domain was completed over an 11-year period for the unbvmfG product, an 8 month period for the unbvmfGcmc product, and a 6 month period for the unbvmfP product. For the comparison in the gridded domain, a common theme throughout the comparisons is the importance in the selection of ray-tracing methods and the selection of the NWP source dataset. All products produced by the UNB-VMF1 service when compared to those of the existing service exhibit a latitude dependent bias, which has been shown to be due to differences in the definition of the radius of the Earth. Secondly, differences in the NWP datasets also contribute significantly in the realization of the mapping function. Results from the NCEP comparison (§5.2.2.1) showed that the underlying assumptions regarding the model orography, as well as the horizontal resolution, can create problems with accurately depicting atmospheric phenomena. Specifically, in regions of steep topography and in regions where there is high topographic relief in relation to a body of water the NCEP based mapping function proved to be noisier than those based from the CMC (The CMC's horizontal resolution is approximately four times more fine).

Overall, the NCEP based product, unbvmfG, performed the worst with respect to the existing service, and the CMC based product, unbvmfGcmc, performed best. The unbvmfGcmc product exhibited approximately a 41% reduction in the standard deviation of the ray-traced hydrostatic zenith delay and a reduction of approximately 20% in the mean bias with respect to the unbvmfG. For the non-hydrostatic zenith delay, the unbvmfGcmc

product exhibited a reduction of approximately 47% in the standard deviation, however the bias did not change significantly (agree at the sub-mm level). For the equivalent height error, the unbvmfGcmc product exhibited a 66% smaller bias and a 24% reduction in the standard deviation for the hydrostatic component and a 40% and 45% reduction in the mean and standard deviation for the non-hydrostatic component respectively.

For the forecast based product, unbvmfP, the results indicated that as the forecast hour increases, so does the standard deviation of the difference. This was more evident with the non-hydrostatic component than with the hydrostatic. The hydrostatic standard deviation of the zenith was only raised by 0.799 mm as compared to 2.701 mm for the non-hydrostatic zenith delay. This is a quality that is inherent to the nature of the NWP and unavoidable, since they are highly non-linear and chaotic, which make them very sensitive to small changes at the initial conditions. Lorenz (1963a,b) demonstrated that due to the chaotic nature of the atmosphere, the predictability of the weather (or any dynamic unstable system) has a finite limit, which makes prediction into the distant future impossible. The results of the forecasted products are subject to the chaotic nature of the model, which explains why the standard deviations increase over time, and the results here follow that of Boehm et al. (2007) and Boehm et al. (2008).

For the position domain comparisons, UNB's GAPS PPP software has been implemented for the computation of station positions for two distinct intervals. First, the NCEP based product, unbvmfG, was compared to the existing service for 11 years starting in January 1st 2001 and ending December 31st 2011. The results of this test illustrated that the overall global bias and RMSE across the 11-years agree well with each other at the sub-mm level. The differences in the two realizations of the VMF1 have very little effect on the horizontal component as it was shown that difference in the coordinates were at the sub-mm level for both the bias and RMSE. The greatest effect is on the height component, where the overall 11-year bias and RMSE has been computed to be -0.6 mm and 1.2 mm respectively. The PPP results confirmed the latitude dependent bias and demonstrated a

small trend where stations located closer to the equator experienced larger RMSE values. The cause of the latitude dependent bias has been discussed in §5.1, which is due to the simplification of the shape of the Earth by the existing VMF1 service. The reason for the increased RMSE in the equatorial regions has been attributed to the non-hydrostatic mapping function differences between the two products (unbvmfG and vmfG) since the non-hydrostatic mapping function differences appear to be the dominant source of the differences in these regions.

Niell (2006) demonstrated through the comparison of radiosonde data that the VMF1 is accurate at the 3 mm level, which has been used as an acceptance criteria. For the gridded products, the NCEP based product, unbvmfG, exceeds this criteria. However, this is mainly due to the issues NCEP's Re-Analysis product has in coastal locations with steep topography. The CMC based product, unbvmfGcmc, meets this criteria and can be used globally since it does not experience any of those topographic based limitations as does the unbvmfG. The predicted product, unbvmfP can be used interchangeably with the unbvmfGcmc product since their discrepancies are well within the 3 mm criteria. However, the predicted product in relation to the existing forecasted VMF1 service exceeds this criteria, but only by a small amount (sub-mm) and only in the hydrostatic case.

Results in the position domain for the 11-year period follow the gridded domain results. Over the entire 11-year period, the NCEP based product can be considered equivalent to the existing VMF1 service at the  $1\sigma$  level, but at the  $3\sigma$  level the overall difference exceeds the 3 mm acceptance criteria at the sub-mm level. Out of the 32 stations studied, only 8 stations exceeded this criteria at the  $3\sigma$  level, where 7 of the 8 stations are located in coastal regions and 1 station is located in the Amazon region (POVE).

A second test was completed that included the comparisons of all products (unbvmfG, unbvmfGcmc and unbvmfP) with respect to the existing VMF1 service covering an 8 and 6 month interval. The comparison of unbvmfG and unbvmfGcmc were completed over 8 months (Jan to Aug 2012) and the forecast base product, unbvmfP, was completed

over 6 months (Mar to Aug 2012). In all comparisons, the NCEP based product, unbvmfG, performed worst, and the standard CMC based product, unbvmfGcmc, performed best followed by the forecast based product. The standard CMC based product, unbvmfGcmc, exhibited a 10% smaller bias and a 30% reduction in the RMSE over the standard NCEP product. All stations studied for the standard CMC based product fell below the 3 mm criteria at the  $1\sigma$  and  $3\sigma$  level and can be considered equivalent to the existing VMF1 service at locations. The forecast based product agrees very well with the standard CMC based product and all stations fall well below the 3 mm criteria at the  $3\sigma$  level. When compared to the existing VMF1 service, the forecast based product also falls below the 3 mm acceptance criteria in a global context, but two individual stations exceed this amount at the  $3\sigma$  level (all stations agree at the  $1\sigma$  level).

Lastly, a small examination regarding the effect of the elevation angle on the difference was completed. It was shown that at an elevation angle of  $10^\circ$  the NCEP based product can be considered equivalent to the CMC based product. Further, at a  $10^\circ$  elevation angle the NCEP based product did not exceed the 3 mm criteria at any location at the  $3\sigma$  level and can be considered equivalent to the existing service at all locations on the globe.

## 6.2 Recommendations

The following are recommendations based on the results of the work presented:

**UNB-VMF1 Service** In spite of the efforts to provide a robust system, there are still some weak points in the overall process. Namely, with the computation of the unbvmfGcmc product. The CMC only offers their data on a 24H rolling basis, so if any outage occurs at the UNB-VMF1 service or at the CMC the source data cannot be obtained (without a nominal fee) and the product cannot be reproduced. It is recommended that the CMC

should be approached where an agreement can be negotiated so that a secure consistent source of data can be made available to the service. Secondly, the UNB-VMF1 web server only resides in a single location, which makes it vulnerable to any server or power outages at UNB. It is recommended that a second backup server be implemented off-site that can be switched over automatically if the main server were to go offline. Thirdly, computational time can be further improved with the parallelization of the raytracing code, which is the main bottleneck in the production of all products, and should be investigated for future applications in a more real time setting.

**UNB-VMF1 Products** The product produced with the NCEP Re-Analysis NWP performed worst in all tests with respect to the existing VMF1 service. This was due to issues with NCEP's Re-Analysis product to accurately depict the topography in coastal regions with complex terrain. Outside of these regions the NCEP based product performed adequately and can be with the same confidence as the existing VMF1 products. It is recommended to avoid the use of the NCEP Re-Analysis based product in these coastal regions (e.g., coast of South America) for the highest precision applications due to the increased variability. The CMC based products, unbvmfGcmc and unbvmfP, can be used globally without restriction as all comparisons with these products to the existing VMF1 service have demonstrated equivalency.

**Numerical Weather Prediction Models** The numerical weather prediction model evaluated experienced increased variability during the winter months and with respect to latitude. Therefore, users can expect to experience more variability in positioning results during these times and locations. In particular, the polar locations exhibit more variability due to the sparse observing network in these locations. Additionally, the numerical weather models studied still exhibited larger variability in the prediction of the water vapour content. As the water vapour content increased (locations close to the equator, during summer months) the variability of the models also increased. Further, the meteorological sensors studied exhibited calibration issues and erroneous measurements, so

within the context of a long term consistent time series the results from the numerical weather models outperformed the meteorological sensors. The results highlight the need to ensure that all meteorological sensors are properly calibrated and ensure erroneous data spikes are filtered from the output files. Further, the use of high resolution numerical weather prediction models showed no appreciable benefit over a global and regional model. It is recommended that the use of high resolution models are unnecessary at this time, and that a regional based model can be helpful over a global model in predicting the atmospheric conditions. Lastly, the application of the numerical weather prediction models in the production of geodetic corrections are becoming commonplace. Therefore, it is essential that the geodetic community begins a dialogue with the weather forecasters to express the specific needs of the community. For example, numerical weather prediction models are generally offered with 6H intervals, but this is not sufficient for the prediction of zenith wet delays due to the temporal variability of the water vapour, and the weather forecasters may be able to provide specialized model runs to suit these applications.

### **6.3 Future Work**

The following summarizes the opportunity for future research based on the results of this work:

**UNB-VMF1 Service** The UNB-VMF1 service has been built on a Linux platform on ACE-NET's super computing resources. Every effort was made to automate the computation process, but much manual administration is still required when one of the nodes goes down for maintenance or for other reasons. Every effort should be made to automate this process to reduce the amount of time required to startup computations when the node is back online. Further, the service can use additional error checking prior to uploading to the web server. All product files should be checked for any abnormal results in the

zenith delays. Currently, all files are only checked for size and for any null characters, which takes care of the majority of possible issues. The current service offers the product in a Bernese format, but other organizations do use other software for their processing. It would be helpful to provide standard conversion scripts to all software formats, which will help to encourage the use of the products. Lastly, mentioned in the recommendations, a second server should be setup at an outside location to protect against any server downtime or power outages at UNB.

**UNB-VMF1 Validation** The UNB-VMF1 has been validated with respect to the existing VMF1 service, so the results can be thought of in a relative sense. The results indicated that the difference between the UNB-VMF1 and the existing service are within the accuracy of the mapping function itself, but this is at the mm-level. Biases do exist between products, so completing a global campaign in the position domain based on each of the VMF1 realizations relative to the IGS solution will help to understand better the implications of this bias and variability of each of the realizations. In addition, to the validation of GNSS datasets, each of the VMF1 realizations should be validated by other techniques such as VLBI. This will help to expand the portfolio of the UNB-VMF1 and possibly highlight any additional limitations that the GNSS results could not identify.

**UNB-VMF1 Orography** The orography selected has been modelled to match the existing VMF1 service, but many points do not represent accurate elevations in some locations, and many points are found outside of the NWP, which require extrapolations to determine meteorological parameters. The development of a suitable orography for the gridded products for both services will help to improve product generation by limiting extrapolations outside of the NWP and help to reduce the extrapolation of the zenith hydrostatic delays in position analysis.

**UNB-VMF1 Products** The UNB-VMF1 service has provided a convenient foundation to build upon. Firstly, the addition of site specific products for VLBI stations and IGS stations will help to expand the usable applications for the service. As a companion to the

site specific product, the associated meteorological parameters at each of the sites should also be offered. This will provide a consistent set of meteorological parameters that are not subject to sensor calibration and maintenance issues. Secondly, the addition of a gridded product based on the CMC's regional NWP may be beneficial as the results from the model comparisons indicated that the CMC's regional model performed best. Thirdly, investigate the use of increased temporal resolution NWP for the application of the Vienna Total Mapping Function. Although the high resolution model did not show an appreciable improvement, it is offered at an increased temporal resolution. Typical models are offered in 6 hour or 3 hour intervals, but CMC's high resolution model is offered at 1 hour intervals. Therefore, it will be worthwhile investigating the impact of this increased temporal resolution on zenith wet delays, which may help in the improvement of the Vienna Total Mapping Function described by Boehm et al., (2006). Lastly, the VMF1 based products are symmetric mapping functions, so they do not take into account the azimuth dependency of the delay. The addition of products that address the azimuth dependency of the delay should be investigated so as to provide a complete suite of correction products.



# References

- ACEnet. (2012a). "ACEnet: Accelerating Discovery" [On-Line] 2013-Jan-12. <http://www.ace-net.ca/wiki/ACEnet>.
- ACEnet. (2012b). "Parallel programming." *User Guide*. [On-Line] 2013-Jan-12. [http://www.ace-net.ca/wiki/User\\_Guide#Parallel\\_programming](http://www.ace-net.ca/wiki/User_Guide#Parallel_programming)
- AERS. (2012). "Special Bureau for the Atmosphere." *Atmospheric and Environmental Research*. [On-Line] 11-Jan-2013. <http://www.aer.com/science-research/earth/earth-mass-and-rotation/special-bureau-atmosphere>.
- Anthes, R. A., Kuo, Y. H., Baumhefner, D. P., Errico, R. M., and Bettge, T. W. (1985). "Predictability of mesoscale atmospheric motions." *Advances in Geophysics*, Elsevier, 28, 159202.
- Aparicio, J. M., and Laroche, S. (2011). "An evaluation of the expression of the atmospheric refractivity for GPS signals." *Journal of Geophysical Research*, 116(D11).
- Asmus, V. V., Dyadyuchenko, V. N., and Nosenko, Y. I. (2007). "A highly elliptical orbit space system for hydrometeorological monitoring of the Arctic region." *Bulletin of the World Meteorological Organization*. October. 56(4).
- Bar-Sevar, Y. (2004). "IGS Tropospheric Products and Services at a Crossroad." *Position paper for the March 2004 IGS Analysis Center Workshop*. 2004 Berne Workshop and Symposium. [http://igsch.jpl.nasa.gov/igsch/resource/pubs/04\\_rtberne/cdrom/Session11/11\\_0\\_Bar\\_Sevar.pdf](http://igsch.jpl.nasa.gov/igsch/resource/pubs/04_rtberne/cdrom/Session11/11_0_Bar_Sevar.pdf)
- Bernard, J. (2012). *Personal Communication*. ACEnet Computational Consultant. University of New Brunswick, Fredericton, NB.
- Bevis, M., S. Businger, S. Chiswell, T. A. Herring, R. A. Anthes, C. Rocken, and R. H. Ware (1994). "GPS Meteorology: Mapping zenith wet delays onto precipitable water." *Journal of Applied Meteorology*, Vol. 33, No. 3, pp. 379386.
- Bock, O., and Nuret, M. (2009). "Verification of NWP Model Analyses and Radiosonde Humidity Data with GPS Precipitable Water Vapor Estimates during AMMA." *Weather and Forecasting*, 24(4), 10851101.

- Boehm, J., and H. Schuh (2003), "Vienna Mapping Functions.", in *Proceedings of the 16th Working Meeting on European VLBI for Geodesy and Astrometry*, Leipzig, May 9-10, 2003, pp. 131-143, Verlag des Bundesamtes für Kartographie und Geodäsie.
- Boehm, J. (2004). "Troposphärische Laufzeitverzögerungen in der VLBI." Inst. für Geodäsie u. Geophysik. Heft. Nr.68. ISSN 1811-8380.
- Boehm, J., and Schuh, H. (2004). Vienna mapping functions in VLBI analyses. *Geophysical Research Letters*, 31(1), L01603.
- Boehm, J., Werl, B., and Schuh, H. (2006). "Troposphere mapping functions for GPS and very long baseline interferometry from European Centre for Medium-Range Weather Forecasts operational analysis data." *Journal of Geophysical Research*, 111(B2), B02406.
- Boehm, J., and Schuh, H. (2007). Forecasting Data of the Troposphere Used for IVS Intensive Sessions. 18th European VLBI for Geodesy and Astrometry (EVGA) Working Meeting, April 12-13th.
- Boehm, J., Heinkelmann, R., and Schuh, H. (2007). "Short Note: A global model of pressure and temperature for geodetic applications." *Journal of Geodesy*, 81(10), 679683.
- Boehm, J., Kouba, J., and Schuh, H. (2009). "Forecast Vienna Mapping Functions 1 for real-time analysis of space geodetic observations." *Journal of Geodesy*, 83(5), 397401.
- Boehm, J., and T. VanDam (2009). "Modeling deficiencies and modeling based on external data." Second GGOS Unified Analysis Workshop, IERS, Grand Hyatt, San Francisco, CA, USA, December 11-12. (Oral presentation).
- Born, M., and E. Wolf (1999). *Principles of Optics: Electromagnetic Theory of Propagation, Interference and Diffraction of Light*. 7th ed., 986 pp., Cambridge University Press, Cambridge, U.K., ISBN 0521642221.
- Bosser, P., O. Bock, J. Pelon, and C. Thom (2007). "An improved mean-gravity model for GPS hydrostatic delay calibration." *IEEE Geoscience and Remote Sensing Letters*, Vol. 4, No. 1, pp. 37.
- Bouteloup, Y. (1995). "Improvement of the spectral representation of the earth topography with a variational method." *Monthly Weather Review*, American Meteorological Society, 123(5), 15601573.
- Bouttier, F. and P. Courtier (1999). "Data assimilation concepts and methods." [On-Line] 2013-Jan-12. [http://www.ecmwf.int/newsevents/training/rcourse\\_notes/DATA\\_ASSIMILATION/ASSIM\\_CONCEPTS/Assim\\_concepts.html](http://www.ecmwf.int/newsevents/training/rcourse_notes/DATA_ASSIMILATION/ASSIM_CONCEPTS/Assim_concepts.html)
- Bromwich, D. H., and Wang, S. H. (2005). "Evaluation of the NCEP-NCAR and ECMWF 15- and 40-Yr Reanalyses Using Rawinsonde Data from Two Independent Arctic Field Experiments\*." *Monthly Weather Review*, 133(12), 35623578.
- Chao, C. (1974). "The tropospheric calibration model for mariner mars 1971." Technical Report 321587, California Institute of Technology, Jet Propulsion Laboratory, Pasadena, Calif., 17 pp.

- Close, F. (2011) *The Infinity Puzzle: Quantum Field Theory and the Hunt for an Orderly Universe*. Knopf. Canada.
- Coiffier, J. (2011). *Fundamentals of Numerical Weather Prediction*. Cambridge University Press, New York.
- COMET-UCAR (2009a). “Spectral: Data Representation.”, *Impact of Model Structure and Dynamics*. University Corporation for Atmospheric Research (UCAR), Cooperative Program for Operational Meteorology, Education and Training (COMET), (Lecture Notes), [On-Line] 2013-Jan-12. [http://www.meted.ucar.edu/nwp/model\\_structure/navmenu.php?tab=1&page=3.4.0](http://www.meted.ucar.edu/nwp/model_structure/navmenu.php?tab=1&page=3.4.0).
- COMET-UCAR (2009b). “Gridpoint Equivalency of Spectral Resolution.”, *Impact of Model Structure and Dynamics*. University Corporation for Atmospheric Research (UCAR), Cooperative Program for Operational Meteorology, Education and Training (COMET), (Lecture Notes), [On-Line] 2013-Jan-12. [http://www.meted.ucar.edu/topics\\_nwp.php](http://www.meted.ucar.edu/topics_nwp.php).
- COMET-UCAR (2009c). “Feature Definition.”, *Impact of Model Structure and Dynamics*. University Corporation for Atmospheric Research (UCAR), Cooperative Program for Operational Meteorology, Education and Training (COMET), (Lecture Notes), [On-Line] 2013-Jan-12. [http://www.meted.ucar.edu/topics\\_nwp.php](http://www.meted.ucar.edu/topics_nwp.php).
- Cote, J., S. Gravel, A. Methot, A. Patoine, M. Roch, and A. Staniforth (1998). “The operational CMC/MRB Global Environmental Multiscale (GEM) model. Part I: Design considerations and formulation.” *Monthly Weather Review*, Vol. 126, No. 6, pp. 1373-1395.
- Cucurull, L. (2010). “Improvement in the Use of an Operational Constellation of GPS Radio Occultation Receivers in Weather Forecasting.” *Weather and forecasting*, 25(2), 749-767.
- CMC (2012a). “Changes to the Canadian Meteorological Centre (CMC) Operational System.” [On-Line] 2013-Jan-13. [http://collaboration.cmc.ec.gc.ca/cmc/cmci/product\\_guide/docs/changes\\_e.html](http://collaboration.cmc.ec.gc.ca/cmc/cmci/product_guide/docs/changes_e.html).
- CMC (2012b). “Numerical Data from High Resolution Deterministic Prediction System (HRDPS) model - GRIB2 format.” [On-Line] 2013-Jan-12. [http://www.weatheroffice.gc.ca/grib/grib2\\_HRDPS\\_HR\\_e.html](http://www.weatheroffice.gc.ca/grib/grib2_HRDPS_HR_e.html).
- CMC (2012c). “High Resolution Numerical Data of the Global Deterministic Prediction System (GDPS) model - GRIB2 format.” [On-Line] 2013-Jan-13. [http://www.weatheroffice.gc.ca/grib/grib2\\_glb\\_HR\\_e.html](http://www.weatheroffice.gc.ca/grib/grib2_glb_HR_e.html).
- Davis, J. L., T. A. Herring, I. I. Shapiro, A. E. E. Rogers, and G. Elgered (1985). “Geodesy by radio interferometry: Effects of atmospheric modeling errors on estimates of baseline length.” *Radio Science*, Vol. 20, No. 6, pp. 1593-1607.
- Davis, J. L. (1986). *Atmospheric propagation effects on radio interferometry*. Ph.D. thesis, Massachusetts Institute of Technology, Dept. of Earth, Atmospheric, and Planetary Sciences, Cambridge, Mass., 284 pp., Also published as AFGL Technical Report 86-0243, U.S. Air Force Geophysics Laboratory, Hanscom AFB, Mass., <http://hdl.handle.net/1721.1/27953>.

- Debye, P., *Polar Molecules*, Dover, New York, 1929.
- Dow, J. M., Neilan, R. E., and Rizos, C. (2009). "The International GNSS Service in a changing landscape of Global Navigation Satellite Systems." *Journal of Geodesy*, 83(3-4), 191-198.
- Doyle, J. (2008). "Numerical Weather Prediction over Complex Terrain: Basic Theory and Overview." AMS/COMET/MSU Mountain Weather Workshop, 5-8 August 2008. (Oral Presentation). [On-Line] 2013-Jan-12. <http://www.meted.ucar.edu/norlat/mtnwxworkshop/lectures.htm>.
- ECMWF. (2011). "WMO Lead Centre for Deterministic Forecast Verification (WMO-LCDNV)." [On-Line] 2013-Jan-12. <http://apps.ecmwf.int/wmolcdnv/>.
- Erfani, A., Mailhot, J., Gravel, S., Desgagn, M., King, P., Sills, D., McLennan, N., and Jacob, D. (2005). "The high resolution limited area version of the Global Environmental Multiscale model and its potential operational applications." Preprints, 11th Conference on Mesoscale Processes, 24-28 October 2005, Albuquerque, NM, Amer. Meteor. Soc., 1M.4.
- EUMESTAT (2013). "IASI." [On-Line] 2013-Jan-12. [http://www.eumetsat.int/Home/Main/Satellites/Metop/Instruments/SP\\_2010053151047495](http://www.eumetsat.int/Home/Main/Satellites/Metop/Instruments/SP_2010053151047495)
- Feynmann, R. (1963). *The Feynmann Lectures on Physics: mainly mechanics, radiation, and heat*. Vol.I. Addison-Wesley Publishing Co. Reading, MA.
- Feynmann, R. (1964). *The Feynmann Lectures on Physics: mainly electromagnetism and matter*. Vol.II. Addison-Wesley Publishing Co. Reading, MA.
- Foelsche, U. (1999). *Tropospheric water vapor imaging by combination of ground-based and spaceborne GNSS sounding data*. (Ph.D. thesis), Wissenschaftl. Ber. No. 10, 164p., Inst. Meteorol. Geophys., Univ. of Graz, Austria. [http://www.uni-graz.at/igam-arsclisys/ARSCliSys\\_writtenpub\\_en.html#Year1999](http://www.uni-graz.at/igam-arsclisys/ARSCliSys_writtenpub_en.html#Year1999).
- Fund, F., Morel, L., Mocquet, A., and Boehm, J. (2010). "Assessment of ECMWF-derived tropospheric delay models within the EUREF Permanent Network." *GPS Solutions*, 15(1), 3948.
- Fund, F., Morel, L., and Mocquet, A. (2011). "A discussion of height reductions for Zenith Hydrostatic Delays derived from weather models." *Journal of Applied Geodesy*, 5(2), 71-80.
- Gaffen, D., A. Robock, and W. Elliott (1992). "Annual cycles of tropospheric water vapor." *Journal of Geophysical Research*, Vol. 97, p. 18.
- GGFC. (2010). "NCEP Loading." *Global Geophysical Fluid Center*. [On-Line] 11-Jan-2013. <http://geophy.uni.lu/ggfc-atmosphere.html>.
- GGOS. (2011). *GGOS Atmosphere*. [On-Line] 10 Jan 2013. <http://ggosatm.hg.tuwien.ac.at/index.html>

- Ghoddousi-Fard, Reza (2009). *Modelling Tropospheric Gradients and Parameters from NWP Models: Effects on GPS Estimates*. Ph.D. dissertation, Department of Geodesy and Geomatics Engineering, Technical Report No. 264, University of New Brunswick, Fredericton, New Brunswick, Canada, 216 pp. <http://gge.unb.ca/Pubs/TR264.pdf>
- Hartmann, G. K. (1993). "The determination of tropospheric conditions (especially H<sub>2</sub>O) affecting the accuracy of position measurements." *Geophysical Monograph 73*, International Union of Geodesy and Geophysics, Washington, DC/Brussels, Belgium, mar, pp. 7382.
- Healy, S. B. (2011). "Refractivity coefficients used in the assimilation of GPS radio occultation measurements." *Journal of Geophysical Research*, 116(D1), D01106.
- Herring, T. A. (1992). "Modelling atmospheric delays in the analysis of space geodetic data." *Proceedings of the Symposium Refraction of Transatmospheric Signals in Geodesy*, eds. J. C. de Munck, and T. A. TH. Spoelstra, No. 36, Netherlands Geodetic Commission, The Hague, The Netherlands, May 1992, ISBN 9789061322436, pp. 157164. <http://www.ncg.knaw.nl/eng/publications/Geodesy/36DeMunck.html>.
- Hill, R. J., Lawrence, R. S., and Priestley, J. T. (1982). Theoretical and calculational aspects of the radio refractive index of water vapor. *Radio Science*, American Geophysical Union, 17(5), 12511257.
- Hobiger, T., R. Ichikawa, T. Takasu, Y. Koyama, and T. Kondo (2008). "Ray-traced troposphere slant delays for precise point positioning." *Earth, Planets and Space*, Vol. 60, No. 5, pp. e1e4.
- Hobiger, T., Shimada, S., Shimizu, S., Ichikawa, R., Koyama, Y., and Kondo, T. (2010). "Improving GPS positioning estimates during extreme weather situations by the help of fine-mesh numerical weather models." *Journal of Atmospheric and Solar-Terrestrial Physics*, Elsevier, 72(2-3), 262270.
- Hopfield, H. S. (1969). "Two-quartic tropospheric refractivity profile for correcting satellite data." *Journal of Geophysical Research*, American Geophysical Union, 74(18), 44874499.
- IGS (2012). "IGS Data." *Data and Products*. [On-Line] 2013-Jan-11.<http://igsceb.jpl.nasa.gov/components/data.html>.
- IGS Troposphere WG. (2012). "Chapter 5. Guidelines for IGS sites submitting meteorological data." *IGS Site Guidelines*. [On-Line] 2013-Jan-12. <http://igsceb.jpl.nasa.gov/network/guidelines/guidelines.html#metsites>.
- Jakobson, E., Vihma, T., Palo, T., Jakobson, L., Keernik, H., and Jaagus, J. (2012). "Validation of atmospheric reanalyses over the central Arctic Ocean." *Geophysical Research Letters*, 39(10), L10802.
- Kalnay, E., Kanamitsu, M., Kistler, R., Collins, W., Deaven, D., Gandin, L., Iredell, M., Saha, S., White, G., and Woollen, J. (1996). The NCEP/NCAR 40-year reanalysis project. *Bull. Amer. Meteor. Soc.*, 77(3), 437471.

- Kalnay, E. (2003). *Atmospheric modeling, data assimilation, and predictability*. Cambridge University Press, New York.
- Kanamitsu, M., Alpert, J. C., Campana, K. A., Caplan, P. M., Deaven, D. G., Iredell, M., Katz, B., Pan, H. L., Sela, J., and White, G. H. (1991). "Recent changes implemented into the global forecast system at NMC." *Weather and forecasting*, 6(3), 425-435.
- Kanamitsu, M., Ebisuzaki, W., Woollen, J., Yang, S.-K., Hnilo, J. J., Fiorino, M., and Potter, G. L. (2002). "NCEP/DOE AMIP-II Reanalysis (R-2)." *Bull. Amer. Meteor. Soc.*, 83(11), 1631-1643.
- Kouba, J. (2008). "Implementation and testing of the gridded Vienna Mapping Function 1 (VMF1)." *Journal of Geodesy*, 82(4-5), 193-205.
- Kouba, J. (2009). "Testing of global pressure/temperature (GPT) model and global mapping function (GMF) in GPS analyses." *Journal of Geodesy*, 83, 199-208.
- Kouba, J., and Hroux, P. (2001). "GPS Precise Point Positioning using IGS orbit products." *GPS Solutions*, 5(2), 12-28.
- Langley, R. (1996). "Propagation of the GPS Signal." in *GPS for Geodesy*. Eds A. Kleusbrg and P.J.G. Teunissen. Vol. 60 *Lecture Notes in Earth Sciences*. Eds. S. Bhattacharji, G. M. Friedman, Brooklyn and Troy H. J. Neugebauer, A. Seilacher. Springer-Verlag Berlin Heidelberg.
- Liebe, H. J. (1985). "An updated model for millimeter wave propagation in moist air." *Radio Science*, 20, 1069-1089.
- Leandro, R. F. (2007). "Precise Point Positioning with GPS: A New Approach for Positioning, Atmospheric Studies, and Signal Analysis." Ph.D. dissertation, Department of Geodesy and Geomatics Engineering, Technical Report No. 267, University of New Brunswick, Fredericton, New Brunswick, Canada, 232 pp. <http://gge.unb.ca/Pubs/TR267.pdf>.
- Le Bail, K., J. Juhl, J.M. Gipson, D.S. MacMillan (2012). "Improving the homogeneity of meteorological data to minimize resulting errors in geodetic analysis." Fall Meeting 2012, American Geophysical Union, San Francisco, Calif., December 3-7, Eos Trans. AGU Fall Meet. Suppl., Abstract G53B-1138. (Poster presentation).
- Lorenz, E. N. (1969). "The predictability of a flow which possesses many scales of motion." *Tellus*, 21(3), 289-307.
- Lutgens, F. and E.J. Tarbuck. (2010). *The Atmosphere: An Introduction to meteorology*. 11th Eds. Pearson. Glenview, Illinois.
- Mailhot, J., Blair, S., Charron, M., Doyle, C., Joe, P., Abrahamowicz, M., Bernier, N. B., Denis, B., Erfani, A., Frenette, R., Giguere, A., Isaac, G. A., McLennan, N., McTaggart-Cowan, R., Milbrandt, J., and Tong, L. (2010). "Environment Canada's Experimental Numerical Weather Prediction Systems for the Vancouver 2010 Winter Olympic and Paralympic Games." *Bull. Amer. Meteor. Soc.*, 91(8), 1073-1085.
- Mailhot, J., Blair, S., Lefavre, L., Bilodeau, B., Desgagn, M., Girard, C., Glazer, A., Leduc, A. M., Methot, A., and Patoine, A. (2006). "The 15°km version of the Canadian regional forecast system." *Atmosphere-Ocean*, Taylor & Francis, 44(2), 133-149.

- Mailhot, J., Milbrandt, J. A., Gigure, A., McTaggart-Cowan, R., Erfani, A., Denis, B., Glazer, A., and Valle, M. (2012). "An Experimental High-Resolution Forecast System During the Vancouver 2010 Winter Olympic and Paralympic Games." *Pure and Applied Geophysics*. August 2012.
- Mass, C. F., Ovens, D., Westrick, K., and Colle, B. A. (2002). "Does increasing horizontal resolution produce more skillful forecasts." *Bull. Amer. Meteor. Soc.*, 83(3), 407430.
- Mendes, V. B. (1999). Modeling the Neutral-Atmosphere Propagation Delay in Radiometric Space Techniques. Ph.D. thesis, University of New Brunswick, Dept. of Geodesy and Geomatics Engineering, Fredericton, N.B., Canada, April, 349 pp., Technical Report 199, <http://gge.unb.ca/Pubs/TR199.pdf>.
- Murphy, D. M., and T. Koop (2005). "Review of the vapour pressures of ice and supercooled water for atmospheric applications." *Quarterly Journal of the Royal Meteorological Society*, Vol. 131, No. 608, pp. 1539-1565.
- Nafisi, V., Urquhart, L., Santos, M. C., Nievinski, F. G., Boehm, J., Wijaya, D. D., Schuh, H., Ardalan, A. A., Hobiger, T., Ichikawa, R., Zus, F., Wickert, J., and Gegout, P. (2012). Comparison of Ray-Tracing Packages for Troposphere Delays. Geoscience and Remote Sensing, IEEE Transactions on Geosciences. 50(2). pp.469-481.
- Navarra, A., Stern, W. F., and Miyakoda, K. (1994). "Reduction of the Gibbs oscillation in spectral model simulations." *Journal of Climate*, Boston, MA: American Meteorological Society, c1988-, 7(8), 1169-1183.
- Niell, A. E. (1996). "Global mapping functions for the atmosphere delay at radio wavelengths." *Journal of Geophysical Research*, Vol. 101, No. B2, pp. 3227-3246.
- Niell, A. E. (2000). "Improved atmospheric mapping functions for vlbi and gps." *Earth, Plant and Space*, Vol. 52, No. 10, pp. 699-702.
- Niell, A. E. (2006). "Interaction of atmosphere modeling and VLBI analysis strategy." *IVS 2006 General Meeting Proceedings*, ed. by D. Behrend and K. Baver, Concepcin, Chile, January 9-11, pp.252-256.
- Nievinski, F. G. (2009). *Ray-tracing Options to Mitigate the Neutral Atmosphere Delay in GPS*. M.Sc.E. thesis, University of New Brunswick, Dept. of Geodesy and Geomatics Engineering, Fredericton, N.B., Canada, May, 232 pp., Technical Report 262, <http://gge.unb.ca/Pubs/TR262.pdf>.
- Petit, G., and Luzum, B. (2010). "IERS Conventions (2010)." Verlag des Bundesamts fur Kartographie und Geodasie, Frankfurt am Main 2010IERS, Technical Note No.36, 1-179. <http://www.iers.org/TN36/>
- Petrov, L., and J. P. Boy (2004). "Study of the atmospheric pressure loading signal in very long baseline interferometry observations." *Journal of Geophysical Research*, Vol. 109, No. B03405.
- Petrov, I. (2012). "Latency." *Atmospheric Pressure Loading Service*. [On-Line] 2013-Jan-12. <http://gemini.gsfc.nasa.gov/aplo/>
- Rife, D. L., and Davis, C. A. (2005). "Verification of temporal variations in mesoscale numerical wind forecasts." *Monthly Weather Review*, 133(11), 3368-3381.

- Rocken, C., S. Sokolovskiy, J. M. Johnson, and D. Hunt (2001). "Improved mapping of tropospheric delays." *Journal of Atmospheric and Oceanic Technology*, Vol. 18, No. 7, pp. 1205-1213.
- Rutt, I. C. (2003). Optimal Filtering of Orography for NWP and Climate Models. PhD Thesis. University of Reading. <http://www.met.rdg.ac.uk/phdtheses/Optimal%20Filtering%20of%20Orography%20for%20NWP%20and%20Climate%20Models.pdf>
- Rueger, J. M. (2002). "Refractive index formulae for radio waves." FIG XXII International Congress, International Federation of Surveyors (FIG), Washington, D.C., April 1926. [http://www.fig.net/pub/fig\\_2002/Js28/JS28\\_rueger.pdf](http://www.fig.net/pub/fig_2002/Js28/JS28_rueger.pdf).
- Saastamoinen, J. (1972). "Atmospheric correction for the troposphere and stratosphere in radio ranging of satellites." *In The Use of Artificial Satellites for Geodesy*, eds. S. W. Henriksen, A. Mancini, and B. H. Chovitz, Vol. 15 of Geophysical Monograph Series, American Geophysical Union, Washington, D.C., ISBN 0-87590-015-1, pp. 247-251.
- Salvador, R., Calb, J., and Milln, M. M. (1999). "Horizontal grid size selection and its influence on mesoscale model simulations." *Journal of Applied Meteorology*, 38(9), 1311-1329.
- Schindelegger M., Bhm J., Salstein D., Schuh H. (2011). "High-resolution atmospheric angular momentum functions related to Earth rotation parameters during CONT08." *Journal of Geodesy*, 85(7), pp. 425-433.
- Seluchi, M. E., Garreaud, R. D., Norte, F. A., and Saulo, A. C. (2006). "Influence of the subtropical Andes on baroclinic disturbances: A cold front case study." *Monthly Weather Review*, 134(11), 3317-3335.
- Smith, E. K., and Weintraub, S. (1953). "The constants in the equation for atmospheric refractive index at radio frequencies." *Proceedings of the IRE, IEEE*, 41(8), 1035-1037.
- Solheim, F. S., Vivekanandan, J., Ware, R. H., and Rocken, C. (1999). "Propagation delays induced in GPS signals by dry air, water vapor, hydrometeors, and other particulates." *Journal of Geophysical Research*, 104(D8), 9663-9670.
- Spilker, J. J., Jr. (1996). "Tropospheric effects on GPS." *In Global Positioning System: Theory and Applications*, eds. B. W. Parkinson, and J. J. Spilker, Jr., Vol. I of Progress in Astronautics and Aeronautics, Chapter 13, American Institute of Aeronautics & Astronautics (AIAA), Washington, D.C., ISBN 156347106X, pp. 517-546.
- Stauffer, D. R., Hunter, G. K., Deng, A., Zielonka, J. R., Tinklepaugh, K., Hayes, P., and Kiley, C. (2007). "On the role of atmospheric data assimilation and model resolution on model forecast accuracy for the Torino Winter Olympics." Preprints, 22th Conference on Weather Analysis and Forecasting/18th Conference on Numerical Weather Prediction, 25-29 June 2007, Park City, UT, Amer. Meteor. Soc.
- Steigenberger, P., Boehm, J., and Tesmer, V. (2009). "Comparison of GMF/GPT with VMF1/ECMWF and implications for atmospheric loading." *Journal of Geodesy*, 83(10), 943-951.



- Stensrud, D. (2007). *Parameterization Schemes: Keys to Understanding Numerical Weather Prediction Models*. Cambridge University Press, New York.
- Talagrand, O. (1997). "Assimilation of Observations, and Introduction." *Journal of the Meteorological Society of Japan*, 75, 191209.
- Thayer, G. D. (1974). "An improved equation for the radio refractive index of air." *Radio Science*, Vol. 9, No. 10, pp. 803807,
- Tesmer, V., Boehm, J., Heinkelmann, R., and Schuh, H. (2007). "Effect of different tropospheric mapping functions on the TRF, CRF and position time-series estimated from VLBI." *Journal of Geodesy*, 81(6-8), 409-421.
- Thessin, R. N. (2005). *Atmospheric signal delay affecting GPS measurements made by space vehicles during launch, orbit and reentry*. Masters thesis, Massachusetts Institute of Technology, Dept. of Aeronautics and Astronautics, Cambridge, Mass., 182 pp., <http://hdl.handle.net/1721.1/33211>.
- Tregoning, P., and Herring, T. A. (2006). "Impact of a priori zenith hydrostatic delay errors on GPS estimates of station heights and zenith total delays." *Geophysical Research Letters*, 33(23).
- Tremblay, M. (2011). "[dd.info] Probleme avec les donnees GRIB2 polaire stereographique / Problem with GRIB2 polar stereographic data." [On-Line] 2013-Jan-12. [http://lists.ec.gc.ca/pipermail/dd\\_info/2011-November/000065.html](http://lists.ec.gc.ca/pipermail/dd_info/2011-November/000065.html)
- Temblay, M. (2012). *Personal Communication*. Canadian Meteorological Centre. Laval, Quebec, Canada.
- Trenberth, K. E., and Paolino, D. A. (1981). "Characteristic patterns of variability of sea level pressure in the Northern Hemisphere." *Monthly Weather Review*, 109(6), 1169-1189.
- UCAR. (2011). "Operational Models Matrix: Characteristics of NWP and Related Forecast Models." [On-Line] 2013-Jan-13. <http://www.met.ed.ucar.edu/nwp/pcu2/>.
- UK Met Office. (2012) "Land Sea Mask." [On-Line] 2013-Jan-12. <http://research.metoffice.gov.uk/research/nwp/numerical/surface/mask.html>.
- Urquhart, Landon (2011). *Assessment of Tropospheric Slant Factor Models: Comparison with Three Dimensional Ray-Tracing and Impact on Geodetic Positioning*. M.Sc.E. thesis, Department of Geodesy and Geomatics Engineering Technical Report No. 275, University of New Brunswick, Fredericton, New Brunswick, Canada, 166 pp.<http://gge.unb.ca/Pubs/TR275.pdf>
- Urquhart, L., Nievinski, F. G., and Santos, M. C. (2011a). "Ray-traced slant factors for mitigating the tropospheric delay at the observation level." *Journal of Geodesy*, 86(2), 149-160.

- Urquhart, L., F.G., Nievinski, M. C. Santos and J.Boehm. (2011b). "Generation and Assessment of VMF1-Type Grids Using North-American Weather Models." XXV IUGG General Assembly, Melbourne, Australia, June 28th July 7th, 2011. (Oral presentation).
- van Dam, T. and J. Wahr, (1987), "Displacements of the Earth's surface due to atmospheric loading: Effects on Gravity and Baseline Measurements", *J. Geophys. Res.*, 92, 1281-1286.
- Velicogna, I., Wahr, J., and Van den Dool, H. (2001). "Can surface pressure be used to remove atmospheric contributions from GRACE data with sufficient accuracy to recover hydrological signals?." *Journal of Geophysical Research*, 106(B8), 1641516434.
- Wahr, J., Molenaar, M., and Bryan, F. (1998). "Time variability of the Earth's gravity field: Hydrological and oceanic effects and their possible detection using GRACE." *Journal of Geophysical Research*, AGU AMERICAN GEOPHYSICAL UNION, 103, 3030.
- VMF1. (2012a). "Readme.txt." [On-Line] 2013-Jan-12. <http://ggosatm.hg.tuwien.ac.at/DELAY/readme.txt>.
- VMF1. (2012b). "VMF1 Grid." *Vienna Mapping Functions 1 VMF1*. [On-Line] 2013-Jan-13. <http://mars.hg.tuwien.ac.at/~ecmwf1/>.
- Warner, T.T. (2011) *Numerical Weather and Climate Prediction*. Cambridge University Press, New York.
- WMO (2010). *Manual on the Global Data-processing and Forecasting System*. Vol. 1, Global Aspects, WMO-No.485. Updated in 2012. World Meteorological Organization, Geneva, Switzerland. [http://www.wmo.int/pages/prog/www/DPFS/documents/485\\_Vol\\_I\\_en.pdf](http://www.wmo.int/pages/prog/www/DPFS/documents/485_Vol_I_en.pdf).
- Yang, X., Sass, B. H., Elgered, G., Johansson, J. M., and Emardson, T. R. (1999). "A comparison of precipitable water vapor estimates by an NWP simulation and GPS observations." *Journal of Applied Meteorology*, 38(7), 941956.
- Yunck, T. P. (1993). "Coping with the atmosphere and ionosphere in precise satellite and ground positioning." *Geophysical Monograph 73*, International Union of Geodesy and Geophysics, Washington, DC/Brussels, Belgium, mar, pp. 116.
- Zumberge, J. F., Heflin, M. B., Jefferson, D. C., Watkins, M. M., and Webb, F. H. (1997). "Precise point positioning for the efficient and robust analysis of GPS data from large networks." *Journal of Geophysical Research*, American Geophysical Union, 102(B3), 5005-5017.

# Appendix A

## Meteorological Parameter Comparison

### Supplemental

#### A.1 Meteorological Data Comparison

The following Appendix provides additional tables and plots to supplement the main text. Table A-1 summarizes the meteorological sensors at each of the selected stations as extracted from their IGS log files. Table A-1 summarizes the sensor name, manufacturer, accuracy, the height difference from the GNSS antenna, and the calibration date. A calibration date of (CCYY-MM-DD) represents that no information is available, and any blanks within the table also indicates that no information was available in the log file. Tables A-2 through A-4 summarize the individual station latitude, mean difference and  $1\sigma$  standard deviation for pressure (A-2), temperature (A-3), specific humidity (A-4).

Table A.1: Summary of meteorological sensor metadata for each sensor used in the meteorological parameter comparison in Chapter 3.

Station	Sensor	Manufacturer	Accuracy	Height Diff	Calibration Date
ADE1	HMP233	Vaisala	(% rel h)	(m)	(CCYY-MM-DD)
ADE1	PTB202A	Vaisala	(hPa)	(m)	(CCYY-MM-DD)
ADE1	HMP233	Vaisala	(deg C)	(m)	(CCYY-MM-DD)
ALBH	HMP-35A	VAISALA	3 %	(m)	(CCYY-MM-DD)
ALBH	PTB-100A	VAISALA	0.1 mb	0.0 m / To	(CCYY-MM-DD)
ALBH	YSI 44212	YSI	0.2 Deg C	(m)	(CCYY-MM-DD)
ALIC	PAROSCIENTIFIC MET3A	Paroscientific, Inc.	2% rel h	2.4 (m)	(CCYY-MM-DD)
ALIC	PAROSCIENTIFIC MET3A	Paroscientific, Inc.	0.1 mbar	2.4(m)	(CCYY-MM-DD)
ALIC	PAROSCIENTIFIC MET3A	Paroscientific, Inc.	0.5 deg C	2.4(m)	(CCYY-MM-DD)
ARTU			(% rel h)	(m)	(CCYY-MM-DD)
ARTU			(mbar)	(m)	(CCYY-MM-DD)
ARTU			(deg C)	(m)	(CCYY-MM-DD)
BOR1	HPTL.3A	NAVI Ltd.,Promienista 5/1, PL 60-288 POZNAN	3	0	(CCYY-MM-DD)
BOR1	SKPS 800/1	Skye Instruments Ltd.	0.25 hPa sigm	0	(CCYY-MM-DD)
BOR1	HPTL.3A	NAVI Ltd.,Promienista 5/1, PL 60-288 POZNAN	+/- 5% in ful	0	(CCYY-MM-DD)
CHPI	Capacitance Probe	Paroscientific	2	0 m	(CCYY-MM-DD)
CHPI	Digiquartz Barometric Standard	Paroscientific	0.010%	0 m	(CCYY-MM-DD)
CHPI	Platinum Resistance Temperature Probe	Paroscientific	0.5 deg C	0 m	(CCYY-MM-DD)
CHUR	HMP-35A	VAISALA	2.0 (% rel h)	-6.67 (m)	
CHUR	PTB-100A	VAISALA	0.1 (hPa)	-2 (m)	
CHUR	YSI 44212	VSI	0.2 (deg C)	-6.67 (m)	
CONZ	809 L 0-100	Lambrecht	2.5	10	(CCYY-MM-DD)
CONZ	740-16B DIGIQUARTZ	PAROSCIENTIFIC	0.1	15	(CCYY-MM-DD)
CONZ	809 L 0-100	Lambrecht	0.3	10	(CCYY-MM-DD)
DARW	PAROSCIENTIFIC MET3	Paroscientific, Inc.	2%	3m	2003-09-03
DARW	PAROSCIENTIFIC MET3	Paroscientific, Inc.	0.1 mbar	3m	2003-09-03
DARW	PAROSCIENTIFIC MET3	Paroscientific, Inc.	0.5 deg C	3m	2003-09-03
GUAO	MET3	PAROSCIENTIFIC	(% rel h)	(m)	(CCYY-MM-DD)
GUAO	MET3	PAROSCIENTIFIC	(hPa)	(m)	(CCYY-MM-DD)
GUAO	MET3	PAROSCIENTIFIC	(hPa)	(m)	(CCYY-MM-DD)
HERS	MP103A-T7-W4W	Rotronics	1.5	1.1 m	(2001-11-20)
HERS	DPI 140 series	Druck	0.1 hPa	1.1 m	(CCYY-MM-DD)
HERS	MP103A-T7-W4W	Rotronics	0.3 deg C	1.1 m	2001-11-20
HRAO	Capacitance Probe	Paroscientific	2	10.6	(CCYY-MM-DD)
HRAO	Digiquartz Barometric Standard	Paroscientific	0.1	10.6	(CCYY-MM-DD)
HRAO	Platinum Resistance Temperature Probe	Paroscientific	0.5	10.6	(CCYY-MM-DD)
IISC	MET3A	Paroscientific	+2	0	(CCYY-MM-DD)
IISC	MET3A	Paroscientific	+0.08	0	(CCYY-MM-DD)
IISC	MET3A	Paroscientific	+0.1	0	(CCYY-MM-DD)
JPLM	MET3	Paroscientific	2	8	(CCYY-MM-DD)
JPLM	MET3	Paroscientific	.1	8	(CCYY-MM-DD)
JPLM	MET3	Paroscientific	0.5	8	(CCYY-MM-DD)
kit3	PTU303	Vaisala	1.5	0.5	2009-12-01
kit3	PTU300 Class A	Vaisala	0.1	-1.5	2009-12-01

kit3	PTU303	Vaisala	0.1	0.5	2009-12-01
LHAZ	MP408A-T4-W4W	ROTRONIC	1.5	-0.5	(CCYY-MM-DD)
LHAZ	APS	ROESSLER + CIE	1	4.9	(CCYY-MM-DD)
LHAZ	MP408A-T4-W4W	ROTRONIC	0.3	-0.5	(CCYY-MM-DD)
LPGS	PTU303	Vaisala	1.5	0.1	2010-01-01
LPGS	PTU300 Class A	Vaisala	0.1	-0.9	2010-01-01
LPGS	PTU303	Vaisala	0.1	0.1	2010-01-01
MDO1			(% rel h)	(m)	(CCYY-MM-DD)
MDO1			(hPa)	(m)	(CCYY-MM-DD)
MDO1			(deg C)	(m)	(CCYY-MM-DD)
MIZU	HMP45A-P	Vaisala	1.5	+3.1m	2005-09-15
MIZU	PTU200	Vaisala	0.1	-0.8m	2005-09-15
MIZU	HMP45A-P	Vaisala	0.1	0	2005-09-15
NRC1	HMP-35A	VAISALA	2.0 (% rel h)	.18 (m)	
NRC1	PTB-100A	VAISALA	0.1 (hPa)	12.59 (m)	
NRC1	YSI 44212	YSI	0.2 (deg C)	.18 (m)	
OHI2	MP408A	ROTRONIC	1.5	-1.1	(CCYY-MM-DD)
OHI2	APS 9215	L-TEC Leibenguth	0.1	1.0	(CCYY-MM-DD)
OHI2	MP408A	ROTRONIC	0.3	-1.1	(CCYY-MM-DD)
OUS2	HMP45A-P	Vaisala	1.5	0.00	2010-07-22
OUS2	PTU200	Vaisala	0.1	-8.30	2010-07-22
OUS2	HMP45A-P	Vaisala	0.1	0.00	2010-07-22
PDEL	Met3	Paroscientific	2	-1.50 m	(CCYY-MM-DD)
PDEL	Met3	Paroscientific	1 hPa	-1.50 m	(CCYY-MM-DD)
PDEL	Met3	Paroscientific	0.5 deg C	-1.50 m	(CCYY-MM-DD)
PETS			(% rel h)	(m)	(CCYY-MM-DD)
PETS			(hPa)	(m)	(CCYY-MM-DD)
PETS			(deg C)	(m)	(CCYY-MM-DD)
REYK	MP408A-T4-W4W	ROTRONIC	1.5	1.0	(CCYY-MM-DD)
REYK	APS 9215	L-TECH LEIBENGUTH	0.1	4.0	(CCYY-MM-DD)
REYK	MP408A-T4-W4W	ROTRONIC	0.3	1.0	(CCYY-MM-DD)
RIO2	PTU303	Vaisala	1.5	3.2	2009-12-30
RIO2	PTU300 Class A	Vaisala	0.1	1.1	2009-12-30
RIO2	PTU303	Vaisala	0.1	3.2	2009-12-30
SCUB	HC 500	TimeTech/Gresinger	1	(m)	(CCYY-MM-DD)
SCUB	PTB1OOB	Vaisala	0.5	-5.50	(CCYY-MM-DD)
SCUB	TM 200	TimeTech	(deg C)	(m)	(CCYY-MM-DD)
TAH1	HMP233		(% rel h)	(m)	(CCYY-MM-DD)
TAH1	PTB220		(hPa)	(m)	(CCYY-MM-DD)
TAH1	HMP233		(deg C)	(m)	(CCYY-MM-DD)
THU2	HMP45D	VAISALA	2 % rel h	(m)	(CCYY-MM-DD)
THU2	PTU200 Class A	VAISALA	0.15 mbar	5.10 m	(CCYY-MM-DD)
THU2	PTU200	VAISALA	0.2 deg C	(m)	(CCYY-MM-DD)
TIX1	Polymer Capacitance Element	Paroscientific, Inc.	+2% rel h	(m)	(CCYY-MM-DD)
TIX1	Digiquartz (R) Barometric Pressure Transducer	Paroscientific, Inc. Paroscientific, Inc.	+0.01%	(m)	(CCYY-MM-DD)
TIX1	Thin-film Platinum 1000-ohm Resistor	Paroscientific, Inc.	+0.5 deg C	(m)	(CCYY-MM-DD)
UNBJ	MET4A-1	Paroscientific	2%	0.991 m	2009-04-16
UNBJ	MET4A-1	Paroscientific	0.08 hPa	1.410 m	2009-04-16

UNBJ	MET4A-1	Paroscientific	0.2 degree C	0.991 m	2009-04-16
VALD	HMP-35A	VAISALA	2.0 (% rel h)	0 (m)	
VALD	PTB-100A	VAISALA	0.1 (hPa)	0 (m)	2006-04-21
VALD	YSI 44212	YSI	0.2 (deg C)	0 (m)	
WIND	HMP45A-P	Vaisala	1.5	-0.6	2001-02-12
WIND	PTU200	Vaisala	0.1	-4.4	2001-02-12
WIND	HMP45A-P	Vaisala	0.1	-0.6	2001-02-12
WTZR	MP 400A	Lamprecht	1.5	0 m	(CCYY-MM-DD)
WTZR	740	Paroscientific Inc. / Digiquarz	0.1 hPa	10.5 m	(CCYY-MM-DD)
WTZR	809 L 0-100	Lamprecht, Goettingen	0.3 deg C	0 m	(CCYY-MM-DD)

Table A.2: Summary of mean difference and standard deviation for the difference in pressure. January 1st to December 31st, 2010 (all values in mbar)

Station	Latitude	GPT		NCEP		CMC	
		$\overline{\Delta p}$	$\sigma$	$\overline{\Delta p}$	$\sigma$	$\overline{\Delta p}$	$\sigma$
artu	56.4298	-4.998	10.372	-0.643	2.190	-0.203	0.564
thu2	76.5370	-7.693	10.817	1.136	1.819	0.454	1.053
lhaz	29.6573	11.180	3.727	15.077	1.666	13.284	2.110
conz	-36.8438	-2.332	3.653	0.250	3.343	0.089	0.938
mizu	39.1352	-2.315	7.185	-0.531	1.737	0.020	0.600
unbj	45.9502	3.939	9.568	-0.668	2.280	0.103	0.535
nrc1	45.4542	-0.240	7.580	-1.385	2.442	-0.682	0.524
wtzr	49.1442	1.545	7.000	0.244	1.886	0.306	0.481
bor1	52.1002	6.382	8.556	3.254	1.791	3.312	0.474
hrao	-25.8901	-2.075	2.922	1.009	0.907	0.668	0.468
reyk	64.1388	-8.441	12.894	3.967	1.695	3.506	0.651
chpi	-22.6871	-1.954	3.019	0.630	1.230	0.210	0.742
jplm	34.2048	4.344	3.537	-0.950	1.319	-0.645	0.841
hers	50.8673	2.046	10.046	-0.188	1.561	-0.324	0.332
lpgs	-34.9067	-1.975	6.037	1.005	1.804	-0.215	0.527
kit3	39.1400	0.801	4.477	2.052	2.250	-0.159	1.135
iisc	13.0212	-3.425	1.900	-0.339	0.895	-0.496	0.647
rio2	-53.7855	3.569	11.978	-1.034	1.760	-0.049	0.712
pdel	37.7477	2.959	7.655	0.058	1.887	0.140	0.495
tah1	-17.5770	-1.759	2.151	-0.110	0.549	-0.782	0.489
ohi2	-63.3211	2.345	11.093	-0.999	1.993	-0.934	1.506
wind	-22.5749	-2.238	1.803	0.468	0.889	0.179	0.649
alic	-23.6701	-1.831	3.410	-0.093	0.847	0.154	0.459
darw	-12.8437	0.194	2.261	0.133	0.724	-0.043	0.532
pets	53.0233	-3.088	10.603	-1.902	2.043	-1.234	0.866
ade1	-34.7290	-1.722	6.350	-0.989	1.446	-0.844	0.539
chur	58.7591	-3.549	8.816	-0.515	2.175	-0.180	0.574
guao	43.4711	2.791	3.897	-0.655	2.370	-0.350	0.906
scub	20.0121	-0.888	2.069	-1.117	0.808	-1.612	0.494
eill	64.6879	-0.017	10.431	0.881	2.304	0.115	0.917
mdo1	30.6805	-2.768	3.920	0.014	0.981	0.309	0.542
albh	48.3898	-0.288	7.379	-0.075	1.582	-0.542	0.579
ous2	-45.8695	-3.468	10.699	0.972	2.667	0.073	0.860
tixi	71.6345	1.556	10.418	0.463	1.403	0.216	0.702
vald	48.0971	1.536	7.038	-1.135	2.263	-0.393	0.494

Table A.3: Summary of mean difference and standard deviation for the difference in temperature. January 1st to December 31st, 2010 (all values in K)

Station	Latitude	GPT		NCEP		CMC	
		$\overline{\Delta T}$	$\sigma$	$\overline{\Delta T}$	$\sigma$	$\overline{\Delta T}$	$\sigma$
artu	56.4298	0.600	6.739	-0.380	3.785	-0.169	2.174
thu2	76.5370	-3.429	4.797	0.771	2.911	-3.338	2.775
lhaz	29.6573	-7.965	3.884	-6.533	2.674	-5.670	2.452
conz	-36.8438	0.781	3.637	2.758	3.139	-0.034	1.678
mizu	39.1352	-0.845	3.896	0.915	2.810	-0.271	1.962
unbj	45.9502	-1.779	4.952	-0.796	2.751	-0.292	1.680
nrc1	45.4542	-2.687	5.044	-0.978	2.404	-0.398	2.029
wtzr	49.1442	0.043	4.369	-0.414	2.213	-0.131	1.581
bor1	52.1002	1.396	4.637	-0.126	2.430	-0.321	1.447
hrao	-25.8901	-0.970	5.271	0.197	4.082	1.399	2.766
reyk	64.1388	0.470	3.130	0.451	1.731	-0.111	1.165
chpi	-22.6871	-0.669	4.879	-1.068	3.663	-1.158	2.072
jplm	34.2048	-1.413	5.283	1.725	3.069	-0.879	2.014
hers	50.8673	2.053	3.552	0.768	2.142	1.035	1.573
lpgs	-34.9067	0.061	4.125	-0.157	2.638	0.415	2.063
kit3	39.1400	0.679	6.003	0.713	3.214	0.709	2.308
iisc	13.0212	-2.845	4.453	-2.421	3.968	-1.632	2.891
rio2	-53.7855	-0.465	3.322	1.399	2.691	1.439	1.750
pdel	37.7477	-1.938	1.805	-0.264	1.343	-0.207	1.121
tah1	-17.5770	-0.962	1.883	-0.152	1.709	-0.094	1.729
wind	-22.5749	-6.136	4.643	-0.179	3.194	-1.256	1.995
alic	-23.6701	0.771	6.000	0.951	4.498	-0.140	2.056
darw	-12.8437	-0.523	3.633	-1.120	2.585	-0.739	1.740
pets	53.0233	-3.061	3.257	0.209	2.244	-1.672	1.664
adel	-34.7290	0.912	4.439	0.183	2.572	-1.012	1.712
chur	58.7591	1.886	5.872	-0.641	3.093	0.213	2.053
guao	43.4711	1.548	4.852	-1.227	3.883	1.809	3.028
scub	20.0121	-0.271	3.464	0.821	2.994	-0.168	1.683
eil1	64.6879	-2.274	6.210	2.914	4.341	-0.391	2.404
mdo1	30.6805	-1.828	5.710	-1.868	4.394	-0.242	4.194
albh	48.3898	2.911	2.516	2.180	2.256	0.292	1.358
ous2	-45.8695	-1.138	3.487	-0.653	2.476	-0.421	1.757
tixi	71.6345	3.854	3.411	-0.955	2.999	-4.082	2.353
vald	48.0971	-2.551	5.746	-0.159	3.049	0.325	1.508

Table A.4: Summary of mean difference and standard deviation for the difference in specific humidity. January 1st to December 31st, 2010 (all values in kg/kg)

Station	Latitude	NCEP		CMC	
		$\overline{\Delta q}$	$\sigma$	$\overline{\Delta q}$	$\sigma$
artu	56.4298	0.00019	0.00106	-0.00022	0.00069
thu2	76.5370	0.00037	0.00045	-0.00033	0.00034
lhaz	29.6573	0.00300	0.00142	-0.00068	0.00109
conz	-36.8438	-0.00095	0.00164	-0.00119	0.00096
mizu	39.1352	0.00150	0.00107	0.00012	0.00091
unbj	45.9502	0.00011	0.00116	-0.00020	0.00066
nrc1	45.4542	0.00144	0.00123	0.00043	0.00088
wtzt	49.1442	0.00012	0.00108	-0.00016	0.00069
bor1	52.1002	-0.00058	0.00213	-0.00113	0.00076
hrao	-25.8901	0.00082	0.00163	-0.00090	0.00116
reyk	64.1388	0.00053	0.00077	0.00003	0.00043
chpi	-22.6871	-0.00059	0.00152	-0.00146	0.00124
jplm	34.2048	-0.00123	0.00153	-0.00056	0.00110
hers	50.8673	-0.00010	0.00096	-0.00021	0.00054
lpgs	-34.9067	0.00074	0.00152	0.00043	0.00089
kit3	39.1400	0.00105	0.00148	0.00020	0.00134
iisc	13.0212	-0.00282	0.00189	-0.00172	0.00187
rio2	-53.7855	0.00079	0.00058	0.00046	0.00042
pdel	37.7477	-0.00015	0.00118	-0.00064	0.00076
tah1	-17.5770	0.00039	0.00182	-0.00078	0.00174
wind	-22.5749	0.00124	0.00204	0.00043	0.00153
alic	-23.6701	-0.00131	0.00198	-0.00108	0.00129
darw	-12.8437	-0.00049	0.00215	-0.00297	0.00161
pets	53.0233	0.00036	0.00061	-0.00055	0.00045
ade1	-34.7290	-0.00068	0.00137	0.00005	0.00092
chur	58.7591	0.00002	0.00076	-0.00026	0.00050
guao	43.4711	-0.00085	0.00045	-0.00035	0.00035
scub	20.0121	0.00129	0.00161	-0.00062	0.00132
eil1	64.6879	0.00175	0.00102	-0.00012	0.00060
mdo1	30.6805	-0.00012	0.00270	-0.00015	0.00269
albh	48.3898	0.00168	0.00092	-0.00008	0.00055
ous2	-45.8695	0.00268	0.00115	0.00256	0.00120
tixi	71.6345	-0.00007	0.00021	-0.00025	0.00010
vald	48.0971	0.00113	0.00110	0.00013	0.00062



## A.1.1 Hydrostatic Zenith Delay

The following section provides a complete set of plots and a station summary for the difference in hydrostatic zenith between the ray-traced values and those computed by Saastamoinen using the measured site pressure. First, Table A.5 summarizes the mean and standard deviation of the difference in zenith hydrostatic delay by NCEP and CMC. Secondly, the differences are plotted in Figure A.1.(1-35) and consist of the raw time series along with the resulting fit by equation 3.7. The results for NCEP are shown in blue and the results for CMC are shown in red. The fitted time series for NCEP is shown as a solid black line and a dashed black line for the CMC product.

Table A.5: Summary of statistics for computed hydrostatic zenith delay differences (all values in mm)

Station	Latitude	NCEP		CMC	
		$\overline{\Delta zh\bar{d}}$	$\sigma$	$\overline{\Delta zh\bar{d}}$	$\sigma$
artu	56.4298	0.780	5.162	0.075	1.369
thu2	76.5370	4.231	4.282	2.107	2.486
lhaz	29.6573	34.016	3.904	28.515	4.819
conz	-36.8438	1.072	8.070	-0.536	2.236
mizu	39.1352	-0.132	3.988	-1.199	1.487
unbj	45.9502	0.514	5.298	0.858	1.305
nrc1	45.4542	-1.404	5.680	-0.779	1.289
wtzt	49.1442	2.240	4.521	-0.128	1.226
bor1	52.1002	9.514	4.231	7.161	1.150
hrao	-25.8901	2.903	2.053	-0.735	1.198
reyk	64.1388	10.446	3.985	7.745	1.603
chpi	-22.6871	2.319	2.788	-0.917	1.899
jplm	34.2048	-1.446	3.204	-1.387	2.049
hers	50.8673	1.101	3.753	-1.112	0.814
lpgs	-34.9067	3.539	4.254	-1.388	1.324
kit3	39.1400	3.032	5.662	-0.450	2.607
iisc	13.0212	0.748	2.090	-1.699	1.678
rio2	-53.7855	-0.583	4.070	0.246	1.667
pdel	37.7477	1.441	4.341	-0.810	1.176
tah1	-17.5770	0.478	1.349	-3.318	1.322
ohi2	-63.3211	-0.519	4.581	-1.572	3.421
wind	-22.5749	1.948	1.994	-2.184	1.687
alic	-23.6701	0.836	1.929	-1.306	1.253
darw	-12.8437	1.452	1.830	-2.473	1.423
pets	53.0233	-2.756	4.800	-2.764	2.031
ade1	-34.7290	-0.795	3.525	-2.423	1.301
chur	58.7591	1.732	5.198	1.400	1.369
guao	43.4711	0.389	5.437	-0.344	2.075
scub	20.0121	-1.914	1.839	-5.334	1.303
eill	64.6879	3.637	5.377	1.127	2.127
mdo1	30.6805	2.009	2.318	-0.445	1.337
albh	48.3898	0.610	3.881	-0.368	1.362
ous2	-45.8695	3.808	6.258	0.358	2.064
tixi	71.6345	3.932	3.538	1.612	1.586
vald	48.0971	-0.437	5.236	0.041	1.206

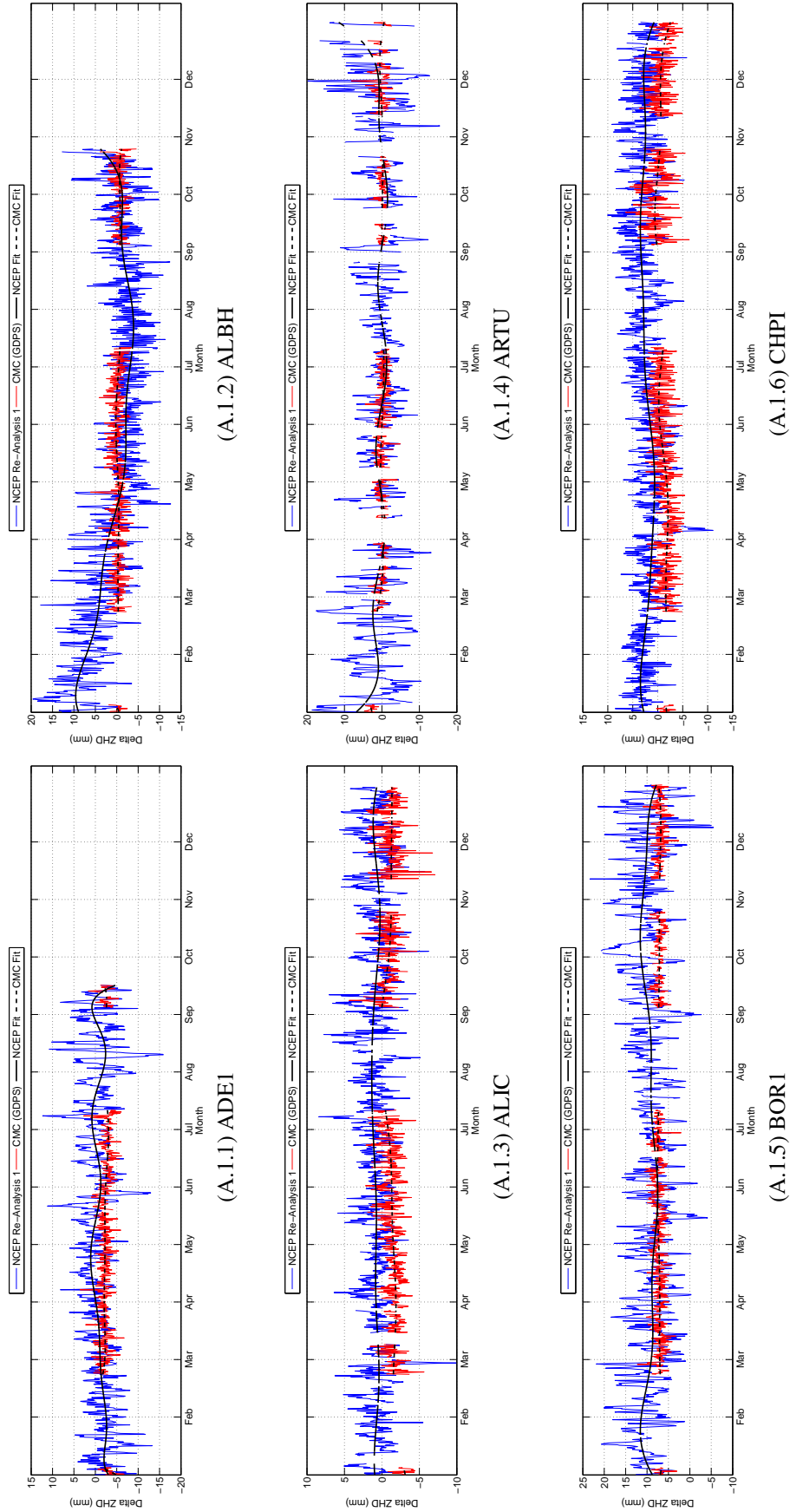
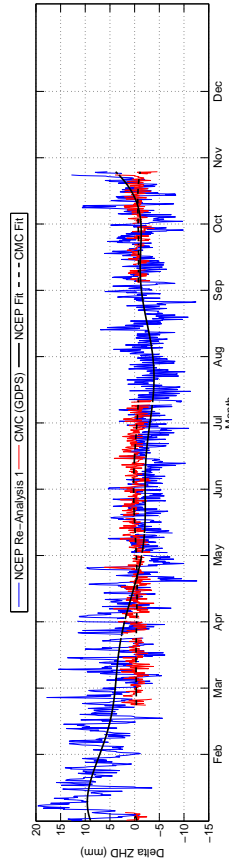
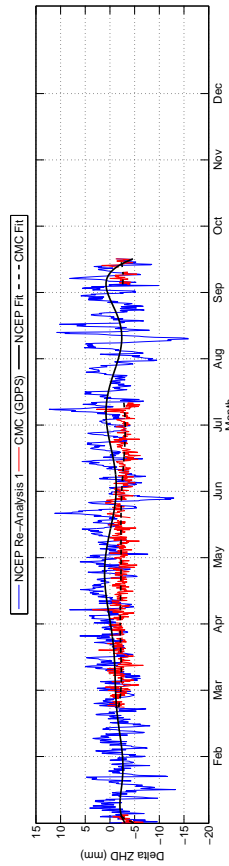


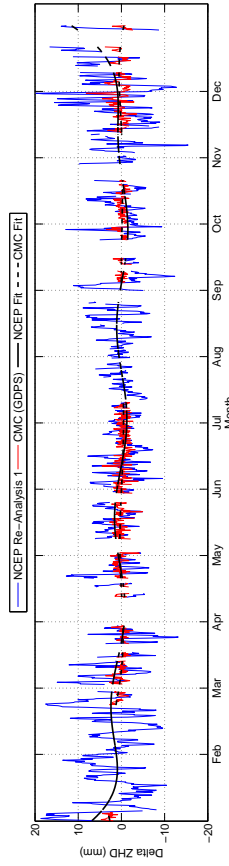
Figure A.1: Difference in ray-traced zenith hydrostatic delay from zenith hydrostatic delay computed from site pressure. (NWP minus SITE). January 1st to December 31st 2010.



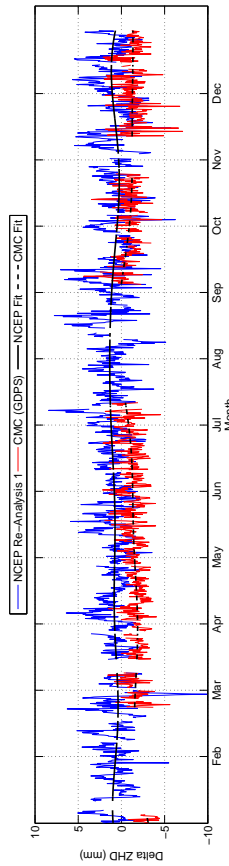
(A.1.8) CONZ



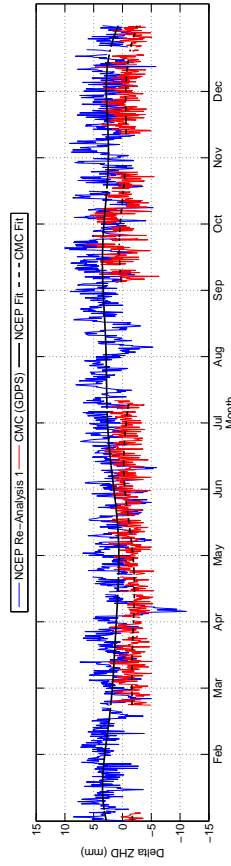
(A.1.7) CHUR



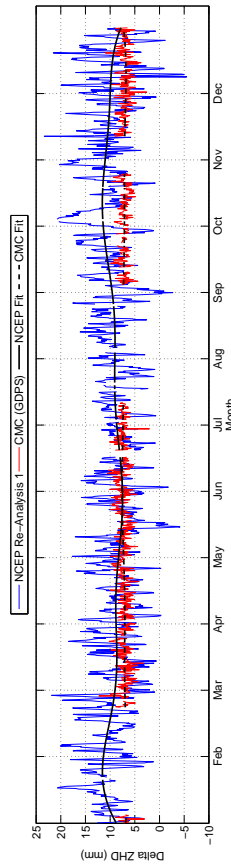
(A.1.10) EILI



(A.1.9) DARW

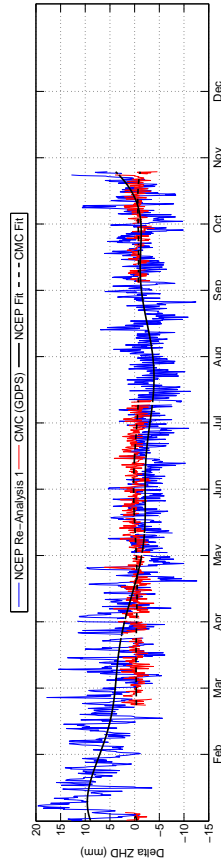


(A.1.12) HERS

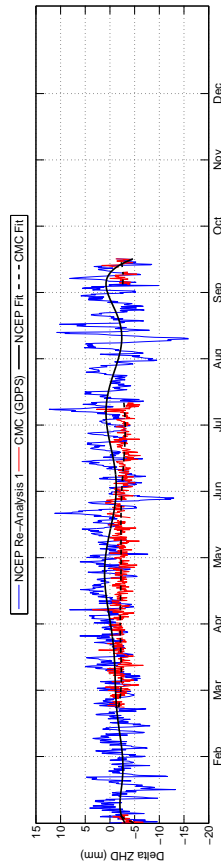


(A.1.11) GUAO

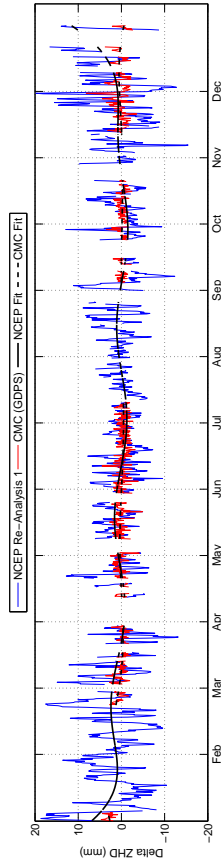
Figure A.1: Difference in ray-traced zenith hydrostatic delay from zenith hydrostatic delay computed from site pressure. (NWP minus SITE), January 1st to December 31st 2010.



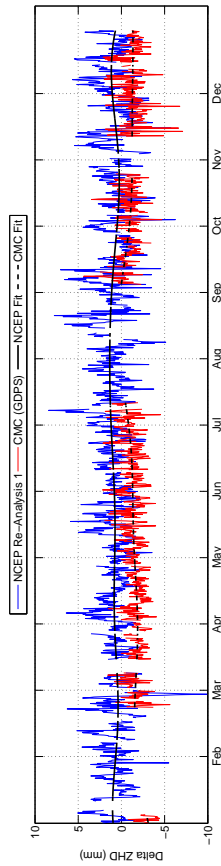
(A.1.14) IISC



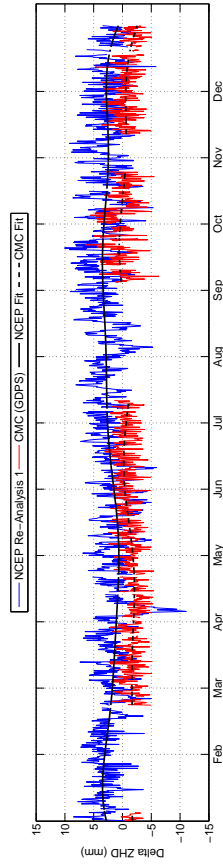
(A.1.13) HRAO



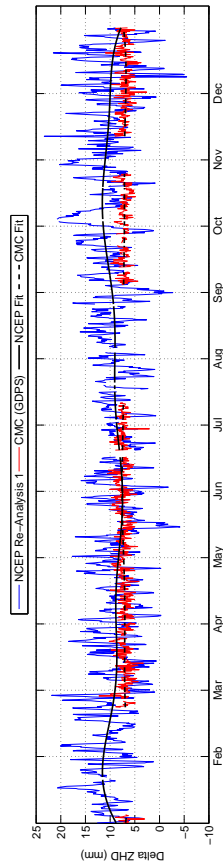
(A.1.16) KIT3



(A.1.15) JPLM

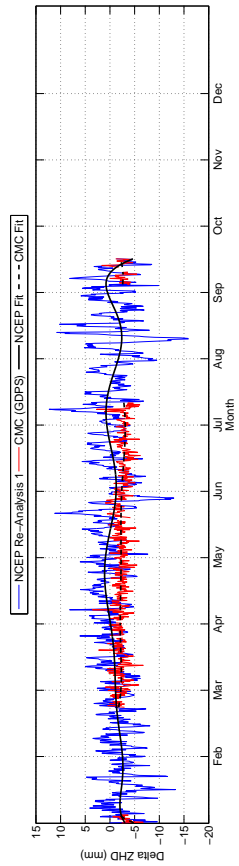


(A.1.18) LPGA

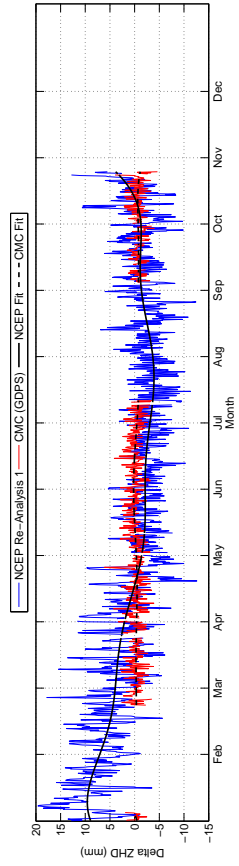


(A.1.17) LHAZ

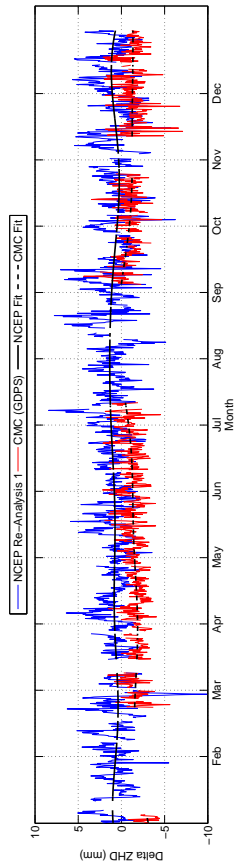
Figure A.1: Difference in ray-traced zenith hydrostatic delay from zenith hydrostatic delay computed from site pressure. (NWP minus SITE), January 1st to December 31st 2010.



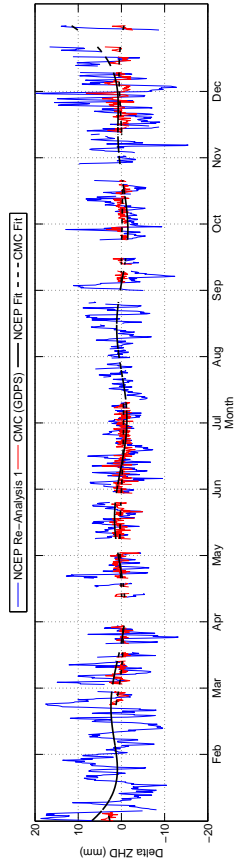
(A.1.19) MDO1



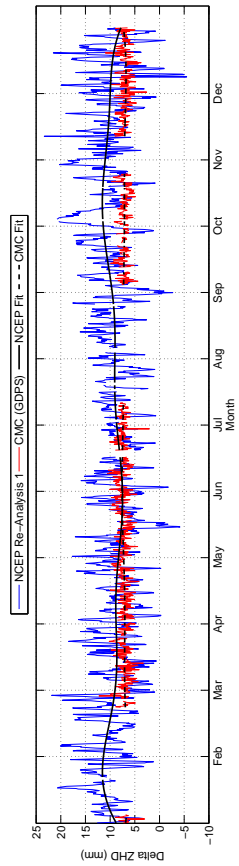
(A.1.20) MIZU



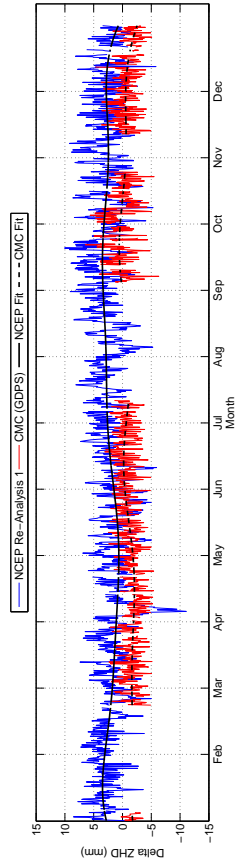
(A.1.21) NRC1



(A.1.22) OHI2

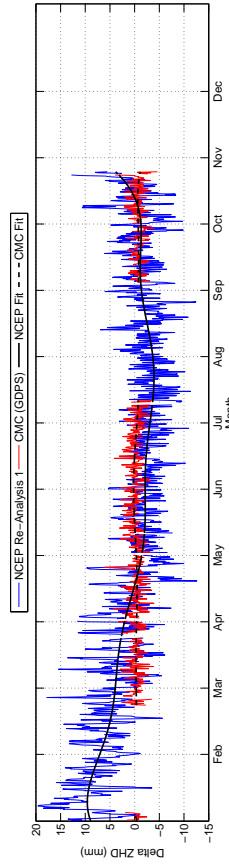


(A.1.23) OUS2

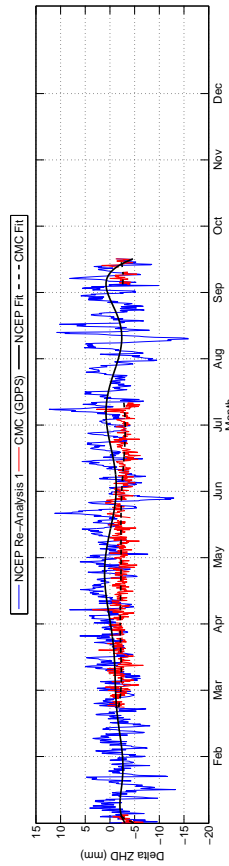


(A.1.24) PDEL

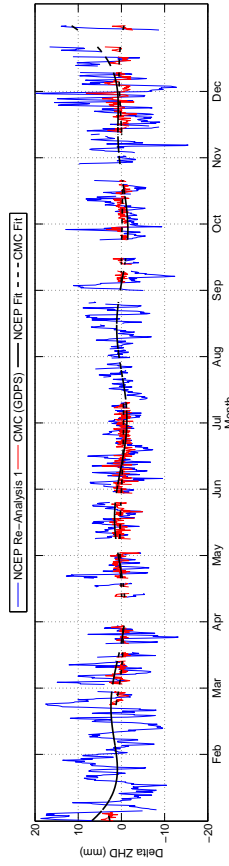
Figure A.1: Difference in ray-traced zenith hydrostatic delay from zenith hydrostatic delay computed from site pressure. (NWP minus SITE), January 1st to December 31st 2010.



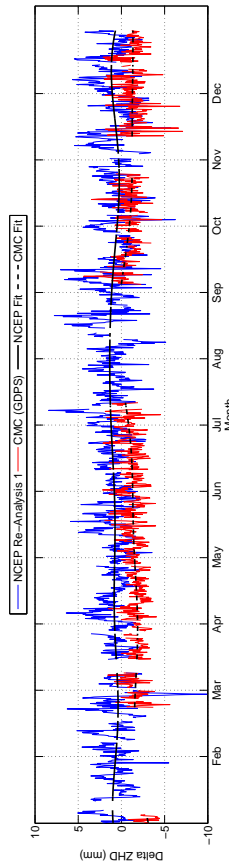
(A.1.26) REYK



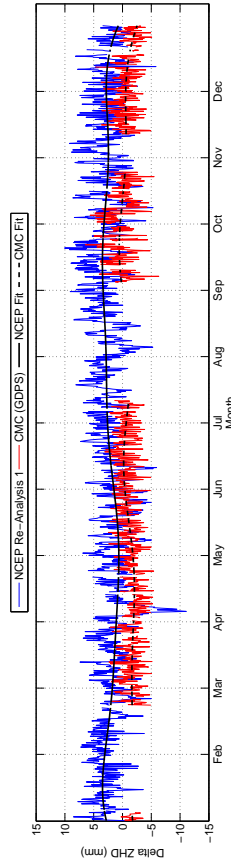
(A.1.25) PETS



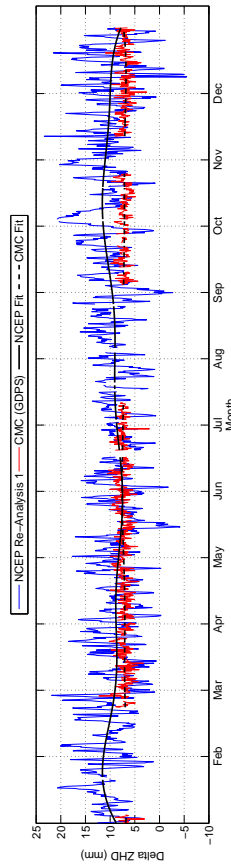
(A.1.28) SCUB



(A.1.27) RIO2

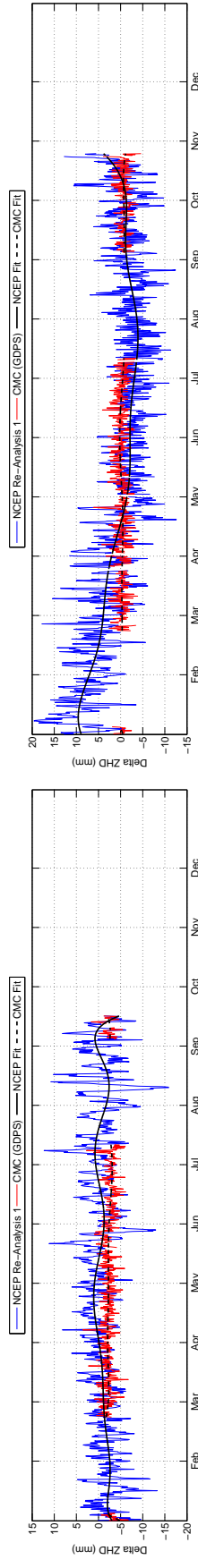


(A.1.30) THU2

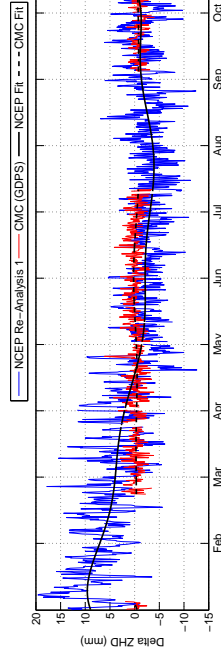


(A.1.29) TAH1

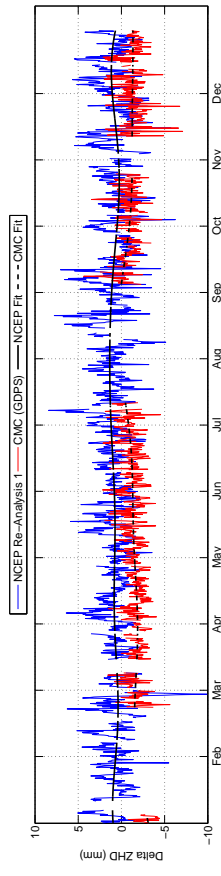
Figure A.1: Difference in ray-traced zenith hydrostatic delay from zenith hydrostatic delay computed from site pressure. (NWP minus SITE), January 1st to December 31st 2010.



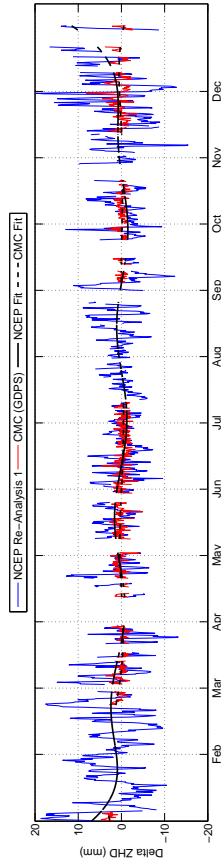
(A.1.31) TAXI



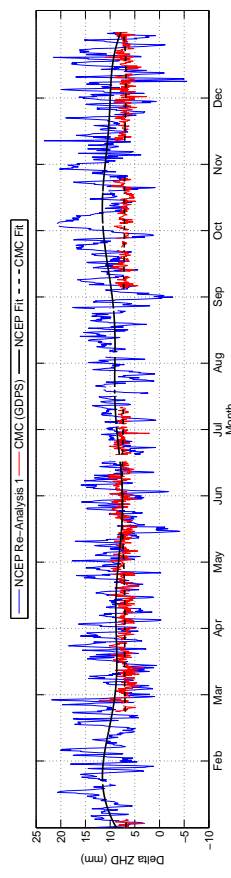
(A.1.32) UNBJ



(A.1.33) VALD



(A.1.34) WIND



(A.1.35) WTZR

Figure A.1: Difference in ray-traced zenith hydrostatic delay from zenith hydrostatic delay computed from site pressure. (NWP minus SITE), January 1st to December 31st 2010.

# Appendix B

## UNB-VMF1 Service Supplemental

This section provides further details regarding the process flow of the UNB-VMF1 service. In particular, the output file format, download process, submission process, run process, and the upload process will be discussed in further detail.

### B.1 UNB-VMF1 Process

The UNB-VMF1 has been designed to operate in a Unix-like environment and is controlled by a series of Unix shell scripts scheduled to trigger at specified times daily. All products produced for the UNB-VMF1 are produced in this fashion and the process flows for the NCEP based product will be presented in this Appendix with comments regarding any deviations for the CMC based products. Tables B.1, B.2, and B.3 summarize the all scripts for all products on all clusters and their associated scheduled run times. Table B.1 summarizes the download scripts for each source NWP used to produce each UNB-VMF1 product. Table B.2. summarizes the computation scripts used to manage job control submission and product generation. Lastly, Table B.3. summarizes the maintenance scripts that are used to summarize the daily jobs, archive daily log files, and email daily job summaries to the administrator.



Table B.1: Summary of download scripts for each cluster on ACE-NET. The date implemented, execution time, and script name are listed for each NWP type.

Product	Fundy			Mahone			Placentia		
	Date	Script Execution/Name	Date	Script Execution/Name	Date	Script Execution/Name	Date	Script Execution/Name	
NOAA NCEP Re-Analysis I	2012-01-15	Every 12 HRS get_ncep_netcdf.sh	2012-01-15	Every 12 HRS get_ncep_netcdf.sh	2012-01-15	Every 12 HRS get_ncep_netcdf.sh	2012-01-15	Every 12 HRS get_ncep_netcdf.sh	
CMC GDPS GRIB2 lat/lon	2012-01-14	Every 6 HRS download_mv_CMC_glb.sh run_wget_glb_grib2.sh run_mkdir_mv_glb_grib2.sh	2012-01-14	Every 6 HRS download_mv_CMC_glb.sh run_wget_glb_grib2.sh run_mkdir_mv_glb_grib2.sh	2012-01-14	Every 6 HRS download_mv_CMC_glb.sh run_wget_glb_grib2.sh run_mkdir_mv_glb_grib2.sh	2012-01-14	Every 6 HRS download_mv_CMC_glb.sh run_wget_glb_grib2.sh run_mkdir_mv_glb_grib2.sh	
CMC RDPS GRIB2 polar	2012-01-14	Every 6 HRS run_wget_reg_grib2.sh run_mkdir_mv_reg_grib2.sh	2012-01-14	Every 6 HRS run_wget_reg_grib2.sh run_mkdir_mv_reg_grib2.sh	2012-01-14	Every 6 HRS run_wget_reg_grib2.sh run_mkdir_mv_reg_grib2.sh	2012-01-14	Every 6 HRS run_wget_reg_grib2.sh run_mkdir_mv_reg_grib2.sh	

Table B.2: Summary of computation scripts for each cluster on ACE-NET. Includes both the submit and run scripts. The date implemented, execution time, and script name are listed for each NWP type.

Product	Fundy			Mahone			Placentia		
	Date	Script Execution/Name	Date	Script Execution/Name	Date	Script Execution/Name			
unbvmfG Computation (NCEP)	2012-02-06	DAILY at 18:00:00 Matlab Executable submitStandaloneUNBVVMF1_single.sh runStandaloneUNBVVMF1_00.sh runStandaloneUNBVVMF1_06.sh runStandaloneUNBVVMF1_12.sh runStandaloneUNBVVMF1_18.sh	2012-02-06	DAILY at 18:00:00 Matlab Executable submitStandaloneUNBVVMF1_single.sh runStandaloneUNBVVMF1_00.sh runStandaloneUNBVVMF1_06.sh runStandaloneUNBVVMF1_12.sh runStandaloneUNBVVMF1_18.sh	2012-02-06	DAILY at 18:00:00 Matlab Executable submitStandaloneUNBVVMF1_single.sh runStandaloneUNBVVMF1_00.sh runStandaloneUNBVVMF1_06.sh runStandaloneUNBVVMF1_12.sh runStandaloneUNBVVMF1_18.sh			
	2012-03-15	DAILY at 19:00:00 Matlab Executable submitStandaloneUNBVVMF1_single.CMC.sh runStandaloneUNBVVMF1_CMC_00.sh runStandaloneUNBVVMF1_CMC_06.sh runStandaloneUNBVVMF1_CMC_12.sh runStandaloneUNBVVMF1_CMC_18.sh	2012-03-30	DAILY at 19:00:00 Matlab Executable submitStandaloneUNBVVMF1_single.CMC.sh runStandaloneUNBVVMF1_CMC_00.sh runStandaloneUNBVVMF1_CMC_06.sh runStandaloneUNBVVMF1_CMC_12.sh runStandaloneUNBVVMF1_CMC_18.sh	2012-03-30	DAILY at 19:00:00 Matlab Executable submitStandaloneUNBVVMF1_single.CMC.sh runStandaloneUNBVVMF1_CMC_00.sh runStandaloneUNBVVMF1_CMC_06.sh runStandaloneUNBVVMF1_CMC_12.sh runStandaloneUNBVVMF1_CMC_18.sh			
unbvmfP Computation (CMC)	2012-03-22	DAILY at 08:00:00 Matlab Executable submitStandaloneUNBVVMF1_single.CMC_predicted.sh runStandaloneUNBVVMF1_CMC_P_00.sh runStandaloneUNBVVMF1_CMC_P_06.sh runStandaloneUNBVVMF1_CMC_P_12.sh runStandaloneUNBVVMF1_CMC_P_18.sh	2012-03-30	DAILY at 08:00:00 Matlab Executable submitStandaloneUNBVVMF1_single.CMC_predicted.sh runStandaloneUNBVVMF1_CMC_P_00.sh runStandaloneUNBVVMF1_CMC_P_06.sh runStandaloneUNBVVMF1_CMC_P_12.sh runStandaloneUNBVVMF1_CMC_P_18.sh	2012-03-30	DAILY at 08:00:00 Matlab Executable submitStandaloneUNBVVMF1_single.CMC_predicted.sh runStandaloneUNBVVMF1_CMC_P_00.sh runStandaloneUNBVVMF1_CMC_P_06.sh runStandaloneUNBVVMF1_CMC_P_12.sh runStandaloneUNBVVMF1_CMC_P_18.sh			

Table B.3: Summary of maintenance scripts for each cluster on ACE-NET. Includes both the submit and run scripts. The date implemented, execution time, and script name are listed for each NWP type.

Product	Fundy			Mahone			Placentia		
	Date	Script Execution/Name	Date	Script Execution/Name	Date	Script Execution/Name			
UNB-VMF1 server Sync	2011-12-01	DAILY at 00:01:00 RSYNC uploadUNBVMF1.sh	2011-12-13	DAILY at 00:10:00 RSYNC uploadUNBVMF1.sh	2011-12-13	DAILY at 00:10:00 RSYNC uploadUNBVMF1.sh			
Create Summary LOG for Daily Activities	2012-04-01	DAILY at 01:00:00 createDailyLogSummary.sh	2012-04-03	DAILY at 01:00:00 createDailyLogSummary_mahone.sh	2012-04-03	DAILY at 01:00:00 createDailyLogSummary_placentia.sh			
Archive and Email all Log Files	2012-04-01	DAILY at 01:00:00 archive_email_daily_logs.sh	2012-04-01	DAILY at 01:00:00 archive_email_daily_logs_mahone.sh	2012-04-01	DAILY at 01:00:00 (NO EMAIL) archive_email_daily_logs_placentia.sh			
UNB-VMF1 Archive	2012-04-03	YEARLY on JANUARY 15, 2012 archive_UNBVMF1.sh	2012-04-03	YEARLY on JANUARY 15, 2012 archive_UNBVMF1.sh	2012-04-03	YEARLY on JANUARY 15, 2012 archive_UNBVMF1.sh			

## B.1.1 UNB-VMF1 Output File Format

Figure B.1 is a portion of an output file for the unbvmfG product for the date January 1st, 2012 at 00H. The first seven lines of the file are part of the header and identified with an exclamation point (!). The header information and its description are summarized in Table B.2.

```
! Version:                1.0
! Source:                 University of New Brunswick (created: 17-Mar-2012)
! Data_types:            VMF1 (lat lon ah aw zhd zwd)
! Epoch:                 2012 01 01 00 00 0.0
! Scale_factor:          1.e+00
! Range/resolution:      -90 90 0 360 2 2.5
! Comment:               Created using NCEP Re-Analysis I
90.0  0.0 0.00114273  0.00045401  2.2659  0.0044
90.0  2.5 0.00114272  0.00045401  2.2659  0.0044
90.0  5.0 0.00114272  0.00045403  2.2659  0.0044
90.0  7.5 0.00114272  0.00045404  2.2659  0.0044
90.0 10.0 0.00114272  0.00045406  2.2659  0.0044
90.0 12.5 0.00114272  0.00045408  2.2659  0.0044
90.0 15.0 0.00114272  0.00045410  2.2659  0.0044
90.0 17.5 0.00114271  0.00045412  2.2659  0.0044
90.0 20.0 0.00114271  0.00045413  2.2659  0.0044
90.0 22.5 0.00114271  0.00045414  2.2659  0.0044
90.0 25.0 0.00114271  0.00045415  2.2659  0.0044
90.0 27.5 0.00114271  0.00045418  2.2659  0.0044
```

Figure B.1: Sample Output from the UNB-VMF1 service for the unbvmfG product on January 1, 2012

## B.1.2 Download Process

The download process is controlled by a set of shell scripts (see Table B.1 for a summary) written to operate in the BASH shell environment set to automatically trigger as a CRON<sup>1</sup>. The NCEP Re-Analysis data is downloaded every 12 hours and the CMC (GDPS) is downloaded every 6 hours. The scripts for both the NCEP data and CMC data are straightforward sequential download commands, but the NCEP script has an additional

---

<sup>1</sup>a CRON is a time based scheduler in Unix-like computer systems

Table B.4: Description of UNB-VMF1 product header

Item	Description
Version	Currently the version is set to 1.0. If any major updates to the UNB-VMf1 service that impact the production of any product, the version will be updated. The version will refer to the product, not the service as a whole. If major changes were made to just the unbvmfGcmc product, its version will only be updated.
Source	The name of the producing body will be placed here followed by the date in which the product was created. For the UNB-VMF1, the source will always be University of New Brunswick.
Data_types	The mapping function name will appear here. For standard products, unbvmfG and unbvmfGcmc, the name VMF1 will appear. For the forecast based product, unbvmfP, the name VMF1 Predicted will appear here. In addition to the name, the data types included in the file will be listed here. Normally, each file will include lat (latitude), lon (longitude), ah (hydrostatic a coefficient), aw (non-hydrostatic coefficient), zed (zenith hydrostaticic delay), and zwd (zenith non hydrostatic delay). The order of this listing indicates the order of parameters listed in the data portion of the file.
Scale_factor	if any of the parameters have been scaled, this value will indicate the value in scientific form (e.g., 1.e+00).
Range/resolution	Indicates the spatial coverage of the product. The first two values are the range of the latitude, followed by the range of the longitude. The final two values given are the resolution of the latitude and longitude respectively.
Comment	The numerical weather prediction model used to produce the product will be identified here. For the forecast based product, unbvmfP, the date of the initialization is given along the forecast hour and initialization time (e.g., Created using CMC (GDPS) 2012-12-31 00z-F24).

step. For the NCEP download script the downloaded data is checked to ensure that the next date scheduled to be produced exists within the data. If the data cannot be found at the specified date, the date is written to external file, ncep\_date\_check.log, which is then checked prior to submission of the daily job. The CMC download scripts do not have this check, and a similar check should added to these scripts as well. Figure B.2. summarizes the process flow for the NCEP product.

## UNB-VMF1 NCEP RE-ANALYSIS I DATA DOWNLOAD FLOW

script: *get\_ncep\_netcdf.sh*

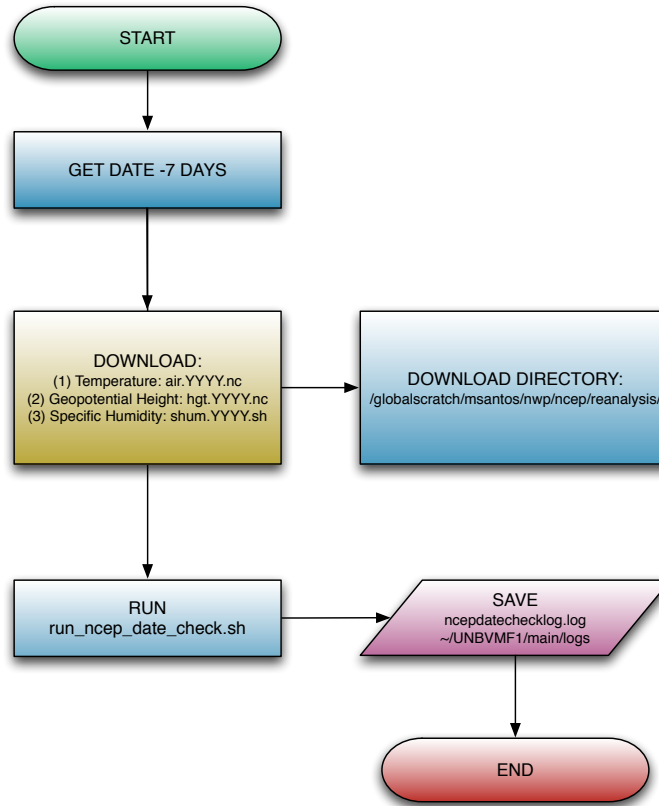


Figure B.2: UNB-VMF1 NWP data download for NCEP process flow

### B.1.3 Submission Process

The production of the UNB-VMF1 on ACE-NET is composed two main operations, namely the submission and the actual run script. ACE-NET's job control system is managed by Grid Engine, so each job is first submitted, which is subsequently scheduled within the job queue. When a submitted job is up in the queue, the specified run script will be executed. This section summarizes the submit script. As with the download script, the

submit script is a Unix shell script written to execute in the BASH shell environment. The NCEP based product's (unbvmfG) submission script is presented here, any deviations from this script for the CMC products will be noted. Figure B.3 illustrates the process flow for the unbvmfG product. First, the script checks to ensure that data is available, and

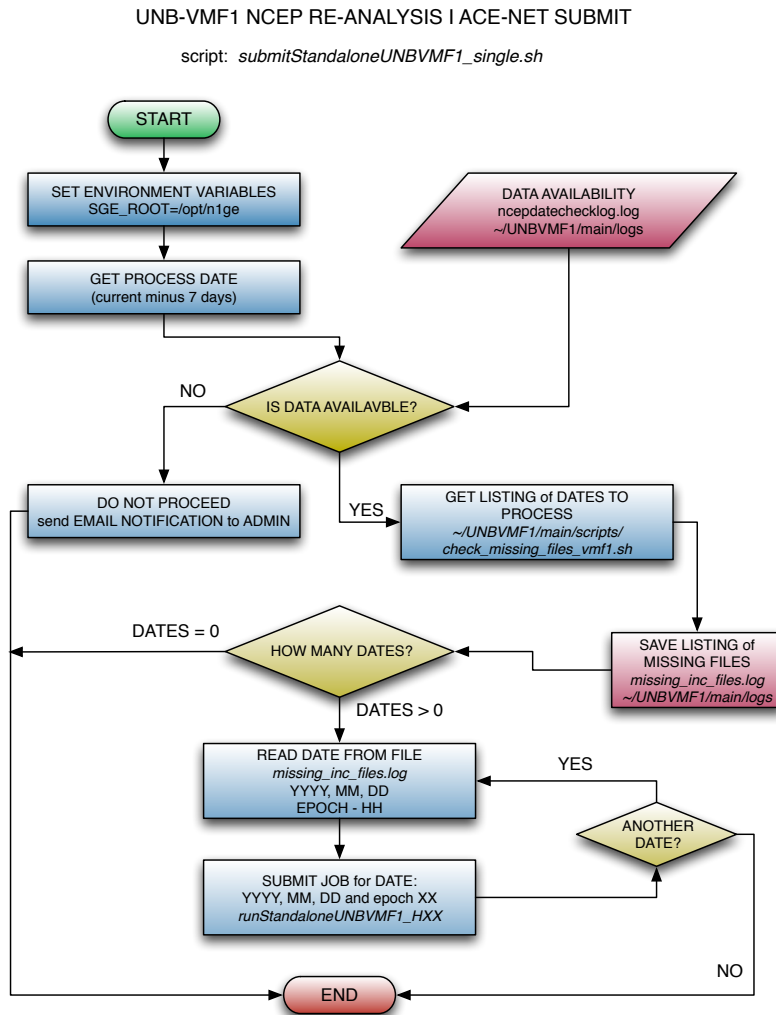


Figure B.3: UNB-VMF1 submission script process flow for unbvmfG.

if no data is available the script stops and sends an email to the administrator. For the CMC based products, this check is not completed, but it should be added in the future. If data is available, a second script is executed, *check\_missing\_files.sh*, which finds all files

within the current year that are missing and saves the corresponding dates to a log file, *missing\_inc\_files.log* (for CMC: *missing\_inc\_file\_cmc*, and *missing\_inc\_files\_cmc\_p* for the forecast based product). Once the dates have been determined, the dates are read from the specified log file, and the script then proceeds to submit the job to the Grid Engine. The benefit of this process, is that the UNB-VMF1 system automatically knows which files are missing and submits all missing files simultaneously. This is important for when nodes are taken offline for multiple days for issues such as maintenance, where during these times the UNB-VMF1 products will not be produced. When the nodes are brought back online the system scripts will execute as normal and all missing products will be produced automatically. The node downtime poses an additional problem for the CMC datasets since they are only offered for a 24hr period and will not be downloaded during these times. Currently, when a node is brought back online, the administrator must manually copy the NWP data from another node and ensure all NWP data is up to date. For the future, an additional script should be developed to address this task will less manual effort. Lastly, the jobs are submitted by specifying the run script name, where the year, month, day and hour (00,06,12 or 18) are passed as input variable to the run script. Each specific epoch is submitted separately, so that the Grid Engine can schedule all product files in parallel.

#### **B.1.4 Run Process**

The run process controls the execution of the production of each individual product file. The run script is also a Unix shell script written for the BASH shell environment. This description is for the unbvfmG product, but the CMC products follow, and any differences will be noted. There are four run scripts for each of the products. The only difference between the run scripts for each product is the interval in which they submit. In particular, there is a run script specifically for the 00H, 06H, 12H and 18H hour intervals for each product (Currently, there are 12 run scripts). These scripts can be combined into a single file per product, and it is recommended to do so since the proliferation of files will only



increase the risk of bugs and unnecessary complexity.

The submit calls the run process script and passes into it the specified year, month, day, and hour to be produced. The run script takes the supplied date variables and passes them into the Matlab executable that actually performs the computations, and writes the output files. Once the Matlab executable completes its operation, the file is checked for completeness. The run scripts checks to ensure that the file exists, and the file size. The file's size is the primary source for the check since any abnormal results or any issues with writing to the file will result in a file size change. For example, if any negative values were written to the output file, the overall file size would increase. If the file size has not met the criteria or the file failed to be created entirely, the run script re-submits the job until these two checks are met. It is important to stress that the script must check for the existence of the file. The ACE-NET system has a way of randomly killing jobs, or jobs failing with no real reason. If this is removed, the administrator will have to manually check and resubmit. Additionally, if any changes are made to the output files header, these scripts must be updated to reflect the new file size. Figure B.4 summarize the standard run script process flow for the unbvmfG product.

### **B.1.5 Upload Process**

The upload process communicates with the UNB-VMF1 web server, which is how the community will interact with the service. The upload script transfers the completed product files from the ACE-NET locations to the UNB-VMF1 web-server through the use of RSYNC. The RSYNC program is embedded within the upload scripts, which are written as Unix shell scripts for the BASH shell environment. Each of the ACE-NET will upload the data to the web server, but the communication times are staggered by 30 minutes. For example, the unbvmfP product is synced at 12 AST, so Fundy will sync first, then Mahone will sync thirty minutes later followed by Placentia 30 minutes later. The complete sync will be completed within the hour.

### UNB-VMF1 NCEP RE-ANALYSIS I ACE-NET RUN FLOW

scripts:  
*runStandaloneUNBVMF1\_00.sh*  
*runStandaloneUNBVMF1\_06.sh*  
*runStandaloneUNBVMF1\_12.sh*  
*runStandaloneUNBVMF1\_18.sh*

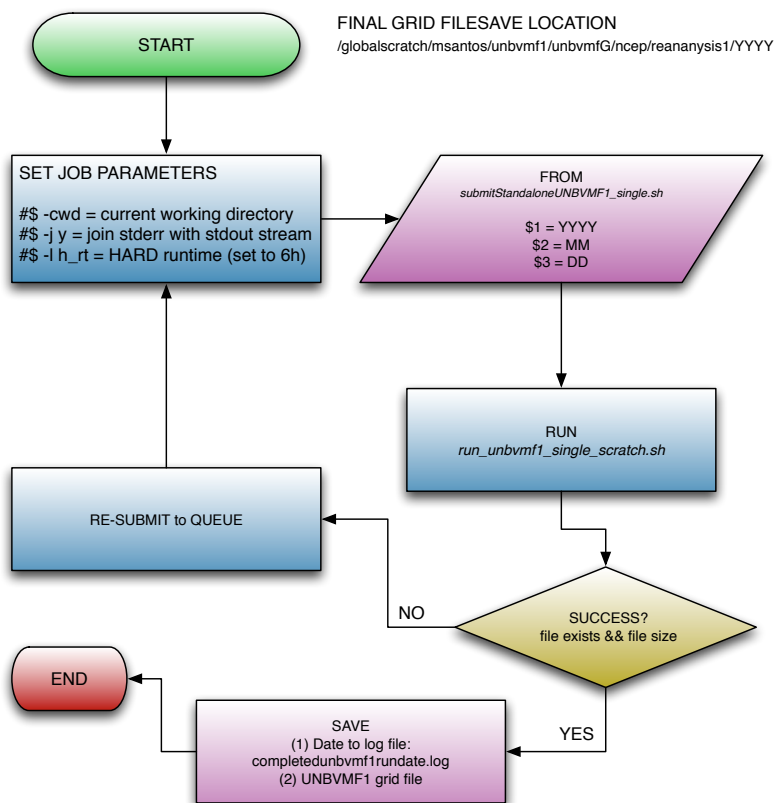


Figure B.4: UNB-VMF1 run script for unbvmfG.

Prior to completing the sync, the files are once checked checked for completeness. Two checks are completed here: (a) file size, and (b) null characters. A check for null characters is important because the file can still be incomplete with the correct file size. There have been incidents where the files size is correct, but the file itself is only half complete. Occasionally, communication issues between the head node and the compute node on the ACE-NET system could results in a file filled with null characters, so this check is made to ensure these files are not uploaded to the web-server. If any null characters are detected,

the affected files will be listed in the daily report (see §B.1.6) and the administrator must delete the files manually so they can be reproduced. Lastly, if any file is detected to be incomplete the filename is written to an excluded file log and RSYNC will ignore these files.

### **B.1.6 Miscellaneous Scripts**

The UNB-VMF1 service contains several maintenance scripts. All of these scripts are written as Unix shell scripts for the BASH shell environment. A summary of all the maintenance scripts can be found in Table B.3. Most notably are the scripts that create the daily logs and reports for the system administrator. First, at the end of day a daily summary of all jobs run on each cluster along with any abnormal files identified during web server sync process are compiled into a single file. This log file is then emailed to the system administrator at 0100 AST the next day. The system administrator can then review if any difficulties/abnormalities occurred throughout the course of the day. This is a valuable resource for the administrator, which removes the need for manually logging into each cluster and checking to ensure each job has completed as intended. The email script is setup to primarily run from Fundy, but if Fundy is down then Mahone will take over duties, and then Placentia if Mahone is not available.

# Appendix C

## UNB-VMF1 Grid Comparison

### Supplemental

#### C.1 Additional Grid Comparison Plots

This appendix provides additional global gridded comparison plots now shown in the main text. This appendix is broken into three sections:

§*C.1.1* Provides the yearly global mean, standard deviation, and absolute value of mapping function difference plotted on the global grid expressed as equivalent height errors from the years 2001 to 2011 for the hydrostatic component and the non-hydrostatic component.

§*C.1.2* Provides the hydrostatic and non-hydrostatic zenith delay differences plotted on the global grid for the standard CMC based product, unbvmfGcmc.

§*C.1.3* Provides the hydrostatic and non-hydrostatic zenith delay differences plotted on the global grid for the forecast based product, unbvmfGP.

#### C.1.1 UNB-VMF1 (NCEP) versus VMF1 (ECMWF)

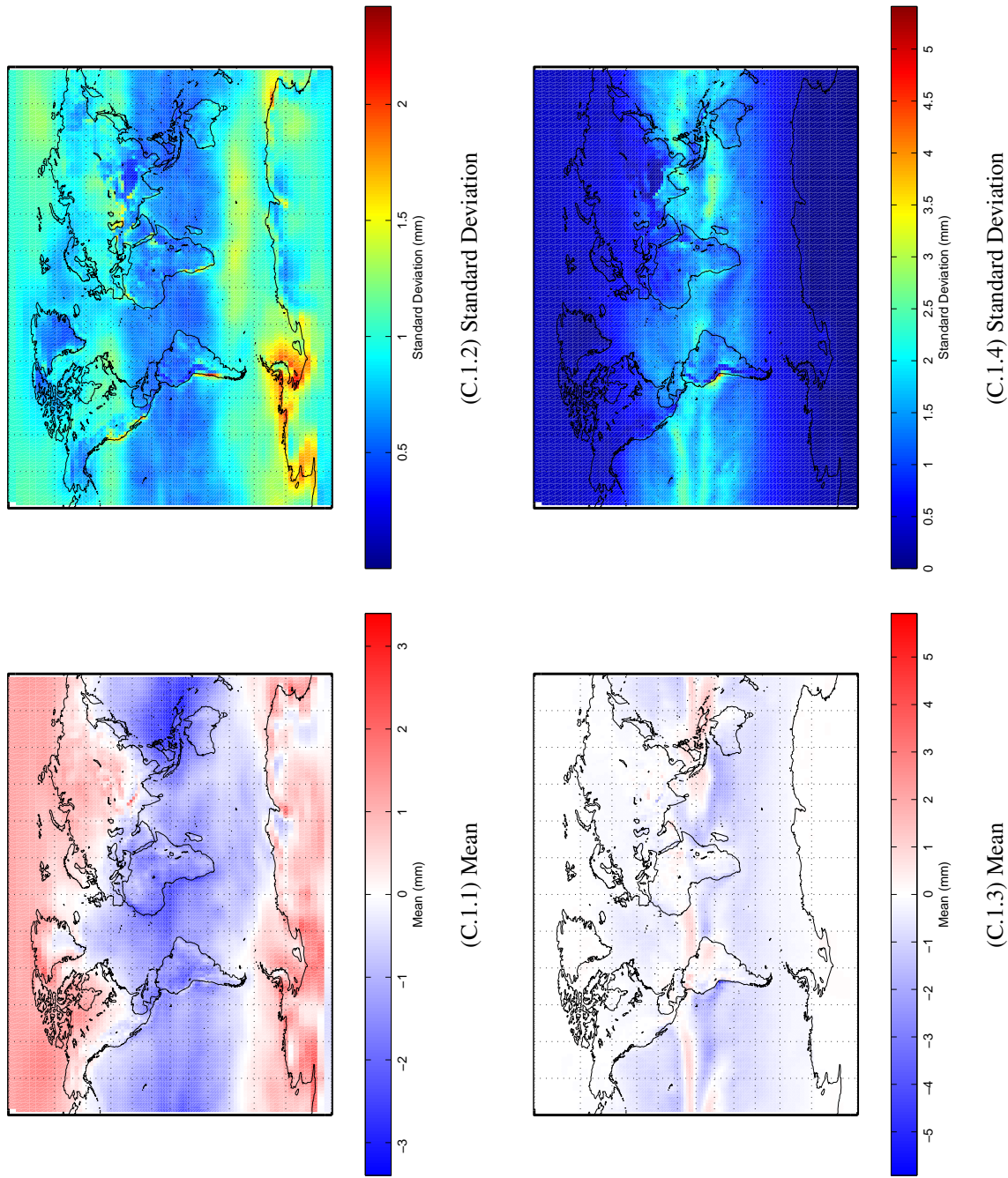


Figure C.1: Difference in hydrostatic (C.1.1 and C.1.2) and non-hydrostatic (C.1.3 and C.1.4) mapping functions expressed as equivalent height errors for UNB-VMF1 (NCEP) minus VMF1 (ECMWF). EPOCH: 2001.

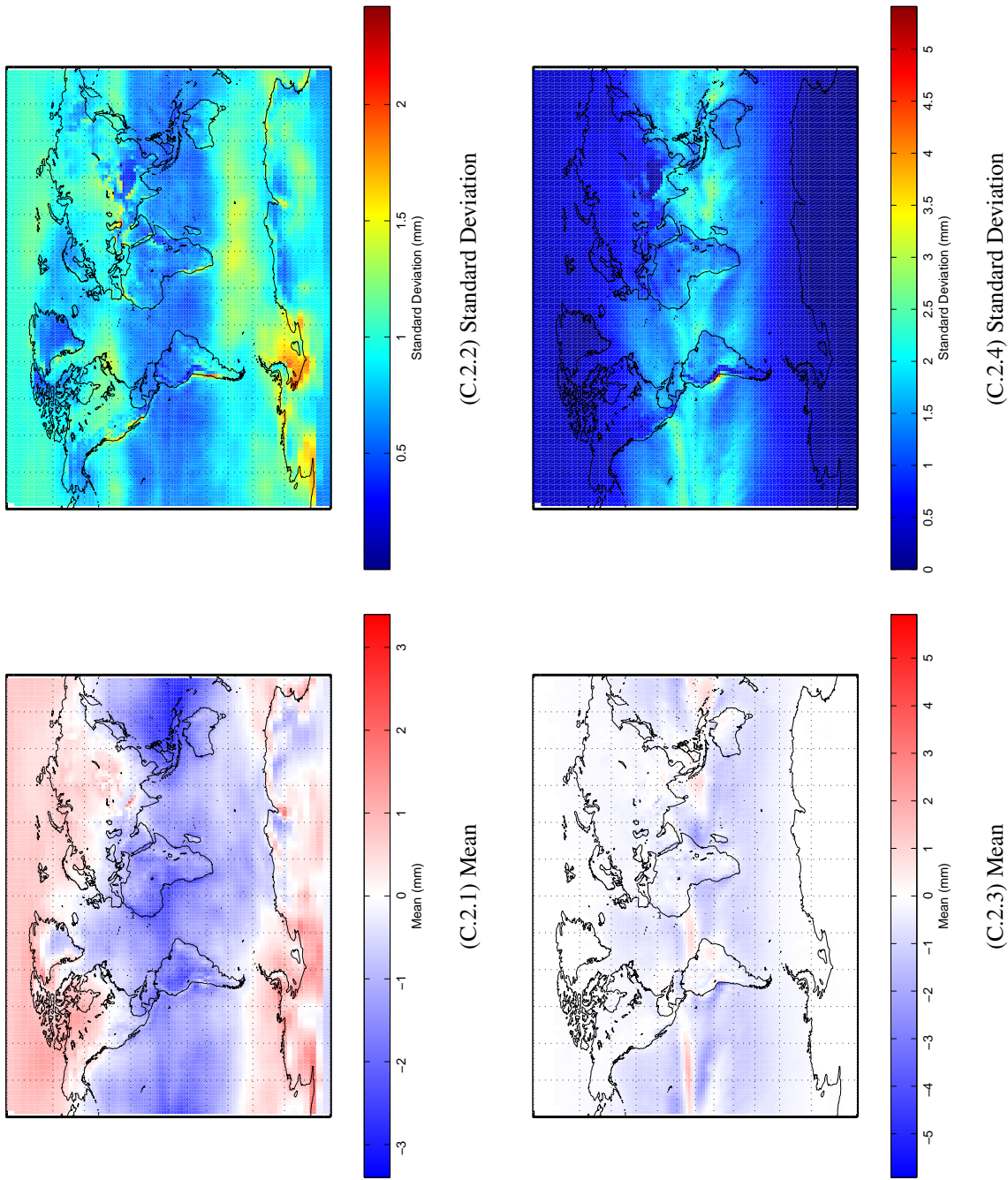


Figure C.2: Difference in hydrostatic (C.2.1 and C.2.2) and non-hydrostatic (C.2.3 and C.2.4) mapping functions expressed as equivalent height errors for UNB-VMF1 (NCEP) minus VMF1 (ECMWF). EPOCH: 2002.



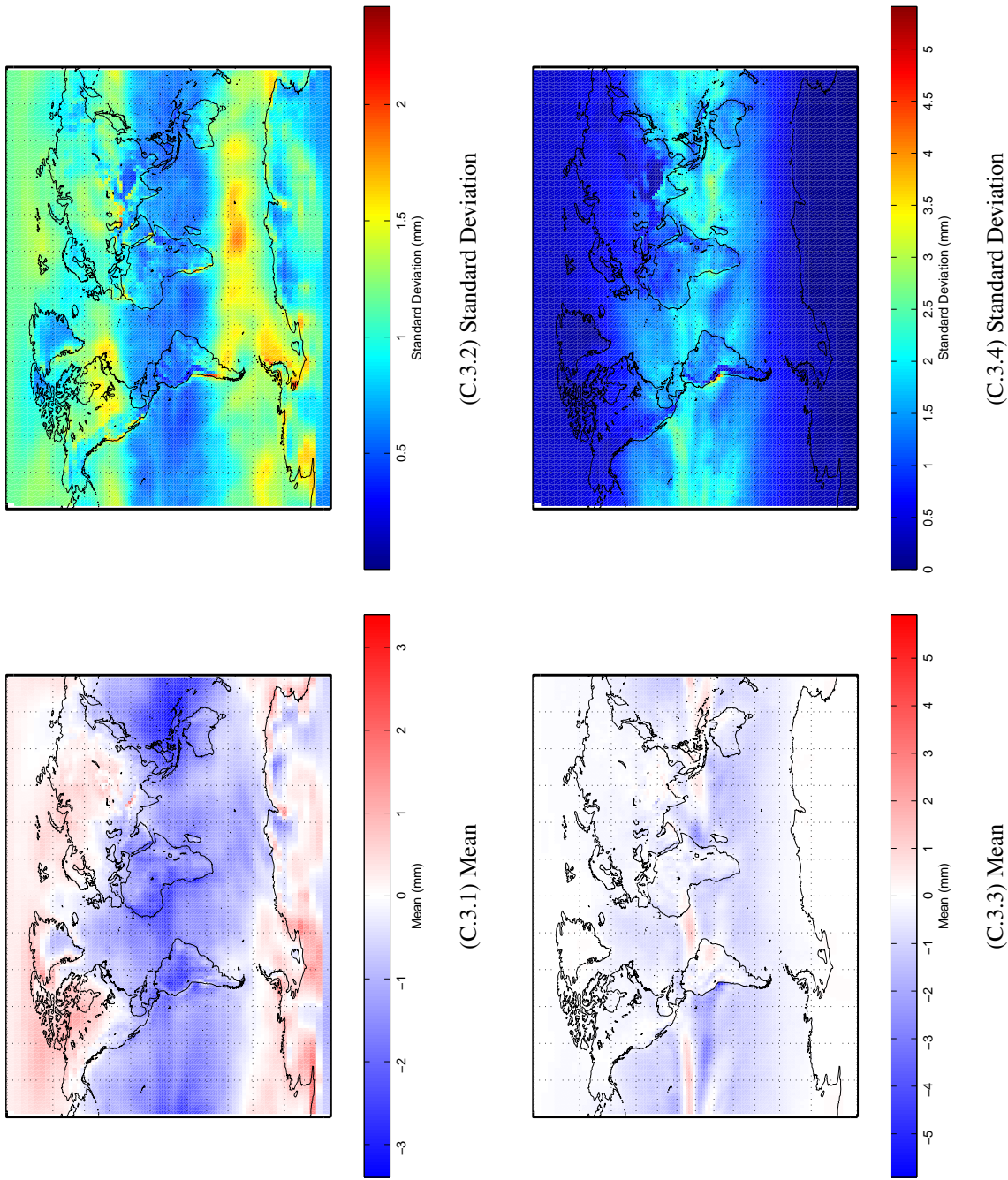


Figure C.3: Difference in hydrostatic (C.3.1 and C.3.2) and non-hydrostatic (C.3.3 and C.3.4) mapping functions expressed as equivalent height errors for UNB-VMF1 (NCEP) minus VMF1 (ECMWF). EPOCH: 2003.

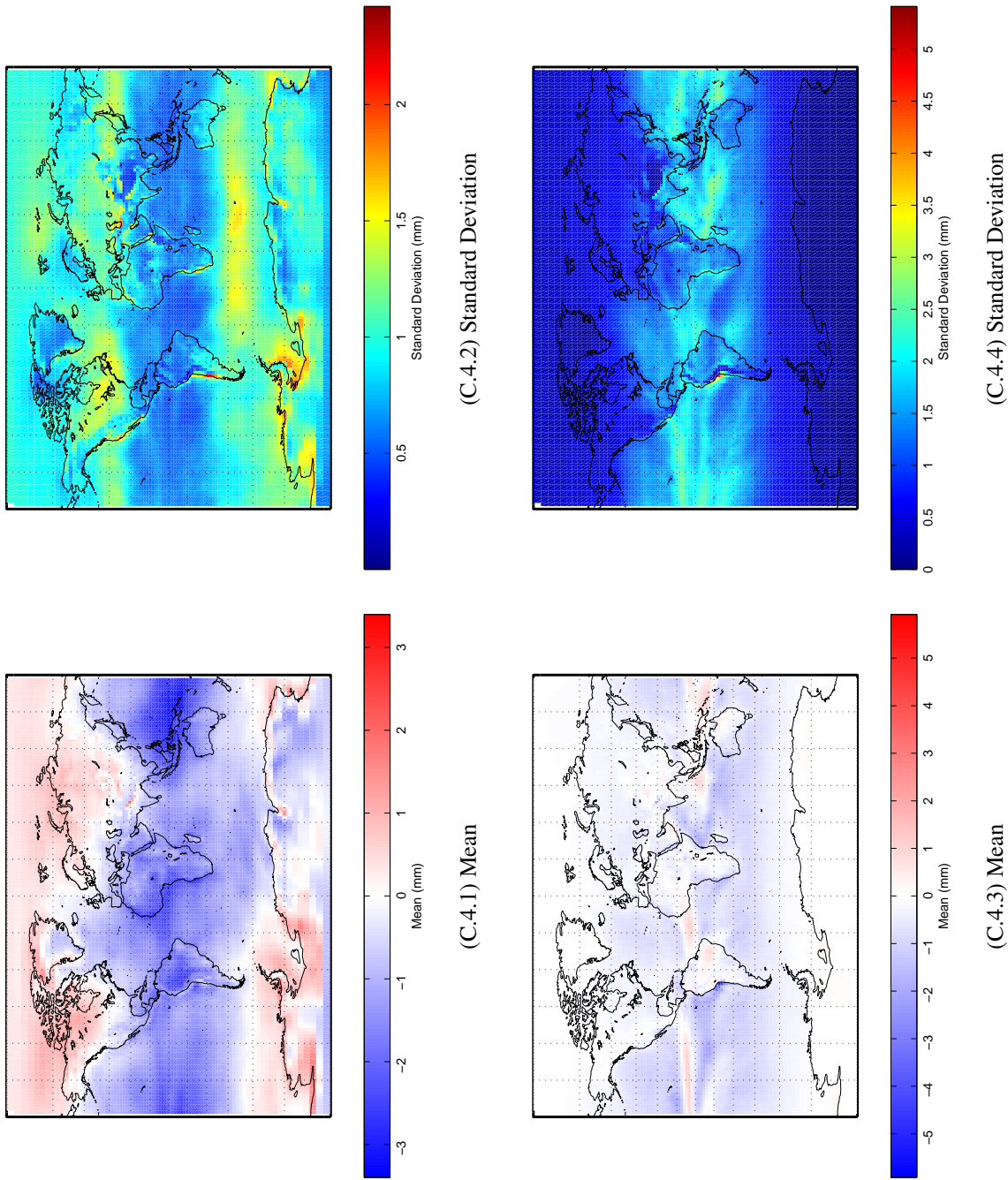


Figure C.4: Difference in hydrostatic (C.4.1 and C.4.2) and non-hydrostatic (C.4.3 and C.4.4) mapping functions expressed as equivalent height errors for UNB-VMF1 (NCEP) minus VMF1 (ECMWF). EPOCH: 2004.



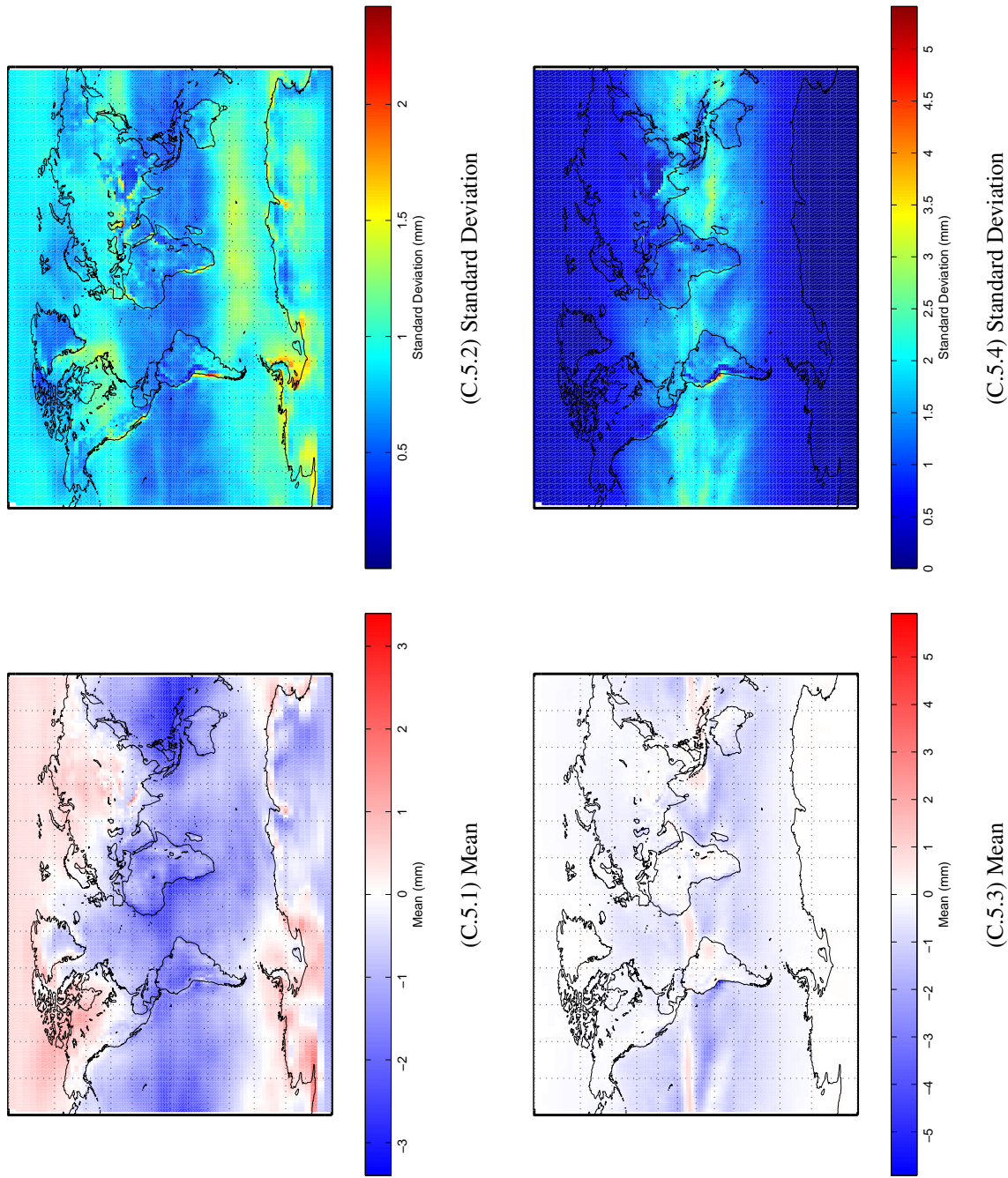


Figure C.5: Difference in hydrostatic (C.5.1 and C.5.2) and non-hydrostatic (C.5.3 and C.5.4) mapping functions expressed as equivalent height errors for UNB-VMF1 (NCEP) minus VMF1 (ECMWF). EPOCH: 2005.

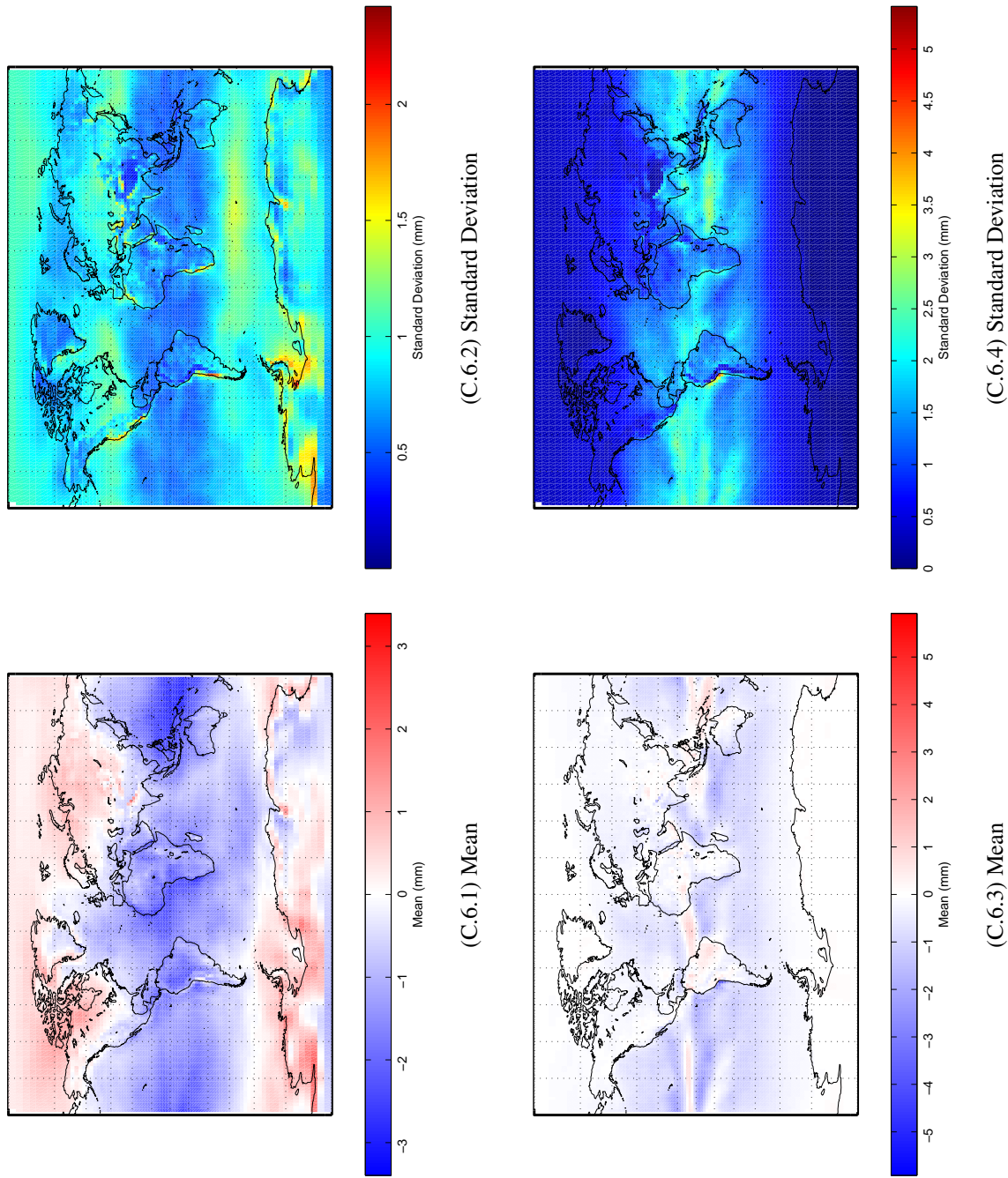


Figure C.6: Difference in hydrostatic (C.6.1 and C.6.2) and non-hydrostatic (C.6.3 and C.6.4) mapping functions expressed as equivalent height errors for UNB-VMF1 (NCEP) minus VMF1 (ECMWF). EPOCH: 2006.



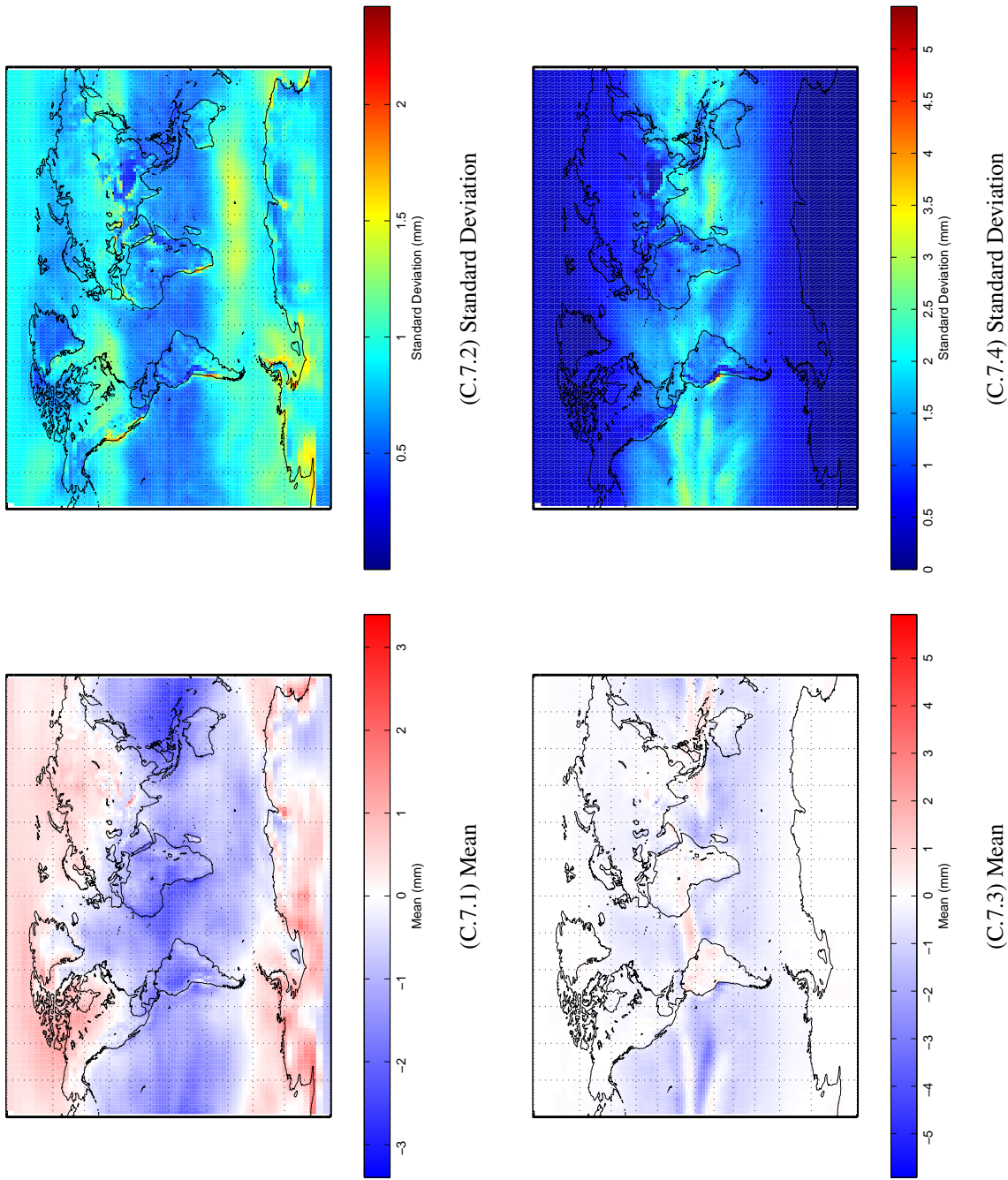


Figure C.7: Difference in hydrostatic (C.7.1 and C.7.2) and non-hydrostatic (C.7.3 and C.7.4) mapping functions expressed as equivalent height errors for UNB-VMF1 (NCEP) minus VMF1 (ECMWF), EPOCH: 2007.

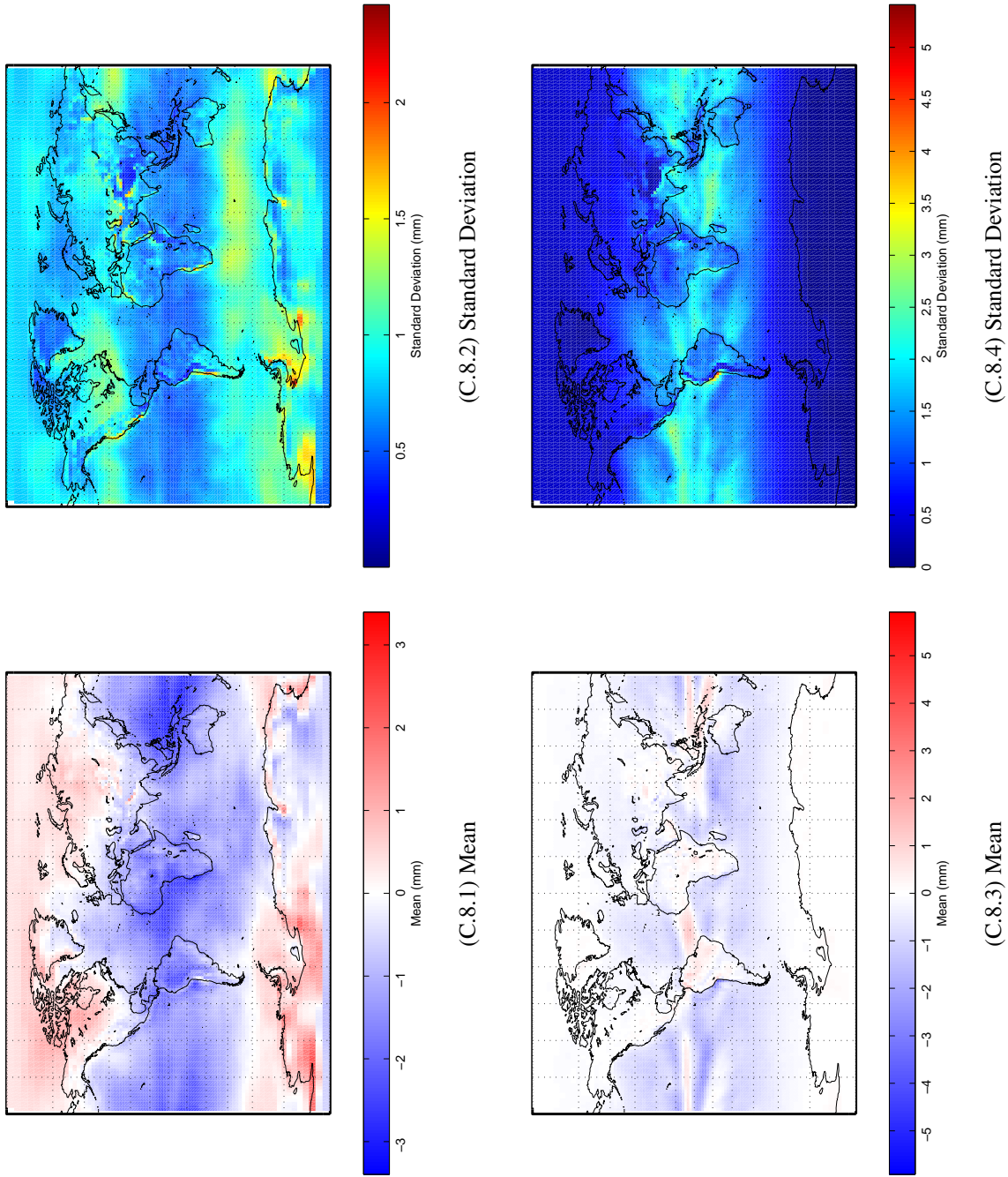


Figure C.8: Difference in hydrostatic (C.8.1 and C.8.2) and non-hydrostatic (C.8.3 and C.8.4) mapping functions expressed as equivalent height errors for UNB-VMF1 (NCEP) minus VMF1 (ECMWF). EPOCH: 2008.

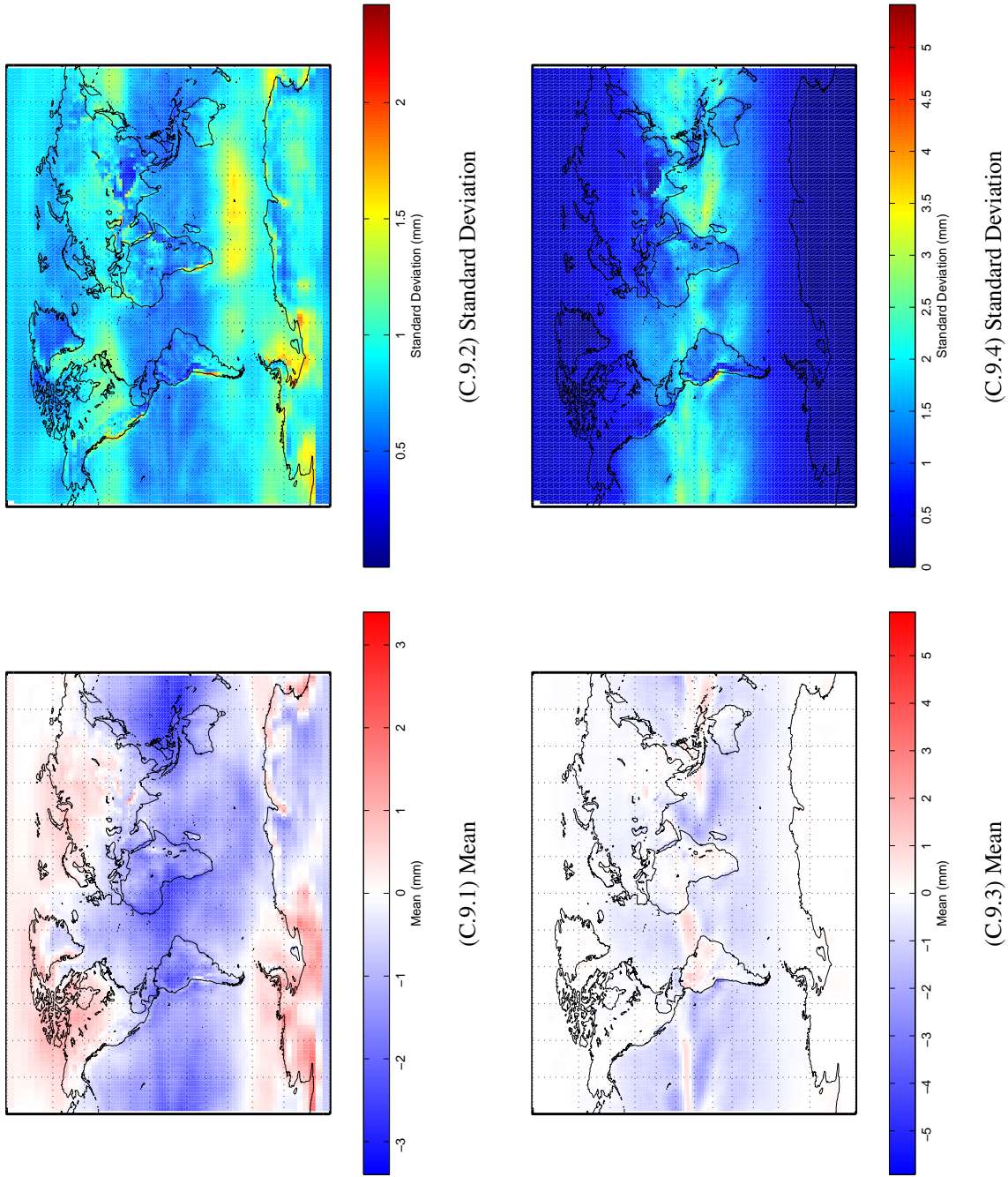


Figure C.9: Difference in hydrostatic (C.9.1 and C.9.2) and non-hydrostatic (C.9.3 and C.9.4) mapping functions expressed as equivalent height errors for UNB-VMF1 (NCEP) minus VMF1 (ECMWF). EPOCH: 2009.



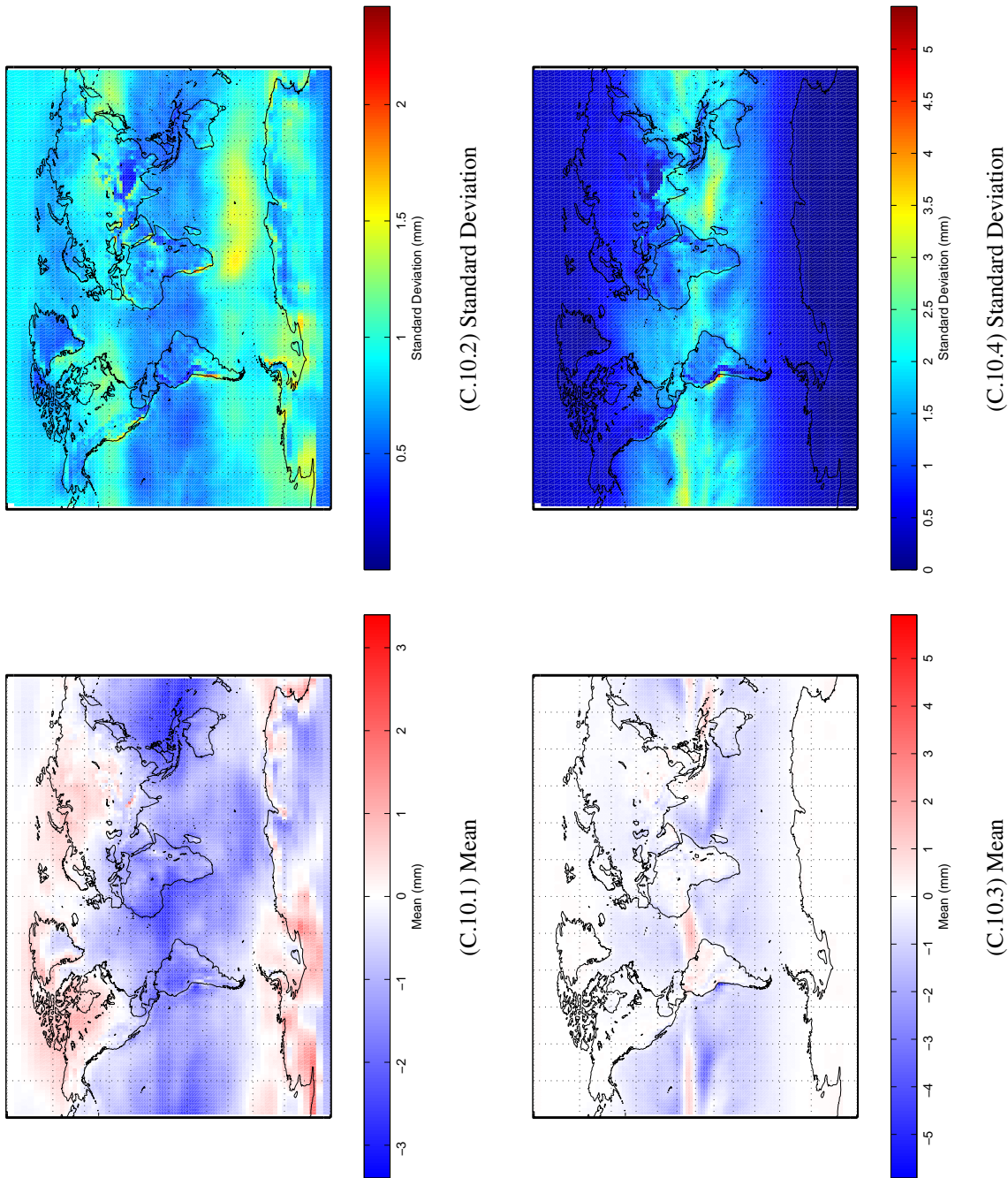


Figure C.10: Difference in hydrostatic (C.10.1 and C.10.2) and non-hydrostatic (C.10.3 and C.10.4) mapping functions expressed as equivalent height errors for UNB-VMF1 (NCEP) minus VMF1 (ECMWF). EPOCH: 2010.

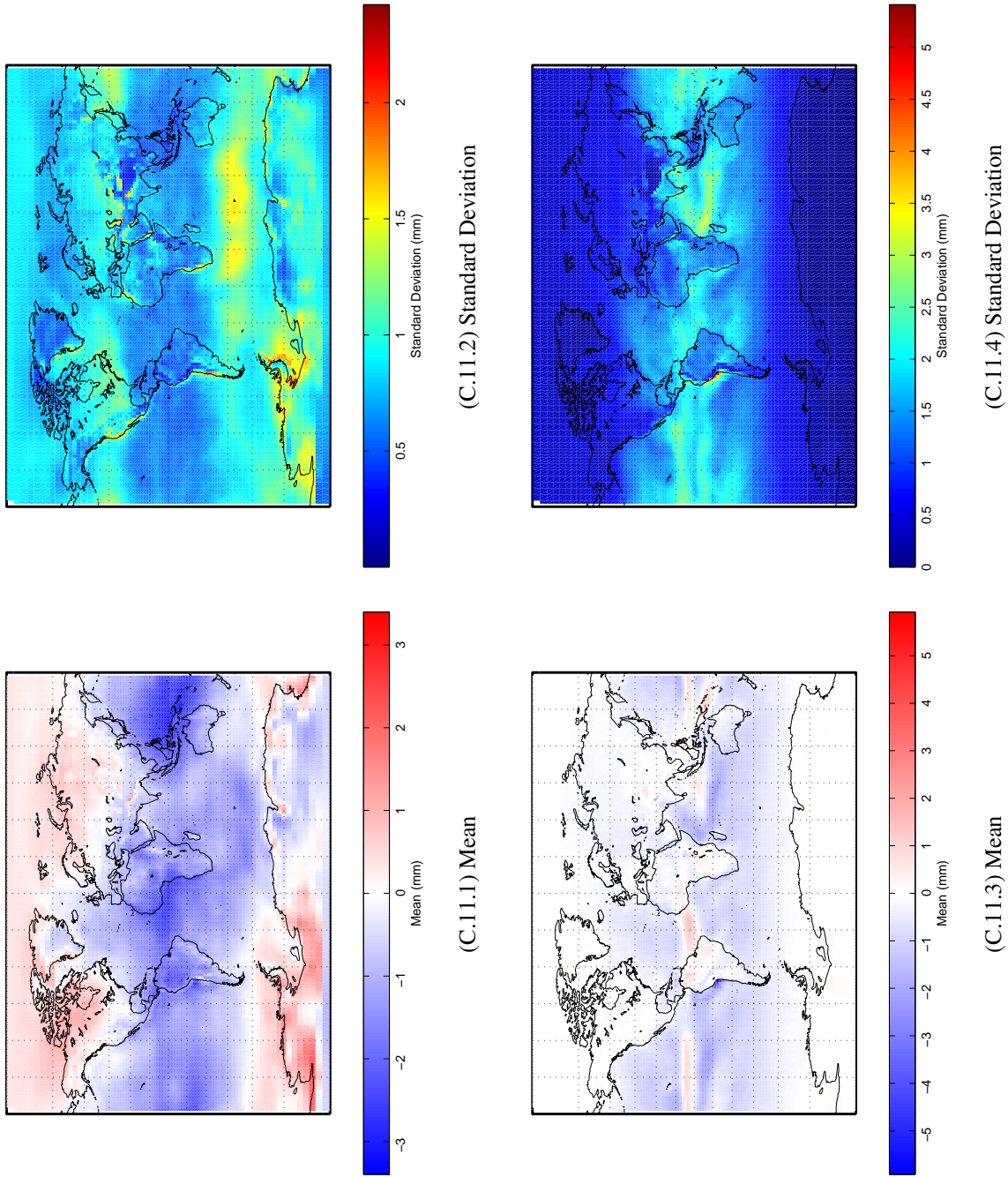


Figure C.11: Difference in hydrostatic (C.11.1 and C.11.2) and non-hydrostatic (C.11.3 and C.11.4) mapping functions expressed as equivalent height errors for UNB-VMF1 (NCEP) minus VMF1 (ECMWF). EPOCH: 2011.

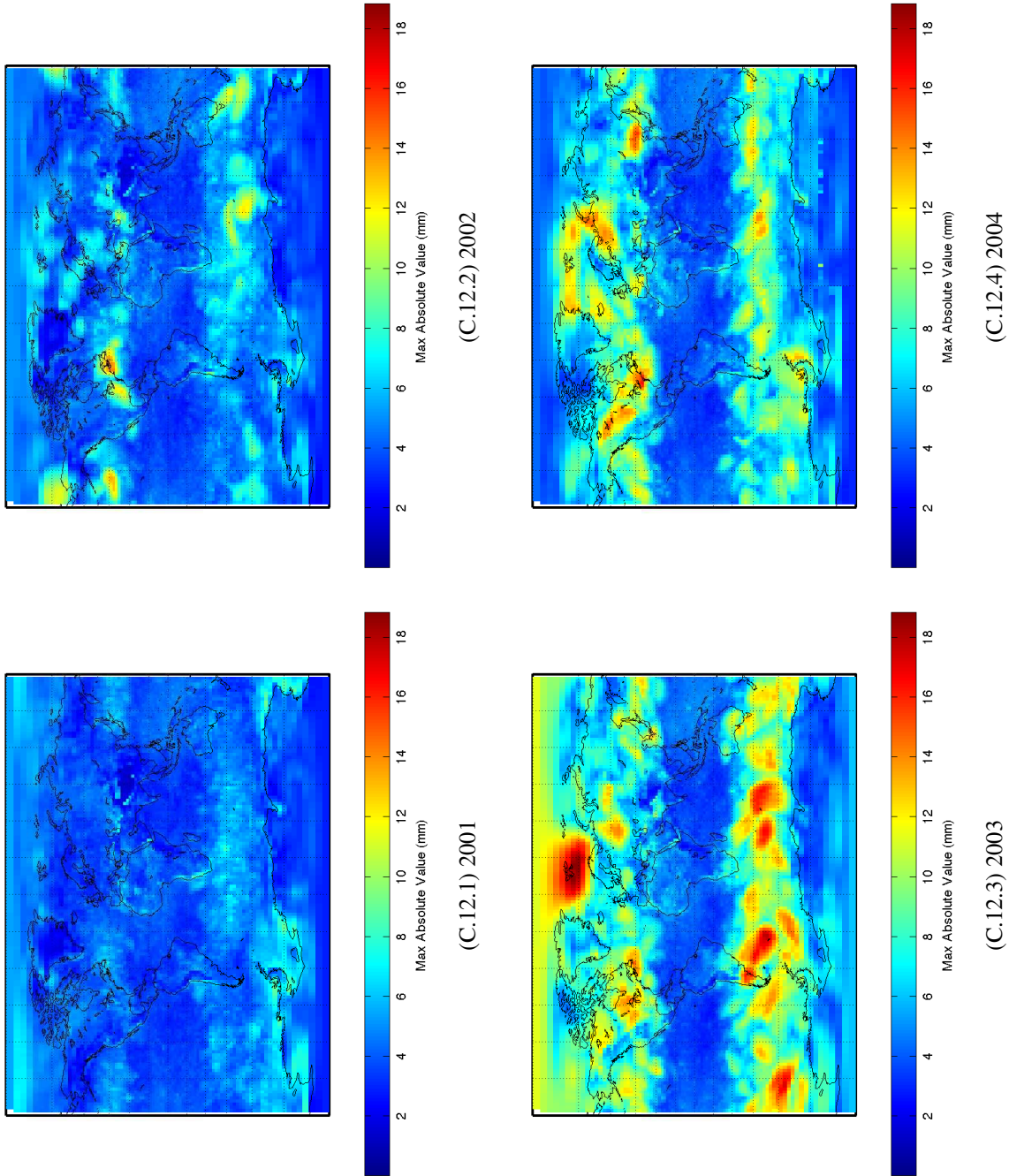


Figure C.12: Absolute value of the difference in hydrostatic mapping functions expressed as equivalent height errors for UNB-VMF1 (NCEP) minus VMF1 (ECMWF), 2001-2011



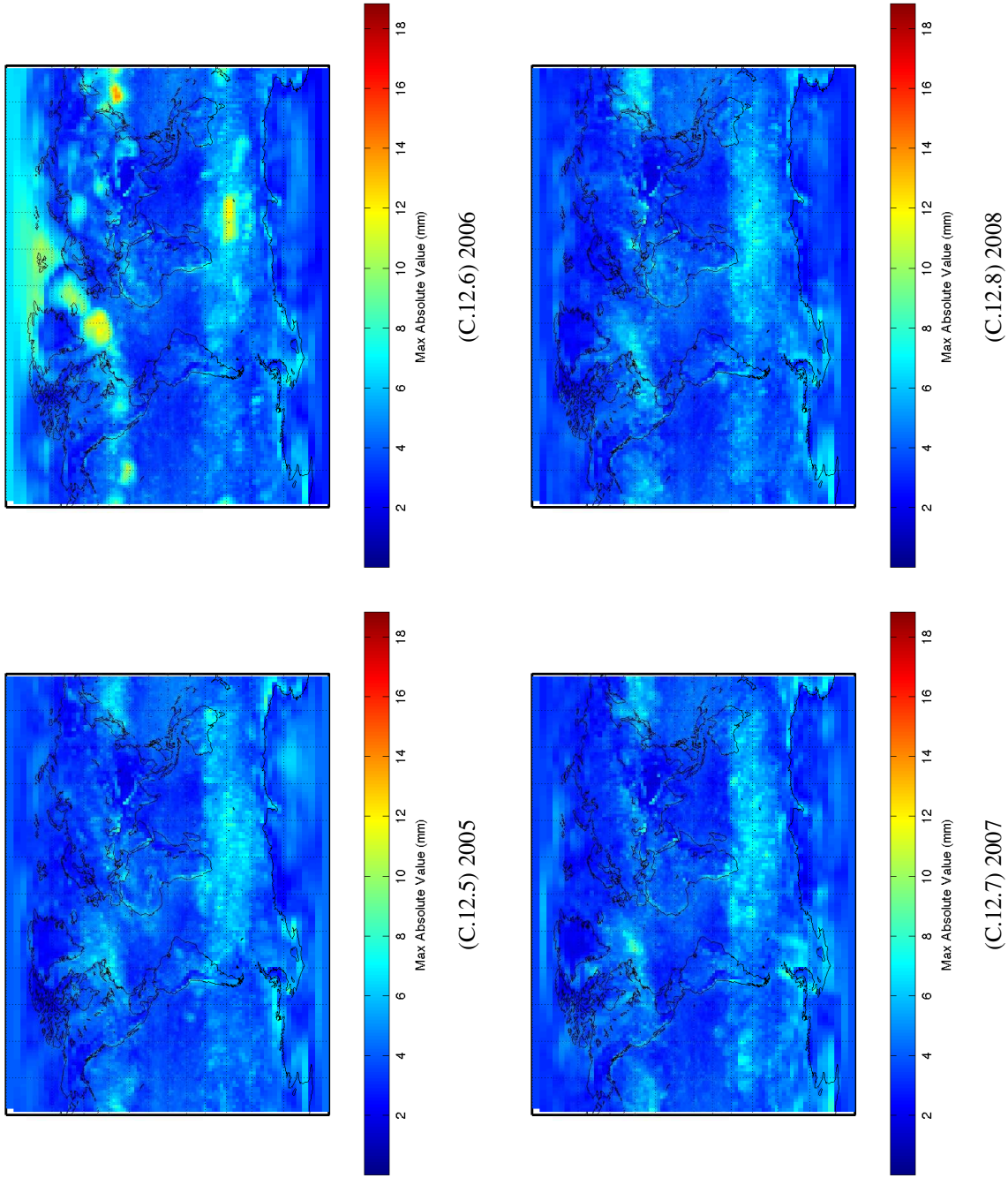
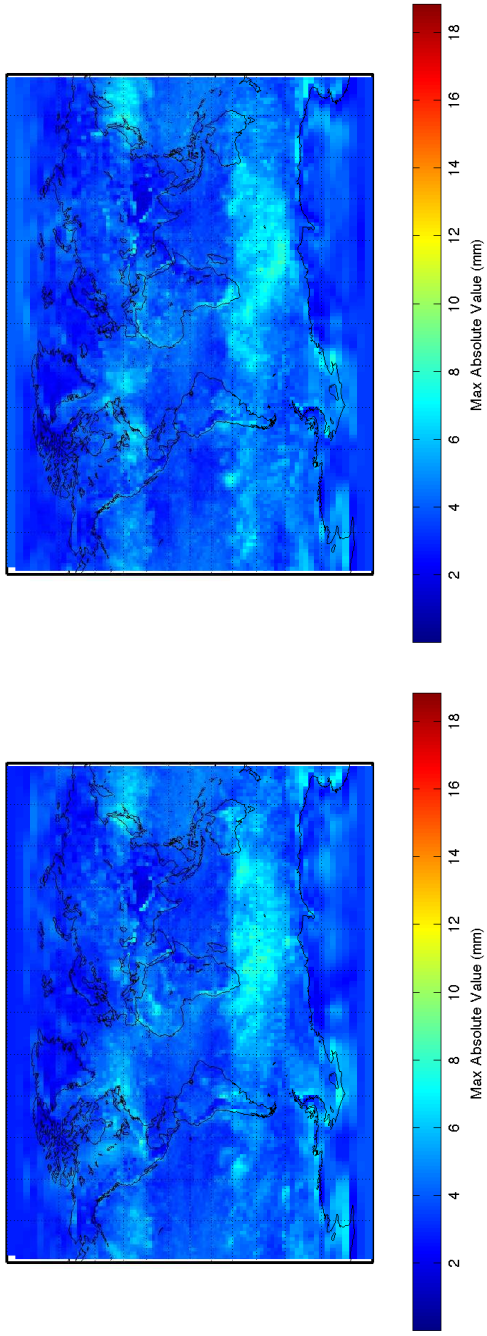
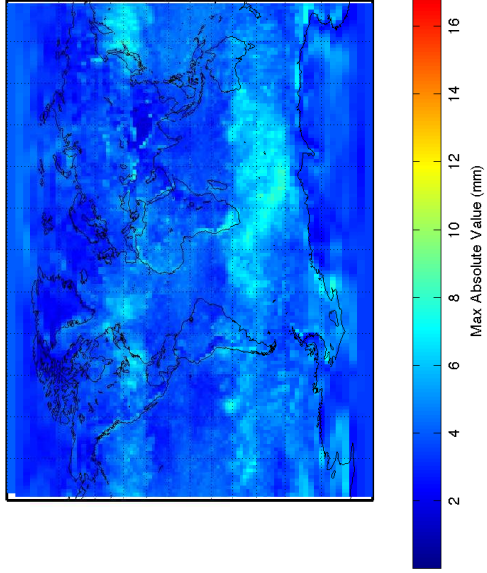


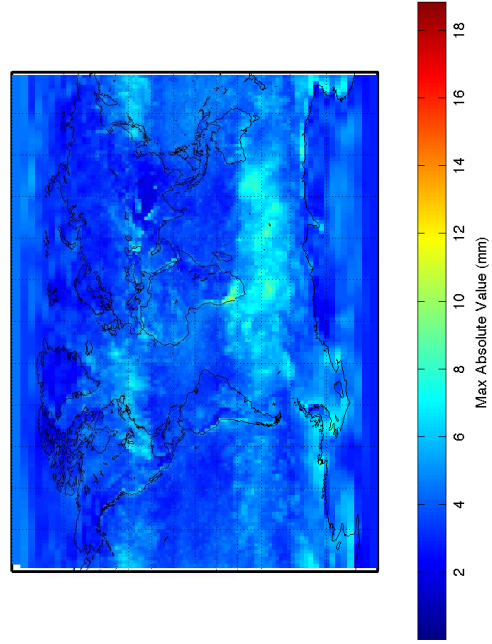
Figure C.12: Absolute value of the difference in hydrostatic mapping functions expressed as equivalent height errors for UNB-VMF1 (NCEP) minus VMF1 (ECMWF), 2001-2011



(C.12.9) 2009



(C.12.10) 2010



(C.12.11) 2011

Figure C.12: Absolute value of the difference in hydrostatic mapping functions expressed as equivalent height errors for UNB-VMF1 (NCEP) minus VMF1 (ECMWF), 2001-2011

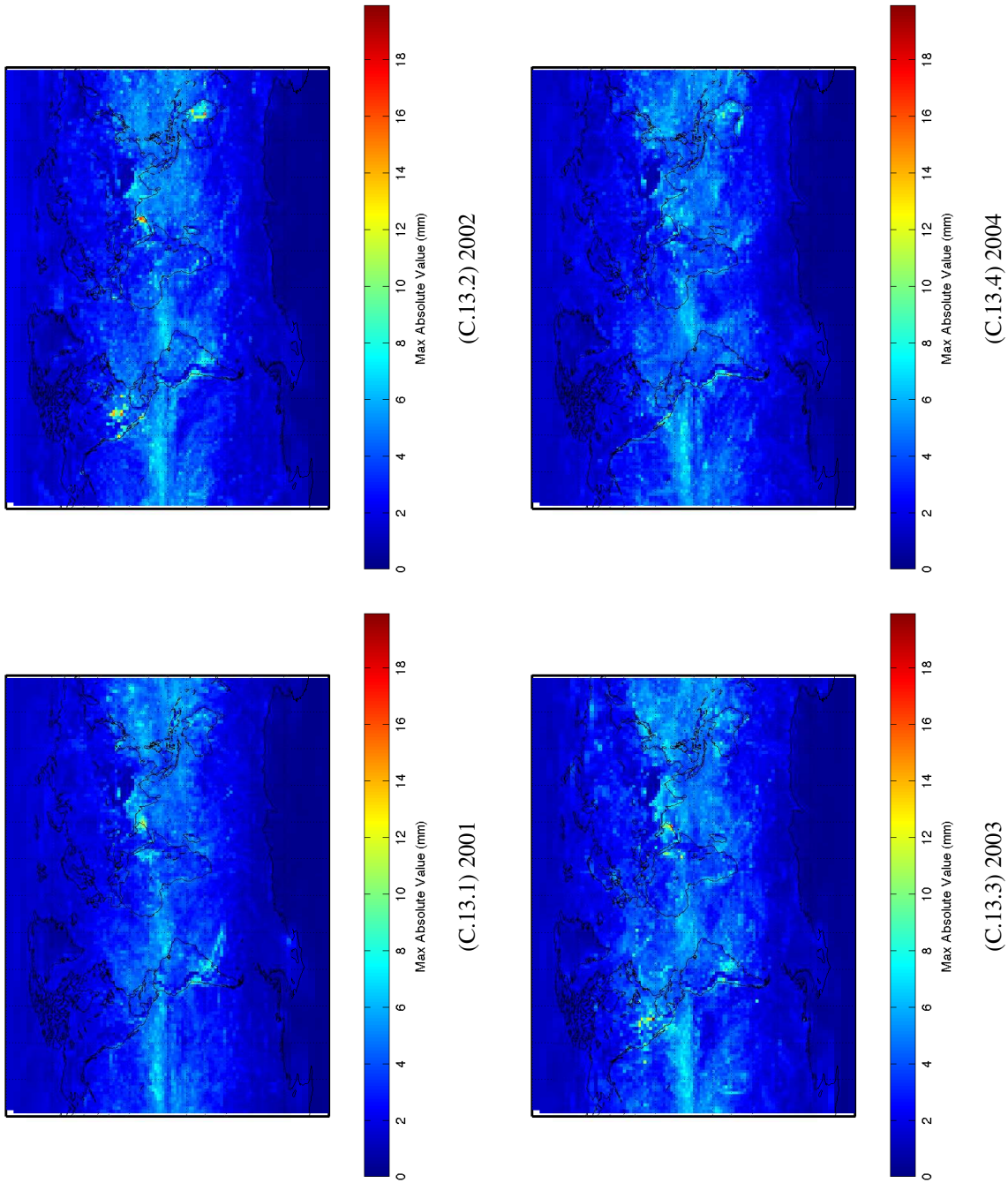


Figure C.13: Absolute value of the difference in non-hydrostatic mapping functions expressed as equivalent height errors for UNB-VMF1 (NCEP) minus VMF1 (ECMWF), 2001 - 2011



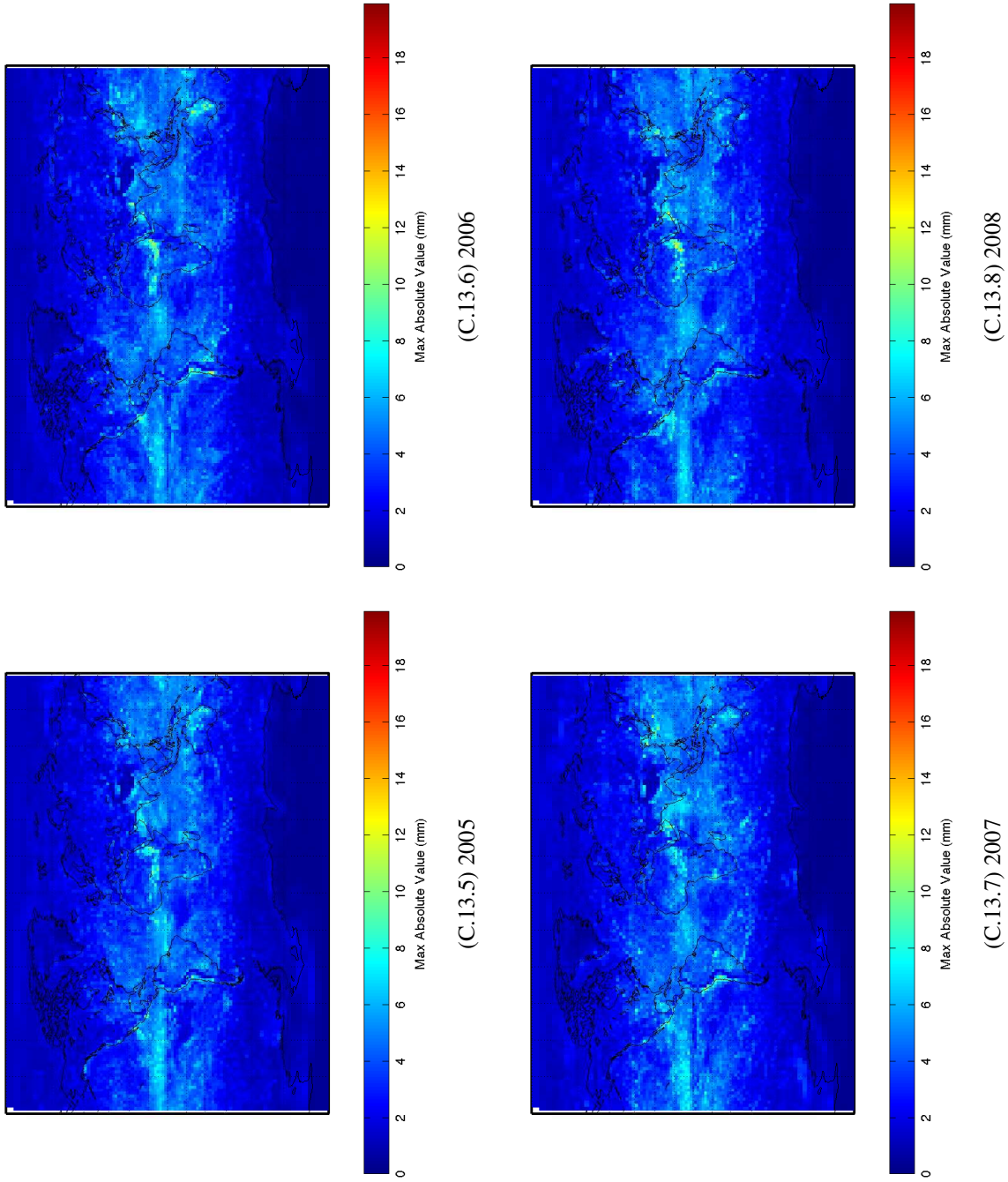
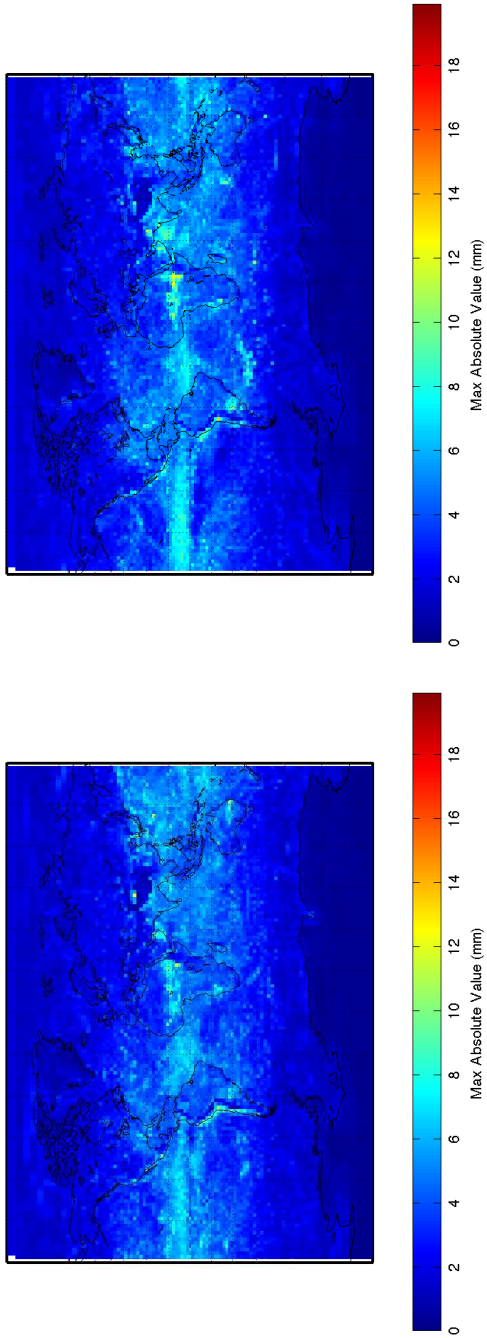
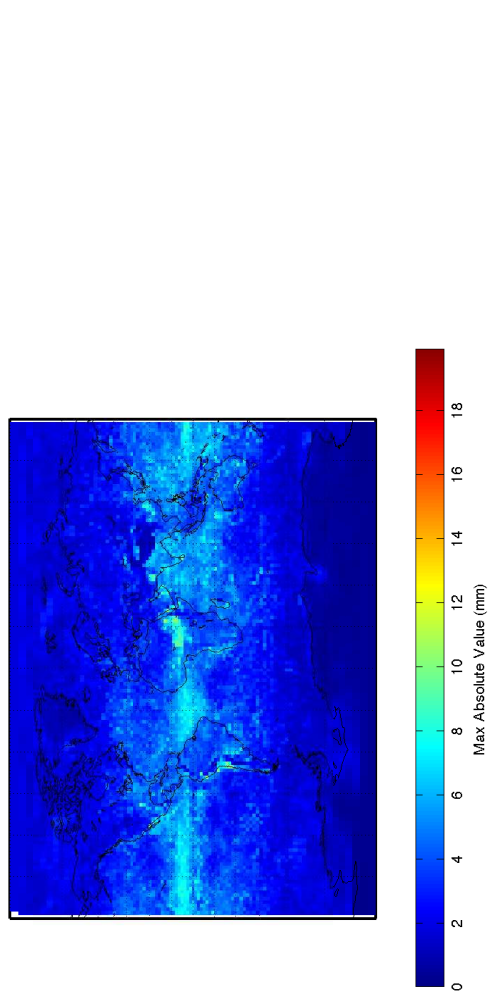


Figure C.13: Absolute value of the difference in non-hydrostatic mapping functions expressed as equivalent height errors for UNB-VMF1 (NCEP) minus VMF1 (ECMWF), 2001 - 2011



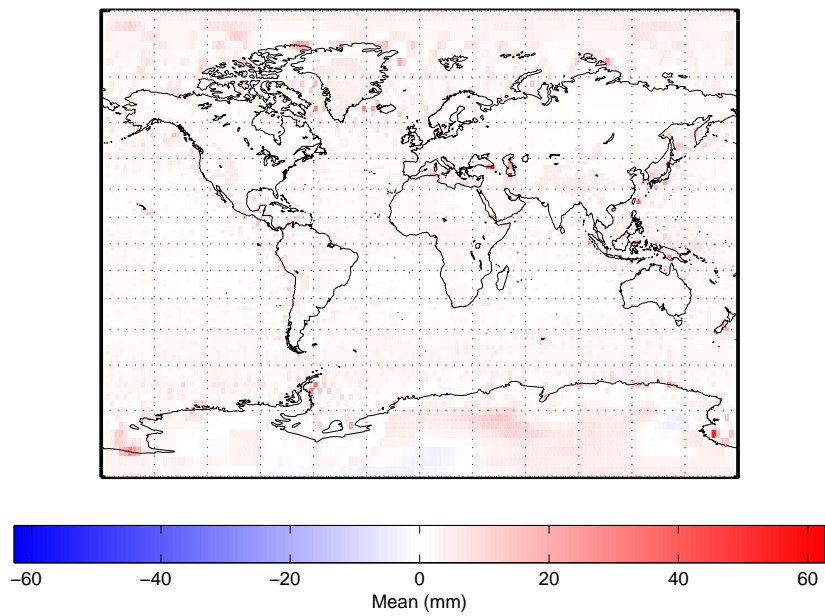
(C.13.10) 2010



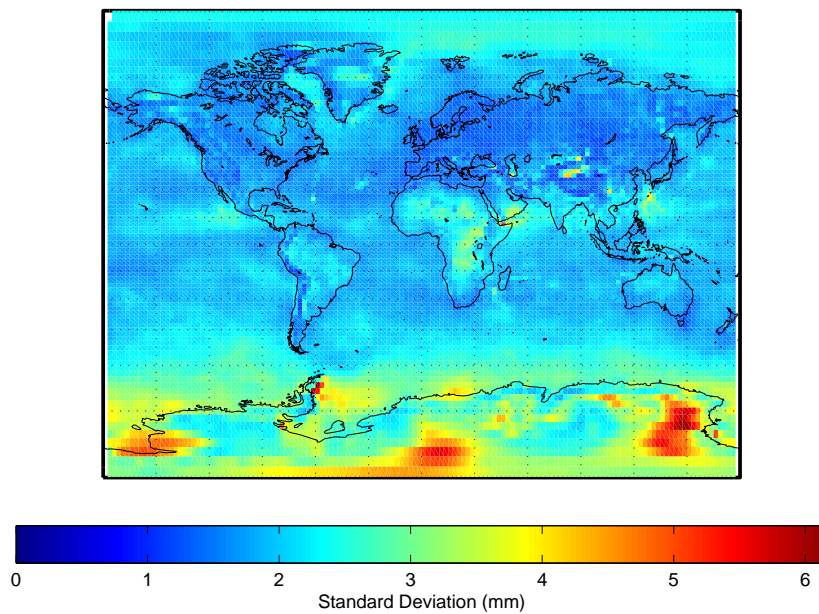
(C.13.11) 2011

Figure C.13: Absolute value of the difference in non-hydrostatic mapping functions expressed as equivalent height errors for UNB-VMF1 (NCEP) minus VMF1 (ECMWF), 2001 - 2011

### C.1.2 UNB-VMF1 (CMC) versus VMF1 (ECMWF)

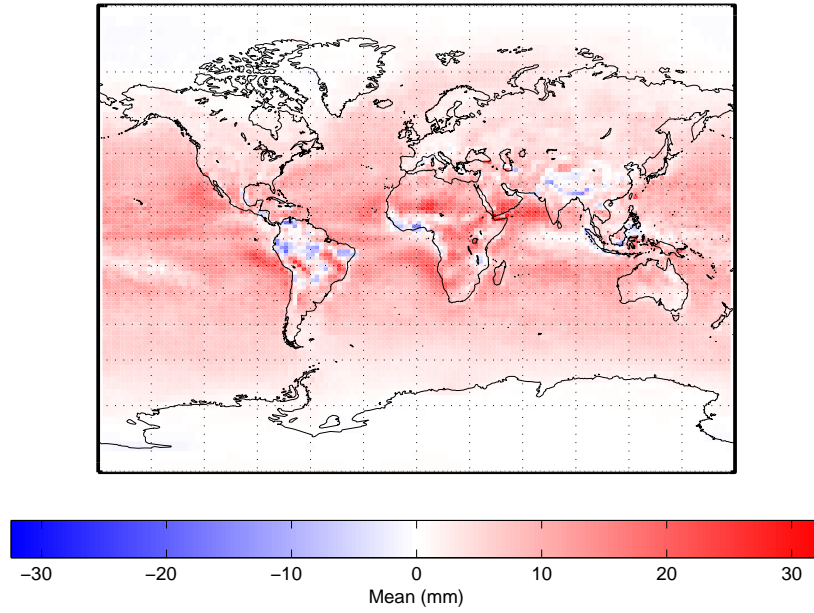


(C.14.1) Mean

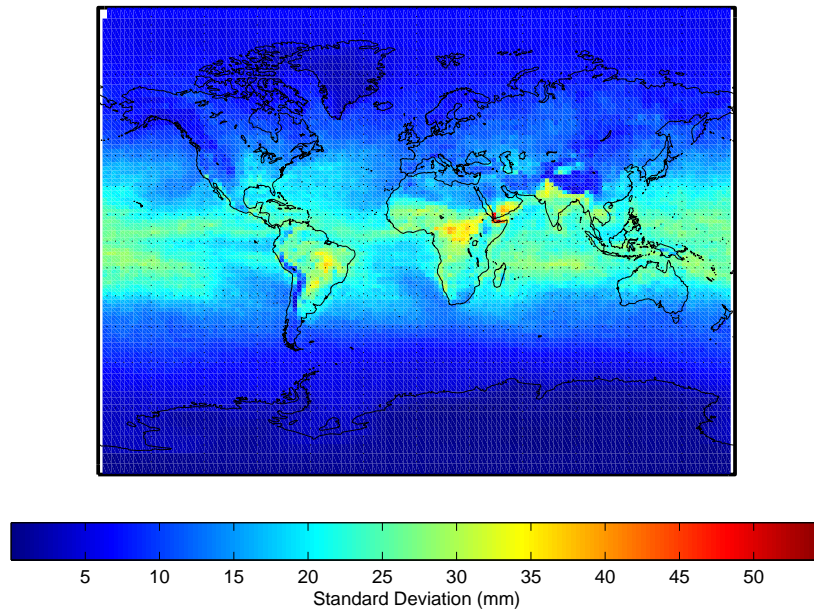


(C.14.2) Standard Deviation

Figure C.14: Difference in the hydrostatic zenith delay for the year 2012 for UNB-VMF1 (CMC) minus VMF1 (ECMWF). (a) Mean (b) Standard deviation. January 1st to September 30th 2012.



(C.15.1) Mean

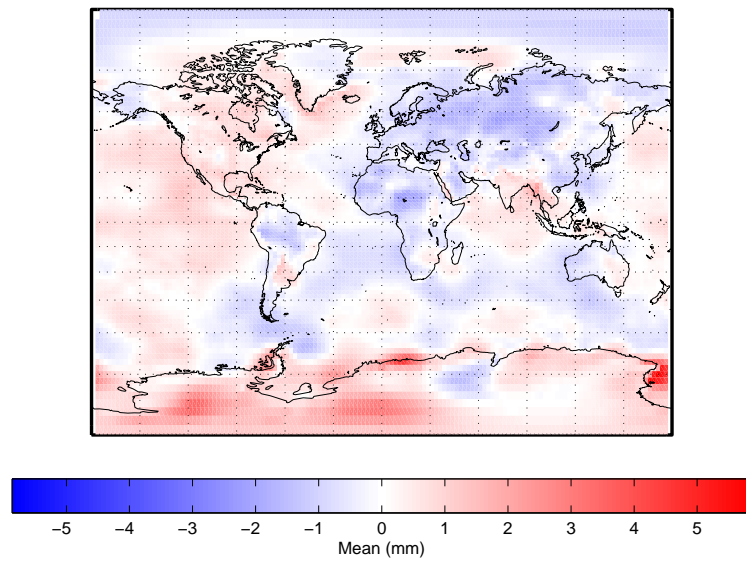


(C.15.2) Standard Deviation

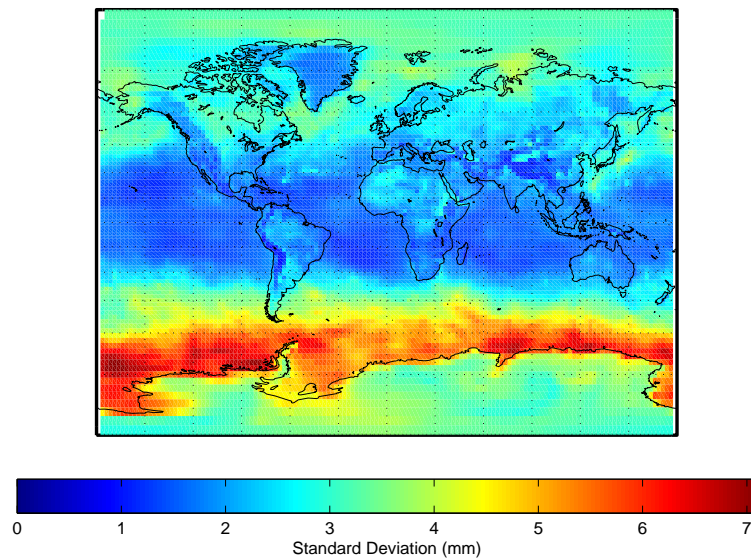
Figure C.15: Difference in the hydrostatic zenith delay for the year 2012 for UNB-VMF1 (CMC) minus VMF1 (ECMWF). (a) Mean (b) Standard deviation. January 1st to September 30th 2012.



### C.1.3 Forecast UNB-VMF1 (CMC-P) versus UNB-VMF1 (CMC)



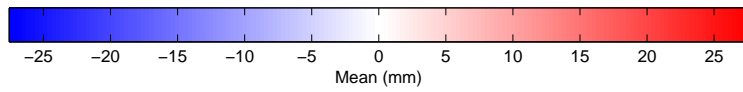
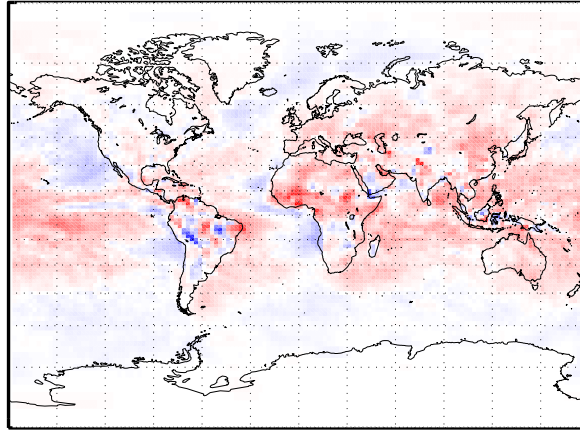
(C.16.1) Mean



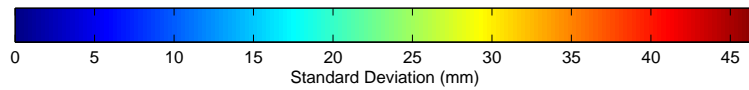
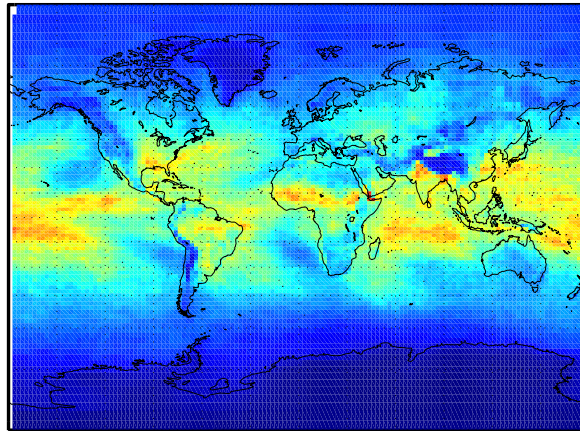
(C.16.2) Standard Deviation

Figure C.16: Difference in the hydrostatic zenith delay for the year 2012 for UNB-VMF1 (CMC-P) minus UNB-VMF1 (CMC). (a) Mean (b) Standard deviation. March 17th to September 30th 2012.





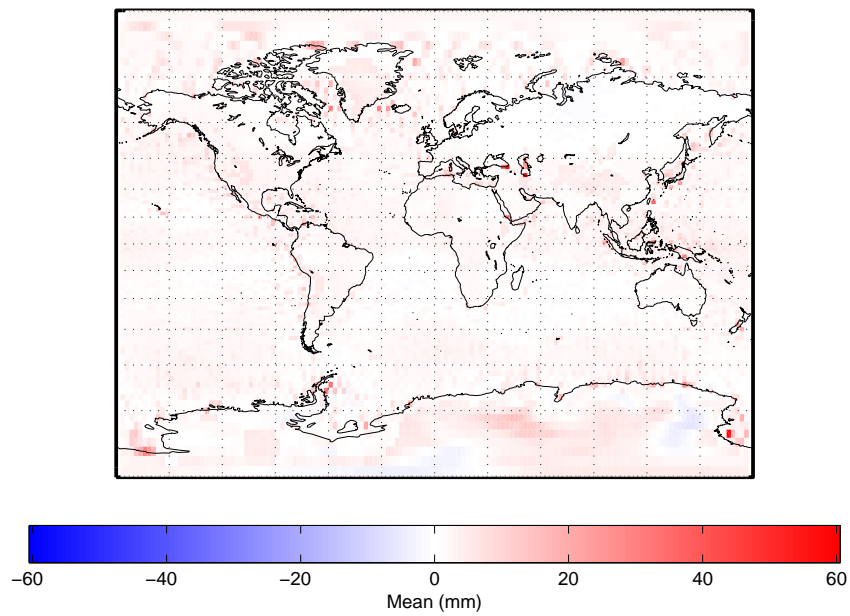
(C.17.1) Mean



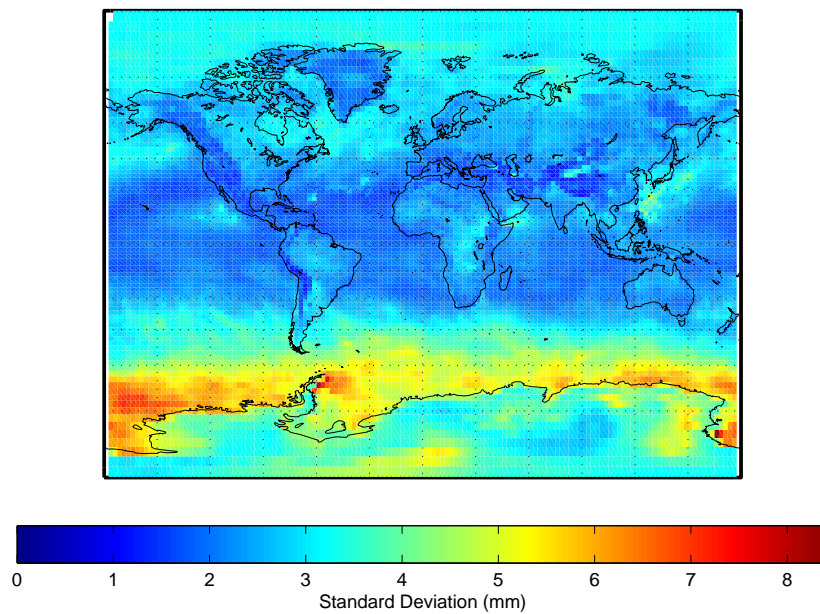
(C.17.2) Standard Deviation

Figure C.17: Difference in the non-hydrostatic zenith delay for the year 2012 for UNB-VMF1 (CMC-P) minus UNB-VMF1 (CMC). (a) Mean (b) Standard deviation. March 17th to September 30th 2012.

### C.1.4 Forecast UNB-VMF1 (CMC-P) versus Forecast VMF1 (ECMWF)

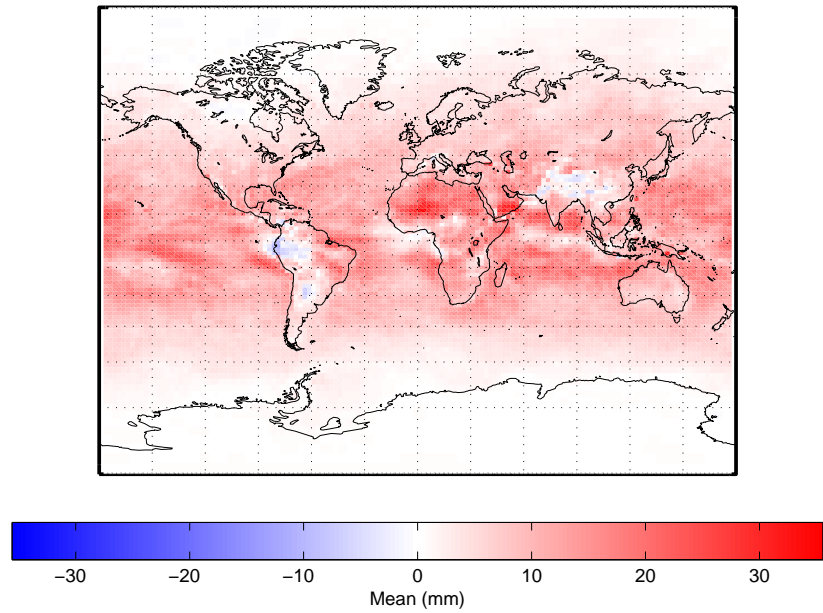


(C.18.1) Mean

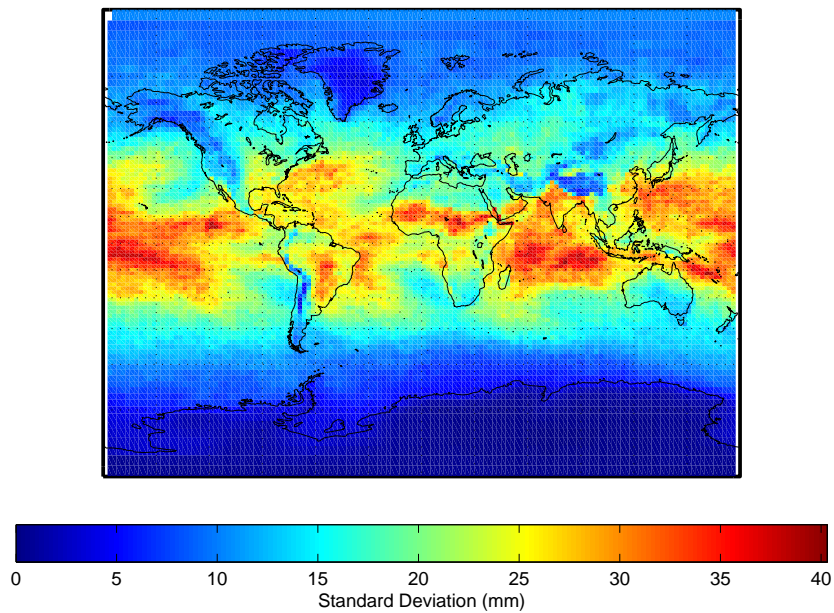


(C.18.2) Standard Deviation

Figure C.18: Difference in the hydrostatic zenith delay for the year 2012 for UNB-VMF1 (CMC-P) minus VMF1 (ECMWF). (a) Mean (b) Standard deviation. March 17th to September 30th 2012.



(C.19.1) Mean



(C.19.2) Standard Deviation

Figure C.19: Difference in the non-hydrostatic zenith delay for the year 2012 for UNB-VMF1 (CMC-P) minus VMF1 (ECMWF). (a) Mean (b) Standard deviation. March 17th to September 30th 2012.

# Appendix D

## UNB-VMF1 Position Domain

### Supplemental

#### D.1 Position Domain Comparisons

The following section provides all coordinate time series plots for all stations studied in the position domain. Section D.1.1 provides the individual stations plots for the 11-year analysis between the NCEP based product, unbvmfG, versus the existing VMF1 (ECMWF) service. Section D.1.2 provides the station plots for all products for the 2012 interval. Additionally, all section provide tabular summaries for each station for the indicated time period.

##### D.1.1 UNB-VMF1 (NCEP) versus VMF1 (ECMWF)

The following section provides a summary of the comparison between UNB-VMF1 (NCEP) and the existing VMF1 service, VMF1 (ECMWF) over an 11-year interval starting in 2001 and ending in 2011. Table D.1 summarizes the yearly mean bias and RMSE for each station from 2011 to 2011. The term listed as N/A indicates that the values have not been computed for these stations due to the lack of observation data from the IGS. Table D.2

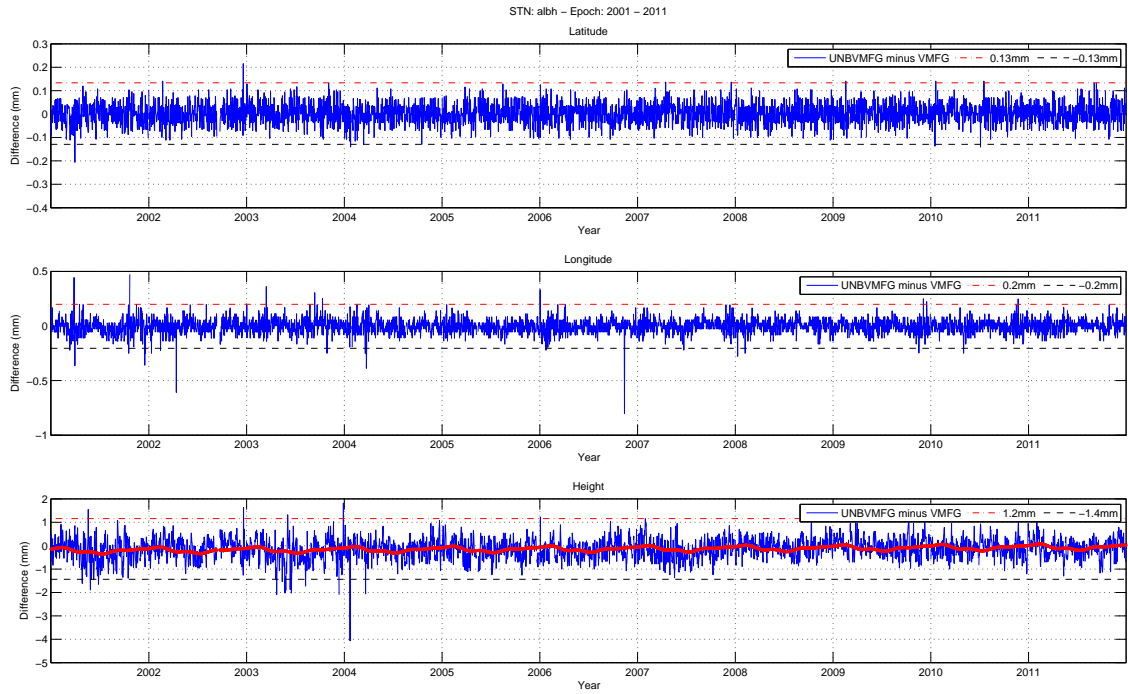
Table D.1: Summary of yearly difference in height between PPP solution with UNB-VMF1 (NCEP) and VMF1 (ECMWF) - (NCEP minus ECMWF). All measurements in millimetres.

Stations	2001		2002		2003		2004		2005		2006		2007		2008		2009		2010		2011	
	Mean	RMSE	Mean	RMSE	Mean	RMSE	Mean	RMSE	Mean	RMSE	Mean	RMSE	Mean	RMSE	Mean	RMSE	Mean	RMSE	Mean	RMSE	Mean	RMSE
iqqe	N/A	N/A	-1.271	1.651	-1.144	1.485	-1.149	1.372	-1.264	1.771	-0.943	1.342	N/A	N/A	-0.754	1.097	-0.827	1.288	-0.897	1.298	-1.171	1.626
jplm	-0.136	0.441	-0.238	0.487	-0.299	0.474	-0.311	0.499	-0.406	0.572	-0.335	0.520	-0.239	0.400	-0.143	0.333	-0.266	0.434	-0.294	0.492	-0.287	0.488
albh	-0.224	0.570	-0.094	0.433	-0.289	0.619	-0.170	0.474	-0.157	0.442	-0.168	0.424	-0.198	0.504	-0.040	0.358	0.010	0.400	-0.111	0.401	-0.103	0.406
areq	-1.073	1.246	-0.798	0.942	-0.729	0.832	-0.730	0.818	-0.741	0.815	-0.611	0.691	-0.412	0.579	-0.792	0.933	-0.921	1.029	-0.951	1.058	-1.172	1.244
comz	N/A	N/A	-0.565	0.853	-0.412	0.709	-0.591	0.765	-0.695	0.958	-0.768	1.062	-0.699	0.988	-0.799	1.031	-0.753	1.033	-0.833	1.050	-0.908	1.117
frdn	N/A	N/A	N/A	N/A	-0.404	0.635	-0.244	0.555	-0.279	0.478	-0.300	0.621	-0.252	0.682	-0.292	0.622	-0.227	0.587	-0.234	0.918	-0.374	0.842
harv	-0.465	0.888	-0.752	1.093	-0.698	1.090	-0.721	1.181	-0.875	1.276	-0.541	1.246	-0.754	1.205	-0.512	1.018	-0.603	1.065	-0.665	1.147	-0.822	1.286
hlfx	N/A	N/A	-0.549	1.345	-0.367	0.570	-0.338	0.620	-0.344	0.537	-0.295	0.495	-0.221	0.479	-0.301	0.509	-0.236	0.472	-0.367	0.901	-0.483	0.880
mkea	-0.900	1.007	-1.268	1.360	-1.276	1.367	-1.315	1.405	-1.274	1.346	-1.094	1.188	-1.130	1.252	-1.046	1.155	-0.883	0.968	-0.941	0.987	-0.872	0.952
pove	N/A	N/A	N/A	N/A	N/A	N/A	N/A	N/A	N/A	N/A	N/A	N/A	N/A	N/A	-1.651	1.800	-1.670	1.820	-1.823	1.997	-1.735	1.871
stjo	-0.330	0.571	-0.393	0.613	-0.407	0.674	-0.503	0.707	-0.446	0.633	-0.452	0.666	-0.447	0.682	-0.395	0.572	-0.353	0.560	-0.443	0.683	-0.404	0.866
tehn	N/A	N/A	N/A	N/A	N/A	N/A	-0.691	0.786	-0.783	0.844	-0.759	0.824	-0.734	0.751	-0.774	0.836	-0.738	0.799	-0.739	0.798	-0.815	0.866
suth	-0.824	0.968	-1.076	1.214	-1.106	1.229	-1.143	1.265	-1.143	1.240	-1.017	1.144	-0.896	1.023	-1.041	1.158	-0.960	1.114	-0.999	1.121	-0.935	1.094
pdel	-0.505	0.646	-0.934	1.229	-1.262	1.508	-1.264	1.473	-1.165	1.382	-1.224	1.438	-1.100	1.311	-1.297	1.521	-1.342	1.588	-1.290	1.549	-1.292	1.501
ksmv	-0.940	1.060	-0.762	0.913	-0.725	0.939	-0.726	0.900	-0.731	0.895	-0.704	0.870	-0.630	0.804	-1.058	1.254	-1.171	1.375	-1.187	1.365	-1.048	1.210
lhaz	N/A	N/A	-0.666	0.824	-0.651	0.801	-0.697	0.802	-0.810	0.935	-0.716	0.795	-0.659	0.831	-0.787	0.890	-0.783	0.875	-0.676	0.760	-0.708	0.806
thu3	N/A	N/A	0.564	1.327	0.448	1.093	0.435	0.890	0.181	0.734	0.446	0.832	0.459	0.833	0.530	0.928	0.554	1.012	0.519	0.976	0.493	0.988
yell	0.270	0.511	0.364	0.609	0.205	0.684	0.314	0.550	0.203	0.430	0.157	0.381	0.298	0.511	0.285	0.427	0.271	0.425	0.419	0.731	0.524	0.850
mas1	-1.255	1.431	-1.196	1.423	-1.008	1.138	-1.093	1.257	-1.056	1.172	-1.040	1.185	-1.059	1.204	-1.380	1.600	-1.637	1.814	-1.642	1.813	-1.661	1.871
darw	-0.704	1.037	-1.279	1.463	-1.378	1.556	-1.217	1.322	-1.370	1.526	-1.198	1.350	-1.154	1.281	-1.303	1.450	-1.281	1.418	-1.245	1.420	-1.341	1.484
iisc	-0.808	1.075	-0.930	1.005	-0.553	0.813	-0.582	0.770	-0.778	0.933	-0.585	0.737	-0.343	0.645	-0.564	0.680	-0.348	0.638	-0.359	0.570	-0.208	0.526
ous2	N/A	N/A	-0.282	0.951	-0.286	1.062	-0.093	0.944	-0.275	0.728	-0.193	1.072	0.037	1.261	-0.164	1.222	-0.206	1.409	-0.247	1.278	-0.121	1.500
pets	N/A	N/A	N/A	N/A	N/A	N/A	-0.859	1.027	-1.108	1.222	-0.990	1.166	-0.820	1.011	-1.001	1.172	-0.912	1.100	-0.872	1.083	-0.798	0.989
tixi	0.515	1.024	0.079	0.771	-0.290	0.920	-0.018	0.705	-0.038	0.567	0.033	0.535	-0.076	0.525	-0.133	0.502	-0.120	0.501	-0.156	0.525	0.028	0.585
wtrr	-0.460	0.858	-0.622	0.925	-0.545	1.030	-0.586	1.047	-0.626	0.916	-0.591	0.846	-0.453	0.762	-0.656	0.929	-0.622	0.949	-0.749	1.017	-0.580	0.850
nyal	0.572	0.981	0.511	1.163	0.047	1.222	0.260	1.035	0.079	0.604	0.050	0.645	0.168	0.548	0.154	0.572	0.108	0.487	0.059	0.476	0.079	0.494
pol2	-0.067	0.617	-0.655	0.850	-0.550	0.748	-0.615	0.748	-0.660	0.768	-0.677	0.785	-0.743	0.824	-0.734	0.816	-0.705	0.784	-0.803	0.916	-0.831	0.942
ohi2	N/A	N/A	0.052	0.664	-0.204	1.240	0.227	0.998	-0.012	0.607	0.149	0.769	0.063	0.863	0.181	0.868	0.033	0.764	-0.200	0.787	-0.038	0.912
scub	N/A	N/A	-2.327	2.500	-2.214	2.414	-2.168	2.357	-1.295	1.466	-2.205	2.394	-1.914	2.096	-2.170	2.365	-2.192	2.373	-2.354	2.612	-2.119	2.331
nico	-0.220	0.497	-0.166	0.516	-0.402	0.567	-0.444	0.599	-0.277	0.695	-0.571	0.717	-0.749	0.855	-1.124	1.324	-1.357	1.525	-1.524	1.690	-1.287	1.438
kerq	-0.473	1.000	-0.630	0.842	-1.035	1.184	-0.889	1.027	-0.917	1.032	-0.839	0.946	-0.861	0.992	-1.216	1.369	-1.398	1.564	-1.558	1.696	-1.518	1.698
mdo1	-0.291	0.451	-0.329	0.489	-0.317	0.434	-0.354	0.444	-0.293	0.368	-0.274	0.395	-0.442	0.590	-0.377	0.566	-0.376	0.567	-0.332	0.549	-0.327	0.520

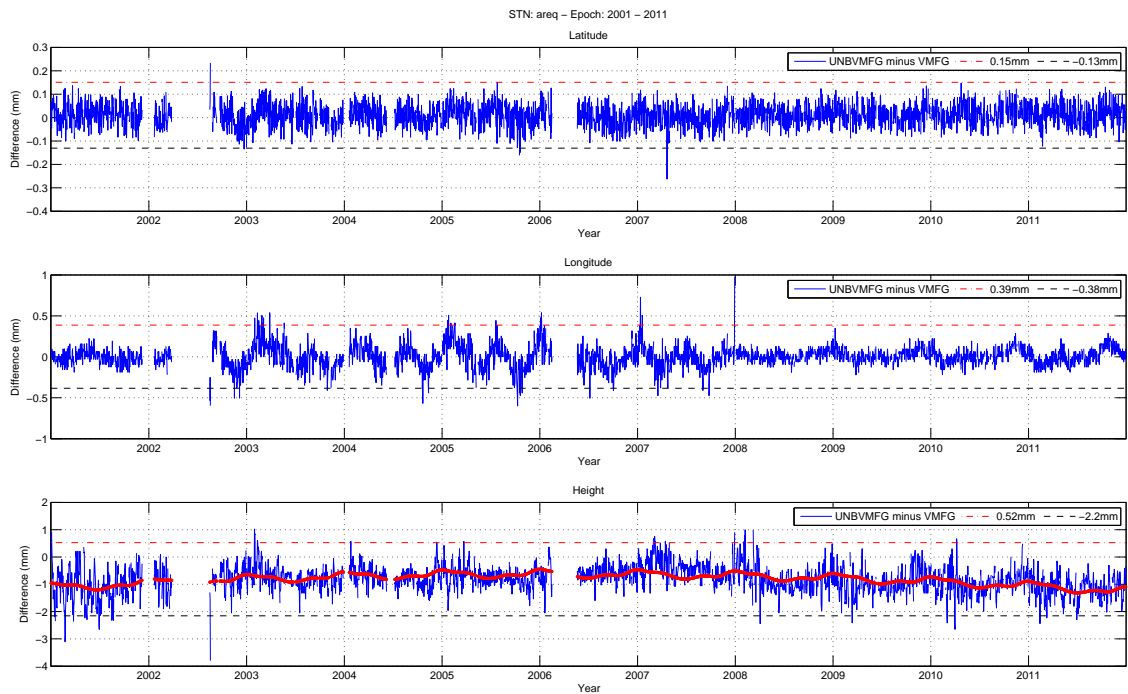
summarizes the overall mean bias, RMSE, standard deviation, and the  $3\sigma$  range for each of the stations studied over the 11-year period. Lastly is Figure D.1.(1-32), which plots the coordinate time series for all stations. For each subplot, the top most figure is the latitude difference, the middle plot is the longitude difference, and then bottom plot is the difference in height. For each position component two horizontal dashed lines are plotted indicated the  $3\sigma$  range. For the height difference plot the fitted line is plotted in red per equation 3.7.

Table D.2: Summary of bias, RMSE, standard deviation, and  $3\sigma$  range of values for the difference in height by PPP between UNB-VMF1 (NCEP) minus VMF1 (ECMWF). Epoch: 2001 to 2011.

Station	Mean	RMSE	$\sigma$	$3\sigma$ Range	
iqqe	-1.043	1.463	1.008	-4.066	1.980
jplm	-0.270	0.471	0.344	-1.301	0.762
albh	-0.140	0.464	0.433	-1.438	1.157
areq	-0.815	0.951	0.446	-2.154	0.525
conz	-0.712	0.974	0.645	-2.648	1.223
frdn	-0.283	0.677	0.606	-2.101	1.535
harv	-0.681	1.144	0.832	-3.176	1.814
hlfx	-0.328	0.633	0.530	-1.918	1.262
mkea	-1.092	1.194	0.449	-2.439	0.255
pove	-1.736	1.891	0.699	-3.833	0.361
stjo	-0.417	0.634	0.465	-1.811	0.978
tehn	-0.765	0.826	0.298	-1.659	0.129
suth	-1.015	1.148	0.531	-2.607	0.577
pdel	-1.155	1.402	0.763	-3.443	1.133
ksmv	-0.881	1.078	0.588	-2.646	0.884
lhaz	-0.716	0.832	0.393	-1.895	0.463
thu3	0.459	0.956	0.820	-2.001	2.919
yell	0.300	0.572	0.456	-1.069	1.670
mas1	-1.277	1.474	0.695	-3.363	0.809
darw	-1.231	1.402	0.639	-3.147	0.685
iisc	-0.534	0.768	0.494	-2.016	0.949
ous2	-0.173	1.181	1.155	-3.638	3.291
pets	-0.923	1.103	0.577	-2.654	0.809
tixi	-0.016	0.674	0.647	-1.956	1.924
wtZR	-0.590	0.924	0.696	-2.679	1.499
nyal	0.189	0.804	0.754	-2.074	2.452
pol2	-0.649	0.802	0.427	-1.930	0.632
ohi2	0.023	0.864	0.841	-2.501	2.547
scub	-2.124	2.336	0.765	-4.418	0.170
nico	-0.805	1.100	0.570	-2.513	0.904
kerg	-1.023	1.243	0.633	-2.921	0.875
mdo1	-0.338	0.494	0.353	-1.397	0.722

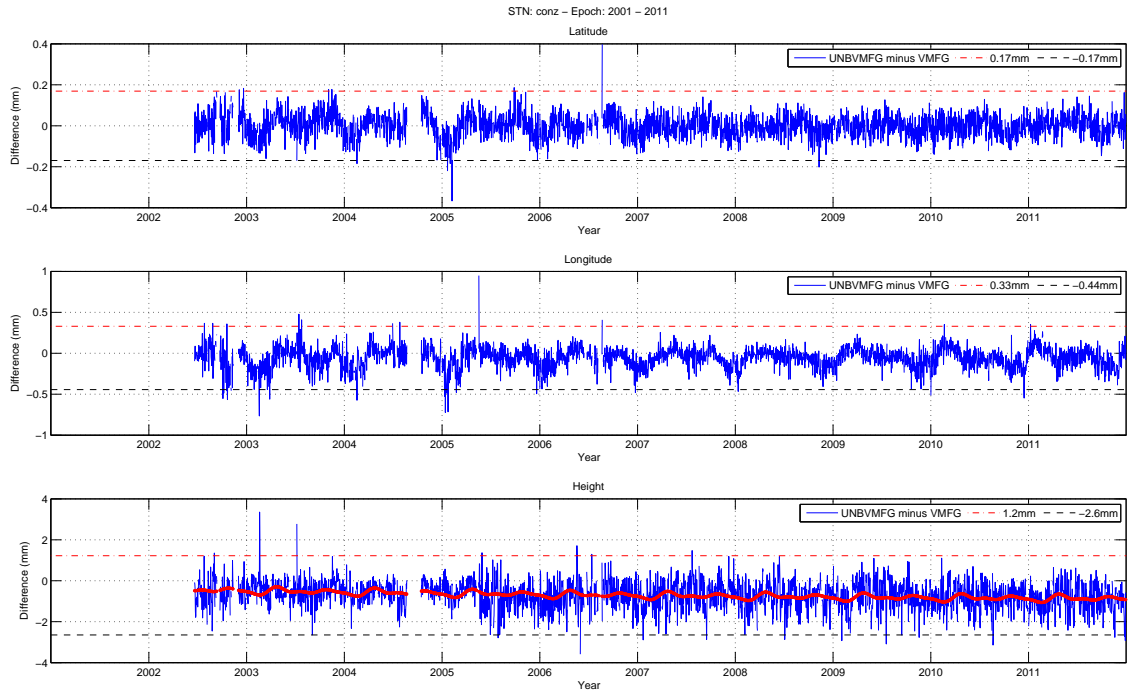


(D.1.1) ALBH

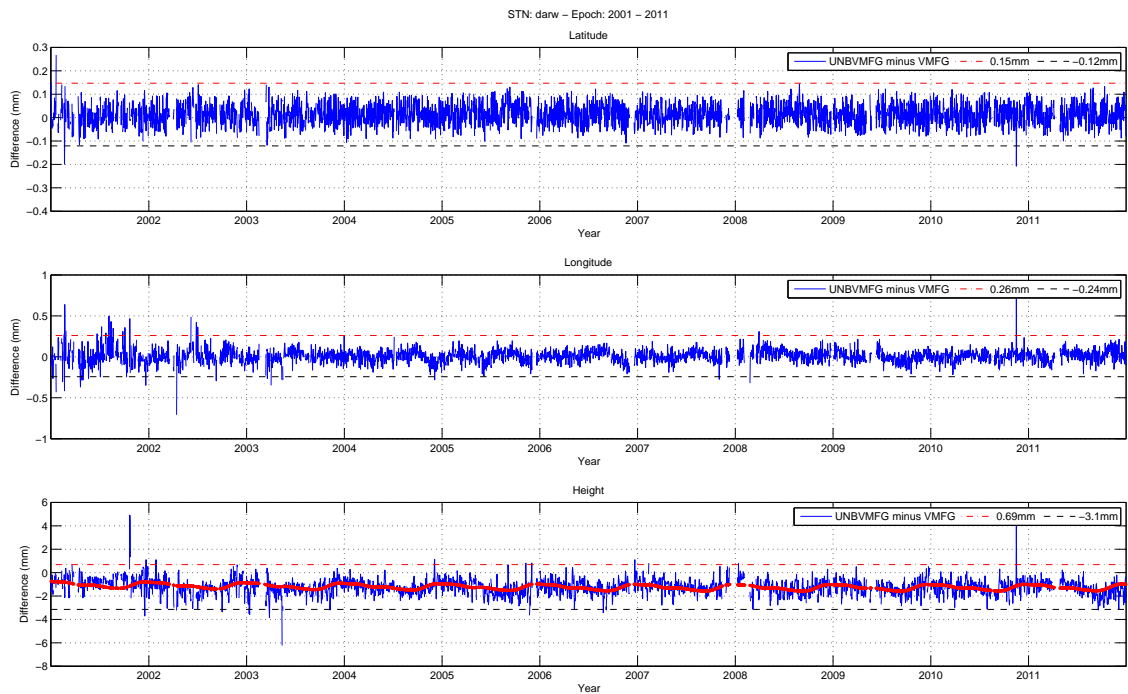


(D.1.2) AREQ

Figure D.1: PPP coordinate time series difference for UNB-VMF1 (NCEP) minus VMF1 (ECMWF) for years 2001 to 2012. Top: Latitude; Middle: Longitude; Bottom: Height.



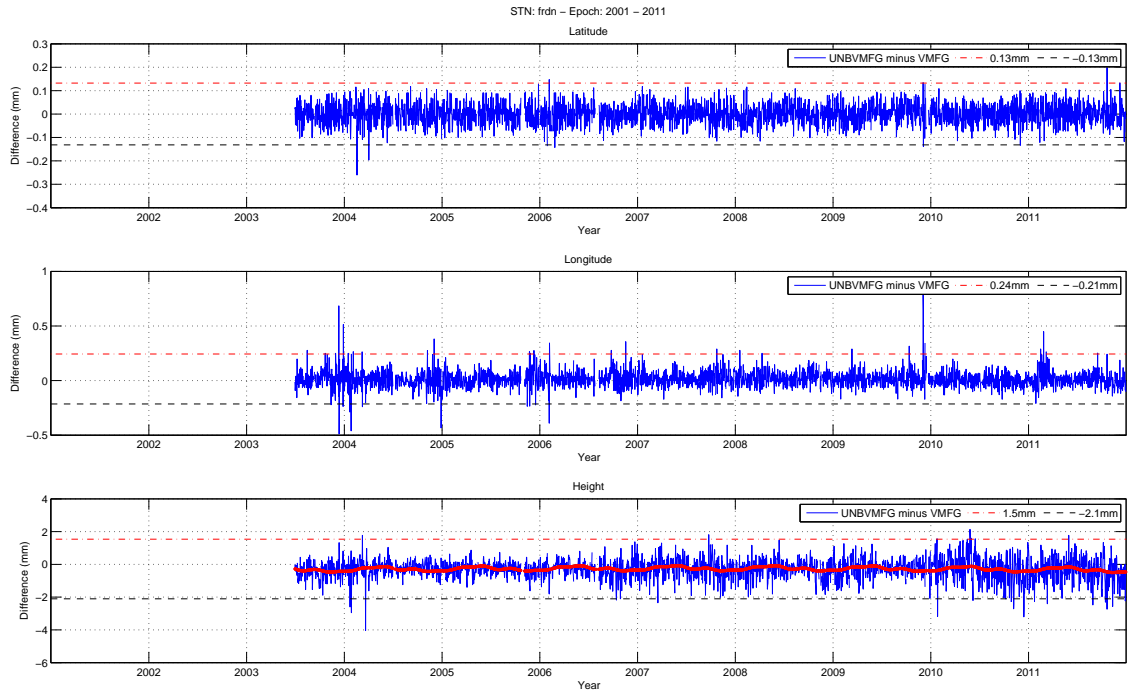
(D.1.3) CONZ



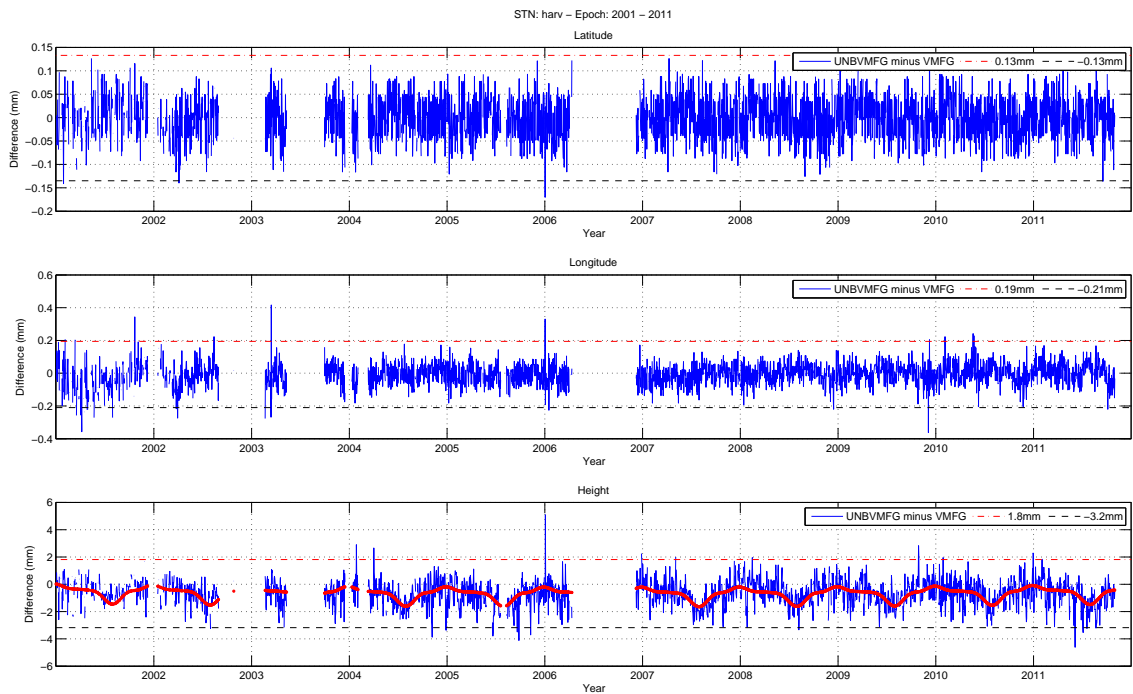
(D.1.4) DARW

Figure D.1: PPP coordinate time series difference for UNB-VMF1 (NCEP) minus VMF1 (ECMWF) for years 2001 to 2012. Top: Latitude; Middle: Longitude; Bottom: Height.



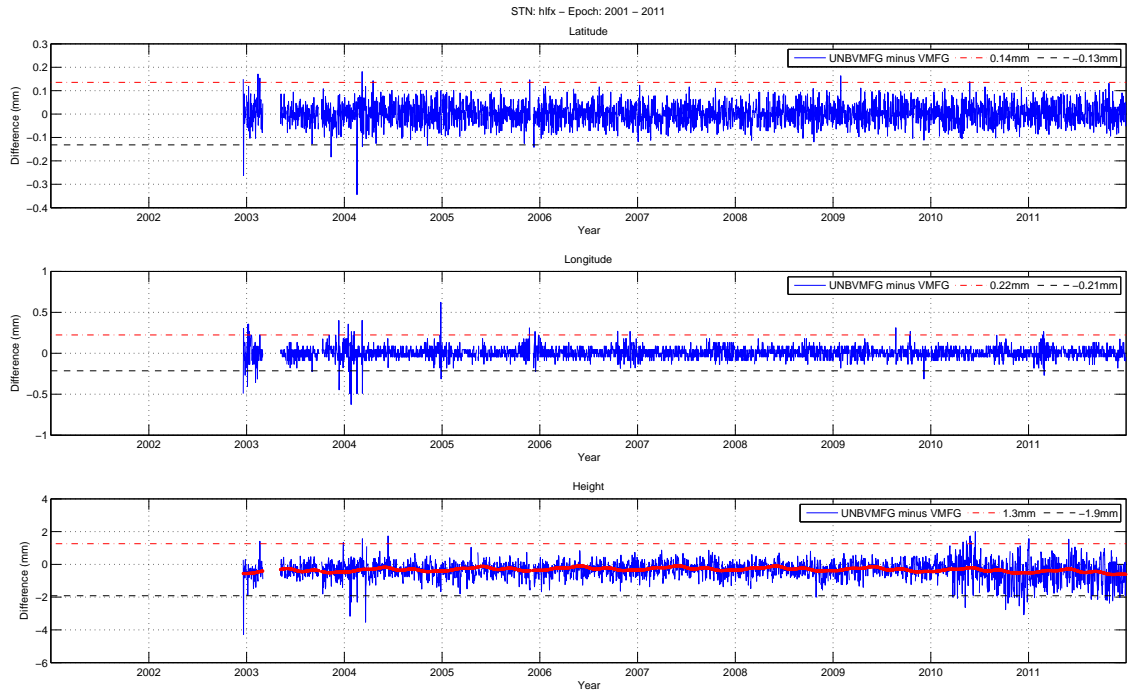


(D.1.5) FRDN

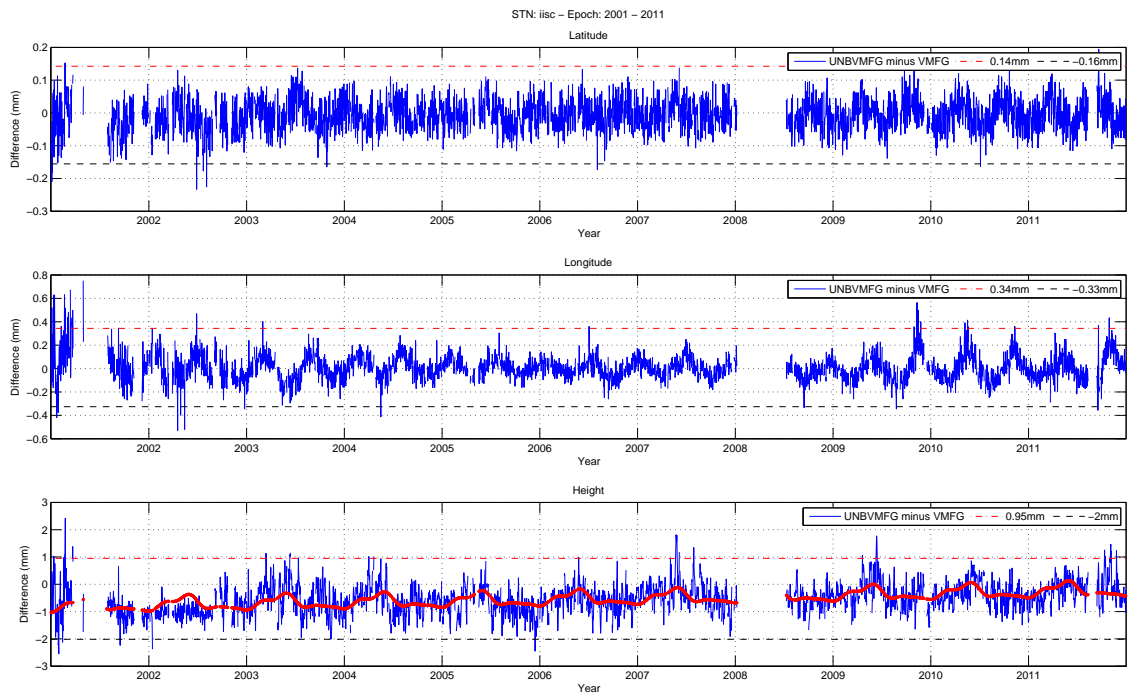


(D.1.6) HARV

Figure D.1: PPP coordinate time series difference for UNB-VMF1 (NCEP) minus VMF1 (ECMWF) for years 2001 to 2012. Top: Latitude; Middle: Longitude; Bottom: Height.

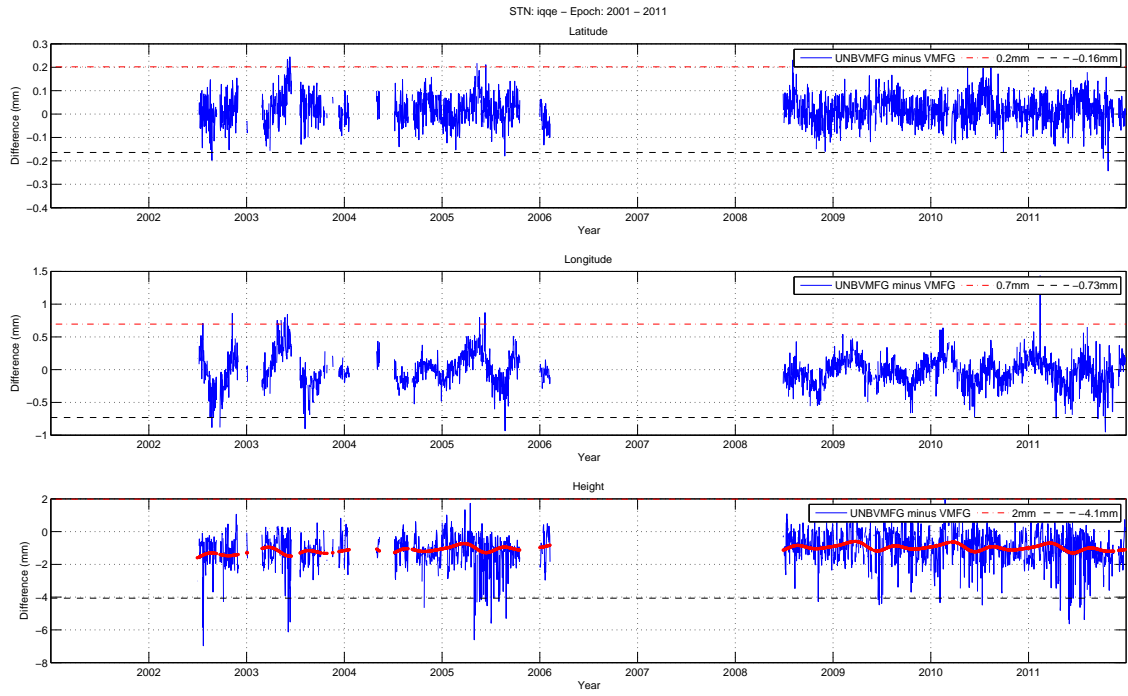


(D.1.7) HLFX

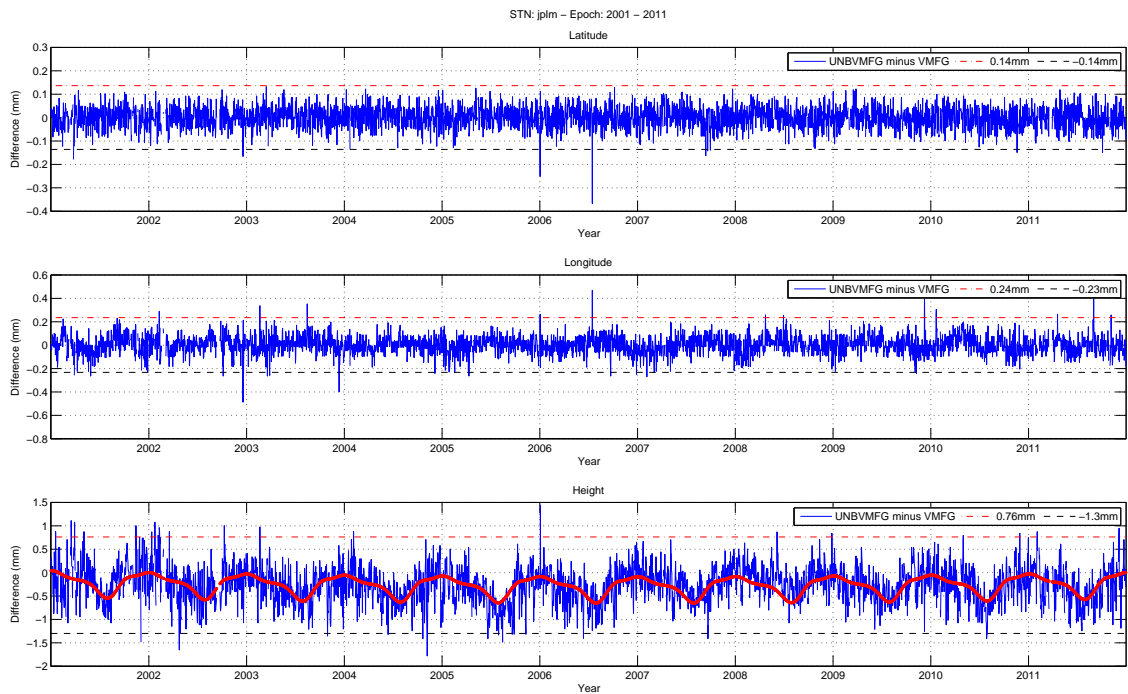


(D.1.8) IISC

Figure D.1: PPP coordinate time series difference for UNB-VMF1 (NCEP) minus VMF1 (ECMWF) for years 2001 to 2012. Top: Latitude; Middle: Longitude; Bottom: Height.

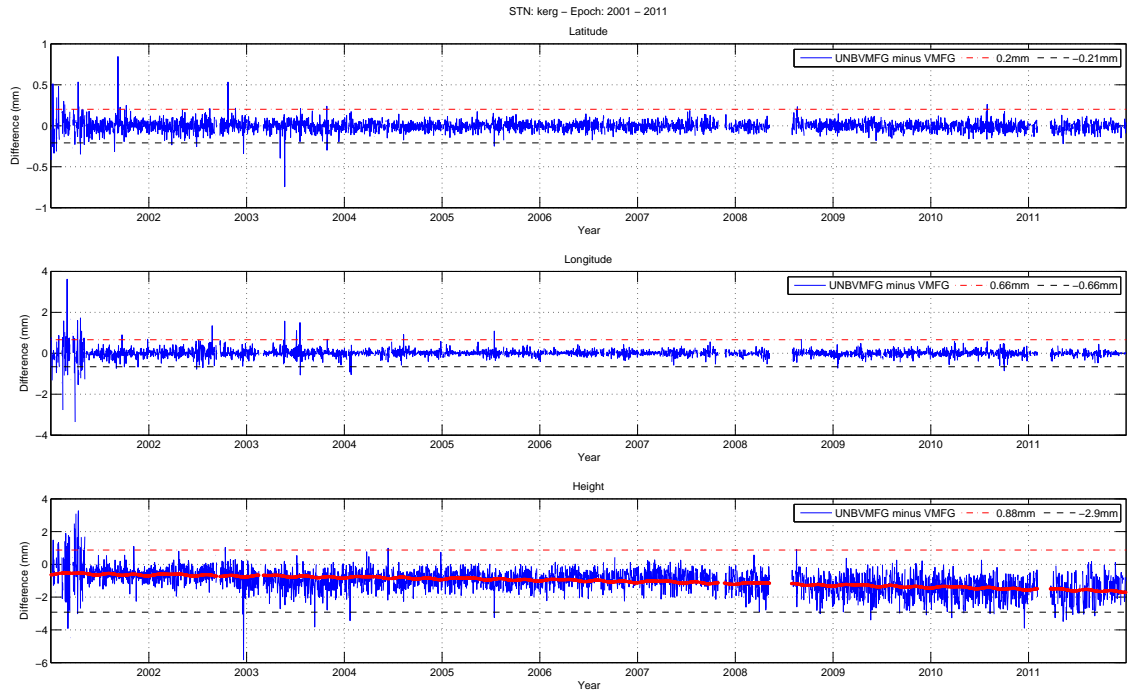


(D.1.9) IQQE

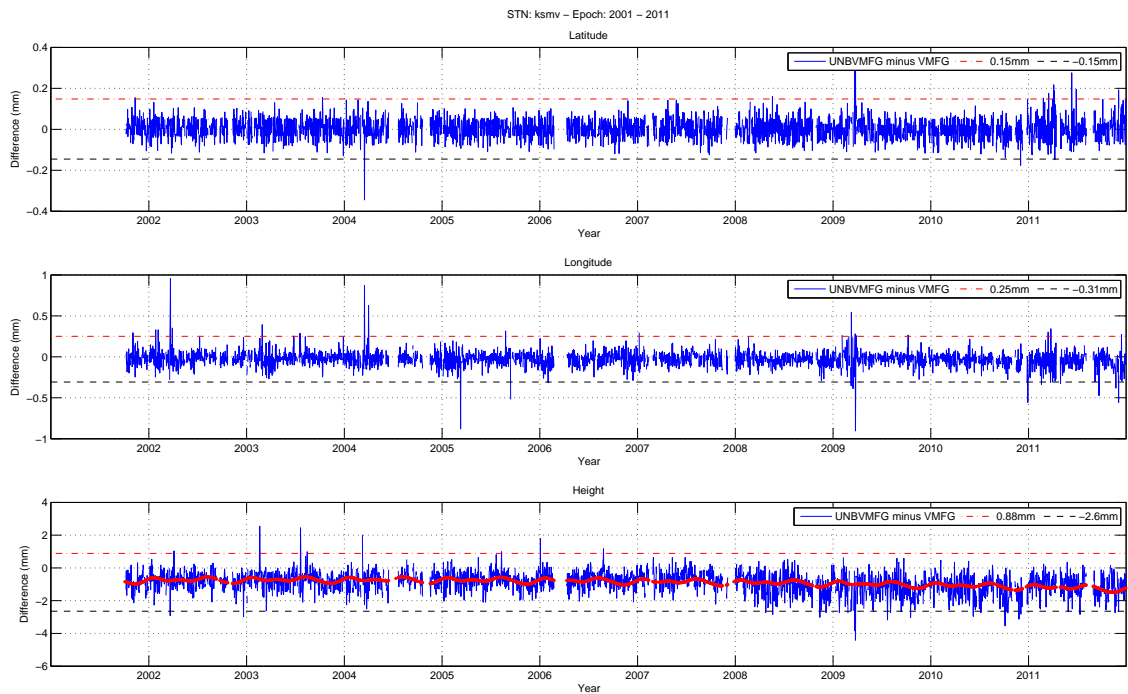


(D.1.10) JPLM

Figure D.1: PPP coordinate time series difference for UNB-VMF1 (NCEP) minus VMF1 (ECMWF) for years 2001 to 2012. Top: Latitude; Middle: Longitude; Bottom: Height.

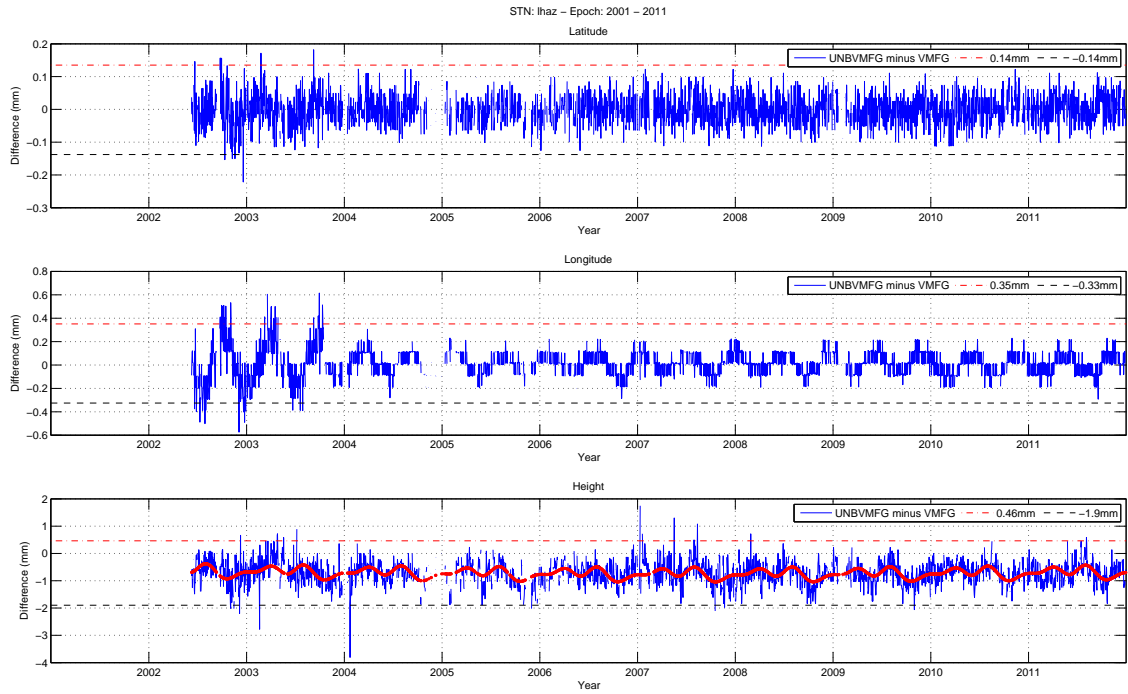


(D.1.11) KERG

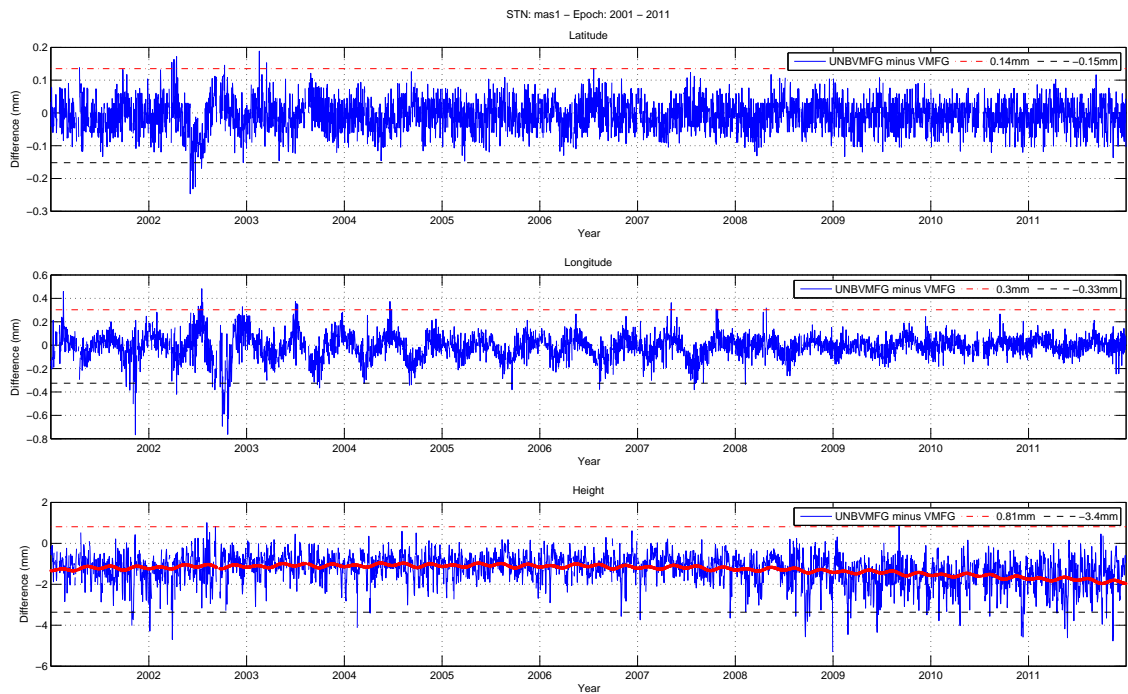


(D.1.12) KSMV

Figure D.1: PPP coordinate time series difference for UNB-VMF1 (NCEP) minus VMF1 (ECMWF) for years 2001 to 2012. Top: Latitude; Middle: Longitude; Bottom: Height.

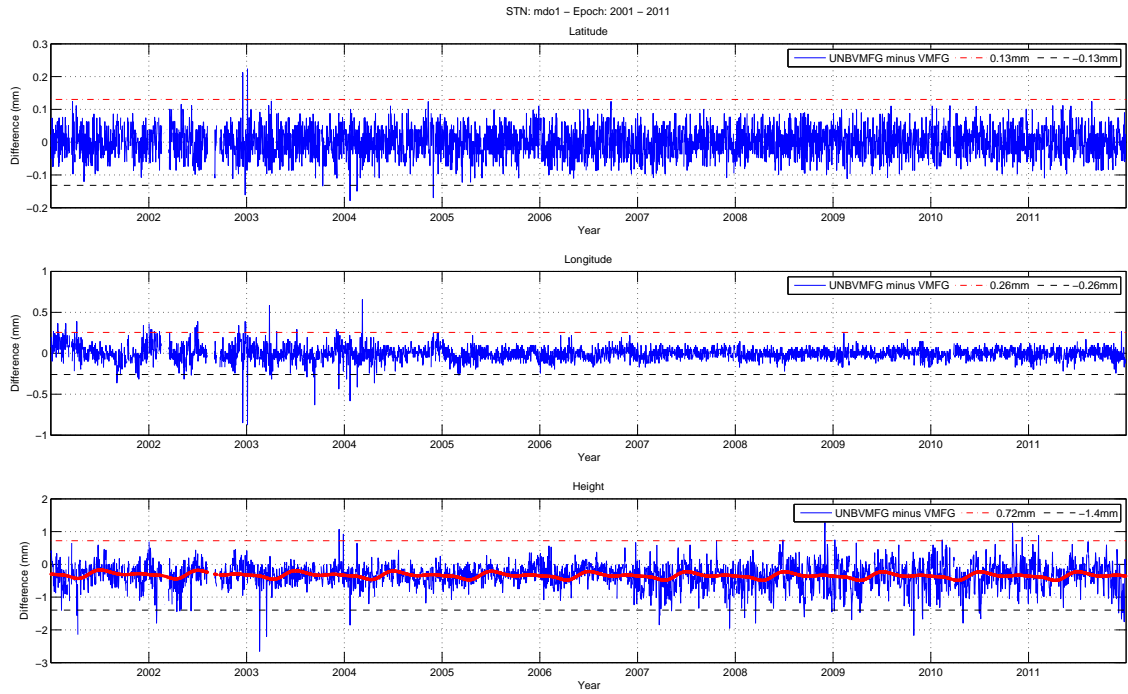


(D.1.13) LHAZ

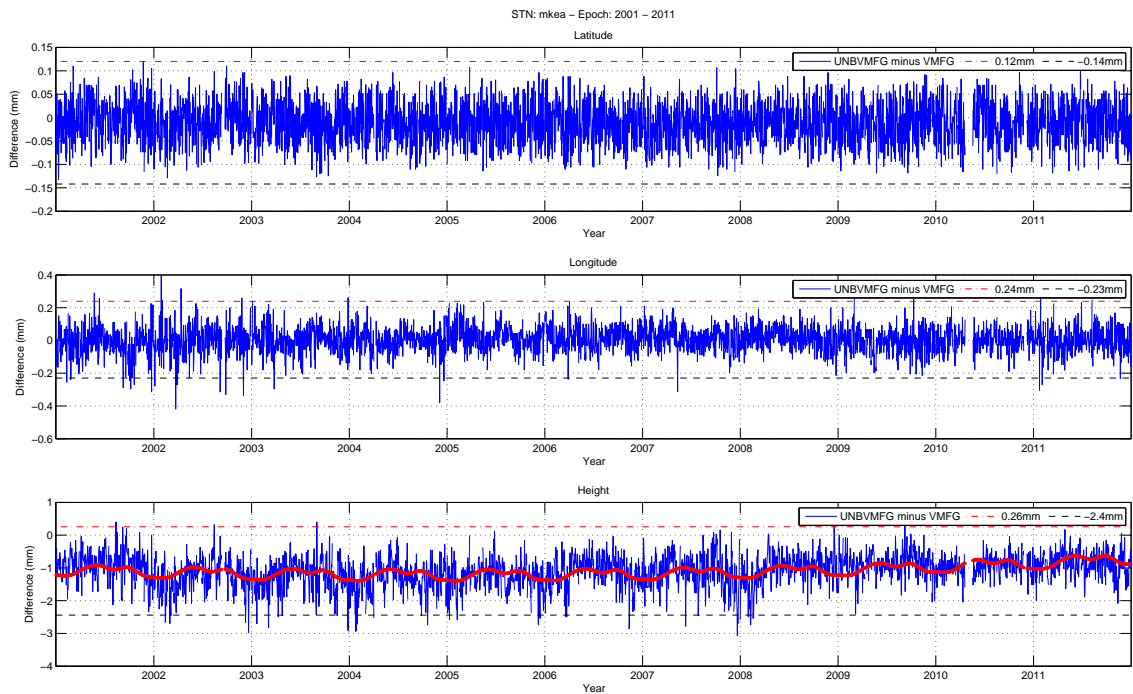


(D.1.14) MAS1

Figure D.1: PPP coordinate time series difference for UNB-VMF1 (NCEP) minus VMF1 (ECMWF) for years 2001 to 2012. Top: Latitude; Middle: Longitude; Bottom: Height.

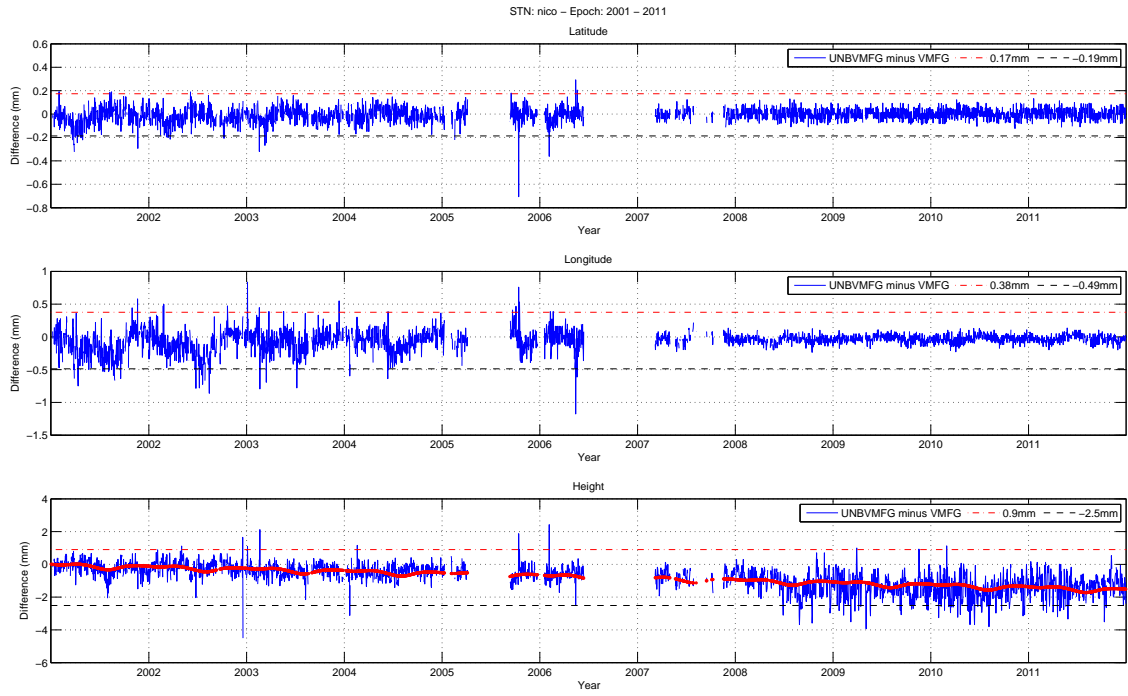


(D.1.15) MDO1

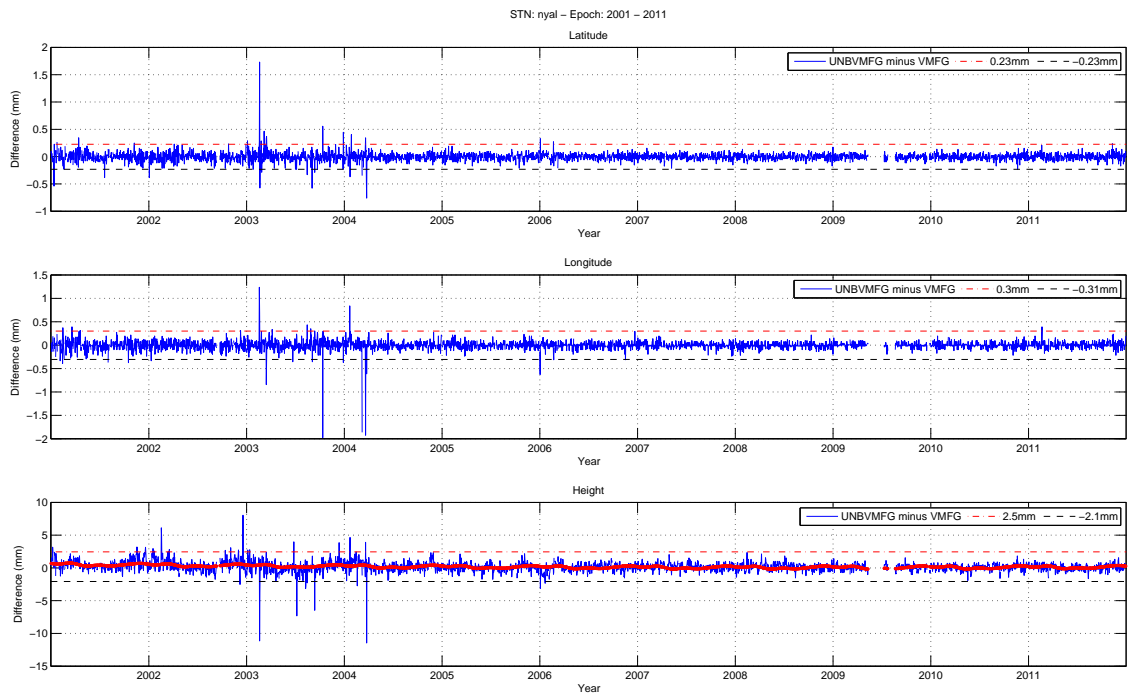


(D.1.16) MKEA

Figure D.1: PPP coordinate time series difference for UNB-VMF1 (NCEP) minus VMF1 (ECMWF) for years 2001 to 2012. Top: Latitude; Middle: Longitude; Bottom: Height.

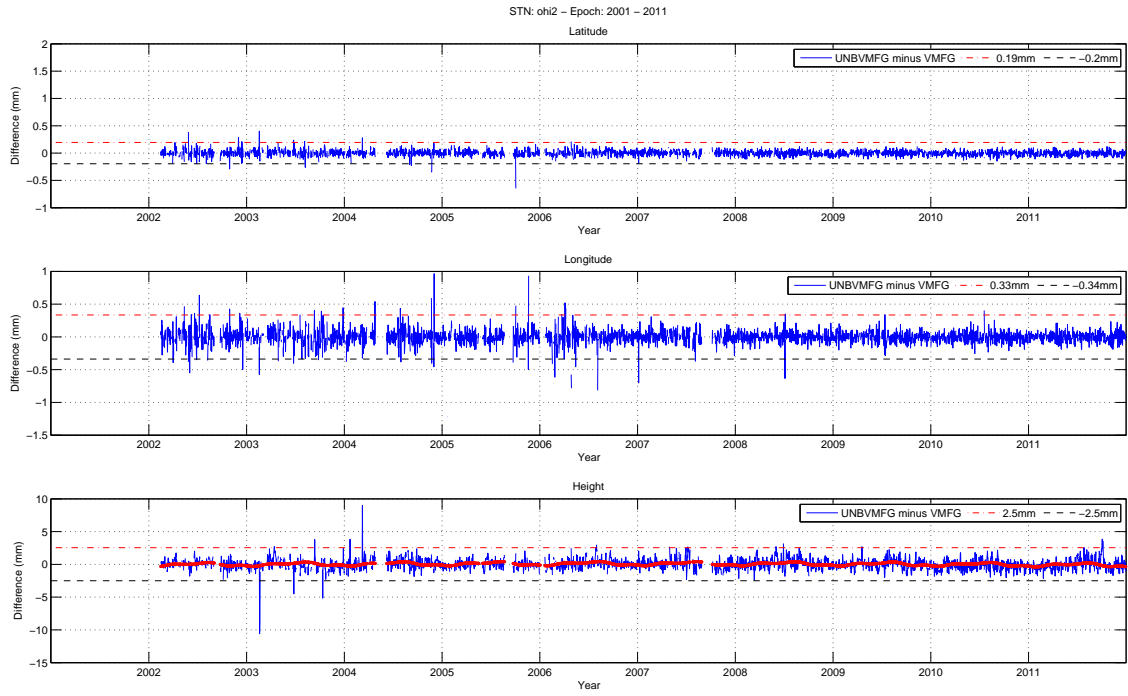


(D.1.17) NICO

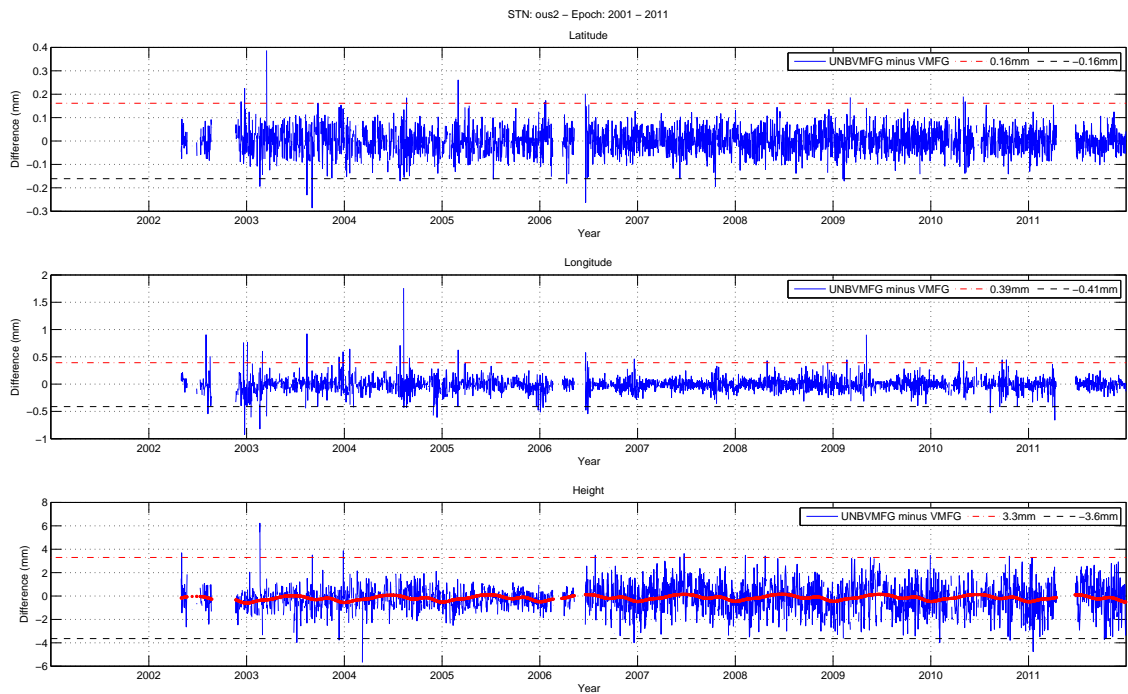


(D.1.18) NYAL

Figure D.1: PPP coordinate time series difference for UNB-VMF1 (NCEP) minus VMF1 (ECMWF) for years 2001 to 2012. Top: Latitude; Middle: Longitude; Bottom: Height.



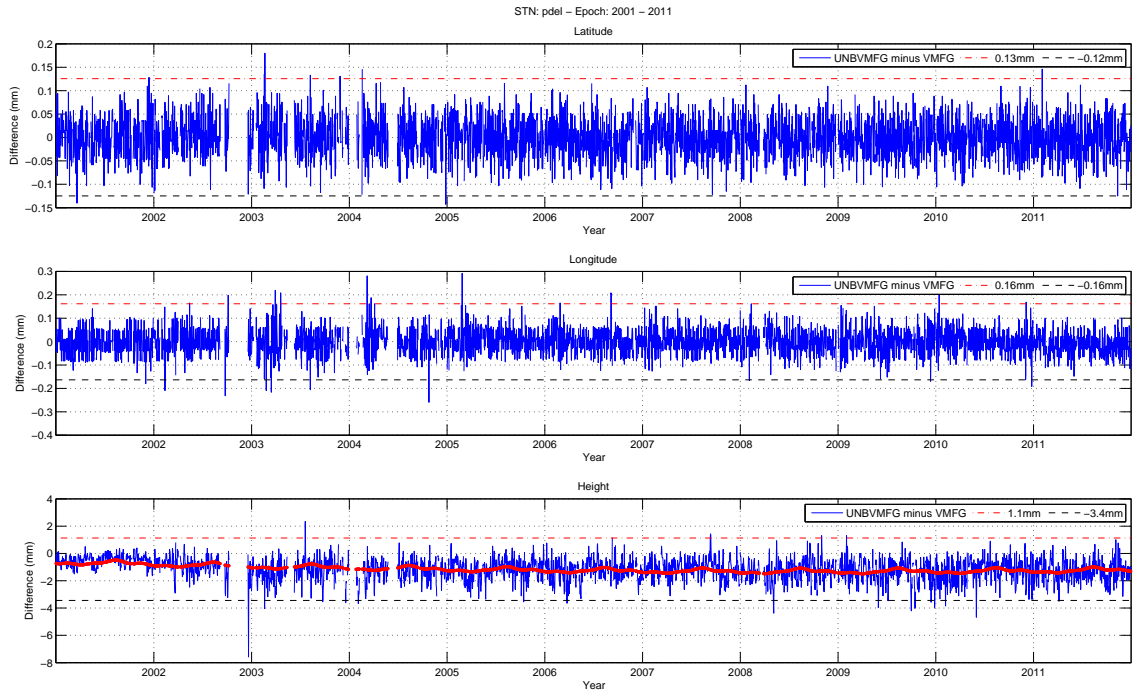
(D.1.19) OHI2



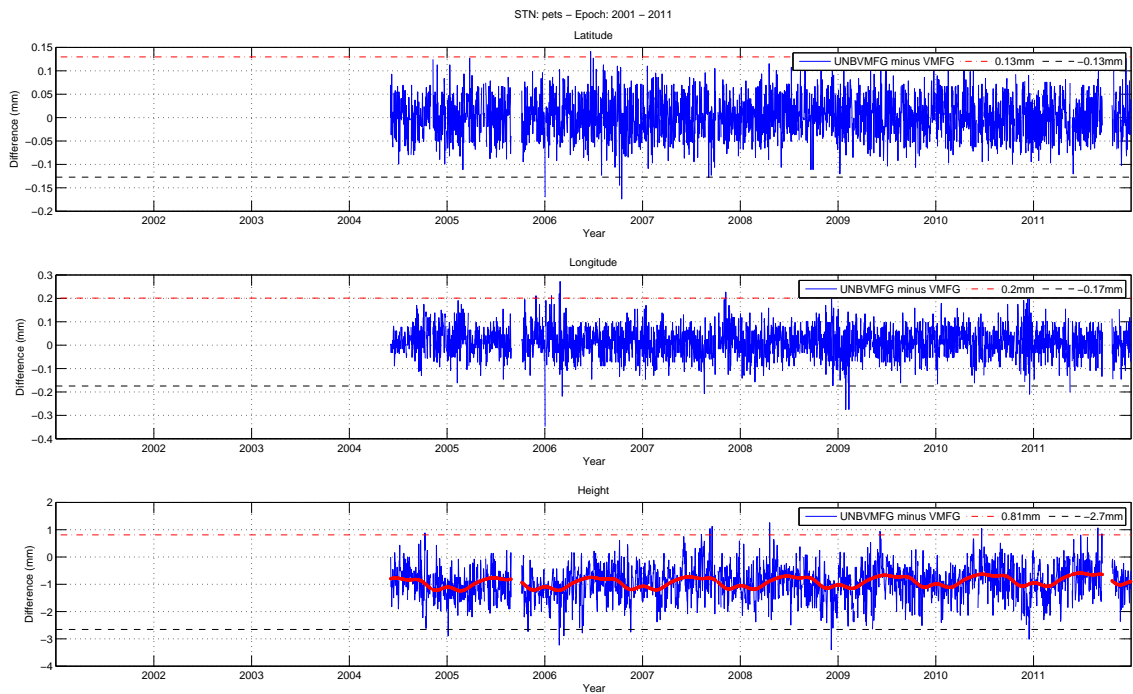
(D.1.20) OUS2

Figure D.1: PPP coordinate time series difference for UNB-VMF1 (NCEP) minus VMF1 (ECMWF) for years 2001 to 2012. Top: Latitude; Middle: Longitude; Bottom: Height.



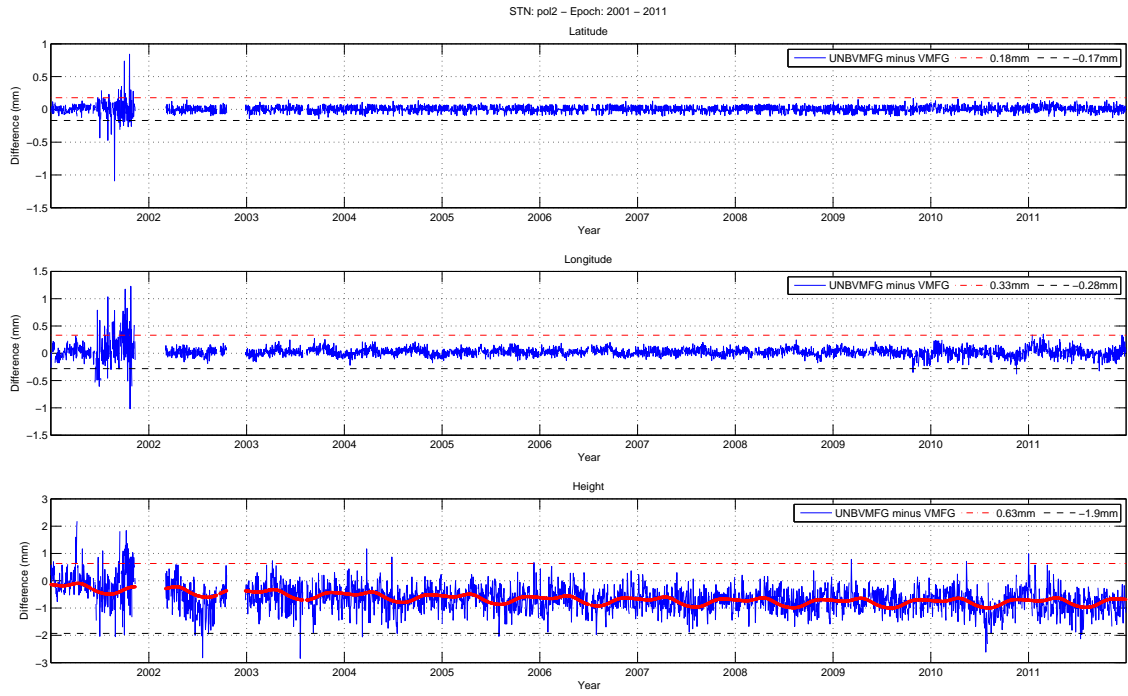


(D.1.21) PDEL

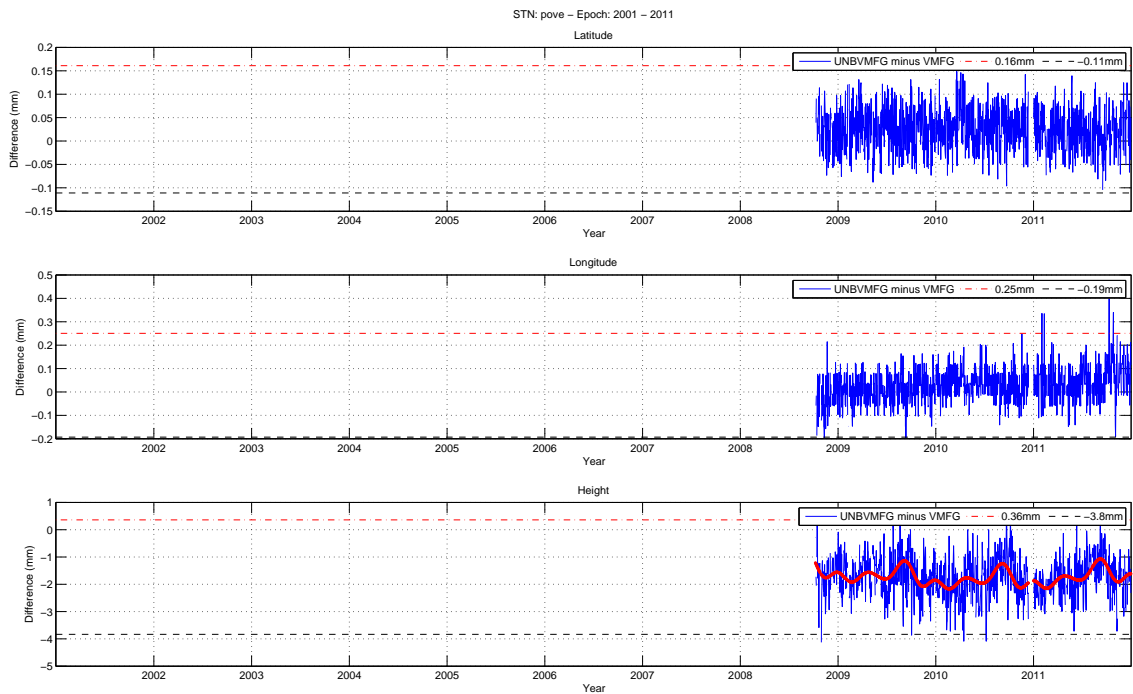


(D.1.22) PETS

Figure D.1: PPP coordinate time series difference for UNB-VMF1 (NCEP) minus VMF1 (ECMWF) for years 2001 to 2012. Top: Latitude; Middle: Longitude; Bottom: Height.

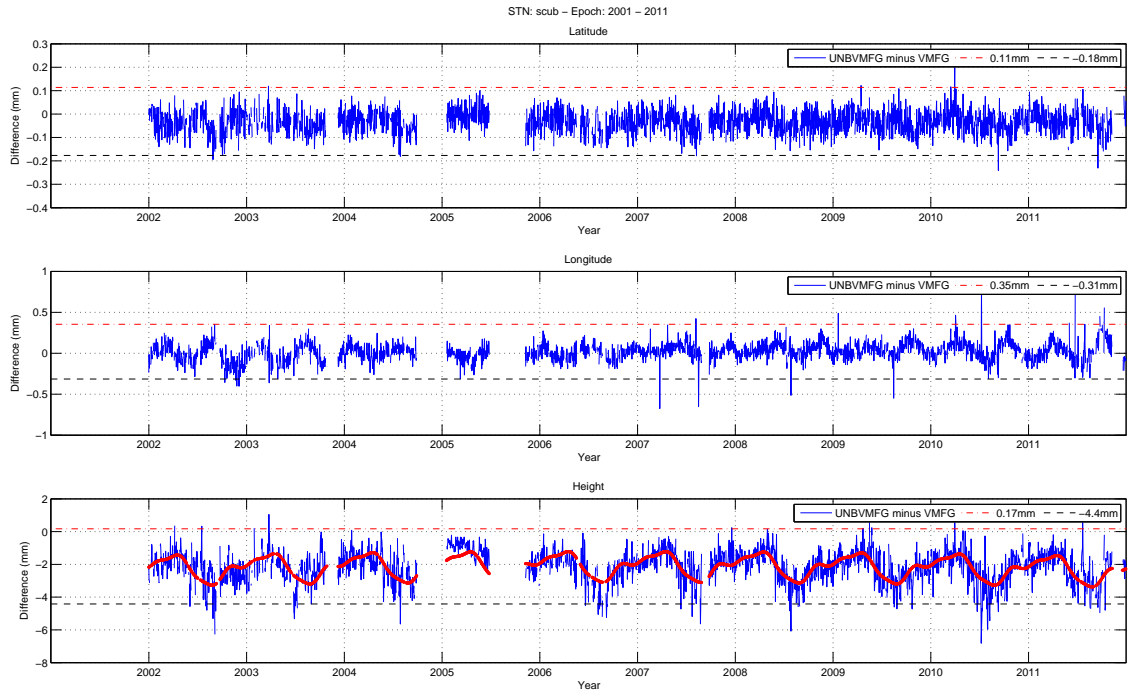


(D.1.23) POL2

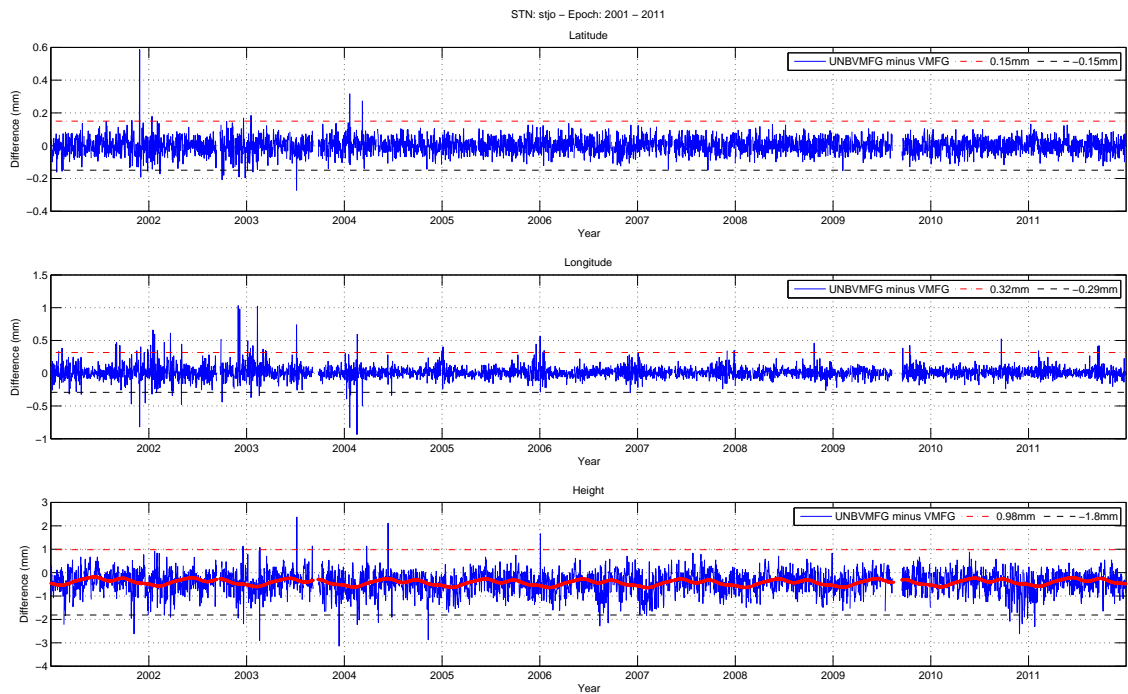


(D.1.24) POVE

Figure D.1: PPP coordinate time series difference for UNB-VMF1 (NCEP) minus VMF1 (ECMWF) for years 2001 to 2012. Top: Latitude; Middle: Longitude; Bottom: Height.

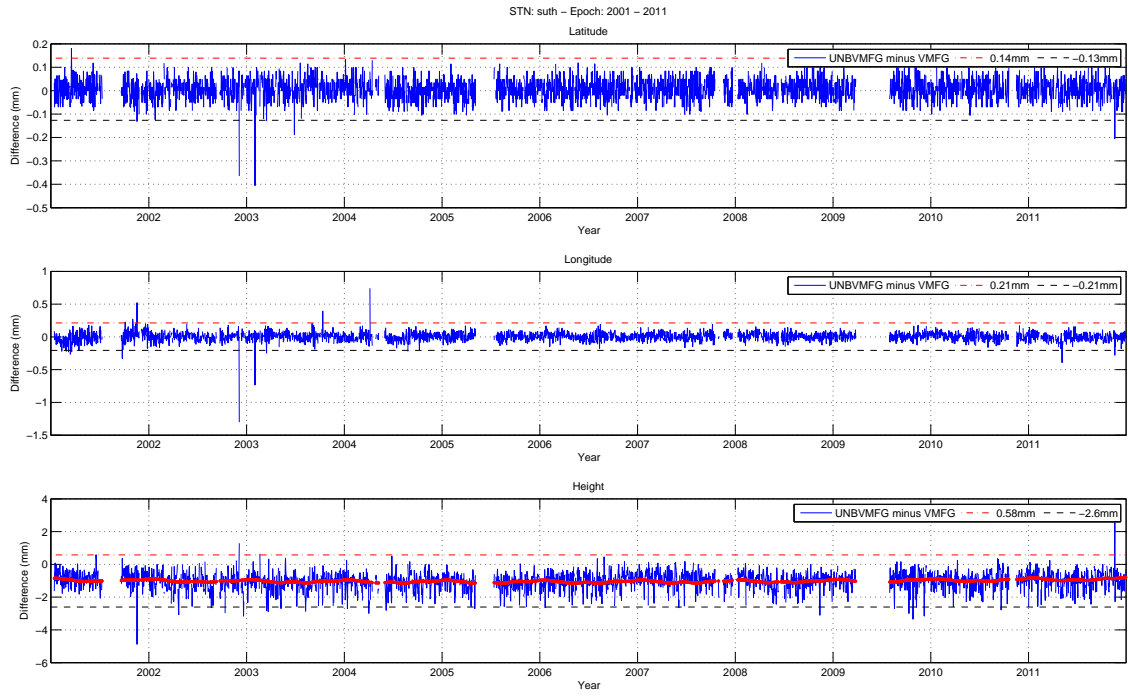


(D.1.25) SCUB

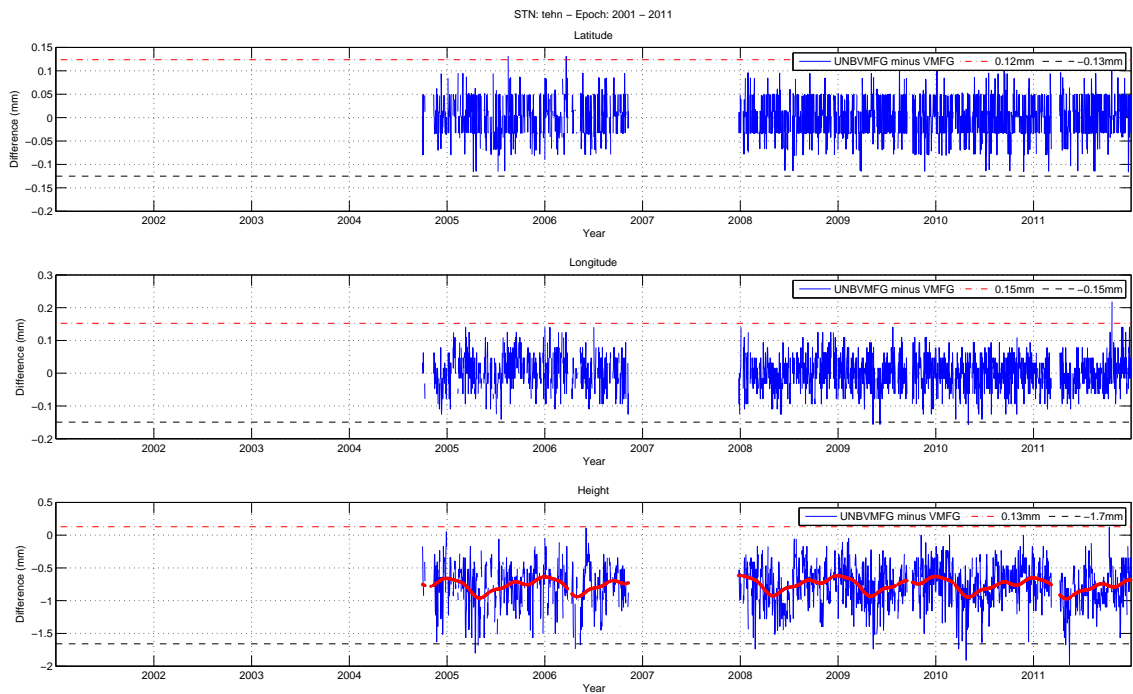


(D.1.26) STJO

Figure D.1: PPP coordinate time series difference for UNB-VMF1 (NCEP) minus VMF1 (ECMWF) for years 2001 to 2012. Top: Latitude; Middle: Longitude; Bottom: Height.

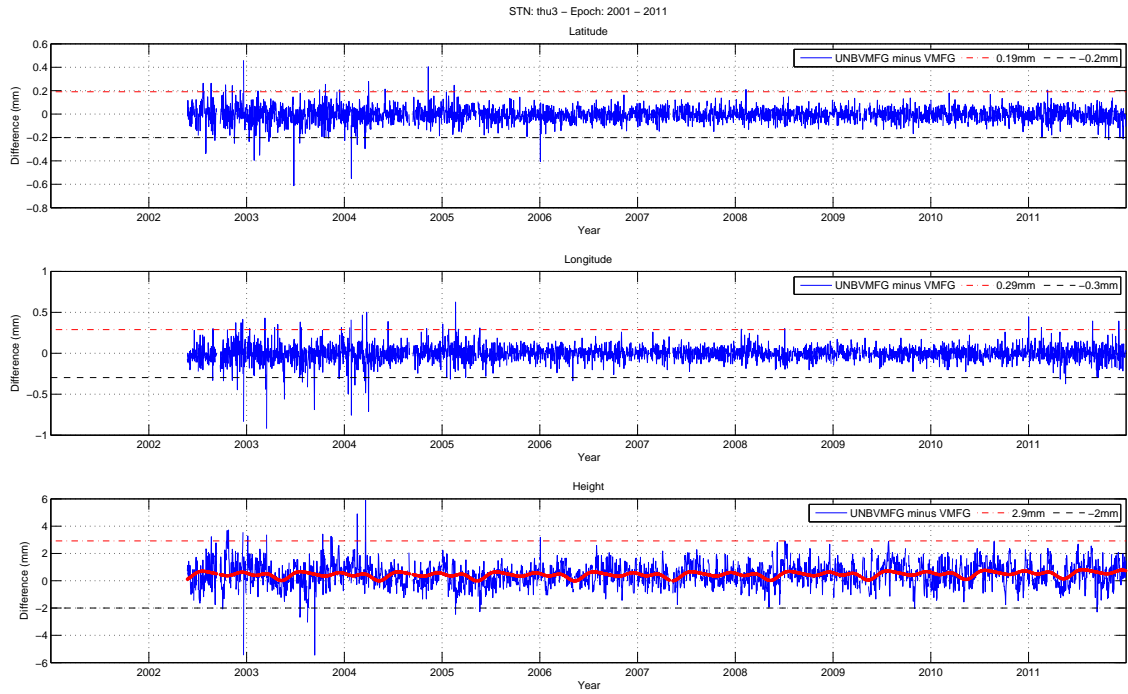


(D.1.27) SUTH

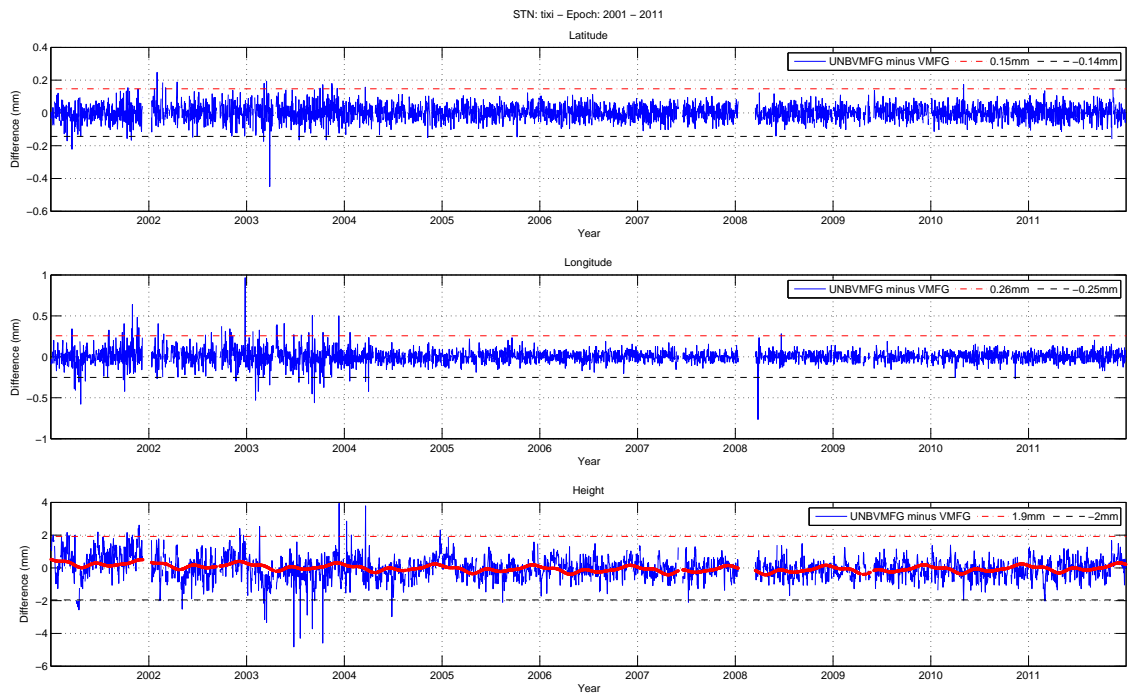


(D.1.28) TEHN

Figure D.1: PPP coordinate time series difference for UNB-VMF1 (NCEP) minus VMF1 (ECMWF) for years 2001 to 2012. Top: Latitude; Middle: Longitude; Bottom: Height.

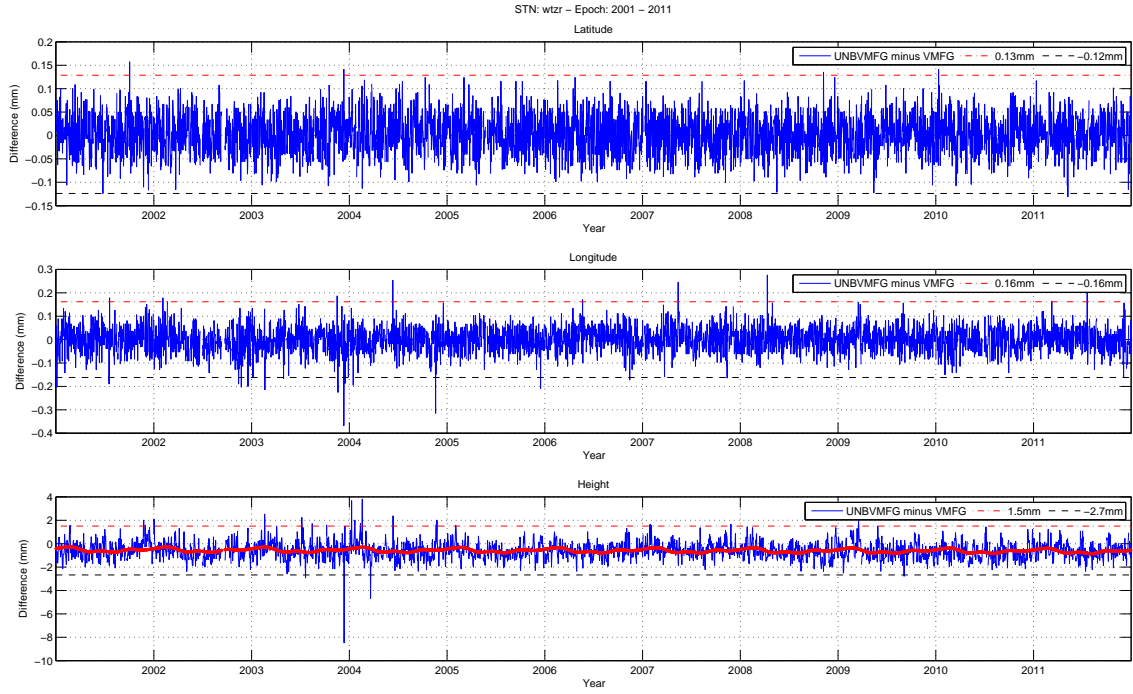


(D.1.29) THU3

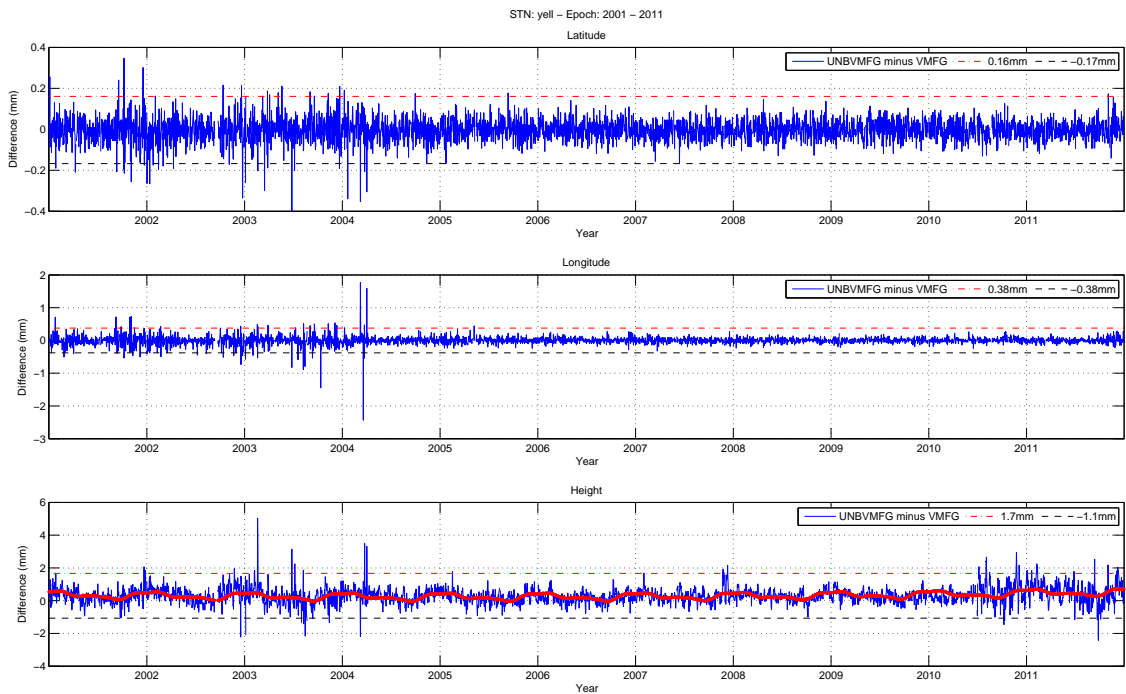


(D.1.30) TIXI

Figure D.1: PPP coordinate time series difference for UNB-VMF1 (NCEP) minus VMF1 (ECMWF) for years 2001 to 2012. Top: Latitude; Middle: Longitude; Bottom: Height.



(D.1.31) WTZR



(D.1.32) YELL

Figure D.1: PPP coordinate time series difference for UNB-VMF1 (NCEP) minus VMF1 (ECMWF) for years 2001 to 2012. Top: Latitude; Middle: Longitude; Bottom: Height.

### **D.1.2 UNB-VMF1 versus VMF1 (ECMWF) - All Products**

This section provides an additional to the main text where a complete set of tables and figures for each station can be found. For the comparison of all of the UNB-VMF1 products the time period extends from January 1st to August 31st, 2012 for the standard NCEP and CMC based products (unbvmfG and unbvmfGcmc respectively), and from March 17th to August 31st for the forecast based product (unbvmfP). Tables D.3 and D.4 summarize the comparison between the standard NCEP and CMC based products, and the comparison of the forecast based product respectively. The forecast based product includes an additional comparison to the standard CMC based product, which evaluates the consistency of the CMC's forecasts. Both Tables D.3 and D.4 include the mean bias, RMSE, and the  $3\sigma$  range for the entire time period. Lastly, Figure D.2 (1-32) plots the time series for the difference in height only for all of the UNB-VMF1 products with respect to the existing VMF1 service. The height component is only included since the impact on the horizontal components is very small at the sub-mm level. The CMC based product, unbvmfGcmc, is shown in blue, the NCEP based product, unbvmfG, is shown in red, and the forecast product, unbvmfP, is shown in black.

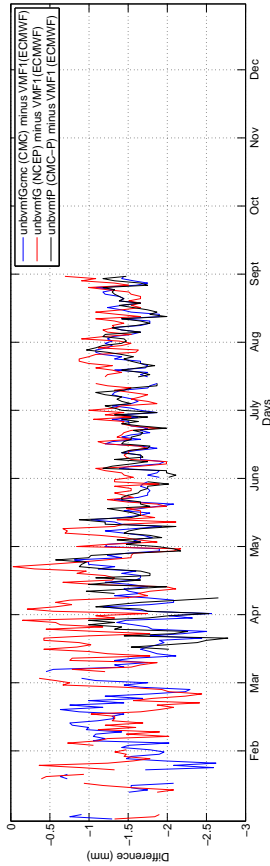
Table D.3: Summary of the PPP solution for the difference in height for UNB-VMF1 (NCEP and CMC) minus VMF1 (ECMWF). January 1st to August 31st 2012. All dimensions in millimetres

Station	unbvmfG (NCEP)				unbvmfGcmc (CMC)			
	Mean	RMSE	$3\sigma$ Range		Mean	RMSE	$3\sigma$ Range	
iqqe	-1.121	1.587	-4.220	1.979	-0.661	0.739	-1.596	0.273
jplm	-0.385	0.559	-1.347	0.577	-0.240	0.278	-0.573	0.092
albh	-0.259	0.464	-1.294	0.776	-0.065	0.108	-0.308	0.179
areq	-1.323	1.399	-2.496	-0.151	-1.530	1.577	-2.510	-0.550
conz	-0.751	1.062	-2.883	1.380	-0.419	0.486	-1.117	0.279
frdn	-0.456	0.966	-2.837	1.924	-0.186	0.255	-0.676	0.305
harv	-1.138	1.491	-3.114	0.837	-0.469	0.547	-1.169	0.230
hlfx	-0.590	1.021	-2.935	1.755	-0.285	0.331	-0.747	0.177
mkea	-0.852	0.913	-1.764	0.060	-0.566	0.604	-1.109	-0.023
pove	-1.810	1.913	-3.541	-0.078	-1.472	1.572	-2.936	-0.008
stjo	-0.440	0.608	-1.556	0.676	-0.160	0.186	-0.429	0.109
tehn	-0.805	0.860	-1.666	0.057	-0.638	0.658	-0.943	-0.332
suth	-0.997	1.140	-2.566	0.571	-0.657	0.689	-1.230	-0.085
pdel	-1.385	1.559	-3.423	0.653	-0.998	1.036	-1.625	-0.370
ksmv	-1.044	1.237	-2.949	0.860	-0.620	0.662	-1.248	0.009
lhaz	-0.729	0.806	-1.657	0.199	-0.466	0.546	-1.097	0.164
thu3	0.322	0.877	-1.950	2.594	0.567	0.660	-0.306	1.440
yell	0.391	0.715	-1.269	2.052	0.261	0.335	-0.331	0.853
mas1	-1.598	1.760	-3.684	0.489	-1.240	1.287	-2.033	-0.448
darw	-1.420	1.604	-3.298	0.458	-1.408	1.486	-2.519	-0.298
iisc	-0.181	0.455	-1.139	0.777	-0.287	0.368	-0.878	0.304
ous2	-0.136	1.477	-4.427	4.155	0.582	0.830	-1.099	2.262
pets	-0.728	0.934	-2.245	0.788	-0.424	0.449	-0.811	-0.037
tixi	0.013	0.519	-1.409	1.436	0.514	0.585	-0.169	1.197
wtzr	-0.648	1.012	-2.451	1.156	-0.532	0.564	-1.035	-0.029
nyal	-0.079	0.495	-1.410	1.252	0.241	0.410	-0.599	1.081
pol2	-0.670	0.769	-1.751	0.411	-0.537	0.567	-0.985	-0.088
ohi2	0.088	0.738	-2.037	2.214	0.150	0.361	-0.359	0.659
scub	-2.072	2.281	-4.098	-0.046	-1.620	1.691	-2.924	-0.317
nico	-1.433	1.595	-3.358	0.491	-1.111	1.157	-1.853	-0.368
kerq	-0.827	0.952	-2.154	0.500	-0.528	0.557	-1.022	-0.034
mdo1	-0.449	0.615	-1.580	0.681	-0.433	0.502	-0.918	0.051

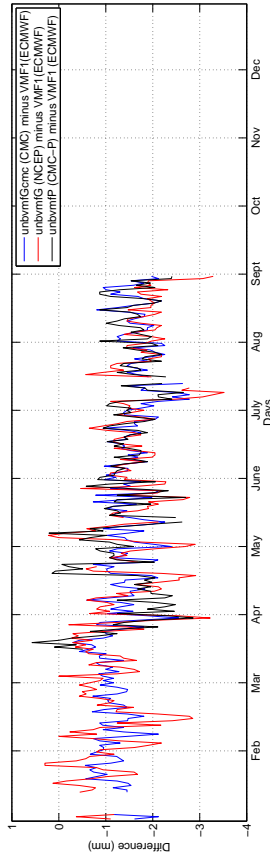


Table D.4: Summary of the PPP solution for the difference in height for the forecast product, unbvmfP. UNB-VMF1 (CMC-P) minus VMF1 (ECMWF). The columns listed as CMC-P minus CMC is relative to the unbvmfGcmc product. Match 17th to August 31st 2012. All dimensions in millimetres

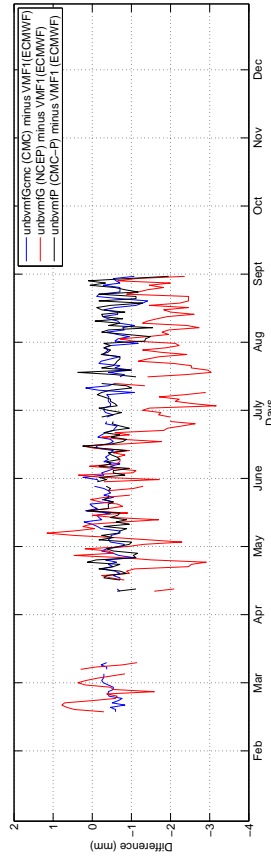
Station	unbvmP (CMC-P)				unbvmfP (CMC-P minus CMC)			
	Mean	RMSE	$3\sigma$ Range		Mean	RMSE	$3\sigma$ Range	
iqqe	-0.653	0.762	-1.656	0.350	0.024	0.285	-0.763	0.810
jplm	-0.279	0.320	-0.668	0.110	-0.009	0.137	-0.374	0.356
albh	-0.058	0.173	-0.522	0.405	0.017	0.150	-0.414	0.447
areq	-1.558	1.602	-2.531	-0.585	0.021	0.235	-0.647	0.688
conz	-0.178	0.454	-1.393	1.037	0.214	0.428	-0.870	1.299
frdn	-0.143	0.344	-1.033	0.746	0.052	0.299	-0.804	0.909
harv	-0.563	0.675	-1.622	0.496	-0.090	0.401	-1.205	1.025
hlfx	-0.248	0.398	-1.150	0.653	0.058	0.303	-0.823	0.939
mkea	-0.548	0.596	-1.165	0.068	0.047	0.169	-0.388	0.481
pove	-1.625	1.879	-3.738	0.489	-0.071	0.819	-1.966	1.824
stjo	-0.153	0.225	-0.595	0.290	0.010	0.148	-0.413	0.434
tehn	-0.667	0.694	-1.092	-0.243	0.012	0.136	-0.363	0.387
suth	-0.563	0.655	-1.504	0.379	0.082	0.265	-0.617	0.781
pdel	-1.048	1.470	-3.085	0.989	0.081	0.732	-1.927	2.090
ksmv	-0.519	0.650	-1.554	0.516	0.068	0.327	-0.777	0.912
lhaz	-0.288	0.413	-1.021	0.446	0.224	0.303	-0.317	0.766
thu3	0.583	0.781	-0.772	1.938	-0.020	0.462	-1.323	1.283
yell	0.084	0.398	-0.981	1.149	-0.179	0.424	-1.202	0.845
mas1	-0.998	1.083	-2.165	0.170	0.339	0.480	-0.590	1.268
darw	-1.467	1.599	-2.875	-0.059	0.055	0.472	-1.018	1.127
iisc	-0.232	0.351	-0.911	0.448	0.092	0.220	-0.450	0.634
ous2	0.753	1.137	-1.653	3.159	0.114	0.783	-2.154	2.382
pets	-0.391	0.470	-1.077	0.296	0.024	0.237	-0.623	0.671
tixi	0.450	0.616	-0.653	1.553	0.012	0.350	-0.934	0.958
wtzt	-0.408	0.522	-1.309	0.493	0.134	0.296	-0.615	0.884
nyal	0.294	0.604	-1.249	1.837	0.070	0.453	-1.241	1.380
pol2	-0.297	0.383	-0.925	0.332	0.261	0.344	-0.375	0.896
ohi2	0.495	0.720	-0.844	1.833	0.195	0.482	-1.070	1.459
scub	-1.293	1.458	-2.905	0.319	0.328	0.586	-0.916	1.571
nico	-0.901	0.987	-1.959	0.157	0.295	0.440	-0.632	1.222
kerq	-0.540	0.603	-1.285	0.205	0.007	0.226	-0.631	0.645
mdo1	-0.560	0.612	-1.161	0.042	-0.070	0.238	-0.647	0.507



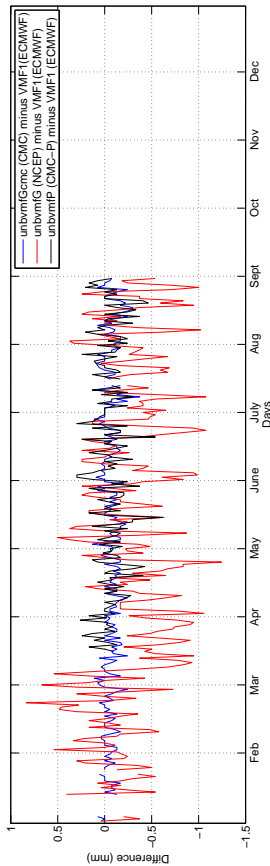
(D.2.2) AREQ



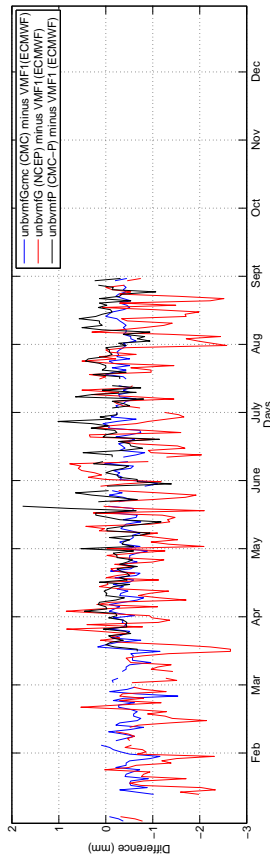
(D.2.4) DARW



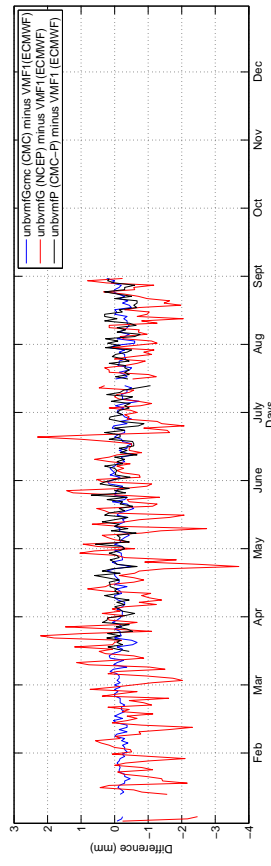
(D.2.6) HARV



(D.2.1) ALBH

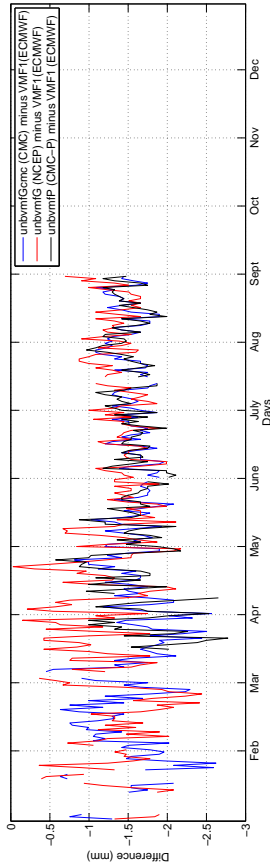


(D.2.3) CONZ

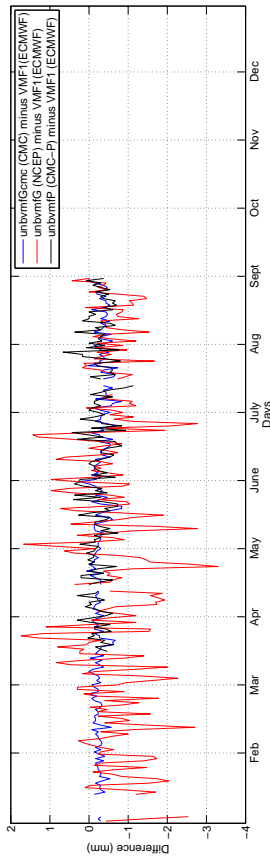


(D.2.5) FRDN

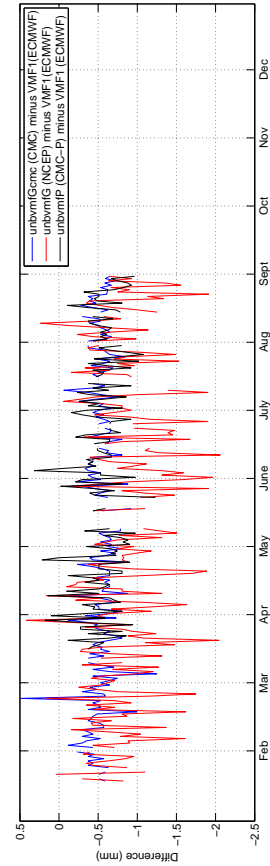
Figure D.2: PPP coordinate time series difference for unbvmfG (NCEP), unbvmfGcmc (CMC), and unbvmfP (CMC-P) minus VMF1 (ECMWF). For unbvmfG and unbvmfGcmc: January 1st to August 31st. For unbvmfP: March 17th to August 31st 2012. All dimensions in millimetres.



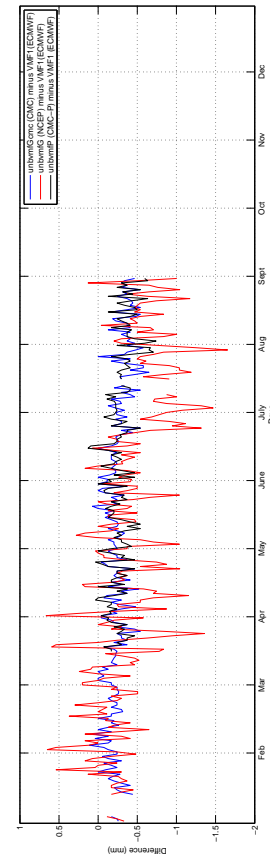
(D.2.8) IISX



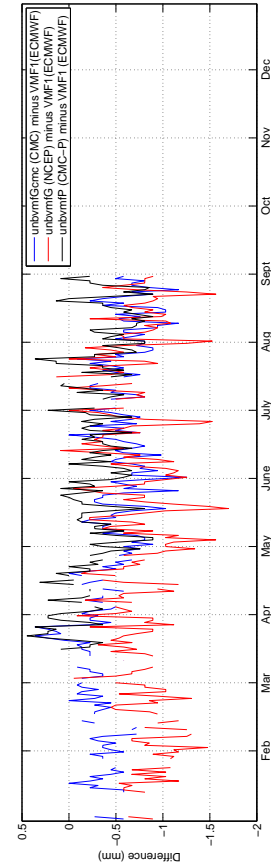
(D.2.7) HLEF



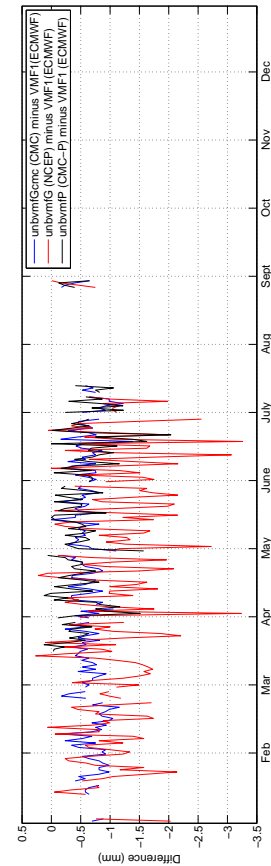
(D.2.10) KERG



(D.2.9) JPLM

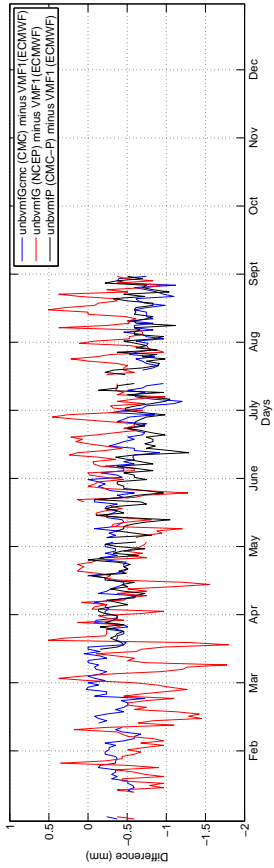


(D.2.12) LHAZ

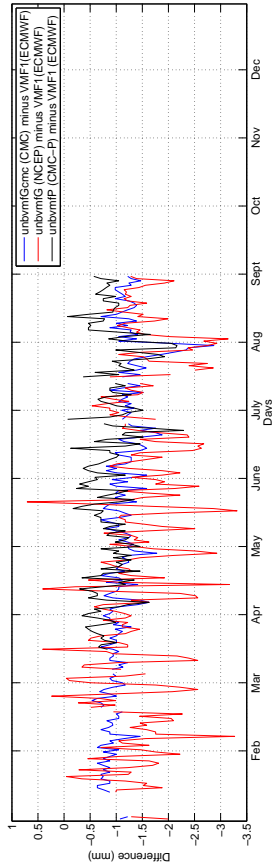


(D.2.11) KSMV

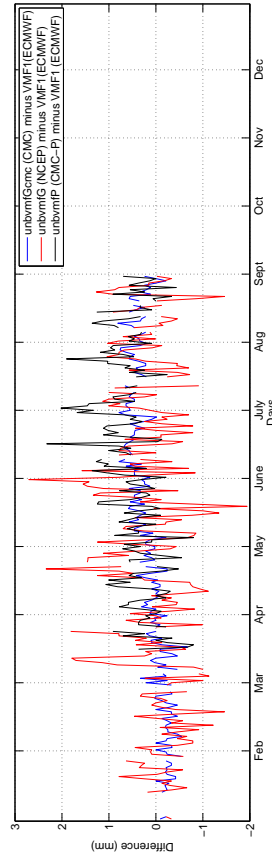
Figure D.2: PPP coordinate time series difference for unbvmfG (NCEP), unbvmfGcmc (CMC), and unbvmfP (CMC-P) minus VMF1 (ECMWF). For unbvmfG and unbvmfGcmc: January 1st to August 31st. For unbvmfP: March 17th to August 31st 2012. All dimensions in millimetres.



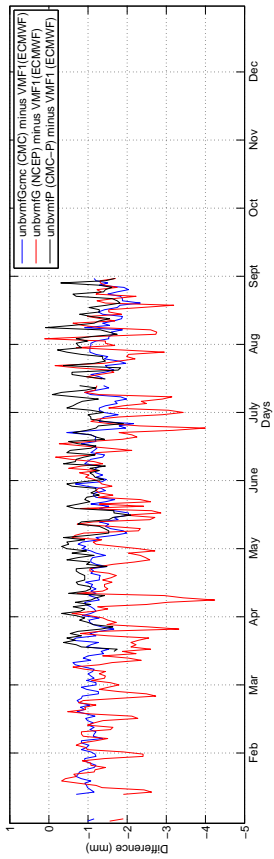
(D.2.14) MDO1



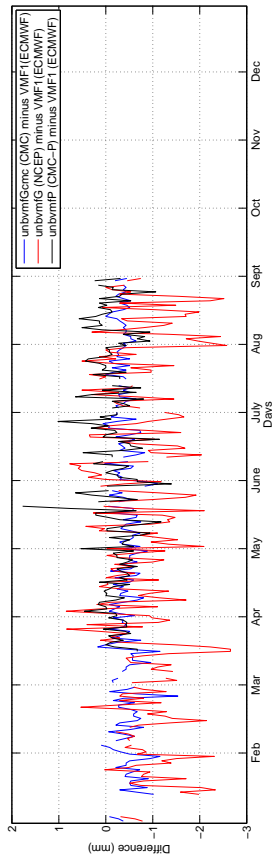
(D.2.16) NICO



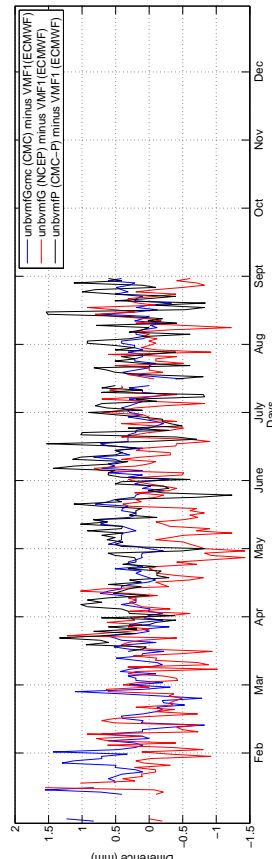
(D.2.18) OH12



(D.2.13) MASI

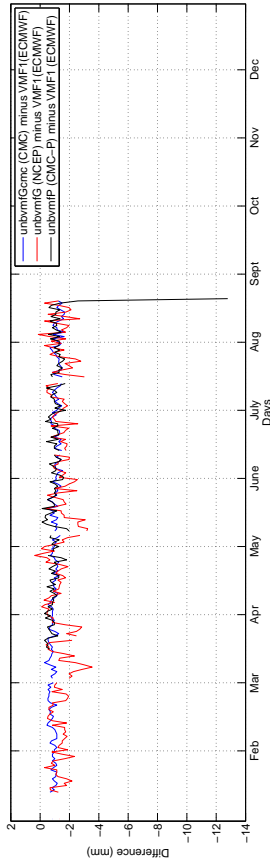


(D.2.15) MKEA

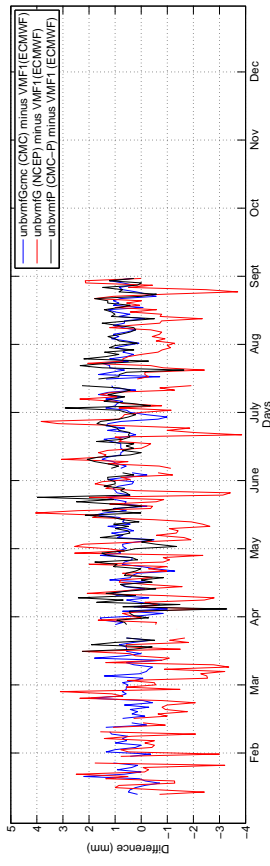


(D.2.17) NYAL

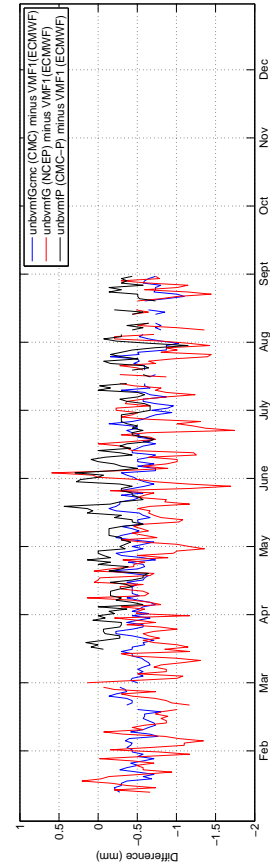
Figure D.2: PPP coordinate time series difference for unbvrmfG (NCEP), unbvrmfGmc (CMC), and unbvrmfP (CMC-P) minus VMF1 (ECMWF). For unbvrmfG and unbvrmfGmc: January 1st to August 31st. For unbvrmfP: March 17th to August 31st 2012. All dimensions in millimetres.



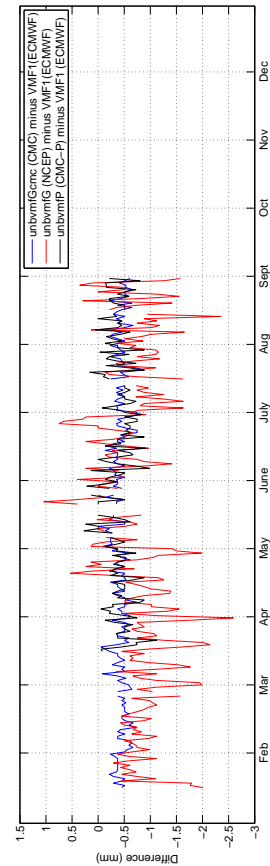
(D.2.20) PDEL



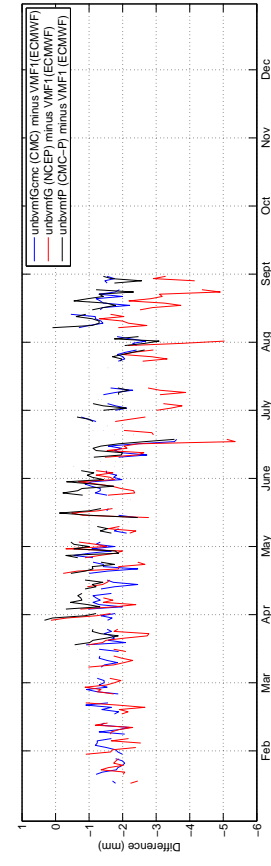
(D.2.19) OUS2



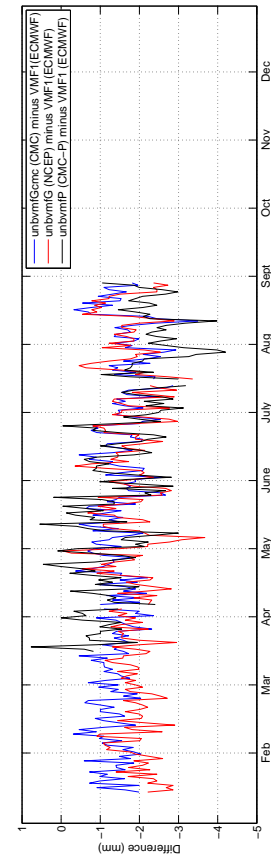
(D.2.22) POL2



(D.2.21) PETS

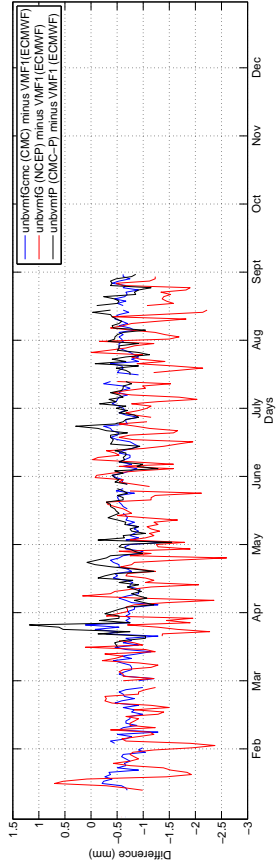


(D.2.24) SCUB

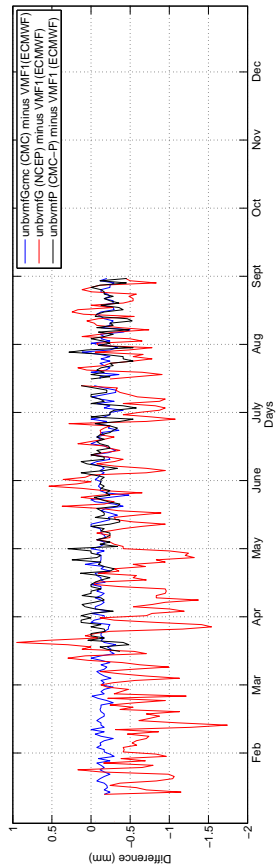


(D.2.23) POVE

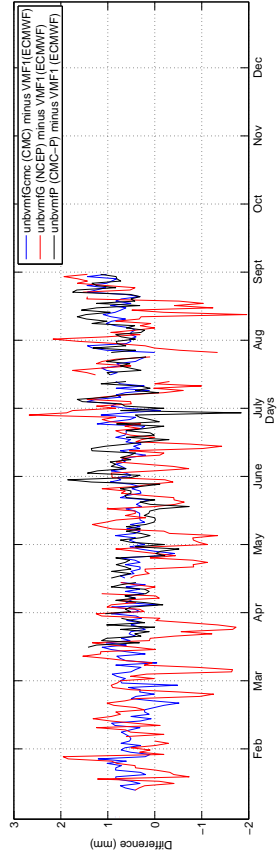
Figure D.2: PPP coordinate time series difference for unbvrmfG (NCEP), unbvrmfGmc (CMC), and unbvrmfP (CMC-P) minus VMF1 (ECMWF). For unbvrmfG and unbvrmfGmc: January 1st to August 31st. For unbvrmfP: March 17th to August 31st 2012. All dimensions in millimetres.



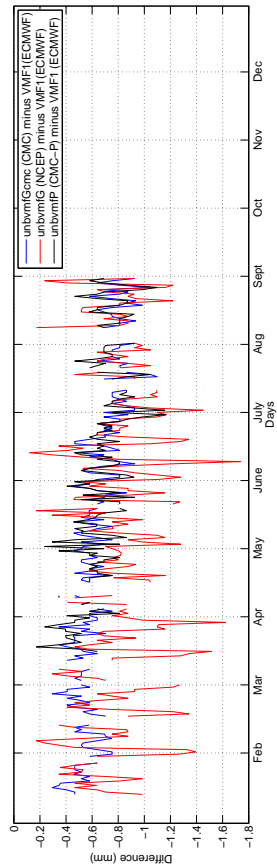
(D.2.26) SUTH



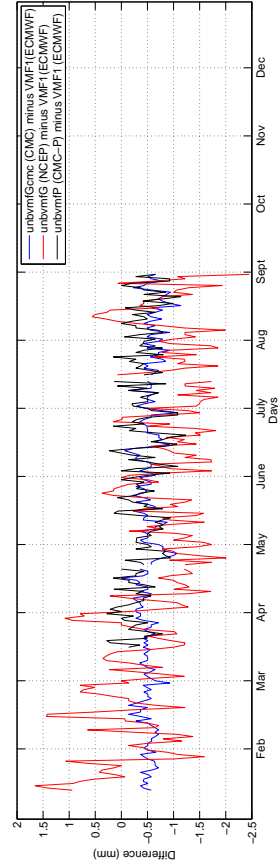
(D.2.25) STJO



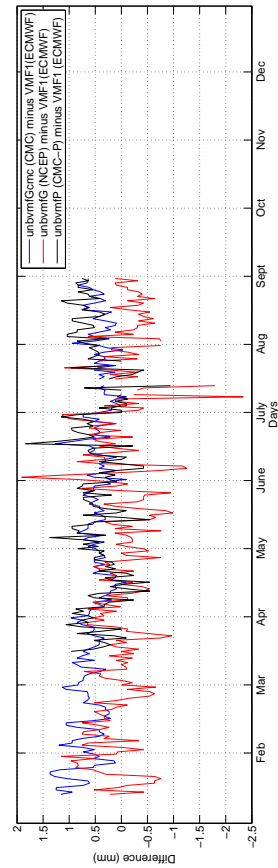
(D.2.28) THU3



(D.2.27) TEHN

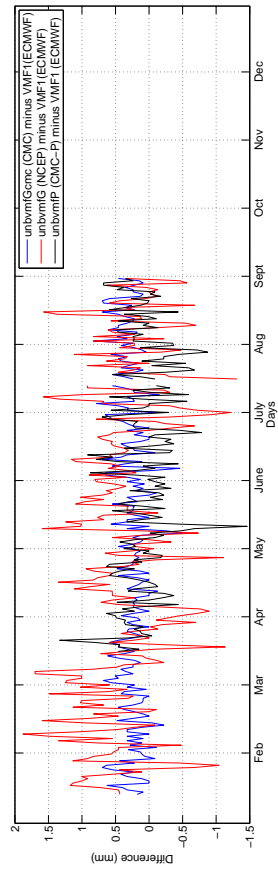


(D.2.30) WTZR

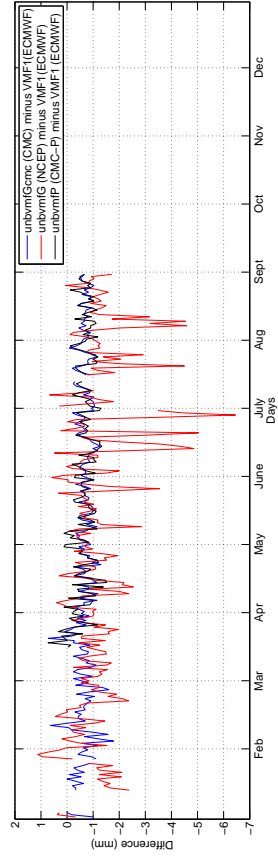


(D.2.29) TIXI

Figure D.2: PPP coordinate time series difference for unbvmfG (NCEP), unbvmfGmc (CMC), and unbvmfP (CMC-P) minus VMF1 (ECMWF). For unbvmfG and unbvmfGmc: January 1st to August 31st. For unbvmfP: March 17th to August 31st 2012. All dimensions in millimetres.



(D.2.31) YELL



(D.2.32) IQQE

Figure D.2: PPP coordinate time series difference for unbvmmfG (NCEP), unbvmmfGcmc (CMC), and unbvmmfP (ECMWF) minus VMF1 (ECMWF). For unbvmmfG and unbvmmfGcmc: January 1st to August 31st. For unbvmmfP: March 17th to August 31st 2012. All dimensions in millimetres.

# Vita

**Full Name:** Matthew McAdam

**Place and Date of Birth:** Hamilton, Ontario, Canada; September 11, 1976.

**Permanent Address:**

101-1904 28 Ave. SW  
Calgary, Alberta  
T2T-1K1

**University's Attended:**

University of New Brunswick — 2007 - 2010  
Bachelors of Science in Engineering (Geomatics Engineering)

University of Windsor — 1995 - 1999  
Bachelors of Applied Science (Mechanical Engineering)

**Presentations:**

Santos, M.C., M.P. McAdam and J.Boehm (2012). "Implementation Status of the UNB-VMF1." Geophysical Research Abstracts, European Geosciences Union General Assembly (EGU 2012), 22-27 April, Vienna, Vol.14, EGU2012-13759. (Poster Presentation).

McAdam, M. (2012). "Implementation and Validation of a UNB Vienna Mapping Functions Service" 2012 Semi-Annual Graduate Seminar, University of New Brunswick, Department of Geodesy and Geomatics Engineering, Fredericton, N.B., November 21. (Oral presentation).

McAdam, M., N.Chai and M. C. Santos (2012). "Evaluation of pressure extracted from NCEP and CMC global numerical weather prediction models against in-situ and GPT pressure." Fall Meeting 2012, American Geophysical Union, San Francisco, Calif., December 3-7, Eos Trans. AGU Fall Meet. Suppl., Abstract G11A-0903. (Poster presentation).



Santos, M.C., and M.McAdam. (2012). "Development and Validation of UNB-VMF1." Fall Meeting 2012, American Geophysical Union, San Francisco, Calif., December 3-7, Eos Trans. AGU Fall Meet. Suppl., Abstract G14A-08. (Oral presentation).